THE UNIVERSITY OF CHICAGO

VAPOR-PHASE GROWTH OF TWO-DIMENSIONAL MOLECULAR CRYSTALS AND THEIR STRUCTURE-PROPERTY RELATIONSHIPS

A DISSERTATION SUBMITTED TO

THE FACULTY OF THE DIVISION OF THE PHYSICAL SCIENCES

IN CANDIDACY FOR THE DEGREE OF

DOCTOR OF PHILOSOPHY

DEPARTMENT OF CHEMISTRY

BY

FAUZIA MUJID

CHICAGO, ILLINOIS

AUGUST 2022

TABLE OF CONTENTS

LIST OF FIGURES

LIST OF TABLES

ACKNOWLEDGEMENTS

A Ph.D. is an incredibly challenging experience for many people, but it is especially trying for the economically-disadvantaged, first-generation American, first-generation college grad. When I started the UChicago Ph.D. program, I did not realize how underprepared I would be to face the challenges of standing beside students from privileged backgrounds, trying to impress professors who lacked the life experiences to understand (much less accommodate) students from minority backgrounds. There were many occasions in the past 6 years where I felt disparaged to the point of nearly quitting. I had even decided a plan for which university I would attend to after leaving UChicago. And yet, somehow, by the grace of God, I made it through to the end. When I think about how or why I stayed, I remember the postdocs and graduate students who, despite coming from very different worlds, went out of their way to support me through this difficult journey.

Kibum, who consistently encouraged me when I was a new student and tried to help build my self-esteem. He assured me I was doing well, acknowledged my hard work and willingness to learn, and even offered to take me as one of his own students if I was unable to pass my candidacy exam.

Kan-Heng, who treated me as an equal even from my first year, sharing his science and bouncing ideas off of me. He is one of the few people I know who judges someone's work solely on the work itself, unaffected by preconceived notions of the person doing the work. I learned what a good scientist is by observing his curiosity, objectivity, critical thinking, and passion for trying new things.

Hui, who could not help me with research but still made a consistent effort to ask me how my project was going and encouraged me to change directions when it was very obviously

not going well. After many group meeting presentations gone horribly wrong, he even offered to start driving me to lab on weekends (30-minute walk from my apartment), with the hope that being able to work more might help me do better.

Josh¸ who always kept me on top of deadlines, especially during our first few years. I probably would have missed the NSF GRFP if it was not for him. He also made me realize that I was not alone in my experience—that it is inevitable for perfectly capable people to struggle when placed in an environment that is not conducive to their success.

Jae-Ung, who let me experience, for a brief three months, the relief that comes with working with a postdoc and not having to shoulder the entire burden of a new project on your own. As one of the kindest human beings I have ever met, he made me realize that excellence in work and excellence in conduct are not mutually exclusive behaviors. He knew how to identify when was the proper time to criticize, and when was the time to let something slide—the most important trait of a good manager. I also credit him with the discovery that allowed me to finally develop an idea to take my seemingly hopeless project to completion.

Chibeom, who had an uncanny amount of knowledge on growth and furnace-building and was always willing to answer my questions (sometimes even the same question multiple times). Although I worked alone for most of my entire PhD, he was the one person who watched what I was struggling with and periodically intervened to teach me how to do something better—all without being asked. Chibeom is the person that I credit for my expertise in material growth and the rigor with which I carry out my science. He is also the only reason I was able to work so hard to get to where I am today, because I always knew that even if the rest of the lab got to go home at 8 pm, I could always count on Chibeom to be working late nights, suffering alongside me.

Andy, who taught me so many random things about surface and vacuum science and made me realize that superhumans do indeed exist. He insisted that I was a valuable scientist, in spite of the people who conditioned me to believe I was inferior to other students. He convinced me that research was my calling, even asking me to be his postdoc multiple times.

Myungjae, who gave an enormous amount of technical advice to someone with zero optics background, and did so patiently, without any judgement. He trusted me and listened to my opinions, really instilling in me the belief that I was a highly capable and competent researcher. We had so much fun doing experiments in the optics lab together.

Yu, who made me realize that I was not the crazy one—assuring me that graduate school should not be as difficult as it was for me. He insisted that I wasn't "slow" and that I was actually a great student, telling me that had I been in a different lab, I would have been much less stressed and had many more publications to show for my hard work. He had a higher level of understanding about how to work with students and motivate the people around him. He is one of the few academics I've met who understood that all students are different, and a good professor should try to work with each student individually, rather than apply the same arbitrary standard to everyone, which forces certain groups of students to fall between the cracks.

And finally, **Jaehyung**, who only knew me for a short time, but somehow believed that I was already ready graduate at the beginning of my 5^{th} year. He really tried to get me to pursue a career in academia because he thought my skills would be "wasted" in industry—something that I would have never, in a million years, thought about myself.

Although there was a lot of hardship, there was also a lot of fun—joking in the office, telling stories at lunch, sharing in our mutual struggles. It was with the support and encouragement of these people, among others, that I was able to realize that I was as worthy of

being in the UChicago Ph.D. program as any of the other students. Through this journey, I learned that everyone has a unique set of skills that they bring to the table—a skillset that depends on their particular background and thus has a unique value. Sometimes you will encounter people who are not open-minded enough to understand the value that you bring, such as my experience when I started first graduate school. Now however, I understand that rather than believing the people who devalue you, you should put your belief in yourself and show them, with your work, that their assumptions were wrong.

ABSTRACT

The wafer-scale synthesis and patterning of thin films forms the foundation of modern technologies. As we continue to scale down the size of electronic systems, we find ourselves pushing the limits of conventional thin-film materials. For this reason, two-dimensional (2D) materials, which exist as stable films that are only few atoms thick, are becoming the center of intense research. For many years, 2D materials simply presented exciting opportunities for exploring exotic physical phenomena. However, similar to how silicon technologies are enabled by the ability to grow large crystals of silicon, scalable synthetic techniques are necessary to take the next step towards implementation of 2D materials in real electronic systems. In this thesis, we present our approaches towards the synthesis of 2D crystals and films of inorganic and organic semiconductors, using gas-phase deposition techniques. Chapter 1 will introduce the unique, anisotropic structure of 2D materials, and use this as a context for understanding the growth mechanics of 2D systems. Chapter 2 will focus on the controllable synthesis of semiconducting 2D transition-metal dichalcogenides (TMDs), such as MoS_2, WS_2, and WSe_2, using kinetically-limited metal-organic chemical vapor deposition. We will discuss the conditions necessary to scale up from single crystals to wafer-scale monolayer films, as well as provide a detailed understanding of the role of each reactant in the growth. Chapter 3 will elaborate more on challenges in producing high-quality films with reproducible physical, mechanical, and surface properties. Chapter 4 will describe how these TMD films can be used as substrates for the physical vapor deposition of highly-crystalline 2D molecular films in the thermodynamic limit. Chapter 5 will present specific studies on the growth mechanisms of perylene-based 2D molecular crystals. Chapter 6 will illustrate how intermolecular forces can be modified through molecular functionalization to grow crystals with different structural

characteristics. These structural differences manifest as unique optical properties, specifically related to responses to polarized light. Chapter 7 will present a number of ideas and proof-of-concept demonstrations for integrating these nanometer-thick hybrid films into functional systems, with a particular focus on electrochromic devices.

CHAPTER ONE

Introduction to Two-Dimensional Film Growth

1.1 Structure of Two-Dimensional Crystals

Since the Nobel Prize winning isolation of graphene in 2004,[1] two-dimensional (2D) nanomaterials—sheets of crystals with thickness on the order of nanometers—have gained traction within the material science research community for their potential applications in electronics and optoelectronics.[2–4] Numerous 2D materials have been isolated since graphene,[5–9] with electronic properties ranging from insulators to metals and optical absorption from the infrared to ultraviolet. One such class of 2D materials is transition-metal dichalcogenides[10,11] (TMDs), which take the general form MX_2 (structure shown in **Fig. 1.1b**).

Two-dimensional TMDs (as well as other 2D materials) are possible to isolate because they come from crystals that have a very unique type of structure: van der Waals (vdW) layered crystals. These crystals are highly anisotropic in their in-plane vs. out-of-plane bonding. **Figure 1.1** elaborates on this structural difference between a conventional crystal and a vdW layered crystal. Most crystals, such as the crystal of silicon shown in **Fig. 1.1a** (top panel), exhibit covalent or ionic bonding throughout their entire structure. The consequence of this is that, when such a crystal is cleaved, the exposed surface atoms will be left with unpaired

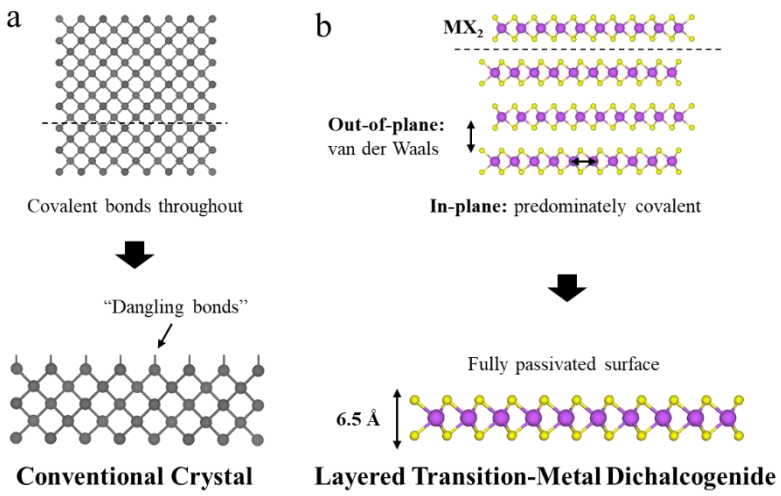

Figure 1.1. Difference between the structure of a) a conventional crystal such as silicon, and b) a layered van der Waals crystal.

electrons, or “dangling bonds” (**Fig. 1.1a**, bottom panel), which are highly reactive and display different chemical and physical properties from the bulk of the crystal. If the material is thinned down to the nanometer-scale, the dangling bonds start to dominate the properties of the crystal, hence rendering them useless for most applications. This is very different for a layered van der Waals crystals, however, such as the layered TMD shown in **Fig. 1.1b** (top panel). These materials exist as layers of covalently-bonded crystals (i.e., in the “in plane” direction) that are held together via van der Waals forces (i.e., in the “out-of-plane” direction). The chalcogen atoms above and below the transition metal are fully bonded within a single layer (i.e., a “monolayer”). Thus, cleaving a TMD crystal results in a fully-passivated surface, producing a crystal that is stable at only three atoms thick.

For many years, the focus of the 2D crystal community has been on inorganic 2D materials, such as the TMDs introduced above. More recently, interest has expanded to molecular crystals (**Fig. 1.2**), which are solids bound by weak intermolecular forces such as van der Waals forces,[12,13] pi-pi interactions,[14] hydrogen bonding,[15] and halogen bonding.[16] Compared to inorganic nanomaterials, organic nanomaterials provide a greater degree of tunability in terms of their optical, electronic, and chemical properties,[17–22] due to the availability of a vast library of organic synthesis and functionalization approaches.

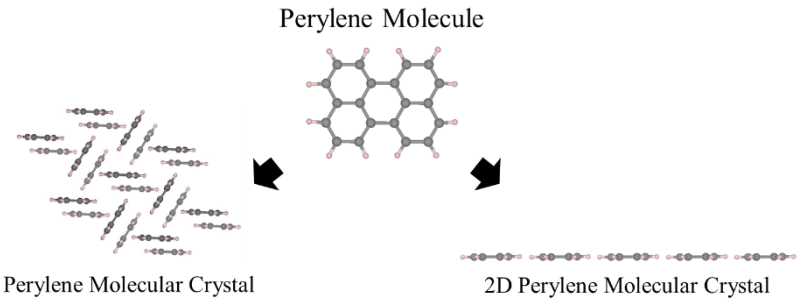

Figure 1.2. Difference between the structure of a traditional bulk molecular crystal (left) and a 2D molecular crystal (right), using perylene as an example.

In order for any of these 2D materials to be implemented in a real-world setting, however, they need to be synthesized on an industrially-relevant scale. For inorganic TMDs, this is done using a process called chemical vapor deposition (CVD),[23] where gas-phase precursors react in a high-temperature environment to deposit a material on the surface of a growth substrate. For molecular crystals, physical vapor deposition (PVD)[24] processes are used, which involve the sublimation and redeposition of a material onto a target substrate. We will first discuss how it is possible to achieve two-dimensional growth in vapor deposition processes, specifically related to the CVD growth of 2D TMD crystals. We will then expand the discussion to the PVD of 2D molecular crystals.

1.2 Mechanics of Gas-Phase Thin-Film Formation

Chemical vapor deposition and physical vapor deposition are inherently nonequilibrium processes. This is because reactions at the vapor-solid interface are carried out under conditions of mass flow. **Figure 1.3** shows a schematic illustrating mass transport in a CVD reactor tube.[25] Because the rate of mass into the system must equal the rate of mass out, there is a necessary change in the velocity of the gas flowing between areas with different volumes. This difference in the flow rate results in turbulence (or turbulent flow) near the region of volume change. There are also regions where the gases flow parallel to each

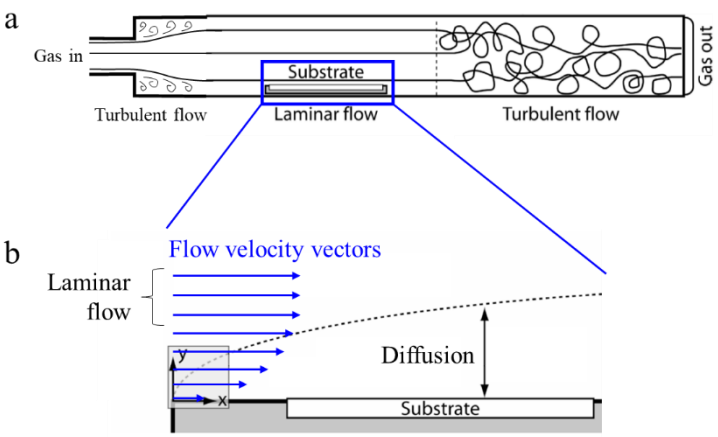

Figure 1.3. Regimes of fluid transport in a CVD reactor. Bulk flow (turbulent or laminar) dominates away from the substrate (a), but gases will move by diffusion near the surface of the substrate (b). Adapted from Ref. 25.

other, without mixing between layers, called laminar flow. Depending on the tube dimensions and gas properties however, laminar flow can only be sustained for a certain distance, at which point the flow becomes turbulent once again. In order to achieve the most homogeneous concentration of reactants (and hence, homogeneous reaction rate) at the surface of the growth substrate, the substrate must be placed in the laminar flow regime (as shown in the blue box in **Fig. 1.3a**). As we approach the surface of the substrate, the velocities of the gases progressively decrease due to friction with the solid surface, and there is a transition from the "bulk flow" regime discussed above to a diffusive transport regime (**Fig. 1.3b**).

The understanding of the growth process of monolayer TMDs presented in this chapter is based on the assumption that that diffusion (not flow) dominates the transport of reactants and products near the surface of the film (also known as the "stagnant film model"). **Figure 1.4** illustrates the major processes that can occur during a CVD reaction.[26] Gaseous precursors diffuse in from the main flow region and are transported to the surface of the substrate, either before or after reacting with other gases present. After the precursors adsorb to the surface of the substrate, a few things can happen: the precursor can diffuse across the surface, desorb from the surface, react with other precursors to initiate nucleation, or can react with the edge of an existing nucleus/island resulting in film growth. The latter two processes typically release volatile species that can desorb from the surface or react with other species in the vicinity to form solid byproducts. Another important process to consider is the adsorption of precursors on top of the existing film. This can result in

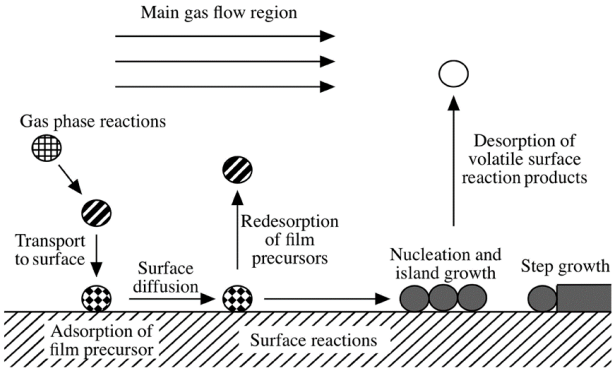

Figure 1.4. Processes that occur during CVD reactions. Reproduced from Ref. 26.

nucleation and growth of a second layer, which is undesirable in the case of 2D film growth. In the next section, we will discuss how it is possible to limit film growth exclusively to two dimensions.

Vacuum reactors for the processes described above are bulky, making it difficult to maintain uniform temperature conditions across the tube. Altogether, it can be understood that CVD processes lack mass conservation and are also subject to concentration and thermal gradients. Consequently, although thermodynamic predictions may give us an idea about which products are stable under what reaction conditions, the actual experimental results will, in general, be very different. We must therefore rely on kinetics to develop a more accurate understanding of CVD reactions. **Figure 1.5** depicts the factors that limit the growth rate in CVD in different temperature regimes.[23] At relatively low temperatures, the growth rate, *R*, is limited by the activation energy barriers, E_a, for the chemical reactions between the precursors. At higher temperatures, where the reaction rates are much faster, the growth rate is proportional to the diffusion coefficients, *D*, of reactants moving across the substrate surface. Growth in the diffusion-limited regime is highly sensitive to the physical environment of the precursors, such as substrate morphology and reactor geometry. The diffusion-limited and reaction-limited regimes are the dominant factors for consideration in the monolayer growth of TMDs by MOCVD. There is one more regime, at extremely high temperatures, where the reaction rate is thermodynamically-limited. This is due to precursor desorption at such high temperatures where solidification becomes thermodynamically unfavorable, resulting in a decreasing reaction rate

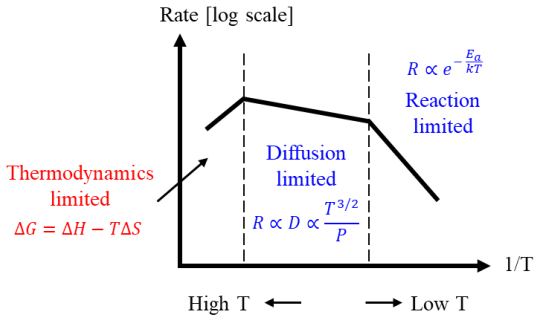

Figure 1.5. Rate-limiting factors in CVD growth as a function of temperature.

with increasing temperature. This growth regime becomes the most important in the PVD of monolayer organic crystals, which will be discussed in more detail in Section 1.5.

1.3 Thermodynamic Requirements for Monolayer Growth

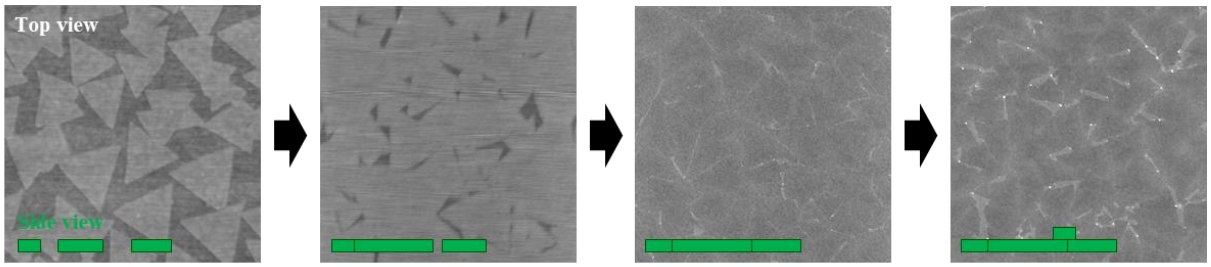

Figure 1.6. AFM images showing the morphology evolution of a polycrystalline MoS_2 film, growing on a SiO_2/Si wafer, at different timepoints during the growth. A schematic of the side view of the growing film is shown in the bottom left of each image.

Figure 1.6 shows atomic force microscopy (AFM) images illustrating how these monolayer TMD films grow when they deposit on substrate surfaces, using MoS_2 growth on a SiO_2/Si wafter as a representative example. A diagram of what each state looks like from the side is depicted in green in the bottom-left of each image. As briefly explained in Section 1.2, during a vacuum deposition process, gaseous precursors react to form tiny nuclei on the surface of the substrate. Then, other reactants add to the edges of the nuclei, resulting in islands that grow outward. If the reaction conditions are controlled carefully, these isolated single-crystal islands (**Fig. 1.6**, first image) grow exclusively in-plane. Eventually, these islands begin to merge, forming a partially-connected, polycrystalline film (**Fig. 1.6**, second image). Reactants continue filling holes in the film until it becomes completely continuous (**Fig. 1.6**, third image). After the entire surface of the substrate is covered, the reactants have nowhere else to deposit, so they begin to nucleate and grow on the existing monolayer film (**Fig. 1.6**, fourth image). Therefore, by controlling the time of the reaction, it is possible to achieve a large-area TMD film that is fully monolayer.

To understand why these films grow in this two-dimensional manner, rather than immediately nucleating a second layer while the first layer islands are still growing, we need to think about the energetics of nucleation and growth phenomena and how these processes relate to a specific material's structure. For simplicity, we start by looking at the free energy changes, ΔG, experienced by a spherical cluster undergoing *homogeneous* nucleation, followed by growth, as a function of the cluster's radius, r, as described by Classical Nucleation Theory, which is shown in **Figure 1.7**.[27] This is the simplest type of nucleation, which occurs in a purely gas-phase or purely solution-phase reaction. We can begin by introducing the concept of surface energy, γ, which is the amount of energy per unit area required to create a surface.[28] The surface energy of a solid increases with the strength of the interactions (e.g., bonds) broken to form the surface. Creating surfaces is an energetically-unfavorable process because it results in atoms that are not in their most stable electron density state (e.g., having missing, or "dangling", bonds).

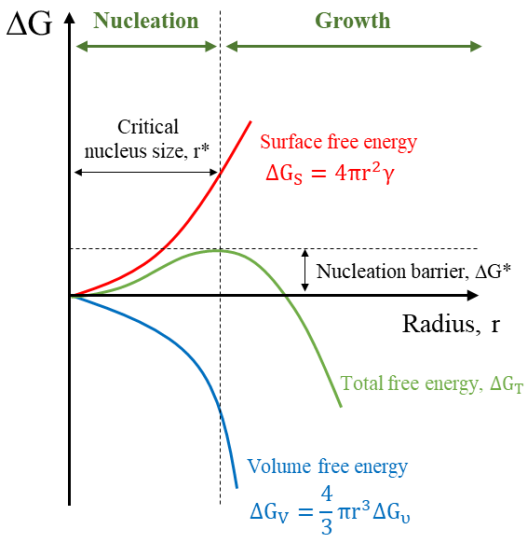

Figure 1.7. Free energy changes during homogeneous nucleation.

Hence, we can see why the red line in **Fig. 1.7**, corresponding to the surface free energy change of a cluster, ΔG_S, increases with radius, r. Surface free energy destabilizes a growing cluster, increasing with increased surface area, which scales as the radius squared for a spherical cluster. However, as a cluster grows, there is a negative (favorable) free energy change—the volume (or bulk) free energy change, ΔG_V—which is associated with the formation of stable bonds within the cluster. This component scales with the volume of the cluster (as radius cubed).

These two forces compete to determine the total free energy change of the system, ΔG_T (green line), which determines whether a cluster will nucleate and then grow. Initially, there is an energy barrier for nucleation (ΔG^*), but after the cluster reaches a critical nucleus size (r^*), then any further increase in size only reduces the total free energy. Hence, when $r > r^*$, the cluster transition from the stage of nucleation to growth.

Although the above description is specific to homogeneous nucleation, these concepts can still be used to understand *heterogeneous* nucleation and growth processes, which are relevant to CVD and PVD. Heterogeneous nucleation is facilitated by the presence of a foreign substance, such as an impurity in the reaction or on a surface.[29] In this process, one "side" of the nucleus is somewhat passivated due to interactions with the impurity or substrate surface, leading to a smaller energy barrier, ΔG^*, for heterogeneous nucleation compared to homogeneous nucleation. Furthermore, growth substrates are usually not uniform, so different sites on the substrate surface (i.e., defects, steps, impurities, etc.) can exhibit drastically different nucleation barriers. Hence, nucleation rates in vacuum deposition processes vary significantly depending on quality of the substrate.

Using the concepts of surface energy and energy barriers for nucleation, we can explain the two-dimensional growth of TMD monolayers. **Figure 1.8** depicts the strengths of various interactions present for MoS_2 nuclei and islands growing on a SiO_2 substrate. Layered TMD materials have very low surface energy, since their weak, out-of-plane van der Waals forces (**Fig. 1.8**, red arrows) results from the chalcogen atoms within each individual layer already being fully bonded. As such, the surfaces of TMD monolayers are largely unreactive. In contrast, the in-plane bonds of TMD materials are strong covalent bonds (**Fig. 1.8**, green arrows), so the edge of a TMD layer has highly-reactive dangling bonds. Because nucleation is an energetically

uphill process, a reactive species diffusing across the surface of the substrate is much more likely to react with the edge of an existing island (i.e., growth, which is has little to no activation barrier), rather than create a new nucleus.

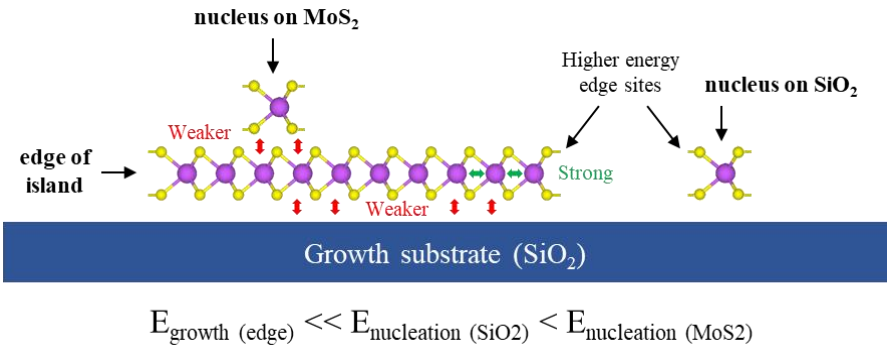

Figure 1.8. Schematic illustrating the forces between species during the growth of MoS_2 on a SiO_2 substrate, where E is the activation energy barrier for a particular nucleation or growth process.

Furthermore, because the MoS_2 islands have exceptionally low surface energy, the barrier for heterogenous nucleation on an existing MoS_2 layer is much greater than that for nucleating on the SiO_2 surface, which is typically riddled with impurities/defects. For this reason, even after the SiO_2 is completely coated with a monolayer of MoS_2, the second layer nucleation does not occur on the basal plane of the MoS_2 domains. The bilayer nucleation actually occurs on top of the regions where two MoS_2 domains merge (i.e., the grain boundaries). Since two crystals with different orientations cannot merge perfectly due to a mismatch in the number and spacing of atoms, grain boundaries exhibit more uncoordinated atoms and defects than other areas of the film. Hence, multilayers nucleate preferentially in these regions.

This also explains why the bilayer regions in the fourth image in **Fig. 1.6** form as elongated structures rather than triangular shapes—they are growing along the grain boundaries of the underlying MoS_2, preferentially passivating the defective regions of the MoS_2 surface. At this point, MoS_2 is now the growth substrate as well as the growing material. For this reason, it is not possible to grow a fully continuous bilayer of MoS_2—the incoming reactants see no difference between nucleating on the first layer or the second, so continuing the growth beyond

this point typically results in multilayer structures lining the domain boundaries of the monolayer film. Conveniently though, these multilayer structures can be used as a quick method for roughly determining the grain size and grain boundary location of monolayer TMD films, which will be applied in later sections and chapters.

To summarize, it is the large anisotropy of bonding forces in layered TMDs that allows the materials to be synthesized directly as 2D monolayers. This understanding can also be applied to the synthesis of molecular 2D systems, which will be discussed in Section 1.5.

1.4 Kinetic Growth Regimes in Two-Dimensional Material Growth

Although we can see that energetics favors the growth of TMD crystals in the lateral (as opposed to vertical) direction, there are, in fact, many cases where the growth will only proceed two-dimensionally until the crystals reach a certain size or the film reaches a specific surface coverage, after which bilayer islands will start depositing on top of the monolayer film. Hence, actually achieving a two-dimensional growth mode requires very careful control of reaction kinetics. There are two kinetic regimes relevant to these MOCVD-synthesized TMD materials, which were previously introduced in **Fig. 1.5**. These are reaction-limited growth and diffusion-limited growth.

Figure 1.9 shows optical images of MOCVD growths in these different regimes. The two growths show strikingly different crystal shapes, which is the hallmark for determining the rate-limiting mechanism behind a surface reaction. We start by discussing the

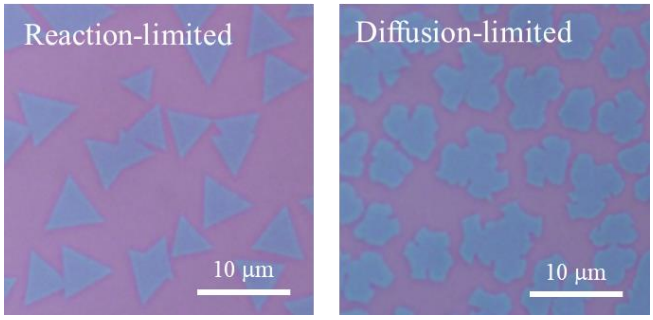

Figure 1.9. Optical images of a WS_2 growth in the reaction-limited regime (left) and a MoS_2 growth in the diffusion-limited regime (right).

reaction-limited regime, also known as attachment-limited growth. Here, the growth rate of crystals is limited by the activation energy barriers, E_A, for reactants trying to attach to a certain edge/face of the crystal. This type of growth dominates at lower temperatures, where $kT < E_A$, and produces highly-faceted crystals, such as those seen in **Fig. 1.9** (left panel). The faceting is a result of different edges of a crystal having different activation barriers for attachment, so the growth rates of specific edges vary. A simple way to explain the (2D) growth rate of a particular edge, R_{edge}, is as follows:[30]

$$R_{edge} = \left(c * v_a * e^{-\frac{E_a}{kT}} - n_o * v_d * e^{-\frac{E_d}{kT}}\right) * s_o \qquad \textbf{Eq. 1. 1}$$

The term highlighted in blue represents the *attachment term*, which is the rate at which chemical species attach to the edge. Here, c is the concentration of the limiting reactant near the edge, v_a is the attachment frequency, and E_a is activation barrier for attachment. In general, however, the chemical reactions will be somewhat reversible, and in many cases, side reactions that etch away at a crystal edge are also possible, such is the case with graphene growth.[31] For these reasons, a *detachment term* (highlighted in red) must also be included, to account for the rate at which chemical species detach from the edge. This term depends on n_o, which is the line density of atoms on edge, v_d, the detachment frequency, and E_d, the activation barrier for detachment from the edge. These two terms are multiplied by the unit cell area of the material, s_o, to get the total growth rate.

From **Eq. 1.1**, there are two dominant factors in determining the growth rate anisotropy of different crystal edges. The first is the activation barrier for attachment (E_a), which was already mentioned briefly, and the second is the concentration of the limiting reactant (c) for the growth of that particular edge. We can understand why different edges have different activation

barriers in terms of symmetry-breaking. **Figure 1.10** depicts the relative growth rates of various edges of a 2D crystal with hexagonal symmetry, such as MoS_2.[32] The growth rate is slower for edges with higher symmetry, such as the zigzag and armchair edges (red and blue traces in **Fig. 1.10**, respectively). This is because growing on these straight edges requires the "nucleation" of an entire new ring (**Fig. 1.10**, dark red circles). This breaks the symmetry of the edge, and hence has a significant activation energy barrier associated. This nucleation step is rate-limiting. Once the ring has been established, the edge is now "kinked", and each addition of two new atoms only propagates the existing kink structure, so there is no additional energy barrier for growth from that point. The various lower-symmetry tilt edges (e.g., green trace in **Fig. 1.10**) are intrinsically kinked, and therefore circumvent that activation barrier. The higher the density of kinks on an edge, the faster the growth rate of that edge.

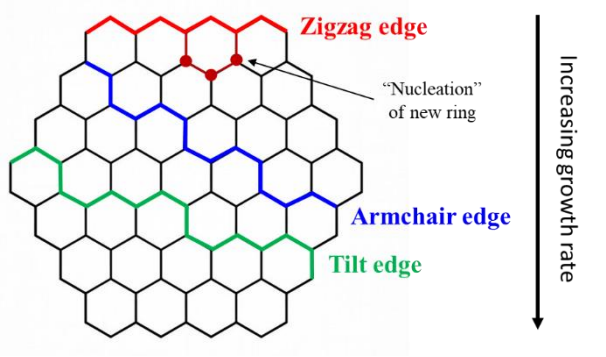

Figure 1.10. Relative growth rates of edges of a 2D crystal with different symmetries.

Rapidly growing edges/faces of a crystal shrink and disappear. This is why 2D hexagonal crystals typically exhibit the zigzag or armchair edges—because the lower symmetry edges grow significantly faster and disappear. Although it is clear that growth from different crystal edges will have largely different activation barriers, it is still possible for edges with higher E_a to grow faster by adjusting certain reaction conditions. This is due to the second dominant factor in **Eq. 1.1**—the limiting reactant concentration. In TMD materials, which are composed of two atomic species, some edges are terminated by the metal species and some by the chalcogen species. Depending on the concentration of the metal or chalcogen precursor near a particular edge

termination, the growth rate will vary.[33] This can be seen more clearly from **Fig. 1.11**, which shows how the shape of a zigzag-terminated monolayer MoS_2 crystal changes according to the ratio between the Mo and S precursors. When there is an excess of Mo, the Mo reacts with the S-terminated edges, causing them to grow faster and resulting in a triangular crystal that is Mo-terminated (**Fig. 1.11**, top row). For an excess of the S precursor, the Mo-terminated edges grow faster, resulting in a triangular crystal that is S-terminated (**Fig. 1.11**, top row). If there are roughly equal concentrations of each reactant, both terminations grow at the same rate, resulting in a hexagonal crystal with equal edge lengths for both terminations.

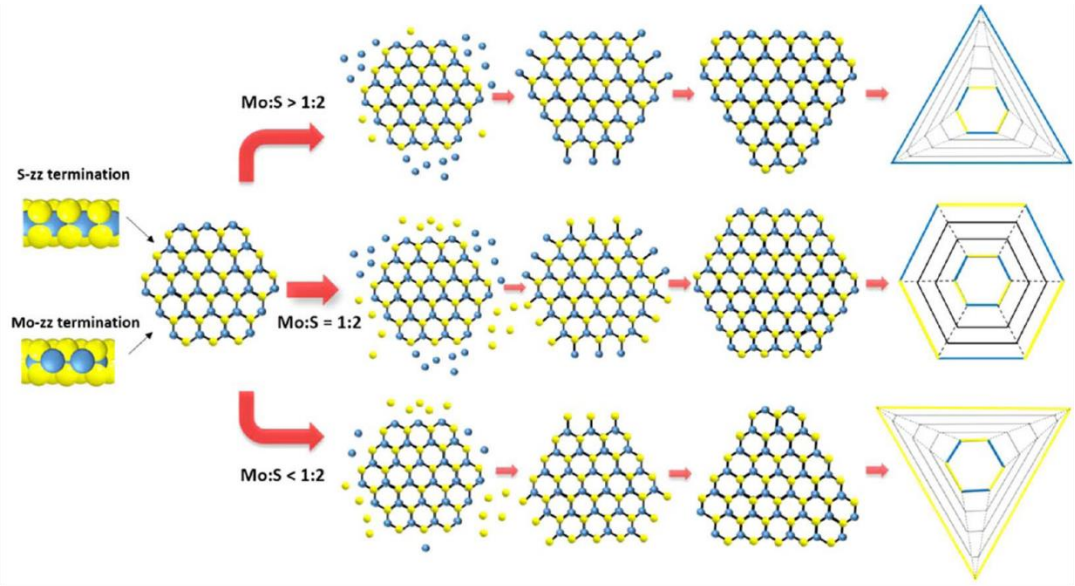

Figure 1.11. Effect of reactant concentration on the growth rate of edges of TMD crystals with different terminations. Reproduced from Ref. 33.

While growth in the attachment-limited regime may be desirable if an application requires the use of single-crystal TMD monolayers, for the growth of large-scale (polycrystalline) films, growth in the diffusion-limited regime is actually necessary. Diffusion-limited growth, also known as mass transport limited growth, occurs at higher temperatures, where reactions rates are faster, and the rate-limiting step for crystal growth is the diffusion of active species across the growth substrate. Contrary to attachment-limited growth, diffusion-

limited growth occurs when chemical species attach to edges more easily than they move around (i.e., $kT > E_A$), and hence typically results in irregularly-shaped domains, such as those seen in **Fig. 1.9** (right panel). We can understand this by recalling that a reactive species that makes its way to the surface of the growth substrate diffuses around until it meets the edge of a growing island. If the species has enough energy, it will react and stick to the edge. If not, the species can detach and diffuse elsewhere, or it can enter a loosely-bound state, where it diffuses around the edges of the island, until it can overcome the energy barrier for attachment.

Because the attachment energy difference between edges is small compared to the reactant's thermal energy, all sites around the crystal island can be treated as equal. Hence, the growth can be understood with a simple sticking probability model, such as that depicted in **Fig. 1.12**, which shows how the shape of an island changes depending on the magnitude of the sticking probability parameter, S.[34] In the limit of high diffusion (small S), the crystal grows as a nearly isotropic mass, which becomes more and more fractal as the diffusion is hindered (large S).

Although diffusion-limited growth ignores attachment energy differences around a crystal island, that does not mean that growth in this regime always produces isotropic fractals or masses such as those seen in **Fig. 1.12**. Elongated structures can be formed if diffusion is slower in certain directions compared to others. Diffusion-limited growth also dominates when diffusion is hindered by the morphology of the growth substrate, such as what we have observed

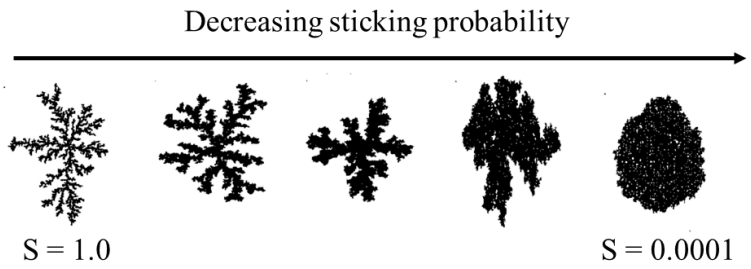

Figure 1.12. Simulated shape of a crystal growth with decreasing sticking probability of the reactant species. Reproduced from Ref. 34.

in our work with Lee and Kang *et. al.*,[35] where MoS_2 was grown on substrates patterned with three-dimensional, dome-shaped structures. Similarly, an anisotropic substrate pattern such as a trench will result in faster diffusion along the trench structure than across it.[30] Anisotropic diffusion can also occur on flat substrates, if the energy barriers for diffusion of a reactant around certain edges of the island are significantly different. This can be due to edges being terminated with different atomic compositions or having different packing densities of atoms.[36] In both cases the growth will be faster along the direction where diffusion is the slowest, resulting in an elongated fractal pattern or nearly-oval mass.

1.5 Thermodynamic Growth Regime for Two-Dimensional Molecular Systems

The above discussion on the nucleation and growth of chemical vapor deposition can be readily extended to the physical vapor deposition of 2D molecular crystals, with some additions. PVD is similar to CVD, except this process does not involve any chemical change in the precursor species, only a physical change: a solid is sublimated, transported down the reactor tube, and then redeposited on a substrate surface.[24]

Until now, we have discussed two of the three growth regimes described in **Fig. 1.5,** which were relevant to the CVD growth of TMD crystals—the diffusion-limited and reaction-limited growth regimes. The third regime is actually where thermodynamics, not kinetics, limits the growth rate. Although the most common approaches[37,38] (i.e., solution-based recrystallization or vacuum-based physical vapor transport) for the growth of molecular crystals occur in the kinetically-limited regimes, these techniques are unable to limit the thickness of the crystals. In this thesis, we carry out growth in the thermodynamically-limited regime to achieve two-dimensional growth of molecular crystals. Here, deposition temperatures are high relative to the strength of the bonds in the crystal, and crystal formation is limited by the desorption of

chemical species from the surface of the growth substrate, resulting in a reduced growth rate with increasing temperature.[23] We can understand growth in this regime based on free energy arguments, using the familiar equation:

$$\Delta G = \Delta H - T\Delta S \qquad \textbf{Eq. 1. 2}$$

Deposition processes, which produce ordered solid phases from disordered gases, aways reduce the entropy of a system, so ΔS for crystallization is negative. Since this results in a more positive ΔG, in order for a certain crystallization process to be spontaneous, it must be highly exothermic (i.e., negative ΔH).[39] The stronger the bonds (or intermolecular forces, IMFs) in the crystallized system, the greater (more negative) the enthalpy change, and hence, the more spontaneous the crystallization process. As the temperature increases, however, ΔG for the deposition process becomes more and more positive, and the driving force for crystallization becomes smaller and smaller, eventually leading to a point where the crystal sublimates.

For crystals that have very stable covalent bonds, such as TMDs, the lattice enthalpy is relatively large, and crystallization is favorable over a wide range of temperature conditions. Furthermore, because of the large bonding anisotropy of layered TMD crystals, crystallization in the in-plane direction can be selectively promoted to achieve two-dimensional growth (i.e., recall the thermodynamic arguments presented in **Fig. 1.8**). On the contrary, molecular solids are bound by weak IMFs (e.g., vdW forces, pi stacking, hydrogen bonding), and typically have a weaker driving force for crystallization. Moreover, the vdW forces and pi-pi interactions that bind most molecular crystals, such as the perylene crystal depicted in **Fig. 1.2** (left image), are very close in strength—with the difference being only a few kJ/mol. This is as opposed to layered vdW crystals, where the in-plane covalent bonding is orders of magnitude stronger than

the out-of-plane vdW bonding. In other words, molecular crystals generally have weak anisotropy.

From the above discussion, we can see that realizing 2D molecular crystals (such as the one shown in **Fig. 1.2**, right image) is much more challenging than growing inorganic 2D crystals. However, growing these materials is theoretically possible if the two aforementioned requirements are met: 1) the molecules must experience strong IMFs for crystallization to be favorable, and 2) there must be a sufficient difference in the strength between the in-plane vs. out-of-plane IMFs of the crystal to selectively promote two-dimensional growth.

Although first requirement may seem infeasible for most molecular systems since their IMFs are weak, heterogenous crystallization processes such as PVD (and CVD) can actually assisted by the growth substrate. This is because it is the free energy change of the entire system must be accounted for, which includes the substrate. A substrate surface that is surrounded by vacuum is energetically unfavorable because of its high surface energy. Deposition of a molecule on the surface results in the generation of vdW interactions between the molecule and the substrate, reducing the total surface energy of the system. Hence, even for a crystal with weak molecule-molecule interactions (i.e., IMFs), strong molecule-substrate interactions can provide an additional driving force for nucleation and growth.

Not every substrate will promote 2D crystallization, however. This is explained in the top-left panel of **Fig. 1.13**, where the roughness of a SiO_2 substrate prevents the conjugated perylene molecules from achieving good vdW contact with the surface (**Fig. 1.13**, orange arrows). Furthermore, the weak vdW forces that should exist between two flat-lying molecules in the crystal (**Fig. 1.13**, green arrows) are not possible to achieve if the crystal is sitting on a surface that is sufficiently rougher than its thickness (i.e., one carbon atom). Because the system

will always try to minimize its total free energy, conjugated molecules deposited on a rough substrate will produce pi-stacked crystals (**Fig. 1.13**, bottom-left panel), since that is the best geometry to maximize both the molecule-molecule interactions (i.e., green arrows) and molecule-substrate interactions (i.e., orange arrows). To realize the flat-lying 2D molecular crystal depicted in **Fig. 1.2**, an atomically-flat surface is necessary. For this reason, van der Waals crystals (such as TMDs) are ideal substrates for promoting the growth of 2D molecular crystals. This can be seen in the right panel of **Fig. 1.13**, where the flat surface allows the system to achieve optimal molecule-molecule and molecule-substrate interactions in the 2D configuration.

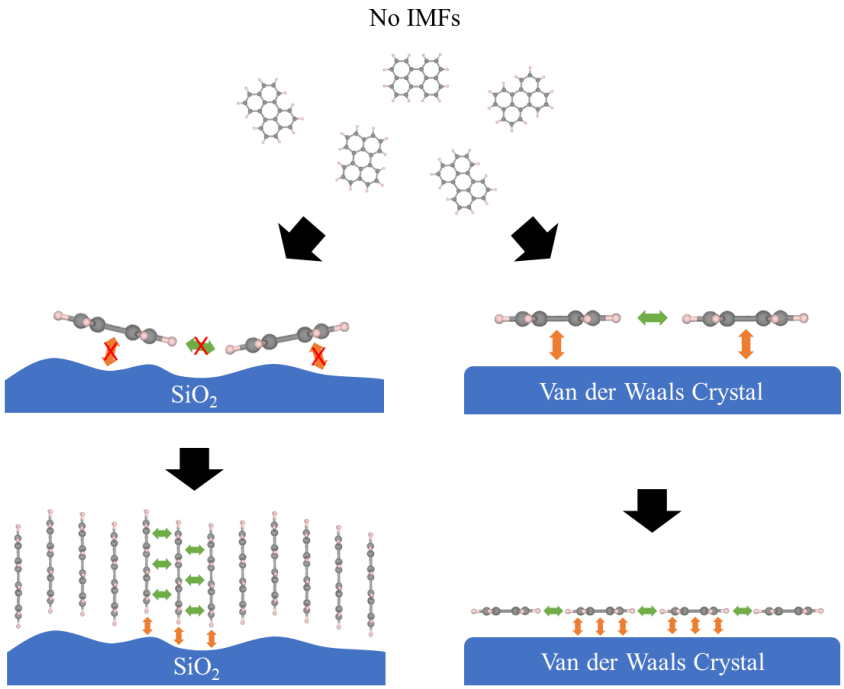

Figure 1.13. How the growth of 2D molecular crystals is influenced by the tendency to optimize molecule-molecule interactions (i.e., intermolecular forces, green arrows) and molecule-substrate interactions (orange arrows).

Even if the energetics of the system favor the formation of flat-lying crystals, however, this does not necessarily prevent subsequent layers from nucleating on the surface of the crystal. This is where the second requirement for two-dimensional crystallization—in-plane vs. out-of-plane anisotropy—becomes important. Similar to the discussion of TMD growth in **Fig. 2.8**, the driving force for in-plane bond formation must be sufficiently larger than that for out-of-plane bond formation. If this is the case, then the reaction conditions can be tuned to greatly reduce the

probability of nucleating a second layer, while still allowing the first layer to grow. The weaker the anisotropy, the narrower the "window" of reaction parameters for two-dimensional growth. In a purely thermodynamically-limited growth regime, the only reaction parameter of importance is temperature, so sufficient anisotropy exists, then we can simply exploit temperature to ensure that the second molecular layer is not a stable phase.

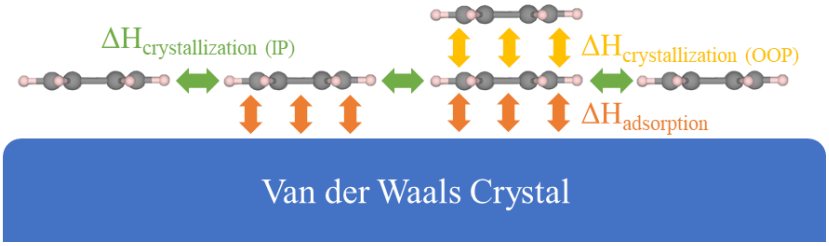

Figure 1.14. The role of thermodynamics in understanding the interactions that exist in a system of a 2D molecular crystal on an atomically-flat surface.

Figure 1.14, a revised version of **Fig. 1.13**, summarizes the concepts we have just discussed in terms of the thermodynamic driving force for crystallization (i.e., ΔH). A more traditional term for the molecule-molecule interactions that we introduced in **Fig. 1.13** is the crystallization enthalpy, or ΔH_{crys}. Here, we want to distinguish between the intermolecular forces associated with ΔH_{crys} in the in-plane (IP) direction (**Figure 1.14**, green arrows) and the out-of-plane (OOP) direction (**Figure 1.14**, yellow arrows). Because the in-plane intermolecular forces in a 2D crystal are so few, an additional driving force for 2D crystallization is necessary: the enthalpy associated with the interactions of the molecules with a substrate (i.e., the molecule-substrate interactions in **Fig. 1.13**). This contribution to the total enthalpy of the crystallization process is known as the adsorption enthalpy, or ΔH_{ads} (**Figure 1.14**, orange arrows). If the substrate is atomically-flat, ensuring a large ΔH_{ads}, then the combination of ΔH_{ads} and $\Delta H_{crys(IP)}$ is enough to overtake the entropic term in **Eq. 1.2**, allowing the spontaneous deposition of flat-lying molecules. So long as the magnitude of $\Delta H_{crys(IP)}$ sufficiently exceeds that of $\Delta H_{crys(OOP)}$, then we can find a temperature above which the second

layer of molecules will sublimate from the surface, while still leaving the first layer of the crystal intact. As the temperature is increased further, the in-plane molecule-molecule interactions will also be broken, resulting in either a disordered film (as opposed to a crystal) or isolated groups of molecules spread across the substrate surface. At even higher temperatures, the molecule-substrate interactions (orange arrows) are broken, and the molecules completely sublimate from the surface. Hence, in order to achieve 2D large crystals, it is critical to supply enough thermal energy for surface diffusion, to facilitate Oswald ripening,[39] but not so much thermal energy that all of the intermolecular forces are broken.

One additional point that may be noticed from the specific perylene crystal in **Fig. 1.14** is that its in-plane interactions (vdW forces) are actually weaker than its out-of-plane interactions (pi-pi interactions). Hence, a monolayer of this crystal should not form under the methodology described in the previous paragraph, where temperature selectivity is used to prevent the formation of multilayers. Actually, the 2D molecular crystals synthesized in this thesis are derivatives of perylene functionalized with hydrogen-bonding moieties that experience stronger in-plane IMFs. However, it is still possible to synthesize the exact 2D crystal in **Fig. 1.14** by relying more on kinetics, which will be elaborated on in Chapter 5. A final note is that growing in a thermodynamically-limited regime works well for relatively simple systems, such as single-component 2D crystals, where there is only one material composition possible. It can be assumed that, in general, 2D TMD crystals cannot be grown in this regime, since it is likely that the dichalcogenide is not the stable phase at high temperatures.

1.6 Summary

In this chapter, we introduced the fundamental concepts necessary for understanding the growth of inorganic and molecular 2D crystals and films. We learned that an anisotropic (in-plane vs. out-of-plane) bonding structure is key to producing stable few-atom-thick materials. For covalently-bonded materials such as TMDs, CVD techniques are used for scalable synthesis, which is carried out in one of two kinetically-limited growth regimes (reaction- or diffusion-limited). For organic materials bound by weak intermolecular forces, PVD techniques performed in the thermodynamic limit provide the necessary scalability, but rely more heavily on the selection of the growth substrate. We will see how these ideas can be applied in an experimental setting in the following chapters.

1.7 References

(1) Novoselov, K. S.; Geim, A. K.; Morozov, S. V.; Jiang, D.; Zhang, Y.; Dubonos, S. V.; Grigorieva, I. V.; Firsov, A. A. Electric Field Effect in Atomically Thin Carbon Films. *Science* **2004**, *306* (5696), 666–669.

(2) Liu, Y.; Weiss, N. O.; Duan, X.; Cheng, H.-C.; Huang, Y.; Duan, X. Van Der Waals Heterostructures and Devices. *Nat Rev Mater* **2016**, *1* (9), 16042.

(3) Novoselov, K. S.; Fal′ko, V. I.; Colombo, L.; Gellert, P. R.; Schwab, M. G.; Kim, K. A Roadmap for Graphene. *Nature* **2012**, *490* (7419), 192–200.

(4) Wang, Q. H.; Kalantar-Zadeh, K.; Kis, A.; Coleman, J. N.; Strano, M. S. Electronics and Optoelectronics of Two-Dimensional Transition Metal Dichalcogenides. *Nature Nanotech* **2012**, *7* (11), 699–712.

(5) Bhimanapati, G. R.; Lin, Z.; Meunier, V.; Jung, Y.; Cha, J.; Das, S.; Xiao, D.; Son, Y.; Strano, M. S.; Cooper, V. R.; Liang, L.; Louie, S. G.; Ringe, E.; Zhou, W.; Kim, S. S.; Naik, R. R.; Sumpter, B. G.; Terrones, H.; Xia, F.; Wang, Y.; Zhu, J.; Akinwande, D.; Alem, N.; Schuller, J. A.; Schaak, R. E.; Terrones, M.; Robinson, J. A. Recent Advances in Two-Dimensional Materials beyond Graphene. *ACS Nano* **2015**, *9* (12), 11509–11539.

(6) Geim, A. K.; Grigorieva, I. V. Van Der Waals Heterostructures. *Nature* **2013**, *499* (7459), 419–425.

(7) Geim, A. K.; Novoselov, K. S. The Rise of Graphene. *Nature Mater* **2007**, *6* (3), 183–191.

(8) Novoselov, K. S.; Mishchenko, A.; Carvalho, A.; Castro Neto, A. H. 2D Materials and van Der Waals Heterostructures. *Science* **2016**, *353* (6298), 419–425.

(9) Duong, D. L.; Yun, S. J.; Lee, Y. H. Van Der Waals Layered Materials: Opportunities and Challenges. *ACS Nano* **2017**, *11* (12), 11803–11830.

(10) Chhowalla, M.; Shin, H. S.; Eda, G.; Li, L.-J.; Loh, K. P.; Zhang, H. The Chemistry of Two-Dimensional Layered Transition Metal Dichalcogenide Nanosheets. *Nature Chem* **2013**, *5* (4), 263–275.

(11) Manzeli, S.; Ovchinnikov, D.; Pasquier, D.; Yazyev, O. V.; Kis, A. 2D Transition Metal Dichalcogenides. *Nature Reviews Materials* **2017**, *2* (8), 17033.

(12) Kronik, L.; Tkatchenko, A. Understanding Molecular Crystals with Dispersion-Inclusive Density Functional Theory: Pairwise Corrections and Beyond. *Acc. Chem. Res.* **2014**, *47* (11), 3208–3216.

(13) Klimeš, J.; Michaelides, A. Perspective: Advances and Challenges in Treating van Der Waals Dispersion Forces in Density Functional Theory. *The Journal of Chemical Physics* **2012**, *137* (12), 120901.

(14) Yao, Z.-F.; Wang, J.-Y.; Pei, J. Control of π–π Stacking via Crystal Engineering in Organic Conjugated Small Molecule Crystals. *Crystal Growth & Design* **2018**, *18* (1), 7–15.

(15) Aakeröy, C. B.; Seddon, K. R. The Hydrogen Bond and Crystal Engineering. *Chem. Soc. Rev.* **1993**, *22* (6), 397–407.

(16) Metrangolo, P.; Meyer, F.; Pilati, T.; Resnati, G.; Terraneo, G. Halogen Bonding in Supramolecular Chemistry. *Angew. Chem. Int. Ed.* **2008**, *47* (33), 6114–6127.

(17) Gobbi, M.; Orgiu, E.; Samorì, P. When 2D Materials Meet Molecules: Opportunities and Challenges of Hybrid Organic/Inorganic van Der Waals Heterostructures. *Adv. Mater.* **2018**, *30* (18), 1706103.

(18) Huang, Y. L.; Wee, A. T. S. Hybrid Organic-2D TMD Heterointerfaces: Towards Devices Using 2D Materials. In *Supramolecular Chemistry on Surfaces*; Champness, N., Ed.; Wiley, 2022; pp 171–198.

(19) Cai, S.-L.; Zhang, W.-G.; Zuckermann, R. N.; Li, Z.-T.; Zhao, X.; Liu, Y. The Organic Flatland-Recent Advances in Synthetic 2D Organic Layers. *Adv. Mater.* **2015**, *27* (38), 5762–5770.

(20) Wei, X.; Wang, M. Two Dimensional Semiconducting Polymers. *Mater. Chem. Front.* **2020**, *4* (12), 3472–3486.

(21) Yang, F.; Cheng, S.; Zhang, X.; Ren, X.; Li, R.; Dong, H.; Hu, W. 2D Organic Materials for Optoelectronic Applications. *Adv. Mater.* **2018**, *30* (2), 1702415.

(22) Duan, J.; Li, Y.; Pan, Y.; Behera, N.; Jin, W. Metal-Organic Framework Nanosheets: An Emerging Family of Multifunctional 2D Materials. *Coordination Chemistry Reviews* **2019**, *395*, 25–45.

(23) Yan, X.-T.; Xu, Y. *Chemical Vapour Deposition An Integrated Engineering Design for Advanced Materials*; Springer: London, 2010.

(24) Mattox, D. M. *Handbook of Physical Vapor Deposition (PVD) Processing*; Elsevier: Amsterdam, 2010.

(25) Rockett, A. *The Materials Science of Semiconductors*; Springer: New York, 2008.

(26) Barron, A. *Chemistry of Electronic Materials*; MiDAS Green Innovations, Ltd: Swansea, UK, 2012.

(27) Polte, J. Fundamental Growth Principles of Colloidal Metal Nanoparticles – a New Perspective. *CrystEngComm* **2015**, *17* (36), 6809–6830.

(28) Tran, R.; Xu, Z.; Radhakrishnan, B.; Winston, D.; Sun, W.; Persson, K. A.; Ong, S. P. Surface Energies of Elemental Crystals. *Sci Data* **2016**, *3* (1), 160080.

(29) Markov, I. V. *Crystal Growth for Beginners: Fundamentals of Nucleation, Crystal Growth and Epitaxy*, 2nd ed.; World Scientific: Singapore ; River Edge, N.J, 2003.

(30) Dong, J.; Zhang, L.; Ding, F. Kinetics of Graphene and 2D Materials Growth. *Adv. Mater.* **2019**, *31* (9), 1801583.

(31) Zhang, Y.; Li, Z.; Kim, P.; Zhang, L.; Zhou, C. Anisotropic Hydrogen Etching of Chemical Vapor Deposited Graphene. *ACS Nano* **2012**, *6* (1), 126–132.

(32) Ma, T.; Ren, W.; Zhang, X.; Liu, Z.; Gao, Y.; Yin, L.-C.; Ma, X.-L.; Ding, F.; Cheng, H.-M. Edge-Controlled Growth and Kinetics of Single-Crystal Graphene Domains by Chemical Vapor Deposition. *Proc. Natl. Acad. Sci. U.S.A.* **2013**, *110* (51), 20386–20391.

(33) Wang, S.; Rong, Y.; Fan, Y.; Pacios, M.; Bhaskaran, H.; He, K.; Warner, J. H. Shape Evolution of Monolayer MoS_2 Crystals Grown by Chemical Vapor Deposition. *Chem. Mater.* **2014**, *26* (22), 6371–6379.

(34) Batabyal, R.; Mahato, J. C.; Das, D.; Roy, A.; Dev, B. N. Self-Organized One-Atom Thick Fractal Nanoclusters via Field-Induced Atomic Transport. *Journal of Applied Physics* **2013**, *114* (6), 064304.

(35) Lee, M.; Kang, J.-H.; Mujid, F.; Suh, J.; Ray, A.; Park, C.; Muller, David. A.; Park, J. Atomically Thin, Optically Isotropic Films with 3D Nanotopography. *Nano Lett.* **2021**, *21* (17), 7291–7297.

(36) Li, M.; Han, Y.; Thiel, P. A.; Evans, J. W. Formation of Complex Wedding-Cake Morphologies during Homoepitaxial Film Growth of Ag on Ag(111): Atomistic, Step-Dynamics, and Continuum Modeling. *J. Phys.: Condens. Matter* **2009**, *21* (8), 084216.

(37) Wang, C.; Dong, H.; Jiang, L.; Hu, W. Organic Semiconductor Crystals. *Chem. Soc. Rev.* **2018**, *47* (2), 422–500.

(38) Virkar, A. A.; Mannsfeld, S.; Bao, Z.; Stingelin, N. Organic Semiconductor Growth and Morphology Considerations for Organic Thin-Film Transistors. *Adv. Mater.* **2010**, *22* (34), 3857–3875.

(39) Kolasinski, K. W. *Surface Science: Foundations of Catalysis and Nanoscience*, 3rd ed.; Wiley: Chichester, West Sussex ; Hoboken, N.J, 2012.

CHAPTER TWO

Controllable Synthesis of 2D Transition-Metal Dichalcogenides:

From Single-Crystals to Wafer-Scale Films

2.1 Introduction

Crystal growth is a complex phenomenon. This is especially true for heterogeneous growth processes such as chemical vapor deposition. This complexity is not only because of the possibility to form different chemical compounds from the same set of reactants, but also different phases of crystals with the same chemical structure. To elaborate, **Fig. 2.1** shows a CVD phase diagram calculated for the reaction between $Mo(CO)_6$ and H_2S diluted in Ar.[1] As expected, various compositions of molybdenum oxides, carbides, and sulfides are possible depending on the temperature of the reaction and the ratio of the two reactants, with carbon being the major byproduct. What is left out of this simplified picture, however, is that each of the compounds on this diagram can exist in different structural forms. For example, a crystal of MoS_2 can occur in one of three common phases: 1H, 2T, or 3R, each with its own unique structure and hence, unique physical and chemical properties.[2] Furthermore, crystalline materials also suffer from the possibility of having *defects*, such as missing or wrongly-placed atoms that can have significant consequences on the material's properties[cite]. Unlike with solution-based synthetic processes, purifying a product that is a thin film or mixture of crystals deposited on a solid surface is largely impossible. Therefore, in such vacuum-based material synthesis

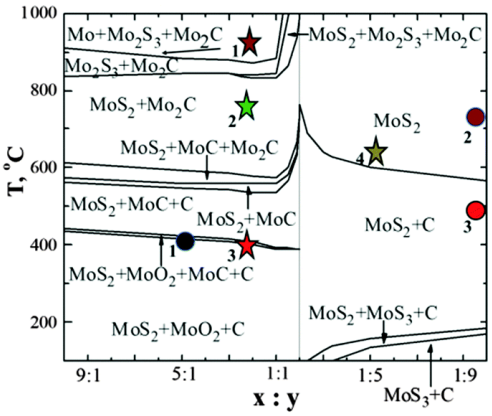

Figure 2.1. CVD phase diagram (calculated) showing the products of the reaction between x = $Mo(CO)_6$ and y = H_2S with 100 parts Ar at a total reactor pressure of 20 torr. Reproduced from Ref. 1.

techniques, it is critical to achieve the desired compound in one shot, with the correct phase and in high purity.

In order to do this, we need to have a reasonable understanding of the general mechanisms by which the material grows and the possible byproducts of our reaction, so that we can adjust our growth recipes to achieve the necessary level of material quality. The discussion in the previous paragraph was very general and applies to crystals with all different morphologies. This work however, focuses on the synthesis of nanomaterials, which are dimensionally-confined—introducing an additional level of complexity. In this chapter, we will discuss an approach for the synthesis of two-dimensional (2D) films of transition-metal dichalcogenides (TMDs), such as MoS_2, WS_2, and WSe_2, which are < 1 nm thick but inches in length and width. This synthesis is enabled by a metal-organic chemical vapor deposition (MOCVD) process adapted from a work by Kang and Xie *et al.*,[3] which allowed for an unprecedented level of control over the synthesis of monolayer TMD materials. We will give a general discussion of how proper control of nucleation and growth rates enables the scale-up from single-crystal TMDs to wafer-scale, polycrystalline films. We will then cover in more detail how control of various reaction parameters affects different aspects of the growth and properties of TMDs generated though this MOCVD process.

2.2 Traditional Powder CVD vs. MOCVD Systems

Figure 2.2 illustrates the general setup of a powder CVD system first developed for the growth of monolayer TMDs on oxide substrates.[4] N_2 carrier gas is flowed into the reaction chamber, upstream of the growth substrates. The gas flows over the chalcogen precursor (e.g., sulfur powder, S_8) and carries it downstream. The gases then reach the metal precursor (e.g.,

metal oxide powder, MoO_3), and the mixture of vapors are carried to the surface of the substrate, where they react to deposit the TMD material. Excess gases are then pumped out of the system.

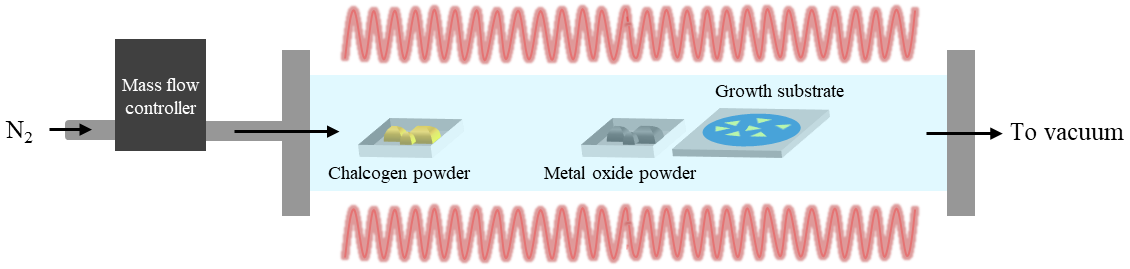

Figure 2.2. Schematic of a traditional powder CVD setup for the growth of monolayer TMDs. S_8 and MoO_3 are the specific precursors used for the synthesis of MoS_2.

Although there are numerous variations of this CVD technique, they all suffer from the same key pitfall: a lack of reaction control (i.e., control of nucleation and growth rates) due to the use of reaction precursors with extremely low room temperature vapor pressures. The precursors need to be heated to extremely high temperatures in order to generate sufficient vapors, and as a result, have to be loaded directly into the growth reactor to achieve any deposition. The only gas in the system whose concentration is properly controlled is the carrier gas. This is done by using a mass flow controller (MFC), which constantly measures the vapor pressure of the gas and uses a valve to adjust the flow rate into the reactor. There is no active control for the reactants—the concentrations of the metal oxide and chalcogen precursors are only decided by their temperatures, which are "controlled" by their positions in the reactor, and their distances to the growth substrate. Usually, the chalcogen powder (which has relatively higher vapor pressure) is placed near the upstream edge of the reactor tube where the temperature is lower, and the metal precursor (which has very low vapor pressure), has to be placed extremely close to the growth substrate.

There are also various other difficulties in a configuration such as this, for example, how the chalcogen precursor will react with the metal precursor in the crucible, changing its composition over time (i.e., "poisoning"). Another issue is that there is no easy way to block the

growth substrate in a hot-walled reactor, resulting in uncontrolled deposition during the heating and cooling stages, as the precursors start sublimating before the reactor reaches the target temperature. As a result, although such CVD systems are sufficient for producing single-crystal islands of monolayer TMDs and small areas of continuous films, they are not able to achieve the proper level of control necessary for wafer-scale, monolayer film growth.

In order to improve the controllability and reproducibility of the reaction, Kang and Xie *et al.* developed an MOCVD process[3] using high-vapor-pressure metal and chalcogen sources: metal hexacarbonyls (such as molybdenum hexacarbonyl, $Mo(CO)_6$), which are solids that sublimate at room temperature, and alkyl chalcogenides (such as diethyl sulfide, DES), which are liquids at room temperature. **Figure 2.3** shows the design of an MOCVD reactor used for the growth of monolayer TMD films, adapted from this work. In the typical MOCVD process, the precursors evaporate/sublimate inside their canisters, and the amount of vapor injected into the gas line can be precisely controlled by MFCs. For an extra level of control, the metal precursor is diluted in

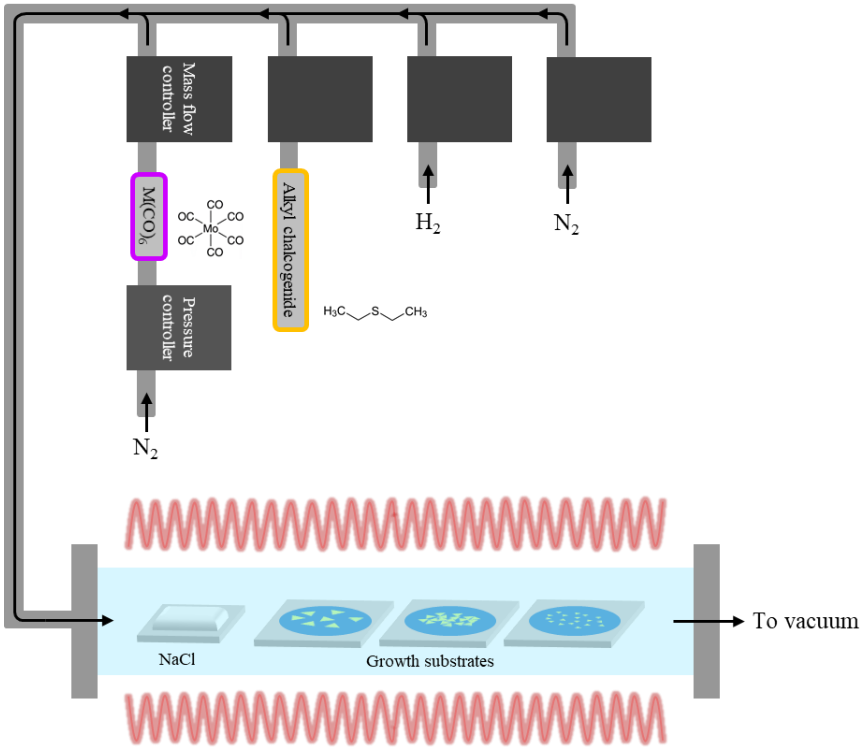

Figure 2.3. Schematic of a MOCVD system for the growth of monolayer TMD films. Molybdenum hexacarbonyl and diethyl sulfide are the specific precursors used for the growth of MoS_2.

N_2 gas before being injected into the line. For this, a pressure controller maintains a set total pressure in the precursor canister as the mixed gas is depleted though the MFC. In the gas line, the precursor vapors mix with N_2 (carrier gas) and H_2 (another reactant) and are carried into a heated quartz tube where they thermally decompose into active species and react to deposit TMD layers onto a wafer substrate, before being evacuated out of the system by a vacuum pump. A pellet of NaCl (another reactant) is placed upstream of the growth substrates. We will revisit the role of each of these reactants in detail in Section 2.4.

2.3 From Single-Crystals to Wafer-Scale Films

The ability to control the flow rates of the precursors (i.e., reactant concentrations) allows us to manipulate the nucleation and growth rates in order to scale up these monolayer TMDs from single-crystal islands to wafer-scale films. The previous chapter mainly discussed the thermodynamics and kinetics of the nucleation and growth of single-crystal TMD islands, which occurs in two dominant kinetic regimes. We have seen that the reaction-limited (or attachment-limited) growth regime is ideal for producing highly faceted single crystals, for applications where high or unambiguous crystallinity is desirable. Examples of this will be explored in Chapters 5-7, where we use large single-crystal TMDs as substrates for the growth of highly crystalline 2D molecular crystals with tunable polarized absorption properties. For application that require continuous films for large-scale processability, the other kinetic growth regime—diffusion-limited (or mass-transport-limited) growth—is ideal.

2.3.1 Realizing Continuous Films

Figure 2.4 illustrates how growths in the reaction-limited and diffusion-limited regimes evolve over time. In the reaction-limited regime (**Fig. 2.4**, top row), the crystals grow faster in certain directions compared to others. Inevitably, there will come a point where the fast-growing

directions merge, leaving holes surrounded by slow-growing edges. We know that a chemical species that lands on the surface of the substrate or film will diffuse around until finds a site where it has enough energy to nucleate or react, and that there is a higher probability that an active species will react with the edge of an island, rather than nucleate on top of an existing layer. However, because the remaining edges have relatively high activation barriers for attachment, the probability that a species that finds an edge but doesn't react, is also significant.

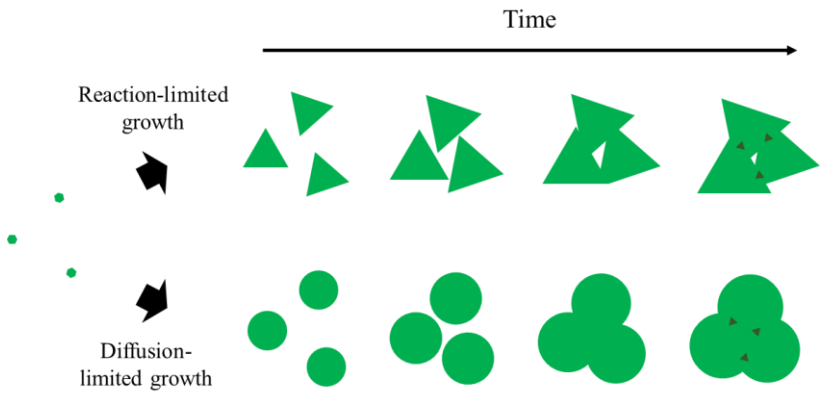

Figure 2.4. Illustration of the morphology change of growths in the attachment-limited vs. diffusion-limited regimes over time.

Hence, a hole in a reaction-limited film will take significantly longer to fill than a diffusion-limited film, where the activation barrier for attachment does not impede the film growth. The reason this time scale is important is because the reactive species have a set average diffusion length that is dictated by the temperature. As the films achieves higher coverage, the species need to diffuse farther to find an edge site. So as time goes on, it becomes more and more probable that one species will have achieved the energy to overcome the barrier to nucleate at a grain boundary site on top of the film before being able to find an edge site that it can attach to. Once this bilayer nucleation event occurs, the growth of the second layer proceeds with little hinderance. The result is that a reaction-limited film will grow bilayer islands before the monolayer becomes completely continuous (**Fig. 2.4**, top row, last image), whereas a diffusion-limited film will have already achieved full coverage before that point (**Fig. 2.4**, bottom row,

third image). The diffusion-limited growth can easily be terminated before the second layer begins to nucleate on the surface, allowing the isolation of a film that is fully monolayer with very few adlayers on top. For this reason, continuous film growth should ideally be carried out in the diffusion-limited regime, and growth in the reaction-limited regime should be applied only in cases where large single-crystals are desired.

2.3.2 Importance of Homogeneous Growth Rates

Although monolayer continuous film growth is theoretically possible with careful thermodynamic and kinetic control, growing these films over a large length scale (i.e., wafer scale) is practically challenging. This is because precursor concentrations and reaction rates vary widely in different locations of a gas-phase growth reactor, which is subject to significant temperature and flow gradients. This results in significant variation in both the nucleation rates and the growth rates across a growth substrate. In order to achieve monolayer growth that is homogeneous over the wafer-scale, one must achieve both a uniform growth rate and a uniform nucleation rate. We will start by introducing a number of tactics that can be employed to achieve a homogeneous growth rate across a wafer, which are illustrated in **Fig. 2.5**.

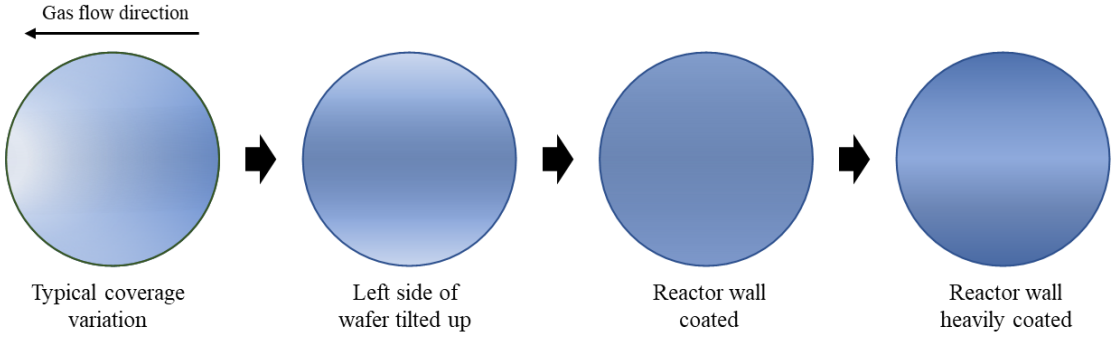

Figure 2.5. Schematic of coverage variation across wafers for growths carried out under different environmental conditions, illustrating how to balance the growth rate and local precursor concentrations to achieve wafer-scale homogeneity.

In a typical MOCVD growth, the coverage across a wafer substrate has dramatic spatial variation due to spatial differences in the growth rate. For example, in a reactor with a 4-inch-

wide tube, usually only a roughly 1” x 1” sized area can be grown as a homogeneous monolayer on a 4” wafer. The growth rate will vary across with wafer according to the distribution shown in the first image of **Fig. 2.5**. Here, the darker blue regions are overgrown areas (> 1 monolayer), and the lighter blue regions are partial (< 1 monolayer coverage). The growth rate is faster in the upstream region of the wafer and drops along the length of the tube (gas flow direction indicated by black arrow). This is because there is a higher concentration of the limiting reactant (i.e., the metal precursor), which dictates the growth rate, upstream. As the reactants near the surface are depleted through deposition, the concentration and reaction rate drops, and by the time the gases reach the left edge of the wafer, there is very little deposition on the substrate surface for the same growth time. Although one might expect that gases further away from the surface (i.e., areas with higher concentration) should diffuse towards the surface to balance the concentration gradient (which may occur in solution-phase reactions), this is not the case for flow-based reactions. This is because of the laminar flow of reactants, as described in Section 1.2. Gases from different “layers” have very little mixing, and so once the reactants in the layer near the substrate surface are depleted, they are not replenished.

Furthermore, there is also a gradient in the precursor concentration across the width of the tube (i.e., in the up-down direction of the images in **Fig. 2.5**. This is because the gas inlet of the reactor is typically a few-millimeter-sized hole, concentrating the cases down the center of the tube. Although the gases do somewhat fan out in the in-plane direction (i.e., the plane of the substrate), the concentration also drops they reach the wall of the tube. So similar to the decreasing growth rate from right to left, the growth rate also decreases from the center of a wafer to the top or bottom edges.

Balancing the growth rate between the left and right edges of the wafer is quite simple actually—one can tilt the slower-growing edge a few millimeters upwards (by, for example, putting a piece of glass under the left side). At a certain tilt angle, one will achieve the growth profile shown in in the second image of **Fig. 2.5**, where the left and right edges now have similar coverage. This tactic works because the areas of the wafer with lower reactant concentration are moved to a higher plane, i.e., to a layer of gases that haven't reacted yet, and hence, have a growth rate more similar to that of the right side of the wafer.

Still, however, there will be a concentration gradient from the middle to the edges close to the tube wall. Dealing this gradient is slightly trickier. Ideally, if the gas inlet was slit-shaped (the plane of the slit parallel to the plane of the wafer), this would not be an issue, but such a design would be extremely technically-challenging to implement and is not commercially-available. As it turns out though, this concentration gradient actually naturally goes away as one continues to grow in a reactor tube without performing any kind of tube cleaning procedure. This is because, over time, the walls of the tube become coated with a thick film of the target material, as well as adsorbed precursor species. During the initial stages of the growth (furnace ramping and nucleation), chemical species desorb from this film and react again to deposit the target material on nearby substrates. As a result, the growth rate of the film near at the top and bottom of the wafer (i.e., near the tube wall) will eventually balance out after many growths, resulting in a uniform, wafer-scale monolayer film, such as the one depicted in **Fig. 2.5** (third image).

This tactic only works for a certain number of growths, however, because eventually the reactor tube coating will become too thick, and the top and bottom edges of the wafer will actually have a much faster growth rate than the center (**Fig. 2.5**, last image). At this point, the reactor must be cleaned to reset the growth rate. Although the third and fourth illustrations in

Fig. 2.5 roughly describe the what happens as one preforms successive growths, the exact distribution can have more local variation depending on the temperature gradient in the furnace and the carrier gas flow, which need to be optimized. Of course, a more reliable solution to this issue could be to install some kind of gas diffuser near the gas inlet of the tube, to spread the reactants out, but this has other challenges, such as temperature compatibility issues and cross-contamination between reactants when growing different materials.

2.3.3 Importance of Homogeneous Nucleation Rates

Even if one can accomplish balancing the growth rate, R, across a wafer substrate, it is still not possible to achieve uniform monolayer coverage unless the nucleation rate, n, is also homogeneous, because the time required to achieve full monolayer coverage depends on both the growth rate and nucleation density. An area of a sample with a lower nucleation density (i.e., large grain size) will always take longer time to achieve full monolayer coverage compared to an area of higher nucleation density (i.e., small grain size), even if the growth rates are exactly the same, simply because there are fewer growing islands.

This concept that is illustrated in **Fig. 2.6**. The nucleation density in a typical growth is low in the upstream region of a wafer and increases as one moves downstream, along the length of the reactor tube. This is because the nucleation rate in this specific MOCVD reaction is

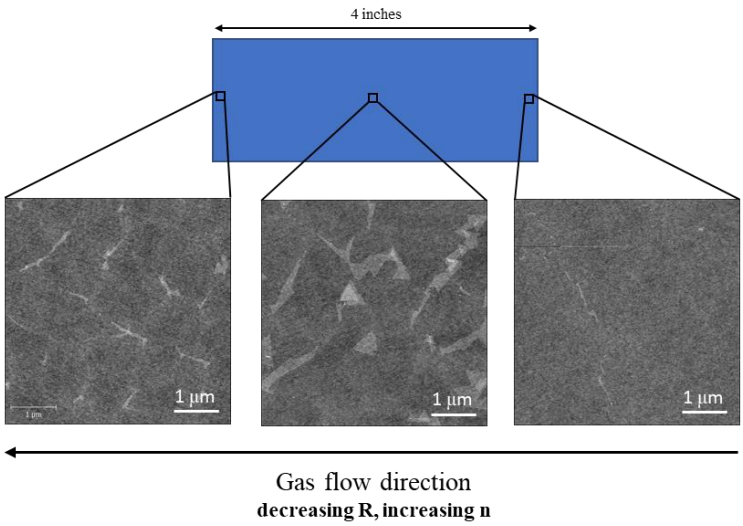

Figure 2.6. AFM images illustrating effect of nucleation density on coverage rate across a 4-inch wafer, where R is the growth rate and n is the nucleation rate.

limited by the chalcogen precursor, which needs time to decompose from its alkylated form into an active species (the reaction mechanisms will be discussed in more detail in the following section). In the upstream region of the growth, the chalcogen precursor has not been heated long enough to form significant quantity of reactive species that can initiate nucleation, so the nucleation density is low (i.e., the film has large domain size). As the precursors travel downstream, the concentration of the active species increases, and so does the nucleation density. Hence, it can be seen from the AFM images in **Fig. 2.6** that the domain size of the film, which is 3-5 μm in the right image and < 1 μm in the left image, decreases in the gas flow direction.

This is why the rightmost image in **Fig. 2.6** has the lowest coverage, even though we know that the growth rate upstream is higher—the low nucleation density results in a much slower time to full coverage. The middle of the wafer is much more overgrown (**Fig. 2.6**, middle image) because the grain size is smaller, but the growth rate has not yet dropped appreciably. The most downstream edge of the wafer (**Fig. 2.6**, left image) actually has a similar film coverage as the upstream region, despite the much slower growth rate, because it has the smallest domain size, and hence, fastest time to coverage. Therefore, a uniform nucleation rate (i.e., grain size distribution), is a prerequisite to actually achieving the coverage distribution illustrated in **Fig. 2.6**.

2.3.4 Reaction Conditions for Achieving Uniform Coverage

Figure 2.5 discussed some environmental conditions that can be adjusted to achieve uniform coverage, but there are also a few reaction parameters that can also be tweaked to promote homogeneous growth rates. If the growth rate is fast enough, then the small differences between growth rates in different areas of the wafer become less significant. Hence, reaction conditions that promote faster growth rates tend to promote more homogeneous samples. Since

the growth rate is dictated by the concentration of the metal precursor, one way is using high metal precursor flow. Another way is to increase the growth temperature, since we know that higher temperature always increases the growth rate in the reactant-limited and diffusion-limited growth regimes. Although faster growth rates do make it easier to grow homogeneous monolayer films, doing so does not necessarily produce the best-quality material, a topic which we will revisit in Section 2.4.

Similar to the to the argument for the growth rate, if the nucleation rate is fast, then the density of nuclei on the substrate surface will be high, so the variation in the nucleation density in different regions of the wafer will be small in comparison. This implies that it is not possible to produce wafer-scale monolayer TMDs with this MOCVD technique unless the sample is grown with small grain size. Because the chalcogen precursor dictates the grain size, a uniform nucleation density can be achieved by increasing the chalcogen flow. Using a higher growth temperature will also result in an increased nucleation density.

The last critical parameter for homogeneous nucleation and growth rates is related to the flow of the carrier gas: use low carrier gas flow during ramping and high carrier gas flow during growth. The reasoning behind flowing very little carrier gas during the temperature ramping stage of the growth (e.g., ~1/100th the amount that is flowed during the actual growth) is similar to a previous argument from **Fig. 2.6**. Because low carrier gas flow means a higher wafer surface temperature, this can increase the reaction rate of the species that coat the tube wall and allow for more deposition at the edges of the wafer during the ramping stage (i.e., sort of like giving the edges a “head start”). Once the furnace is at the set temperature however, the carrier gas flow rate should be increased to a high value before beginning to flow the reactants. This is because higher carrier gas flow helps spread out the reactants to make the precursor concentrations in

different areas more uniform. Of course, flowing too much carrier gas can make the flow turbulent, which results in less uniform concentrations, so a compromise should be reached.

2.4 Reaction Parameters and Mechanisms

As explained briefly in Section 2.2, this MOCVD technique for monolayer TMD synthesis is enabled by the careful choice of precursors for the growth. The metal sources are metal hexacarbonyl compounds, such as $Mo(CO)_6$ for the molybdenum-series TMDs (e.g., MoS_2, $MoSe_2$, etc.) and $W(CO)_6$ for the tungsten-series TMDs (e.g., WS_2, WSe_2, etc.). The chalcogen sources alkyl chalcogenides—diethyl sulfide and dimethyl selenide. The decomposition of the alkyl chalcogenides is assisted by H_2 gas and solid alkali metal halides, such as NaCl, are used as nucleation inhibitors. Either N_2 or Ar and be used as a carrier gas. This section will discuss in detail the role of each of these reactants in the TMD synthesis and a proposal of reactions that might be occurring in these systems.

2.4.1 Metal Precursor

Metal hexacarbonyl compounds are used at the metal source in this MOCVD process because of their significantly higher vapor pressure than the metal oxides used in traditional CVD synthesis. $Mo(CO)_6$ and $W(CO)_6$ are both solids with similar room temperature vapor pressures of ~0.1 torr.[5] Although this value appears low, the vapors generated through sublimation at room temperature are sufficient to achieve decent reaction rates if a carrier gas (N_2 or Ar) is used to assist transport of the gases out of the precursor canister, allowing for the continual regeneration of the vapor (see Section 3.2 for a comparison of methods for introducing the metal precursor into the reaction chamber).

The metal hexacarbonyls undergo thermal decomposition at the elevated temperatures in the growth chamber, according to the reaction:[6]

$$M(CO)_6 \xrightarrow{\Delta} M + 6CO \qquad \textbf{Eq. 2. 1}$$

Although both compounds have similar sublimation temperatures, the temperatures where this decomposition reaction occurs is significantly higher for $W(CO)_6$. This can be seen from the quadrupole mass spectrometry thermal profiles in **Fig. 2.7**, showing the loss of CO from $Mo(CO)_6$ and $W(CO)_6$ as a function of temperature.[7] $Mo(CO)_6$ experiences the most CO loss between 150-175°C, while $W(CO)_6$ does not exhibit significant loss until 250-400°C. One implication of this is a difference in reaction rate between the molybdenum and tungsten precursors, and as a result, the tungsten-based TMDs must often be grown at reaction temperatures to accommodate this difference. Another point to notice from the data in **Fig. 2.7** is that the CO ligands are not released simultaneously or at the same temperature, which is consistent with the presence of various $Mo(CO)_x$ species in the temperature-dependent residual gas analysis of the reaction exhaust from the original MOCVD work.[3]

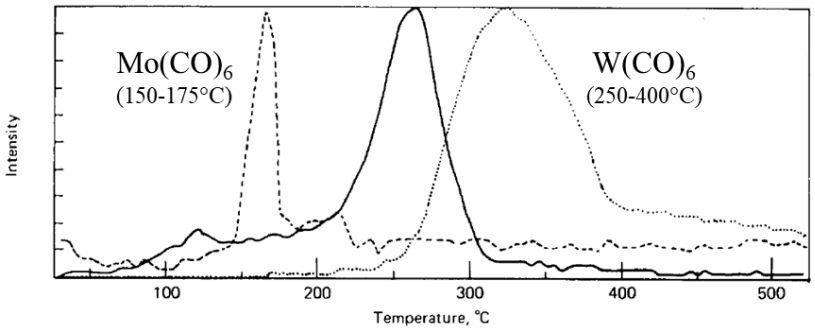

Figure 2.7. Quadrupole mass spectrometry thermal profiles of $Mo(CO)_6$ and $W(CO)_6$ showing temperature ranges for major CO evolution. Reproduced from Ref. 7.

The metal precursor is the limiting reactant in the TMD growth, which is apparent because changing its flow rate changes the growth rate of the film dramatically. For $Mo(CO)_6$ diluted in 760 torr of carrier gas, the time to achieve full monolayer coverage of MoS_2 in a 4-inch reactor can be tuned from ~20 hours for a flow rate of 0.5-1 sccm to 1-2 hours for a flow rate of ~10 sccm. Flowing too much metal precursor can cause the growth to deviate from the two-dimensional growth mode, resulting in films that nucleate multilayers when the first layer is

not yet complete. Another consequence of flowing increased amounts of the hexacarbonyl precursor is that it results in increased carbon deposition on the walls of the tube (i.e., the tube turns gray). This is due to the disproportionation of carbon monoxide, also known at the Boudouard Reaction,[8] which dominates at the temperatures used for the growth:

$$2CO \rightarrow C + CO_2 \qquad \textbf{Eq. 2. 2}$$

This reaction is presumably the main source of carbon contamination on MOCVD-grown TMD films. Higher metal precursor flow also usually results in more particles on the surface of the films (reaction byproducts), both topics that will be discusses further in Section 3.4.

In general, different amounts of metal precursor flow (and different growth rates) produce samples with very different physical and chemical properties, although these behaviors are not very predictable. The original work by Kang and Xie *et al.* achieved good sample quality using slow growth rates (~25 hrs),[3] although this was partially due to necessity resulting from the inability to flow more metal precursor, since it was not diluted in carrier gas (see Section 3.2 for more on the implications of these geometry differences). We have found that higher metal precursor flow, although may not produce the cleanest samples, tends to produce samples with higher photoluminescence. Extremely fast growth rates, however, (e.g., < 1 hr) can result in films with poor mechanical stability, which sometimes spontaneously crack while sitting on the substrate after being removed from the growth chamber.

The metal precursor usually contributes little to the nucleation rate, although it will start to dominate the nucleation behavior at extremely low concentrations. For example, we find that the growth of giant single-crystal TMDs (> 100 μm) can be achieved using tiny amounts of metal precursor (~0.1 sccm) and growing for a very long time. Even though it is possible to grow giant crystals in this way, it is not our preferred method, since we have sometimes experienced

odd growth behaviors in the limit of tiny metal precursor flow. Films grown with extremely slow growth rates are also subject to high temperature for longer, which may have implications on the film quality. An alternate method for growing giant single-crystals using a normal metal precursor flow and reducing the concentration of the chalcogen precursor, which is the main nucleation-limiting reactant, as discussed in the following subsection.

2.4.2 Chalcogen Precursor

Alkyl chalcogenides, which are liquids at room temperature, are good alternatives to the sulfur and selenium powders or hydrogen sulfide gas used in tradition CVD systems. Diethyl sulfide (DES) and dimethyl selenide (DMSe) have significantly higher vapor pressures than the corresponding powder precursors (~60 torr for DES[9] and ~220 torr for DMSe[10] at room temperature) and are much safer than hydrogen sulfide gas. The vapor pressures are high enough to simply use the evaporated molecules directly from the precursor canisters, without relying on carrier gas dilution to push them into the reaction chamber. Although this is how the chalcogen precursors were introduced in the original work, it does not always give the most reproducible flow rate, as will be explained in Section 3.2.

There are a number of routes to alkyl chalcogenide decomposition at the elevated temperatures used in MOCVD synthesis. A pure thermal decomposition mechanism is unlikely, given that these reactions don't proceed until extremely high temperatures are reached. For example, the lowest molecular weight alkyl sulfide, dimethyl sulfide, does not thermally decompose until roughly 800°C:[11]

$$(CH_3)_2S \xrightarrow{\Delta} \text{no reaction below } \sim 800°C \qquad \textbf{Eq. 2. 3a}$$

Although the decomposition temperature is greatly reduced for increasingly substituted and branched species, such as ethyl mercaptan[11] (more similar to DES),

$$CH_3CH_2SH \xrightarrow{\Delta} \text{no reaction below } \sim 520°C \qquad \textbf{Eq. 2. 3b}$$

the reaction barely initiates at the reaction temperatures used in MOCVD of monolayer MoS_2, which is usually between 500-550°C. Therefore, it is more likely that the decomposition follows a hydrodesulfurization (HDS) mechanism, where, for example, DES is hydrogenated to produce hydrogen sulfide gas and various carbon products:[12]

$$(CH_3CH_2)_2S + H_2 \xrightarrow{\Delta,Cat} H_2S + C_2H_6 + (\text{see Fig. 2.18}) \qquad \textbf{Eq. 2. 4}$$

The reaction produces radical intermediates, which can recombine to form a number of carbon species, as shown in **Fig. 2.8**, although these products are expected to be volatile and easily carrier out of the growth chamber. Hydrogen sulfide is likely the active species to be used in the reaction for forming the TMD films.

HDS is a common process used in oil refining to break down organosulfides, and the reaction temperatures are much lower due the use of a metal catalyst. Interestingly, bulk MoS_2 and WS_2 are actually primary catalysts for this industrial process, and reduce the decomposition temperature for methyl mercaptan (similar to the compound in **Eq. 2.3a**) to 200-300°C.[13] This is can produce a reasonable reaction rate at the temperatures used in MOCVD. The catalytically-active sites of TMD crystals are actually the edges (not the basal plane).[14] This edge catalysis suggests that another driving force for two-

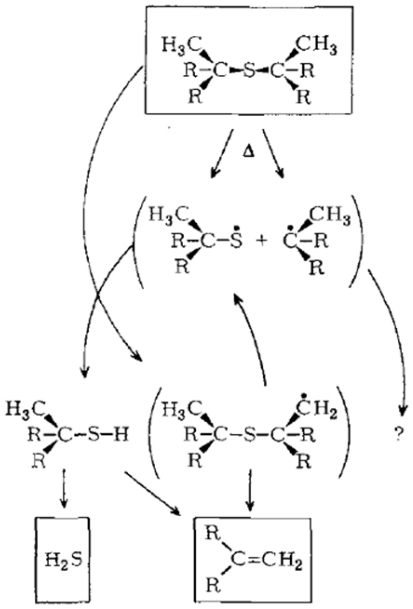

Figure 2.8. Proposed thermal decomposition pathway for alkyl sulfides, involving the production of radical species. Eventual products are hydrogen sulfide gas and volatile carbon species. Reproduced from Ref. 11.

dimensional (vs. three dimensional) growth of these TMDs may be increased alkyl chalcogenide decomposition near the edge of a growing island, selectively promoting edge growth.

The chalcogen precursor is used in great excess for monolayer TMD growth. Indeed, from the CVD phase diagram in **Fig. 2.1**, we can see that MoS_2 can be produced as the most stable phase at much higher concentrations of sulfur precursor. Higher concentrations of the hexacarbonyl produce significant portions of oxides and carbides. Because of their excess presence, the chalcogen precursor has little to no effect on the growth rate of the film. Instead, it is found to dictate the nucleation rate of the film, as illustrated by the optical images in **Fig. 2.9**. The nucleation density decreases as the DES flow rate is reduced from 0.3 to 0.2 to 0.1 sccm, resulting in films with increasing grain size, from <1 μm to ~10 μm to no nucleation (and hence no film growth) for the condition in the third image of **Fig. 2.9**. Although the major avenue to control the nucleation in this MOCVD technique is through the use of alkali metal halide salts (see subsection below), it is actually not possible to grow films with large grain sizes if the chalcogen precursor flow is above a certain threshold. We will revisit this topic in Section 3.2, when we discuss of the effect of ambient temperature conditions on the ability to control chalcogen precursor flow.

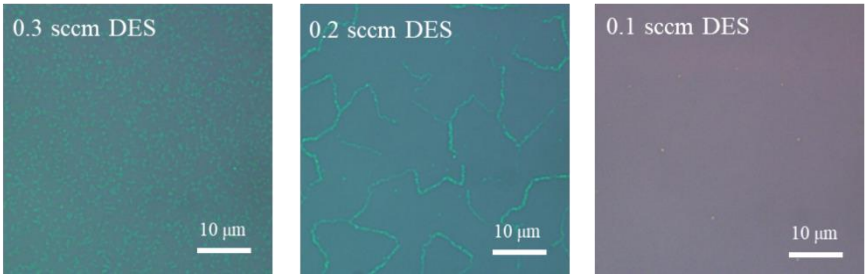

Figure 2.9. Optical images of three MoS2 growths carried out under the same reaction conditions, except flowing different amounts of sulfur precursor.

While it is decently easy to control the nucleation of sulfide-based TMDs, the selenides are significantly more difficult. This may partially be a consequence of the lower decomposition temperatures of alkyl selenides, which are less thermally-stable than their alkyl sulfide

counterparts,[15] leading to a more difficult to control reactivity. **Fig. 2.10** shows an example of the large differences seen between WS_2 and WSe_2 grown using this MOCVD technique. WS_2 growth with DES typically produces highly-faceted single-crystals with homogenous grain size, but WSe_2 growth with DMSe, even using similar reaction temperature and metal precursor flow, usually exhibits uncontrolled nucleation, resulting in crystals with different sizes (i.e., nucleating at different times) and spikey shapes indicative of additional nucleation on the edges of existing crystals. We attribute these nucleation differences to the chemical reactivity of the DMSe precursor because we know that highly-faceted WSe_2 crystals are easily achievable using traditional CVD with other precursors.[16]

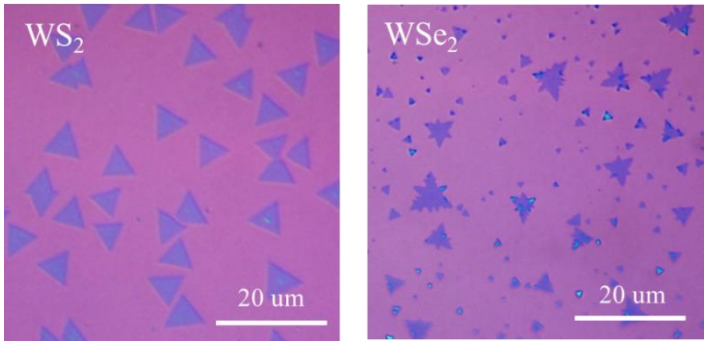

Figure 2.10. Optical images of typical single-crystal growths for WS_2 using diethyl sulfide (left) and a WSe_2 using dimethyl selenide (right).

Interestingly, although the nucleation rate of the selenide precursor is exceedingly difficult to control, the growth rate using this precursor is extraordinarily slow. We have observed this in trying to grow alloys of WSe_2 and WS_2. The Raman and PL spectra of $WSe_{2x}S_{2-2x}$ alloys grown with different percent compositions of selenide are shown in **Fig. 2.11**. Even an alloy that is composed of only 20% W-Se bonds (**Fig. 2.11**, orange lines) requires a mass flow rate of DMSe that is 8x higher than that of DES (this is using MFCs with identical configurations, so a comparison is justifiable). (Note: alloy compositions were determined from a previously published study.[17]) We have made similar observations when growing WS_2-WSe_2 lateral heterostructures, where we find that the WSe_2 component requires 10-20x longer growth

time to achieve the same width of the WS_2 component for comparable precursor flow rates. It is unclear if these observations are related to the specific reaction of DMSe with $W(CO)_6$, or if this it

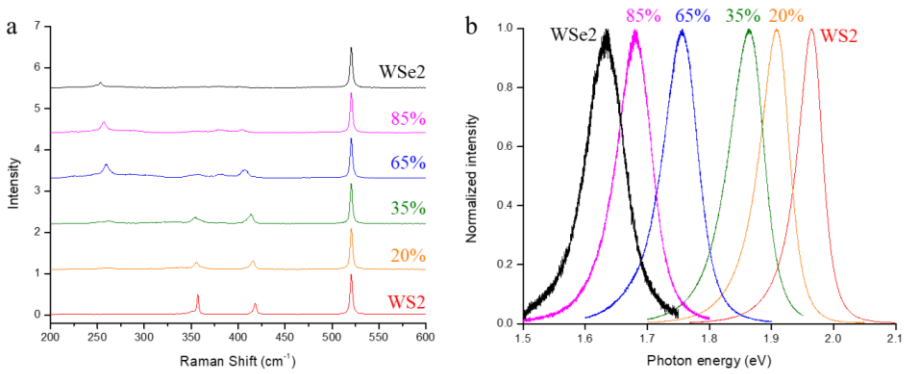

Figure 2.11. a) Raman and b) photoluminescence of $WSe_{2x}S_{2-2x}$ alloys grown using MOCVD. Percentages indicate the amount of selenide in the alloy (determined from Ref. 17), where the flow rate of DMSe was 0.8 sccm in all cases, and the flow rate of DES was incrementally increased: 0.01 sccm (pink), 0.05 sccm (blue), 0.025 sccm (green), 0.1 sccm (orange). Spectra of pure WSe_2 and WS_2 are shown for comparison in black and red, respectively.

2.4.3 Hydrogen gas

From the previous subsection, we can see that the major role of the H_2 gas is as a reactant in the decomposition of the alkyl chalcogenide precursors. It was also suggested in the work by Kang and Xie *et al.* that another role of the H_2 gas was to remove carbonaceous adsorbates from the walls of the reactor,[3] but this is highly unlikely considering the necessity of a catalyst for the feasibility of such a reaction, especially at these relatively low MOCVD temperatures. This could be possible if we assume there are sufficient active Mo or W species coating the reactor wall, but confirming this reaction would require a more careful investigation. It was also suggested that H_2 causes etching of the growing TMD islands. This is also unlikely, given that this reaction is only possible in nearly 100% concentration of H_2 relative to the other gases,[18,19] which is not the case for this MOCVD method.

It is more likely that the crystal shape changes observed in the original work were related to increased alkyl sulfide decomposition at higher hydrogen flow, rather than etching effects, since we know from the discussion of reaction-limited (or attachment-limited) kinetics in

Chapter 1 (**Fig. 1.11**) that the shape of TMD crystals depends heavily on the concentrations of the precursors at the growing edge. Actually, for larger reactors where the H_2 gas is much more dilute (≥2 inches in diameter; 500-2000 sccm carrier gas flow), we typically find that flowing the minimum (1 sccm) or maximum (100 sccm) amount of H_2 does not result in appreciably different crystal shape or nucleation density. Both of the assumptions about the role of H_2 mentioned in the previous paragraph likely come from the understanding of graphene CVD growth, where carbon decomposition by H_2 plays a dominant role.[20] These processes, however, are only possible because of the extremely high temperatures, high concentrations of H_2, and presence of a catalytic substrate in graphene synthesis, and likely do not play a dominant role in the MOCVD of TMDs on SiO_2 substrates.

2.4.4 Alkali metal halide Salt

Although the use of high vapor pressure metal and chalcogen precursors allows for better control of nucleation rates compared to traditional CVD, these changes mostly improve the homogeneity and monolayer yield—they are not enough to grow crystals or films with large domain sizes. Conventional CVD processes implement a number of tricks to grow large monolayer TMD crystals (e.g., > few μm) on nonepitaxial substrates,[21–25] but these methods only produce very small areas in random patches on the wafer, and the crystals cannot merge to form continuous films of usable size. One of the key achievements of this MOCVD technique was the introduction of alkali metal halide salts[3] to the TMD synthesis as nucleation inhibitors. The large grain size TMDs shown in **Fig. 2.9** and **Fig. 2.10** are actually only possible because NaCl was used to assist in the reaction.

A pellet of salt is made by spreading the alkali metal halide precursor surface of a quartz plate, adding water to fuse together the salt crystals, and baking to solidify the pellet. For a

routine growth with target grain size ~1 μm, the salt plate should be made very thin (< 5 mm) with an extremely smooth surface, and the water should be completely baked off before loading into the reactor. For large grain size film growth, the salt plate should be thicker and the surface should be made rough before the drying is complete, to promote more reaction with the TMD precursors. This preparation is mainly so that the salt crystals aren't blown away when evacuating or venting the reactor, but also provides a way to control the surface area. Although a number of alkali metal halides were originally found to be effective,[3] NaCl is used as the standard due to its effectiveness, low cost, and low toxicity. The salt plate is placed upstream of the growth substrates, such that the reactants flow over the salt plate before reaching the growth substrates. Because the grain size of the TMDs films is highly sensitive to the temperature of the NaCl, the plate is placed where the temperature of the reactor tube is significantly lower (probably ~100-300°C).

Moving the salt closer to the growth substrates (and concurrently increasing its temperature) reduces the nucleation rate, resulting in samples with larger grain size, as shown in **Fig. 2.12a**. Here, two WS_2 growths were carried out under the same reaction conditions, except with the salt plate moved 2 cm closer for the growth in the right image. Because of the large

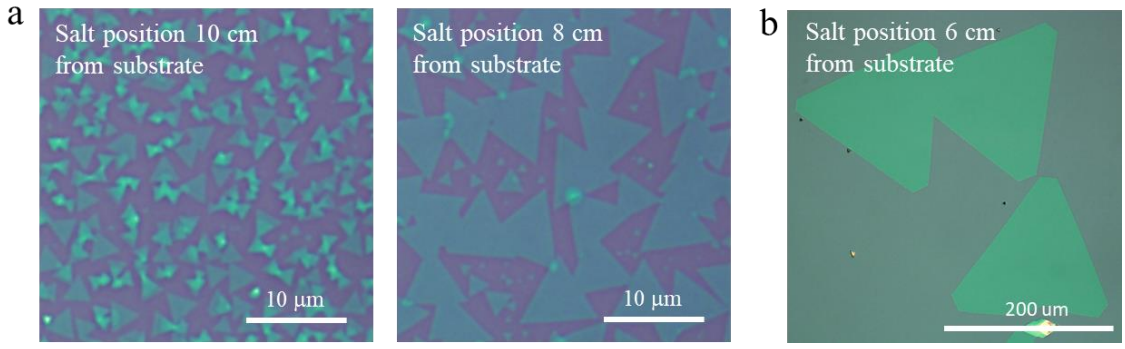

Figure 2.12. Optical images of a) a typical WS_2 growth using NaCl (left) and another WS_2 growth carried out under the same conditions except with the NaCl moved closer to the growth substrate (right), and b) giant WS_2 triangles grown with similar reaction conditions to (a), with the NaCl even closer to the growth substrate.

temperature gradient at the edge of the tube, pushing the NaCl closer by the same increment (here, another 2 cm) for a similar reaction condition, can produce a dramatically larger change in the nucleation density, such as seen in **Fig. 2.12b**. Usually, the more NaCl introduced to the reaction, the less homogeneous the domain size (i.e., nucleation happens multiple times during the growth, not just at the beginning). So, although this method can be used to grow up to 200 μm single-crystal TMDs, samples like the one shown in **Fig. 2.12b** will contain a mixture of crystals with various domain sizes across the substrate. Reactions with the salt plate closer to the substrate also usually result in more faceted crystals, although the mechanism for this change is unknown.

In general, growing large single-crystal monolayers using these alkali metal halide inhibitors is technically quite straightforward—the salt plate only needs to be moved incrementally closer until the desired nucleation density is achieved. Growing continuous films with large grain size, however, requires much more careful control of reaction conditions and other environmental factors (discussed more in Section 3.7). This is because larger domain size films require much longer growth times for a given set of reaction conditions, and the nucleation of bilayer islands on top of the existing film becomes inevitable after a certain amount of time (similar to the idea presented in **Fig. 2.4**).

The use of alkali metal halide nucleation inhibitors have even been adapted into conventional CVD processes, but the mechanism of how/why they work is still unclear. The original work suggested that the salt acts as a desiccant, reducing the concentration of water vapor in the growth environment.[3] This was proposed because it is possible for water to engage in a hydrolysis reaction to decompose the chalcogen precursor (similar to the hydrogenation by H_2). Since more active chalcogen species results in more nucleation, reducing the water content

in the reactor might reduce the nucleation. This explanation is not very plausible, however, given that NaCl does not hold water above ~110°C[26] (and certainly not under reduced pressure), as can be seen from the phase diagram in **Fig. 2.13**.

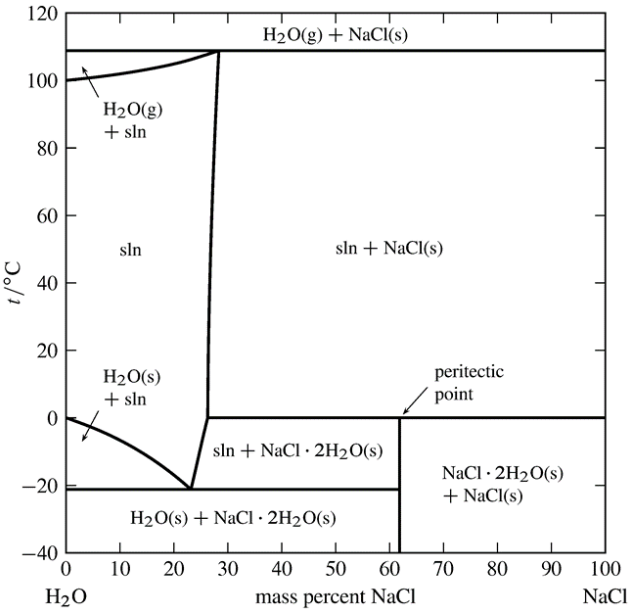

Figure 2.13. Temperature-composition phase diagram of NaCl-H_2O at 1 atm. Reproduced from Ref. 26.

Later, it was suggested that the NaCl sublimates during the reaction and is transported to the surface of the growth substrate. This was proposed because we generally see a white film depositing on the quartz tube on the upstream side near the salt plate and also downstream. We also routinely find sodium-containing adsorbates on the surface of these MOCVD TMD films (see XPS data in Section 3.4). A direct sublimation mechanism is also unlikely though, since the vapor pressure of NaCl is only $1x10^{-4}$ torr even at 500°C,[27] which is well over the expected temperature of the salt plate. It is more plausible that the NaCl reacts with the metal precursors to form a more volatile species that can transport down the length of the reactor tube. The mechanism may be similar to reactions occur between NaCl and various metals at reduced pressures or elevated temperatures,[27,28] or it may be similar to conventional physical vapor transport (PVT) process, where halide gases are used as transport agents for metals oxides, forming volatile metal oxyhalide species.[29] Presumably, the intermediate species formed by the reaction with the alkali metal halide would have to be less reactive than the original metal precursor, allowing for a suppression of the nucleation rate, although we have not performed any studies related to these

theories. Since the original work, however, numerous papers have been published by other groups,[30–33] studying in more detail the mechanism of nucleation suppression by alkali metal halides in CVD, which can be referred to instead.

One final note regarding the use of solid alkali metal halide precursors is that, although the synthesis is decently reproducible and works well for the most common TMDs (the molybdenum and tungsten sulfides and selenides), any kind of solid-phase precursor can leave residues on the grown films, as we see for the sodium-containing residues left from our MOCVD process. Residues are also left on the reactor walls, which affect subsequent growths, adding an element of unpredictability. Furthermore, the surface area of a solid precursor is what determines the reaction rate, and this is more difficult to reproduce than the flow rate of a gaseous precursor (i.e., similar the issues that people experience with powder CVD). For this reason, the preparation of the salt plate (e.g., the thickness, surface roughness, bakeout time, etc.) matters a great deal in determining the grain size of TMD growths. Changing to a gas-phase nucleation inhibitor would likely mitigate these problems. Halide gases, such as those used in PVT processes (e.g., Br_2 and I_2), would probably be good starting points, although safety would be a concern in these cases. Alkyl halides or ammonium halides can be other options, since a very high vapor pressure is likely not necessary. Using transition metal halides that are not the metal of interest is not recommended, since it would lead to contamination of the growth reactor and doping of the TMD film.

2.4.5 Carrier Gas

The carrier gas used in an MOCVD process can be any nonreactive gas, but Ar and N_2 are the most common due to cost and availability. Different carrier gases can result in different nucleation and growth rates if the physical properties of the gases (e.g., specific heat capacity,

viscosity, etc.) are different enough. One reason for this is, for example, carrier gases with different heat capacities will result in different substrate surface temperatures, which can affect the precursor decomposition rates, nucleation rates, and growth rates. Between N_2 gas and Ar gas, however, the growth rate and nucleation density of the films produced are very similar (within the normal expectation for growth rate fluctuation), as seen from the data in **Fig. 2.14**, even though the specific heat capacity of N_2 is twice that of Ar.[34]

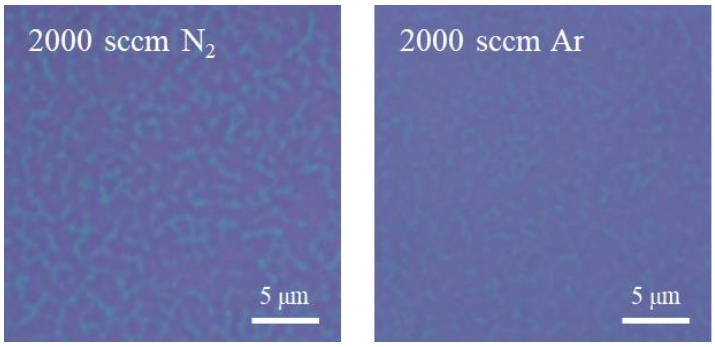

Figure 2.14. Optical images of two MoS_2 growths carried out under the exact same reaction conditions, except with different carrier gases.

Some effects of the carrier gas flow rate were discussed previously in Section 2.3. More carrier gas typically produces more homogenous film coverage due to the distribution of the reactants across the growth substrate, although the overall nucleation and growth rates drop, likely because of the reduced reactant concentration at the surface of the substrate. Having extremely high carrier gas flow, however, has two possible consequences. The first is that the flow in the reactor may become turbulent, leading to locally inhomogeneous reactant concentrations and film growth rates. Although this is theoretically possible, we have not actually experienced this for our MOCVD process, even with a flow rate of 2000 sccm in a 4-inch reactor.

The second drawback of high carrier gas flow is that it can impede the flow of the lower vapor pressure reactants into the gas line. This is because gases will only flow of an area of higher pressure to an area of lower pressure. The room temperature vapor pressure of DES is ~60

torr, so it is only possible for DES vapor to flow from the precursor canister into the gas line (and then into the reactor) if the total pressure of the other gases occupying the gas line is less than 60 torr. These MOCVD processes are carried out at total pressures between 1-20 torr, depending on the amount of carrier gas flow. That pressure, however, is the pressure measured for the gases in the 1-inch exhaust line (i.e., exiting the growth chamber), which is much wider the gas line (3-4 mm). Because the pressure depends on the volume occupied by the gas, one would expect that the pressure in the gas line would be 40-70x higher than what is being measured at the exhaust. Hence, it is indeed possible for the pressure in the gas line to significantly exceed the room temperature vapor pressures of the chalcogen precursors depending on the flow of the carrier gas, which makes up the majority of the pressure in the gas line.

This is what we experimentally observe in our MOCVD systems, where the chalcogen precursor will simply not flow above a certain carrier gas flow rate. A similar problem often occurs when new MOCVD systems are built, if there is a sizable air leak anywhere in the system. Even if there is a leak downstream of the gas line, such as a crack in the quartz tube, it is still possible to experience zero to low chalcogen flow, because the pumping speed of the vacuum pumps on the system is limited regardless of where the leak occurs. Usually, the chalcogen precursor will never reach the maximum flow rate achievable by the mass flow controller even if no carrier gas is being flowed, since there will always be air leaking into the line.

This issue does not occur with the metal precursor, which is diluted in Ar to at least atmospheric pressure. Thus, the solution would be to also backfill the chalcogen precursor canisters with carrier gas, to guarantee that the pressure is always much higher than the pressure in the gas line. This geometry, however, is slightly tricky to implement with liquids, which is

explained in more detail in Section 3.2. Typically, the amount of chalcogen flow without dilution in carrier gas is enough to achieve decently reproducible monolayer growth of many TMDs, including MoS_2, $MoSe_2$, WS_2, and WSe_2.

2.4.6 Reaction Temperature

The final reaction parameter that needs to be considered for monolayer TMD growth is the temperature of the growth chamber. Typical reaction temperatures in the growth of molybdenum and tungsten-based TMDs using MOCVD are between 500-650°C. This is lower than the temperatures used in conventional CVD processes for these materials, since metal hexacarbonyls and alkyl chalcogenides decompose into active species at much lower temperatures than the metal oxides and chalcogen powers used in conventional CVD growth. The choice of reaction temperature has multiple effects on the properties of the material. The most straightforward effect is increased nucleation and growth rate at higher temperatures. In general, this will always be the case for growths in the reaction-limited and diffusion-limited growth regimes (recall **Fig. 1.11**), since reactants are more likely to have enough thermal energy to overcome activation barriers for reactivity and diffusion. This is also because these reactions rely on the thermal decomposition of precursor gases into active species, which will be present in higher concentrations at higher temperatures.

Temperature-control of nucleation and growth are only possible when the nucleation-limiting reactant (chalcogen precursor) and growth-rate-limiting reactant (metal precursor) are in low

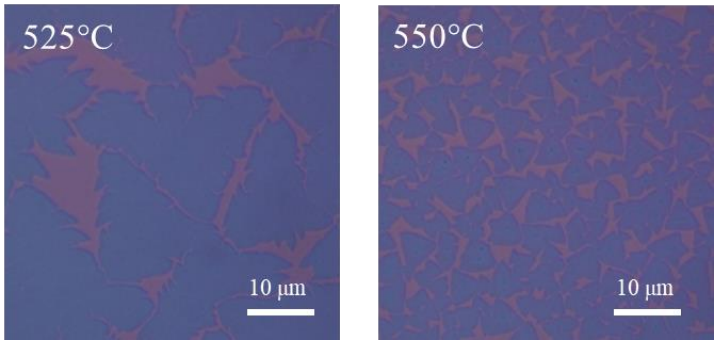

Figure 2.15. Optical images of two MoS_2 growths carried out under the same reaction conditions, with low metal precursor flow, at different furnace temperatures.

concentrations and also only at lower temperatures. Changing the temperature will show little effect when the nucleation and growth rates are already very fast. At slower nucleation and growth rates, one may observe something similar to **Fig. 2.15**, which shows a significant increase in the nucleation density for a small temperature change of 25°C. The growth temperature also affects the shape of the TMD crystals, although not necessary in a predictable way. **Fig. 2.16** shows this effect for a different reaction condition, where a 25°C temperature increase results in more notably faceted crystals. Typically, we would expect lower temperatures to promote reaction-limited growth, and hence form more faceted crystals, but in general we find that the kinetics of these multi-component MOCVD systems are more complicated.

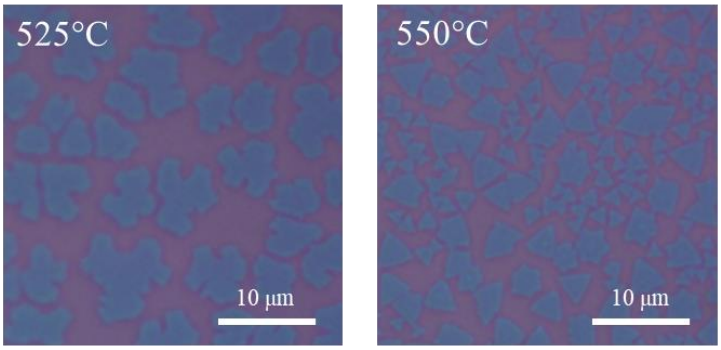

Figure 2.16. Optical images of two MoS_2 growths carried out under the same reaction conditions, at different furnace temperatures.

Usually, however, we would not rely on the reaction temperature to control the nucleation or growth rates, since we have independent control over precursor concentrations (as opposed to powder CVD, where the precursor concentration is tied to the furnace temperature). The reason we do not do this is because, above a certain temperature threshold, we find it is impossible to achieve a two-dimensional growth mode—at very high temperatures, multilayers will start to grow before the first layer is complete, and this occurs no matter how little metal precursor is used. Hence, the temperature selection is first and foremost based on where the material will exhibit two-dimensional growth.

Still, monolayer TMD materials can be grown in a relatively wide temperature range. There are pros and cons to using higher or lower temperatures. We have found that films grown at higher temperatures are more difficult to remove from their growth substrate. For example, we have found our work with Gao *et al.*[35] that MoS_2 grown at temperatures above 700°C do not delaminate in water, nor can they be mechanically peeled by a polymer. Although the reason for this strong adhesion is not entirely clear, it could be that the bonding to the substrate is no longer truly vdW in nature, specifically in areas of the films where there are electronic deficiencies (such as grain boundaries).

Higher reaction temperatures also tend to produce films that exhibit more strain, which changes their optical and mechanical properties.[36] This is because of the thermal expansion coefficient (TEC) mismatch between the TMD and the substrate, as illustrated in **Fig. 2.17a**. The TMD film deposits on the substrate at elevated temperature, so when the system is cooled, the substrate and TMD contract by different amounts depending on their TECs. If the TEC of the substrate is less than that of the TMD (**Figure 2.17a**, left panel), the TMD will contract more than the substrate. However, the interactions between the TMD and the substrate prevent the TMD from contracting all the way to its equilibrium state at room temperature, hence leaving the TMD slightly "stretched". The resulting film experiences tensile strain, which causes the band

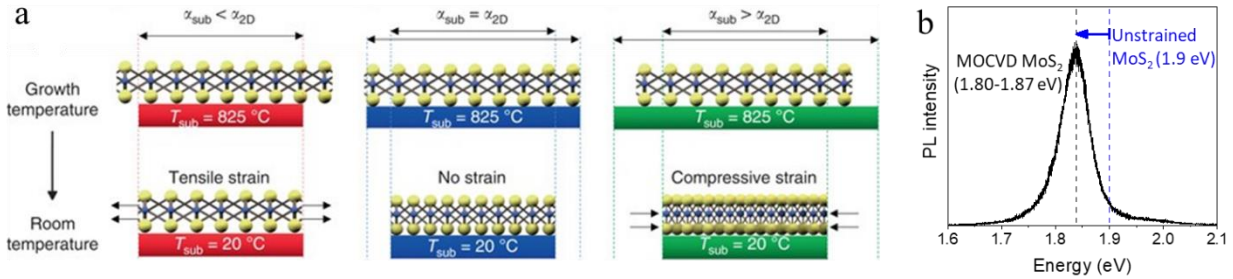

Figure 2.17. a) Schematic illustrating how strain in a CVD-grown TMD film is related to the relative thermal expansion coefficients of the TMD material (α_{2D}) and the substrate (α_{sub}). Adapted from Ref. 36. b) Repersentative PL spectrum of an MOCVD-grown MoS_2 film on an SiO_2/Si wafer, indicating the presence of tensile strain.

gap to narrow. If the relative TECs were flipped (i.e., substrate > TMD), the film would experience compressive strain and a widened band gap (**Figure 2.17a**, rightmost panel). The former is the case for the most common TMDs grown on SiO_2 wafers (e.g., MoS_2, WS_2, WSe_2), which is why our as-grown MoS_2 films typically exhibit PL redshifts between 0.3 to 1.0 eV relative to the value for exfoliated crystals (**Figure 2.17b**). (We note that PL shifts can also be caused by other factors, but we believe that strain is the dominant one here, since transferring the as-grown film to another substrate causes the peak to shift up very close to the unstrained value; see Section 3.7, **Fig. 3.13**.)

It is effectively impossible to form an unstrained film for elevated-temperature reactions, since that could only happen if we found a substrate with the exact same TEC as the TMD (**Figure 2.17a**, middle panel). Since thermal expansion coefficients are also temperature-dependent, the magnitude of the strain will increase with growth temperature. At very high temperatures, one would expect compressively-strained films to wrinkle upon cooling and films experiencing tensile-strained films to crack upon cooling. One should also take into consideration the chemical or phase changes that can occur in a material while cooling from a high temperature, a topic that will be covered in detail in Section 3.3.

From the aforementioned issues, it may seem prudent to run the reaction at the lowest temperature possible, but we find that many side reactions seem to dominate at lower temperatures, leading to contamination buildup, although this may seem counterintuitive. These reactions will be discussed throughout Chapter 3, but we have found that samples grown at lower temperatures seem to have greater proportions of adsorbed carbon, more surface adsorbates, and even intercalated species underneath the TMD film. We will also see that higher-temperature

reactions are more reproducible over the long-term. Hence, many factors must be considered in choosing a suitable reaction temperature, depending on the application of the film.

2.5 Summary

In this chapter, we discussed how the ability to manipulate reactant concentrations, enabled by the use of high-vapor-pressor precursors in MOCVD, is key to controlling the nucleation and growth rates of monolayer TMDs. This control allows us to realize TMD materials with morphologies ranging from highly-faceted single-crystals grown in a reactant-limited kinetic regime to wafer-scale monolayer films grown in a diffusion-limited kinetic regime. By having a fundamental understanding of the role of each reaction parameter, we can grow crystals and films with properties suited for different applications. Unfortunately, more than just a fundamental understanding is necessary for high-quality TMD growth in these exceedingly complex vacuum deposition processes. The following chapter will describe the practical understandings necessary for achieving reproducible growth two-dimensional of films.

2.6 References

(1) Dhar, S.; Kranthi Kumar, V.; Choudhury, T. H.; Shivashankar, S. A.; Raghavan, S. Chemical Vapor Deposition of MoS_2 Layers from Mo–S–C–O–H System: Thermodynamic Modeling and Validation. *Phys. Chem. Chem. Phys.* **2016**, *18* (22), 14918–14926.

(2) Song, I.; Park, C.; Choi, H. C. Synthesis and Properties of Molybdenum Disulphide: From Bulk to Atomic Layers. *RSC Adv.* **2015**, *5* (10), 7495–7514.

(3) Kang, K.; Xie, S.; Huang, L.; Han, Y.; Huang, P. Y.; Mak, K. F.; Kim, C.-J.; Muller, D.; Park, J. High-Mobility Three-Atom-Thick Semiconducting Films with Wafer-Scale Homogeneity. *Nature* **2015**, *520* (7549), 656–660.

(4) Lee, Y.-H.; Zhang, X.-Q.; Zhang, W.; Chang, M.-T.; Lin, C.-T.; Chang, K.-D.; Yu, Y.-C.; Wang, J. T.-W.; Chang, C.-S.; Li, L.-J.; Lin, T.-W. Synthesis of Large-Area MoS_2 Atomic Layers with Chemical Vapor Deposition. *Adv. Mater.* **2012**, *24* (17), 2320–2325.

(5) Ohta, T.; Cicoira, F.; Doppelt, P.; Beitone, L.; Hoffmann, P. Static Vapor Pressure Measurement of Low Volatility Precursors for Molecular Vapor Deposition Below Ambient Temperature. *Chem. Vap. Deposition* **2001**, *7* (1), 33–37.

(6) Ganske, J. A.; Rosenfeld, R. N. Molybdenum-Carbon Bond Dissociation Energies in Molybdenum Hexacarbonyl. *J. Phys. Chem.* **1990**, *94* (10), 4315–4318.

(7) Fillman, L. M.; Tang, S. C. Thermal Decomposition of Metal Carbonyls: A Thermogravimetry-Mass Spectrometry Study. *Thermochimica Acta* **1984**, *75* (1–2), 71–84.

(8) Janisch, D. S.; Lengauer, W.; Dreyer, K.; Rödiger, K.; van den Berg, H. Can We Influence Hardmetal Properties by Sintering in Carbon Monoxide? In *PM Tool Materials*; 2005.

(9) Daubert, T. E.; Danner, R. P. *Physical and Thermodynamic Properties of Pure Chemicals: Data Compilation*; Taylor & Francis: Washington, DC, 1989.

(10) Karlson, U.; Frankenberger, W. T.; Spencer, W. F. Physicochemical Properties of Dimethyl Selenide and Dimethyl Diselenide. *J. Chem. Eng. Data* **1994**, *39* (3), 608–610.

(11) Bock, H.; Mohmand, S. Unstable Intermediates in the Gaseous Phase: The Thermal Decomposition of Alkyl Sulfides RSnR. *Angew. Chem. Int. Ed. Engl.* **1977**, *16* (2), 104–105.

(12) Mudt, D. R.; Pedersen, C. C.; Jett, M. D.; Karur, S.; McIntyre, B.; Robinson, P. R. Refinery-Wide Optimization with Rigorous Models. In *Practical Advances in Petroleum Processing*; Hsu, C. S., Robinson, P. R., Eds.; Springer New York: New York, NY, 2006; pp 705–727.

(13) Wilson, R. Catalytic Reactions of Methyl Mercaptan on Disulfides of Molybdenum and Tungsten. *Journal of Catalysis* **1964**, *3* (5), 426–437.

(14) Daage, M.; Chianelli, R. R. Structure-Function Relations in Molybdenum Sulfide Catalysts: The "Rim-Edge" Model. *Journal of Catalysis* **1994**, *149* (2), 414–427.

(15) Plano, D.; Lizarraga, E.; Font, M.; Palop, J. A.; Sanmartín, C. Thermal Stability and Decomposition of Sulphur and Selenium Compounds. *J Therm Anal Calorim* **2009**, *98* (2), 559–566.

(16) Zhang, Z.; Liu, Y.; Dai, C.; Yang, X.; Chen, P.; Ma, H.; Zhao, B.; Wu, R.; Huang, Z.; Wang, D.; Liu, M.; Huangfu, Y.; Xin, S.; Luo, J.; Wang, Y.; Li, J.; Li, B.; Duan, X. Highly Selective Synthesis of Monolayer or Bilayer WSe_2 Single Crystals by Pre-Annealing the Solid Precursor. *Chem. Mater.* **2021**, *33* (4), 1307–1313.

(17) Duan, X.; Wang, C.; Fan, Z.; Hao, G.; Kou, L.; Halim, U.; Li, H.; Wu, X.; Wang, Y.; Jiang, J.; Pan, A.; Huang, Y.; Yu, R.; Duan, X. Synthesis of $WS_{2x}Se_{2-2x}$ Alloy Nanosheets with Composition-Tunable Electronic Properties. *Nano Lett.* **2016**, *16* (1), 264–269.

(18) Li, X.; Li, X.; Zang, X.; Zhu, M.; He, Y.; Wang, K.; Xie, D.; Zhu, H. Role of Hydrogen in the Chemical Vapor Deposition Growth of MoS_2 Atomic Layers. *Nanoscale* **2015**, *7* (18), 8398–8404.

(19) Cristol, S.; Paul, J. F.; Payen, E.; Bougeard, D.; Clémendot, S.; Hutschka, F. Theoretical Study of the MoS_2 (100) Surface: A Chemical Potential Analysis of Sulfur and Hydrogen Coverage. *J. Phys. Chem. B* **2000**, *104* (47), 11220–11229.

(20) Dong, J.; Zhang, L.; Ding, F. Kinetics of Graphene and 2D Materials Growth. *Adv. Mater.* **2019**, *31* (9), 1801583.

(21) Chen, W.; Zhao, J.; Zhang, J.; Gu, L.; Yang, Z.; Li, X.; Yu, H.; Zhu, X.; Yang, R.; Shi, D.; Lin, X.; Guo, J.; Bai, X.; Zhang, G. Oxygen-Assisted Chemical Vapor Deposition Growth of Large Single-Crystal and High-Quality Monolayer MoS_2. *J. Am. Chem. Soc.* **2015**, *137* (50), 15632–15635.

(22) Wang, S.; Rong, Y.; Fan, Y.; Pacios, M.; Bhaskaran, H.; He, K.; Warner, J. H. Shape Evolution of Monolayer MoS_2 Crystals Grown by Chemical Vapor Deposition. *Chem. Mater.* **2014**, *26* (22), 6371–6379.

(23) Rong, Y.; Fan, Y.; Leen Koh, A.; Robertson, A. W.; He, K.; Wang, S.; Tan, H.; Sinclair, R.; Warner, J. H. Controlling Sulphur Precursor Addition for Large Single Crystal Domains of WS_2. *Nanoscale* **2014**, *6* (20), 12096–12103.

(24) van der Zande, A. M.; Huang, P. Y.; Chenet, D. A.; Berkelbach, T. C.; You, Y.; Lee, G.-H.; Heinz, T. F.; Reichman, D. R.; Muller, D. A.; Hone, J. C. Grains and Grain Boundaries in Highly Crystalline Monolayer Molybdenum Disulphide. *Nature Mater* **2013**, *12* (6), 554–561.

(25) Ling, X.; Lee, Y.-H.; Lin, Y.; Fang, W.; Yu, L.; Dresselhaus, M. S.; Kong, J. Role of the Seeding Promoter in MoS_2 Growth by Chemical Vapor Deposition. *Nano Lett.* **2014**, *14* (2), 464–472.

(26) DeVoe, H. *Thermodynamics and Chemistry*; Prentice Hall: Upper Saddle River, NJ, 2001.

(27) Bourgès, G.; Faure, S.; Fiers, B.; Saintignon, S.; Lemoine, O.; Cardona-Barrau, D.; Devillard, D. Vacuum Distillation of Plutonium Pyrochemical Salts. *Procedia Chemistry* **2012**, *7*, 731–739.

(28) Rørvik, P. M.; Lyngdal, T.; Sæterli, R.; van Helvoort, A. T. J.; Holmestad, R.; Grande, T.; Einarsrud, M.-A. Influence of Volatile Chlorides on the Molten Salt Synthesis of Ternary Oxide Nanorods and Nanoparticles. *Inorg. Chem.* **2008**, *47* (8), 3173–3181.

(29) *Advanced Topics on Crystal Growth*; Ferreira, S. O., Ed.; InTech: Rijeka, 2013.

(30) Li, S.; Wang, S.; Tang, D.-M.; Zhao, W.; Xu, H.; Chu, L.; Bando, Y.; Golberg, D.; Eda, G. Halide-Assisted Atmospheric Pressure Growth of Large WSe2 and WS2 Monolayer Crystals. *Applied Materials Today* **2015**, *1* (1), 60–66.

(31) Wang, P.; Lei, J.; Qu, J.; Cao, S.; Jiang, H.; He, M.; Shi, H.; Sun, X.; Gao, B.; Liu, W. Mechanism of Alkali Metal Compound-Promoted Growth of Monolayer MoS_2 : Eutectic Intermediates. *Chem. Mater.* **2019**, *31* (3), 873–880.

(32) Zhou, J.; Lin, J.; Huang, X.; Zhou, Y.; Chen, Y.; Xia, J.; Wang, H.; Xie, Y.; Yu, H.; Lei, J.; Wu, D.; Liu, F.; Fu, Q.; Zeng, Q.; Hsu, C.-H.; Yang, C.; Lu, L.; Yu, T.; Shen, Z.; Lin, H.; Yakobson, B. I.; Liu, Q.; Suenaga, K.; Liu, G.; Liu, Z. A Library of Atomically Thin Metal Chalcogenides. *Nature* **2018**, *556* (7701), 355–359.

(33) Kim, H.; Ovchinnikov, D.; Deiana, D.; Unuchek, D.; Kis, A. Suppressing Nucleation in Metal–Organic Chemical Vapor Deposition of MoS_2 Monolayers by Alkali Metal Halides. *Nano Lett.* **2017**, *17* (8), 5056–5063.

(34) Gases - Specific Heats and Individual Gas Constants. *The Engineering Toolbox*; 2003.

(35) Gao, H.; Suh, J.; Cao, M. C.; Joe, A. Y.; Mujid, F.; Lee, K.-H.; Xie, S.; Poddar, P.; Lee, J.-U.; Kang, K.; Kim, P.; Muller, D. A.; Park, J. Tuning Electrical Conductance of MoS_2 Monolayers through Substitutional Doping. *Nano Lett.* **2020**, *20* (6), 4095–4101.

(36) Ahn, G. H.; Amani, M.; Rasool, H.; Lien, D.-H.; Mastandrea, J. P.; Ager III, J. W.; Dubey, M.; Chrzan, D. C.; Minor, A. M.; Javey, A. Strain-Engineered Growth of Two-Dimensional Materials. *Nat Commun* **2017**, *8* (1), 608.

CHAPTER THREE

Considerations for Reproducible MOCVD of High-Quality Monolayer TMDs

3.1 Introduction

In the previous chapter, we discussed fundamental aspects of how a MOCVD approach can enable the controllable synthesis of 2D TMD crystals and films. It turns out, however, that vacuum-based crystal growth techniques are often not limited by fundamental challenges, but practical ones. For example, although the use of high-vapor-pressure precursors in MOCVD enables a greater level of control compared to the solid precursors used in traditional CVD processes, the quantities of gases injected into a reaction are actually quite difficult to measure reproducibly, since the concentration will change with temperature, pressure of other reactants, and the geometry of the flow path that the gas must traverse to reach the reactor. These are not issues in solution-phase reactions, where the amount of liquid or solid reactants can be measured accurately and independently of other reactants.

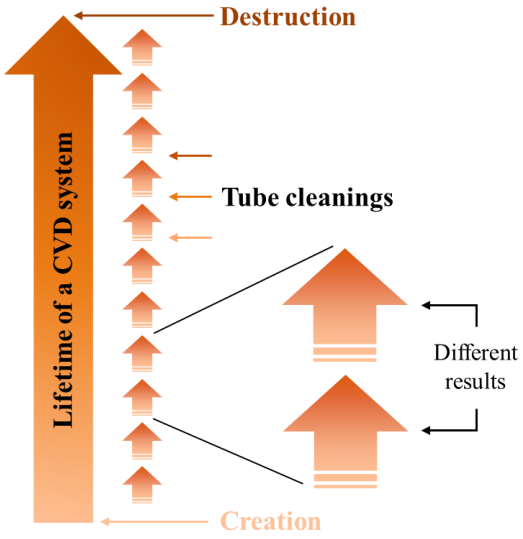

Figure 3.1. Schematic illustrating the concept of how running similar reactions at different point in the life cycle of a CVD system will generally produce very different results.

Another major challenge in the reproducibility of gas-phase crystal growth is the fact that the reactor tube and gas lines cannot be easily cleaned between reactions. This is akin to running a solution-phase reaction, partially pouring out the product, and then running the next reaction in the same flask, while also reusing the spatulas and weight boats. Even if one repeats the exact same experimental conditions, the results will not be the same. If this is done continually,

contaminants from previous reactions build up progressively, and eventually the results will become irreproducible. This concept is schematically depicted in **Fig. 3.1**, where the long arrow illustrates how the condition of a CVD system changes over time. Even if cleaning of the reactor is attempted (short arrows), residues from previous reactions always remain. Consequently, running the same exact reaction condition at different points in the system's lifetime (or even subsequently) will usually give different results.

Furthermore, although the direct growth of 2D crystals is convenient and necessary for any real application, the properties of materials synthesized in this way are generally different from 2D crystals that are achieved via top-down methods (e.g., growing bulk vDW crystals and exfoliating those down to 2D). This is because vdW crystals are inherently three-dimensional, so direct 2D growth requires restricting the reaction conditions to a narrow window of temperatures and precursor concentrations to forcefully confine the growth in-plane. It is unlikely that these restricted conditions also produce the material with the best physical/mechanical properties, or the cleanest surface, or one with minimal defects. In contrast, bulk vdW crystals are simply grown under whichever conditions produce the material with the desired property, and the dimensional-confinement is taken care of in subsequent steps.

For the reasons discussed above, even if we understand the theory and growth mechanism of vacuum-deposited 2D materials, the quality of the material achieved will be dominated by external factors. Being able to identify these factors is key to finding workable solutions that enable reproducible growth of high-quality 2D crystals and films. In this Chapter, we will investigate the practical challenges in the MOCVD growth of TMDs, how these issues affect the growth morphology and the physical, mechanical, and surface properties of the materials, and methods for mitigating these effects.

3.2 Factors Affecting Reactant Concentrations

3.2.1 Precursor Introduction Geometry

As alluded to in Section 3.1, one major source of experimental variation is the inability to properly measure and control the concentration of gas-phase reactants during MOCVD synthesis. **Fig. 3.2** depicts three different geometries used for introducing low-vapor-pressure precursors into the reaction. The configuration shown in **Fig. 3.2a** ("Configuration A") was the original geometry that this MOCVD technique was developed with.[1] Here, the metal hexacarbonyl precursor is heated to 100-120°C to increase its vapor pressure, which is measured by a mass flow controller (MFC) that regulates the flow rate (i.e., amount of gas that enters the reactor). From thermogravimetric analysis data of $Mo(CO)_6$ and $W(CO)_6$ (see **Fig. A3.1**),[2] it can be seen that these metal precursors will see start to see rapid sublimation above ~100°C. Although this configuration allows for sufficient metal precursor to be transported to the reactor, it will result in condensation of the precursor in the MFC and the gas lines, since they are at room temperature. Because the orifice in the MFC is tiny relative to the size of the precursor canister

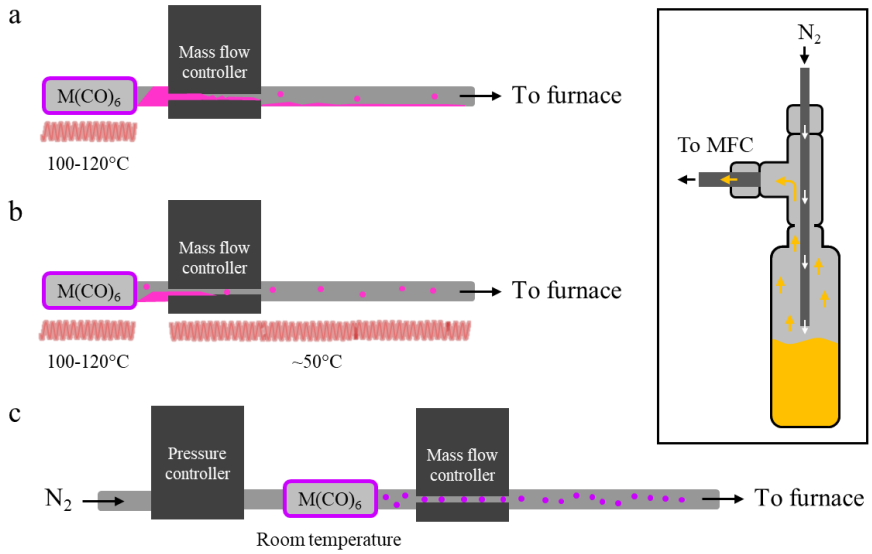

Figure 3.2. Different geometries for introducing low-vapor-pressure precursors. a) Heating the precursor canister, b) heating the precursor canister and the gas line, c) diluting the precursor in carrier gas at room temperature. The precursors in (a) and (b) are drawn in pink to emphasize that geometries that heat $Mo(CO)_6$ cause it to chemically change before it reaches the reactor. Inset: geometry for diluting a liquid precursor in carrier gas.

outlet, the MFC is can become completely blocked by the condensation. This results in dramatic fluctuation in the growth rate over time, as the line undergoes cycles of blockage and then random rapid release of precursor. Using this geometry, the growth time for full monolayer coverage in a 4-inch reactor changes uncontrollably between 15-35 hours, and the growth time is completely unrelated to both the precursor heating temperature and the flow rate of the MFC.

A slightly better configuration is shown in **Fig. 3.2b** ("Configuration B"), where the gas line is heated to above room temperature (using flexible heating tape). This results in less precursor deposition in the line, and hence, somewhat more reproducible growth rates. Unfortunately, the maximum temperature that can be used here is ~50°C before the electronics in the MFC start to be affected (the rest of the line can technically be heated higher, but the limiting factor is the extremely tiny orifice in the MFC). In both Configurations A and B, any small increase in the pressure in the line causes the flow rate of the metal precursor to drop (similar to the explanation in Section 2.4 regarding the sulfur precursor), since the vapor pressure in the precursor canister is lower than the pressure in the line. This results in a limit to how much precursor can be introduced into the reaction, restricting the growth rate. Additionally, both Configurations A and B both work better in a newly-built reactor, because the buildup of precursors over time starts to heavily deteriorate the growth quality. This is especially in the case of $Mo(CO)_6$, which we know from **Fig. 2.7** actually starts decomposing ~100°C (note that this is not the case for $W(CO)_6$). We can therefore assume that the actual form of Mo that makes its way into the reactor in Configurations A and B (drawn in pink in **Figs. 3.2a** and **3.2b**) is some version of $Mo(CO)_x$, where $x < 6$, and that over time there is a buildup of these species in the precursor canister and gas line. As in any case where a precursor is heated above its decomposition temperature before reaching the reactor, the decomposed species will have

different reactivities than the original precursor. Furthermore, the decomposition products can also react with other active species/contaminants to form byproducts that may have unpredictable effects on the synthesis. We have experienced such effect when using Configurations A and B for extended period of time, which will be elaborated on in Section 3.6.

The best geometry to introduce low vapor-pressure precursors is shown in **Fig. 3.2c** ("Configuration C"), which dilutes the precursor in a higher pressure of carrier gas, as explained in Section 2.4. Since the system is at room temperature, there is no preemptive degradation or chemical change of the precursor (hence, drawn in purple), and little buildup in the gas line due to the precursors being pushed downstream by the flow of the carrier gas. Furthermore, using high pressures of the dilution gas makes the precursor flow less sensitive to pressure changes (or leaks) in the line. As a result, the growth rate in Configuration C is sufficiently reproducible and highly controllable by changing the MFC flow rate (with growth times that can be controlled from as short as 0.5 hrs to over 30 hrs). Ideally, this configuration should be implemented with all low-vapor pressure precursors, including the chalcogen sources. For such liquid precursors, the carrier gas introduction geometry should be slightly modified to a bubbler-type configuration using bore-though fittings to prevent spillage, as shown in **Fig. 3.2** (inset).

One additional consideration is that gas lines should be built without tangling (such as what occurs when using excessive flexible tubing), and care should be taken to ensure that the tubes are not pinched or constricted at joints. These two issues greatly increase the flow resistance of the system, and can often be another factor limiting the maximum precursor flow.

3.2.2 Ambient Temperature Fluctuations

Another factor that greatly effects the amount of precursor flow into the reactor is the fluctuation of the ambient temperature, since the vapor pressures of liquids and solids are highly

temperature-sensitive. Although one might expect that the MFC, which measures the precursor's vapor pressure in real-time, should adjust the flow rate accordingly, this does not work very well in practice. We find that even if the flow rate reading is stable, the actual amount of gas flowing can be very different. If the room temperature decreases, the amount of precursor flow will be lower. Below a certain temperature, it is actually possible for the vapor pressure of the precursor to fall so below the pressure in the gas line that the precursor actually stops flowing altogether. We have observed this for the sulfur precursor, DES, where a 3°C drop in the ambient temperature causes the precursor to stop flowing, until the temperature rises again. This point is indicated in **Fig. A3.2a**, which shows how the temperature of the metal and chalcogen precursors fluctuate over the course of a 16-hour growth. Here, the $Mo(CO)_6$ has an average higher temperature because it is located closer to the furnace heater, and fluctuates less than the DES, which is closer to the front of the hood and has a similar temperature fluctuation profile as the outside of the hood.

If the room temperature increases, the MFC cannot properly adjust the flow rate, and the amount of precursor gas flowing into the chamber will actually be higher. Although having higher vapor pressure may not seem like an issue, we find that if we increase the room temperature beyond a certain point, then it becomes more difficult to control the nucleation (i.e., more difficult to grow large grain size crystals) during the film growth. This is presumably because of the increased DES precursor vapor pressure and the failure of the MFC to properly regulate it.

Diluting the chalcogen precursor in carrier gas would definitely prevent this issue of the flow stopping upon temperature drop, although it does not help the issue of the vapor pressure fluctuating. Thus, selecting a proper room temperature and then ensuring the temperature is

stable is pertinent to achieving controllable and reproducible precursor injection. Once common solution is to heat the canister and gas lines just above room temperature (similar to **Fig. 3.2b**). When doing this, the vacuum components should be rigorously clean, and the heating unit should have very good PID temperature control to prevent overshooting, which can cause problems such as the one that will be described in Section 3.6. Water-cooling is a safer option, although difficult to implement with space constrictions. We actually find that, simple fiberglass insulation works quite well for dampening temperature fluctuations, as seen in **Fig. A3.2b**, which shows a drastic reduction in the temperature fluctuation of the DES precursor relative to the room temperature after insulation.

3.2.3 Mass Flow Controller Limitations

As described in the previous subsection, the measurement tool for controlling the flow of gases, MFCs, are not always reliable, especially for gases with low vapor pressures, such as the ones used in this MOCVD technique. There are two main issues here: precision and accuracy. MFCs should never be assumed to be accurate in their flow rate, especially if the gas is a non-standard gas. For common gases, MFCs typically can use the known physical properties of the gas (e.g., viscosity, conductivity, heat capacity) at a given temperature to calculated the flow rate of that gas, by using what is knows about the flow rate of a well-known gas (such as N_2). Unfortunately, most MOCVD precursors do not have well-characterized physical properties, making accurate determination of the flow rate an impossibility. This is less of an issue for standard gases, as long as the pressure in the inlet of the MFC is much higher than the pressure in the gas line (i.e., there is nothing to impede the flow). It is therefore hard to make conclusions on small differences in the reactivity of different precursors in CVD processes, since it is realistically not possible to measure the same amount of both.

The previous point is a fundamental limitation on accurate gas flow measurements, but there are also technical limitations. Even MFCs set to flow the same amount of the same gas can actually be flowing very different amounts depending on the diameter of the MFC flow channel. For example, a MFC with a full-scale flow of 10 sccm has a significantly smaller channel diameter than a MFC with full-scale flow of 100 sccm. We find that if we flow DES through both of these MFCs and use an independent pressure measurement, the 10 sccm MFC actually results in ~1/3 less pressure of DES than the 100 sccm MFC, even though the flow value set on both MFCs is the same. This is probably related to the fact that a larger channel volume can accommodate more molecules (i.e., more mass) for the same pressure drop between the precursor canister and the gas line. Ideally, the MFC with the larger channel should account for this difference, but in practice this does not work very well. And although the 100 sccm MFC will be able to flow more (which is ideal for low vapor pressure precursors), the flow will be less reproducible since the resolution of the flow rate will be in large steps for the larger flow range. This is why, when selecting a MFC for low vapor pressure precursors, it is better to buy a MFC with a wider channel (e.g., a full range of 100 sccm), and then add a finer custom calibration range (e.g., 10 sccm) to achieve maximum flow with the best precision.

For the reasons introduced above, MFCs are better used for *precision*, rather than accuracy, as long as a number of conditions are met. A few of these have been touched on already: the ambient temperature should be stable, and the pressure in the gas line should be relatively constant and low in comparison the pressure of the gas being controlled. In this case, flowing “10 sccm” today should be similar to flowing “10 sccm” tomorrow for any particular gas, if the MFC is installed and maintained properly. For the installation, we find that the actual amount of flow by the MFC, even for high-pressure carrier gases, will fluctuate significantly

(using an independent pressure reading) if the MFC is installed with its valve on the high pressure (i.e., precursor canister) side. This is because the pressure reading occurs on the opposite side of the valve. The pressure should be read on the side of the gas being controlled, so that the MFC can know the pressure of the gas and calculate how much to open or close the value when the gas pressure fluctuates. If the pressure is being read after the valve, then we find that there is a feedback lag that results in a fluctuation of the flow rate. Installing the value on the low pressure (i.e., gas line) side greatly improves the precision of the precursor measurement.

Over long periods of time, however, condition of the MFCs can change, and so the amount of gas flow can slowly drift. This is one aspect of the "lifetime of a CVD system" mentioned in Section 3.1—the tube, gas lines, and MFCs all change as precursors build up in them over time. We experience this long-term lack of precision of MFCs particularly with the chalcogen precursors. Although these gases are not corrosive, we find that if the chalcogen MFC is not used for a very long period of time (months), the MFC will experience severe problems upon attempting to restart the flow. Sometimes the controller will simply not flow at all, but sometimes it will read as if it is flowing the proper amount, but experimentally the growth shows that it is flowing almost nothing (i.e., extremely reduced nucleation). Furthermore, we experience this effect even for MFCs where the entire flow channel and value are constructed of stainless steel, and oddly enough, this drastic change does not occur if the MFC is constantly being used.

Although the reasons for this irreproducibility in flow after periods of stagnation are not clear, we suspect that the issue is related to the fact that MFCs that are constantly being used are also constantly being purged (as the vacuum pulls the gases into the reactor). When the MFC is not being used, the valve is closed, so there is no vacuum to pull adsorbed gases out of the

channel and pressure gauge in the MFC. It is reasonable to think that over long periods of time, certain gases might diffuse into the pressure gauge and adsorb strongly. In such a case, proper pressure measurement would not be possible (even if the gases are not corrosive), and so proper flow may not be achieved. Indeed, we find that this degradation of the MFC is reversible if the flow is restarted and the MFC is used continually for long enough (although this can take more than a week in some cases). In order to improve the long-term precision of MFCs, it is better to install an additional valve between the precursor canister and the MFC inlet, to block precursor gases from entering the flow channel when the instrument is not in use. Going even further, one can install an additional gas line going into the inlet of the MFC, which can be used to flush the flow channel of any precursor residues between growths.

One final note is that, even if the temperature and pressure conditions are extremely well-controlled, the actual nucleation and growth rates depend on the concentration of gases at the surface of the substrate, which changes with total volume and flow distribution. Therefore, even if the same amount of gas is injected into two different reactors, the results will still be different depending on the width of the furnace, the height of the substrates, the flow pattern, etc. For all of these reasons, vacuum deposition processes typically work based on constant optimization—pick a reaction condition and then adjust the gas flow rates based on the result.

3.3 Spatial and Temporal Temperature Gradients

3.3.1 Furnace Temperature Gradients

Another important factor to understand in high-temperature vacuum systems is the effects of temperature changes in the furnace, both spatial and temporal. As one might expect, the temperature in a reactor will not be spatially uniform. Heat transport is impeded in vacuum, where there is little mass to thermally conduct. The heater coils are directly in contact with the

walls of the quartz tube, so looking at a cross-section of the tube, one would expect the temperature near the tube walls to be highest, decreasing towards the center of the tube. Furthermore, the temperature drops rapidly near the left and right ends of the heating zone, so placing substrates in these regions can result in growth and nucleation kinetics that are very different from areas where the temperature is more uniform. Temperature gradients that exist along the length of a tube are depicted in **Fig. 3.3**.

The temperature in the reactor drops near the upstream and downstream ends of the tube, which are located outside of the heating zone, so the uniform temperature region is much shorter for a one-zone furnace tube compared to multi-zone furnaces, as shown in **Fig. 3.3a** and **3.3b**. For this reason, chambers with only a single heating zone (usually 1 to 2-inch reactors) often need to be heated to higher temperatures to achieve the same growth quality as multi-zone furnaces. More specifically, this is because precursors flowing into the chamber need to be heated for a certain amount of time at a minimum temperature in order to decompose sufficiently to achieve decent growth and nucleation rates. Heating a single-zone furnace to a higher temperature increases the average temperature of the gradient, allowing a longer length of the tube to meet the minimum

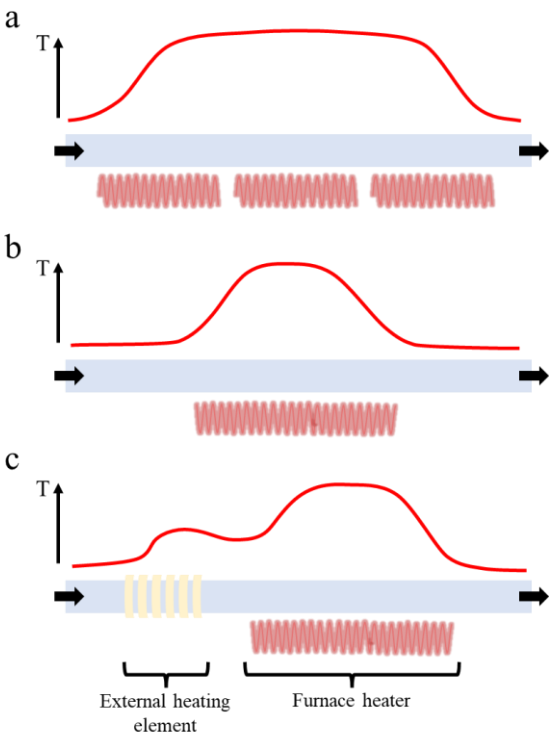

Figure 3.3. Temperature profile vs. position along the furnace tube for different heater geometries. a) three-zone furnace, b) single-zone furnace, c) single-zone furnace using an external heating element around the tube upstream. Black arrows indicate gas flow direction.

temperature threshold for decomposition. This method is not the most effective, however, since we know that a two-dimensional growth mode is not always achievable above certain temperatures.

An alternate way to increase the length of the heating zone in a single-zone furnace is to use a longer quartz tube and wrap a flexible heating element (such as heating tape) around the area of the tube that sticks out of the furnace heater on the upstream end (see **Fig. 3.3c**). This can help mitigate the temperature gradient in the reactor and begins exposing the reactant gases to elevated temperatures to initiate decomposition before the gases reach the substrate. The drawback of this geometry is that there ends up being a "cold zone" in the length of the tube between the external heating element and the furnace coils, where the temperature dips. In this region, one typically will see deposition of reaction byproducts, that can over time offgas into the main heating zone. The consequences of this, however, is highly specific to the precursors being used in the vacuum system.

Still, the extra heating length in the configuration in **Fig. 3.3c** allows time to generate more active species for a lower reaction temperature. This can be used as an alternative method for growth with precursors with extremely low room temperature vapor pressures, such as the $NbCl_5$ and $Re_2(CO)_{10}$ used in the work by Gao *et al*.[3] In this study, extremely high reaction temperatures were used instead, which produced TMD films that could not be removed from their growth substrates, limiting the applications of the work. Overall, it can be seen that multi-zone furnaces offer more control over reaction kinetics and can enable the synthesis of materials that cannot be realized in reactors with shorter heating zones.

3.3.2 Furnace Ramping Stage

In high-temperature reactors such as those used for MOCVD, the spatial temperature gradients are relatively insensitive to ambient temperature fluctuations once the furnace has achieved the target temperature. During the ramping and cooling stages of the growth, however, the temperature profile in the reactor will be different from those depicted in **Fig. 3.3**, especially for multi-zone furnaces where the temperature controllers of different heating zones will often overshoot by different amounts before cooling to the target temperature. Typically, one would not flow any reactants during the temperature ramping stage, since it is likely that the material that deposits during that time would not be the desired composition or thickness. However, we know from Section 2.3 that in a vacuum reactor there is always precursor residue adsorbed to the walls, which will desorb and deposit on the substrate during the ramping stage. In other words, nucleation starts even before any precursors start flowing, and so the gases that are flowed during the ramping period will determine the nature of what nucleates.

Fig. 3.4 illustrates one example of the importance of understanding ramping conditions, related to a common pyramid-shaped nanostructure observed on CVD-grown TMD films. **Fig. 3.4a** shows optical images of different areas of a large grain size (>1 μm) MoS_2 film grown using similar reaction conditions as the original MOCVD work, which used low carrier gas flow

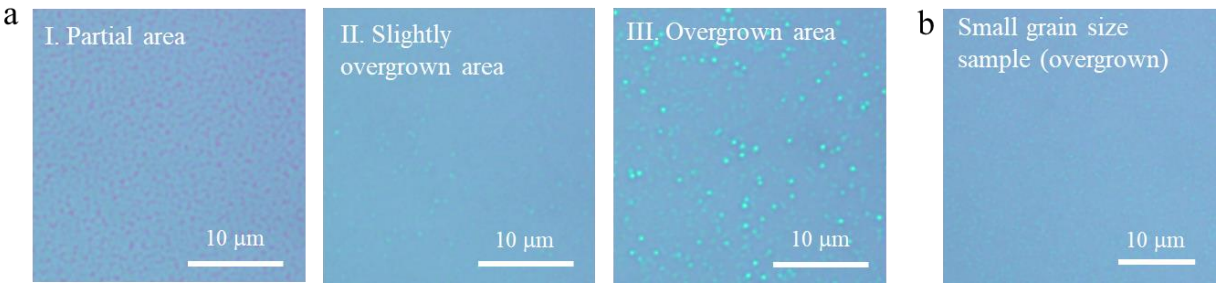

Figure 3.4. a) Optical images of a large grain size MoS_2 film taken at various different areas along the wafer, from partial (I) to overgrown (III), and b) an optical image of an overgrown MoS_2 film with small grain size.

during ramping.[1] The sample is monolayer until the film just becomes continuous, at which point tall, triangular-spaced structures start rapidly depositing on the surface (bright blue spots in **Fig. 3.4a**, image III). Furthermore, these features are never observed on small grain size films, even if the sample is very overgrown (**Fig. 3.4b**). From AFM measurements, we can see that the features are actually pyramid structures of multilayer MoS_2 that are up to ten nanometers in height (**Fig. A3.3**). These sparse nanostructures were unknown and largely ignored, since most applications do not require large grain size films. Later, however, they became detrimental to studies of stacked TMD structures with controlled thickness. For example, in our work with Lee, *et.al.*,[4] we studied the use of stacked TMD films as tunnel barriers for Josephson junctions, that required films thin enough to observe electron tunneling across them. In our work with Kim, *et.al.*,[5] we studied the thermal transport properties of stacked TMD films, including the effects of the grain size. Both of these studies required large-area films, where the thickness can be controlled via layer-by-layer stacking of TMD monolayers with uniform and well-defined thickness.

Because the multilayer nanostructures shown in **Fig. 3.4a** (image III) are on average ten times thicker than the TMD monolayer, they dominate the thickness of any stacked TMD film and prevent adjacent monolayers from making good contact with each other. In order to enable the aforementioned studies, we investigated the source of these nanostructures. Growths performed in a clean reactor tube typically do not show these features, which build up after a few reactions. Since the tube coating is the only difference between these two cases, it seems that the formation of these nanostructures is decided in the ramping/nucleation stage, even though they do not actually form until the film becomes continuous. We also tested multiple cooling procedures, and none had any effect.

After testing a number of ramping procedures, we found that flowing high carried gas (i.e., similar amount to what is flowed during the growth) during the ramping stage actually reduced nanostructure formation. However, as mentioned in the previous chapter, ramping with low carrier gas flow (i.e., ~1/100th of what is flowed during the growth) actually produces more homogeneous samples, as material from the tube walls start to deposit at the edges of the substrate before the actual precursors start flowing, to balance out the growth rate. Since producing stacked TMD films requires large areas of the monolayer starting material, flowing high carrier gas is not a viable solution.

An alternate solution we found was that flowing the chalcogen precursor during the ramping (with low carrier gas flow) completely removed these nanostructures, as shown in **Fig. 3.5**, and did not seem to have other impacts on the sample homogeneity. The chalcogen precursor is generally benign in terms of its impact on film quality—it is usually high metal precursor concentration that is usually associated with multilayer formation, excessive carbon deposition, etc. Assuring that there is an excess amount of chalcogen available during the ramping assures that the nuclei that form will be more similar to the nucleation that occurs when the precursors actually start flowing (i.e., where there is large excess of chalcogen). Although it is still not clear why these structures only form on films with low nucleation density (i.e., large grain size), the above investigation

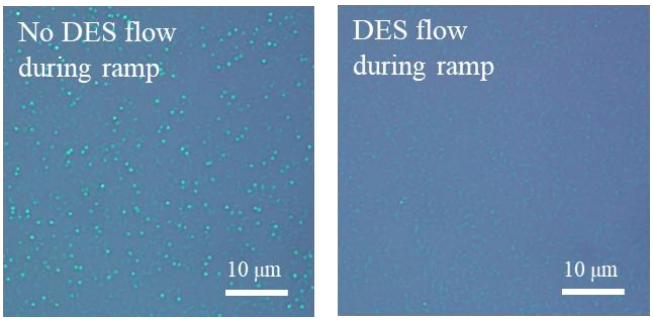

Figure 3.5. Optical images of two subsequent MoS_2 growths carried out without (left) and with (right) flowing sulfur precursor during the ramping stage.

illustrates how much the environment during the ramping and nucleation can affect the morphology of the final film.

3.3.3 Furnace Cooling Stage

Just as the reactor environment during ramping can significantly impact the quality of the TMD film, so can the reactor environment during cooling. The most straightforward impact one must consider, which was alluded to in the previous chapter, is the chemical changes a material might experience while cooling from very high temperatures. In general, we can consider a crystal grown under a certain temperature and precursor concentration to be a stable phase under those specific conditions. If the precursor concentration is reduced while the film is held at the same temperature, is it possible that certain atoms will "sublimate" out of the crystal because of the reduced vapor pressure environment, producing defects. Another common issue in vacuum deposition processes is oxidation of a material during cooling. It is also possible for more exotic materials to exhibit a phase change under cooling conditions.

For TMD materials, it is generally thought that the most common vacancy—the sulfur vacancy—is generated when the crystals are held at high temperatures for extended periods of time, such as during annealing processes.[6] To avoid these issues, the best way would be to quench the growth by rapidly cooling the furnace, allowing no time for any chemical changes to occur. Because that is difficult for large deposition reactors, which hold an enormous amount of heat, cooling conditions should be chosen carefully to minimize the effect on film properties. Cooling with higher carrier gas flow reduces the oxygen concentration in the cooling environment can help minimize oxidation during the cooling stage. One may also consider flowing a small amount of chalcogen precursor during the early stages of the cooling, in an attempt to offset vacancy formation. Continuing to flow chalcogen at lower temperatures,

however, may have certain unintended consequences, such as leaving residual precursor on the surface of the film. Although we have tested this factor, it is difficult to make conclusions about whether it improves film quality or not, since in practice, MOCVD has significant growth-to-growth variation resulting from uncontrollable factors (i.e., the topic of discussion for this entire chapter).

Similar to the ramping stage, we typically do not flow precursors during cooling, since the temperature-changing environment likely would not promote nucleation and growth of monolayer material. There are instances, however, where it appears that material deposition continues during cooling despite the absence of precursor flow. This results in films that exhibit multilayer growth even in areas of the film that are not continuous. This occurs even in a clean furnace, where it is unlikely that this deposition is occurring at other stages of the reaction (multilayer deposition resulting from a dirty reactor will be addressed in the following section). We experience this issue when there is excessive buildup of metal precursor in the line, which offgases into the reactor during cooling and continues depositing on the substrate. This can occur if the carrier gas flow suddenly stops during the reaction, or even when the carrier gas flow is simply too low. This can also be observed when a new metal precursor is installed, if there is accidental spillage of the precursor into the gas line. We find that flowing sulfur during the cooling stage after events such as these returns the reaction to the normal two-dimensional growth mode, suggesting that the multilayer deposition was indeed the result of metal from the line reacting in a chalcogen-deficient environment during cooling. Eventually, all the metal precursor buildup in the line will be depleted, and the issue will go away, but flushing the lines with high quantities of carrier gas will speed up the process.

Overall, the cooling phase is one of the most unpredictable stages of CVD reactions. We believe that how the material cools (e.g., cooling rate, environment) is a large source of variation in the mechanical properties (i.e., because of thermal contraction; see Section 2.4) or surface properties (from surface residues) of 2D films.

3.4 Surface Residues from Growth

3.4.1 Residual Carbon

One major drawback to using metal-organic precursors in CVD reactions is the deposition of carbon on the surface of the film. For carbonyl-containing precursors, this is especially an issue, due to the disproportionation od carbon monoxide into carbon and carbon dioxide:

$$2CO \rightleftharpoons C + CO_2 \qquad \textbf{Eq. 3.1}$$

This reaction, known at the Boudouard equilibrium, depends strongly on temperature,[7] as seen in **Fig. 3.6**. The equilibrium is shifted towards the formation of carbon below ~670°C, but above ~800°C, there is almost no carbon produced. Indeed, we can even see from the CVD phase diagram in **Fig. 2.1**, that carbon is a major byproduct of the reaction between $Mo(CO)_6$ and H_2S at lower temperatures.

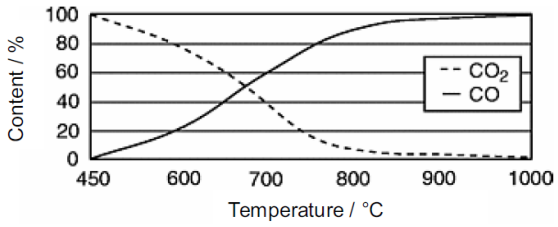

Figure 3.6. Temperature dependence of Boudouard equilibrium. Reproduced from Ref. 6.

For most applications, however, carbon residues on the surface of the film are generally benign and unavoidable, since carbon from the ambient environment deposits on the surface of anything after is it removed from vacuum. The critical thing is to understand what is on the surface before performing any surface-sensitive experiments or measurements. As one example, we previously attempted large-scale

functionalization of MoS_2 films in collaboration with another group, based off of a study that used Lewis acid-base chemistry to modify TMD crystals with various metals with Lewis acid character.[8] After extensive STEM analysis, we found that the locations of the cobalt atoms on the MoS_2 surface were confined only to regions where there were patches of gray contrast, which are usually attributed to carbon adsorbed to the surface. The conclusion was that the cobalt complexes were modifying the carbon on the surface of the film, rather than binding to the sulfur atoms.

From this, we can see why substrate cleaning is an import step in any growth or functionalization process. Unfortunately, the surfaces of 2D materials cannot be easily cleaned, because effective cleaning processes usually involve removing the top layer of a substrate, which for a 2D material, is the entire film. This is one difficulty in growing 2D molecular crystals on TMD surfaces—the effects of 2D substrate variation can be significant. This topic will be addressed in more detail in Chapter 5. Even so, these containments are sparsely distributed across the surface of the films, so we have had success in performing local surface-sensitive measurements after annealing these MOCVD-grown films in ultra-high vacuum. For example, in the work by Herbig, *et al.*, we were able to achieve atomic-resolution scanning tunneling microscopy (STM) imaging of WS_2 and WSe_2 heterostructures, and even perform scanning tunneling spectroscopy (STS) measurements across the interface between the two materials. This work required annealing the films at ~300°C for several hours, but we have also had success imaging MoS_2 with ~120°C annealing overnight for the work which will be presented in Chapter 6.

Since thorough post-synthetic cleaning is usually not possible for 2D films, we can consider modifying the reaction conditions to minimize adsorbed carbon. A different MOCVD

study suggested that using a purer form of $W(CO)_6$ (99% vs. 98%) results in less carbon deposition, although the mechanism of this is not clear.[9] One straightforward modification to the reaction would be to just grow the films at higher temperatures, which is possible for this MOCVD method, as we have seen in our work with Gao *et al*.[3] XPS data of MoS_2 samples grown at these high reaction temperatures (> 750°C) seemed to indicate reduced surface carbon, although we did not study this systematically. As discussed in previous chapters and sections, however, there are other disadvantages to growing TMD films at high temperatures. One could also consider trying to push the equilibrium towards the CO side by flowing CO_2 gas during the reaction. Another option would be to explore inorganic metal precursors, such as chlorides. Indeed, the same work by Gao *et al.* showed promise for 2D NbS_2 growth using $NbCl_5$ as the precursor, although such precursors have significantly lower vapor pressures and different reactivities, which would require much testing.

3.4.2 Sodium-Containing Adsorbates

The other dominant surface residue observed in this MOCVD technique is related to the alkali metal halide salt used as a nucleation inhibitor. **Fig. 3.7a** (top panel) shows an AFM image of a partially-grown MoS_2 film using NaCl as the halide salt, showing few-nanometer-tall particles on the surface of the film. These particles are not usually found on the basal plane of the MoS_2, but typically line the edges of the TMD crystals or the grain boundaries between where two islands meet. This is presumably because these regions are more reactive due to the presence of dangling bonds. X-ray photoelectron spectroscopy (XPS) of as-grown films always exhibit a peak in the Na 1s region, indicating the presence of sodium-containing species on the surface of the TMD films (**Fig. 3.7a**, bottom panel).

These adsorbates are easily removed, however, by dipping the sample in a polar solvent such as methanol. The result of this processing is shown in **Fig. 3.7b** (top panel), which is an AFM image of the same sample as **Fig. 3.7a** (top panel), except after rinsing the surface with methanol. XPS data of methanol-treated MoS_2 films indicate that the only change to the sample after this processing is the removal of the sodium-containing adsorbates (**Fig. 3.7b**, bottom panel). This information confirms that the particles on the surface are indeed the source of Na in the XPS spectra. As for the identity of the compound, we know that it is not NaCl, since no chlorine peaks are ever observed in the XPS of the as-grown films. Since the only other elements present in the XPS spectra are Mo, S, C, and O, we presume that these residues are some sodium-molybdenum compound, such as sodium molybdate (Na_2MoO_4). It is difficult to confirm this from the XPS spectrum, however, since the Mo(IV) peaks overlap with the molybdenum dioxide and trioxide peaks that are expected due to oxidation of parts of the MoS_2 film.

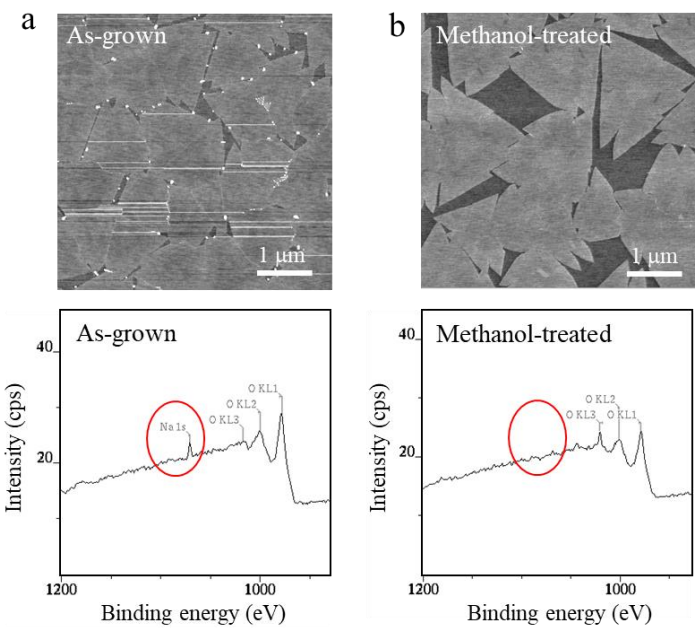

Figure 3.7. a) AFM image (top panel) and typical Na 1s XPS spectrum (bottom panel) of an as-grown MoS_2 film, and b) AFM image (top panel) and Na 1s XPS spectrum (bottom panel) of an MoS_2 film after treating the surface with methanol.

Unlike the small amount of carbon residues that pose little issue in applications of these TMD materials, the presence of ionic residues can affect charge transport in devices made with these materials. Furthermore, the particles are large, posing a similar problem in experiments

involving stacking TMD films as were described in Section 3.3. Although these adsorbates can be dissolved in polar solvents, we know from our work with Poddar and Zhong *et al.*[10] that even volatile solvents that touch the surface of 2D materials can significantly affect their electrical properties. The optical properties of 2D materials can also be affected, as seen by the starkly different PL intensities produced by the same polymer-transferred MoS_2 films where the only difference was the solvent used for polymer removal (see **Fig. 3.13b**). For these reasons, we have investigated ways to modify the reaction conditions to reduce the amount of surface residues on these films.

As mentioned in the previous section, the cooling process seems to contribute to the quantity of surface adsorbates. Although this aspect is difficult to control, cleaning the reactor tube is one way to help reduce the particle adsorption during cooling, which is worse in a dirty reactor. We also find that faster growth rates (i.e., high metal precursor flow) typically produce a higher concentration of surface adsorbates, so keeping growth time long (~10 hours or more) is better. For a given precursor concentration, we also find that higher growth temperatures generally result in cleaner samples, possibly due to the desorption of the residue-forming species at these temperatures.

Furthermore, we found that certain procedures from the original MOCVD work promoted excessive sodium deposition onto the growth substrates. An example of this is given in **Fig. A3.4**. The alkali metal halide precursor is only effective in inhibiting nucleation for a certain number of reactions and needs to be replaced routinely. As described in the previous chapter, the halide salt is prepared on the surface of a quartz plate that is placed directly upstream of the growth substrates. Because of the temperature variation near the edges of the reactor where the salt is positioned, as well as the difficulty of precisely controlling the surface area of the salt

precursor, a newly-replaced salt plate would always result in uncontrolled reaction, excessive nucleation inhibition, and increased deposition of sodium-containing compounds for the first few growths. This can be seen in **Fig. A3.4a**, where replacing the salt plate and repeating the exact same reaction conditions causes the grain size to change dramatically from < 1 μm to > 50 μm domains, which are so large that they no long exhibit a two-dimensional growth mode.

We found that lowering the position of the salt precursor, so that it is no longer in the same plane as the growth substrates (see schematic in **Fig. A3.4b**), allows for better control of the nucleation density while preventing excessive deposition of sodium-containing residues on the TMD films. Since implementing the modifications describe above, TMD films with much cleaner surfaces have been achieved. Indeed, one can see that the AFM images of the as-grown MoS_2 films shown in **Fig. 1.6** and **Fig. 2.6** are all quite clean in comparison to **Fig. 3.8a**, although XPS spectra of even samples like these still indicate the presence of small amounts of sodium-containing adsorbates, which is unavoidable.

3.5 Substrate Effects

3.5.1 Growth Variation of Different Substrates

As alluded to in previous sections and chapters, any type of surface reaction will vary heavily depending on the chemical nature, morphology, and cleanliness of the growth substrate. The key requirements for substrate selection in the growth of TMD materials are 1) the substrate should not react with the precursors, 2) it should not melt/degrade at the high reaction temperatures, 3), it should be relatively flat compared to the thickness of the TMD, and 4) the thermal expansion coefficient difference should be minimal. Since TMDs are bonded to their substrates by week van der Waals forces, lattice constant or symmetry matching with the substrate is not necessary, unless epitaxial growth is desired.

Metals do not make good substrates for this MOCVD process because they will change composition throughout the growth—either reacting with the chalcogen precursor to form metal sulfides or selenides or forming oxides that do not desorb at the TMD growth temperatures. Since oxides, such as SiO_2, Al_2O_3, or HfO_2, are typically unreactive and stable at the temperatures of interest, they make decent substrates for TMD synthesis. The oxides should be highly pure, so that they do not melt at the growth temperature. As such, borosilicates, soda lime glass, or other doped forms of SiO_2, which have significantly lower meting temperatures than quartz (crystalline SiO_2) or fused silica (amorphous SiO_2), should not be used. Graphite is also a stable substrate, but is not good for large-scale TMD film growth because it is not flat over the millimeter scale (see Chapter 4, **Fig. 4.2**).

Even for oxide surfaces, the growth can vary significantly depending on the surface preparation of the substrate. This is because, as described in Chapter 1, contaminants or defects on the surface of a substrate provide a great environment for initiating heterogeneous nucleation events. Although a cleaner or more defect-free substrate may seem ideal, very "perfect" surfaces can make growth extremely challenging because of a lack of nucleation. Hence, there should be a compromise—the substrate should have enough imperfections to promote nucleation, but not so many that the nucleation becomes uncontrollable. Reaction conditions can usually be modified to accommodate growth on many oxide substrates, for example, if nucleation is too low, one can simply try flowing more metal, but the properties of the resulting material may be different. Furthermore, some substrates have greater variation in their surface quality than others.

Thermally-oxidized silicon wafers, which were the substrates used for all of the TMD growths shown in previous sections and chapters, usually provide the most reproducible results, since the oxides are grown onto an ultraflat, single-crystal Si surface using a gas-phase process

that leaves few surface contaminants. TMD growth on CVD-deposited oxides also work, since the deposition is clean, but SiO_2 prepared in this way is not as flat or dense and can have more defects than thermally-oxidized Si. Although we find that TMD films can grow reproducibly on these substrates, the undulating surfaces result in less flat films, which are not ideal for applications that require stacking of the TMDs post-growth.

Some applications, such as optical measurements, require the growth on transparent substrates, most commonly, fused silica or sapphire (crystalline Al_2O_3). Because these transparent substrates are prepared by mechanical polishing processes using chemical slurries, the growth is highly variant compared to SiO_2/Si wafers. Mechanically polished substrates are generally less clean, less flat, and highly dependent on the vendor. We have attempted MoS_2 growth on many different fused silica and sapphire substrates for various optical studies, and we have found that a specific fused silica substrate from University Wafer (#514), results in very similar material growth as the SiO_2/Si wafers, as shown in **Fig. 3.8a**. The nucleation rate on these fused silica wafers is very similar to the SiO_2/Si wafer placed in the same growth (i.e., similar grain size), but the growth rate is marginally (~10%) slower on fused silica, which could just be due to the fact that fused silica wafers are rougher and have slightly higher surface area to cover. We have tried numerous

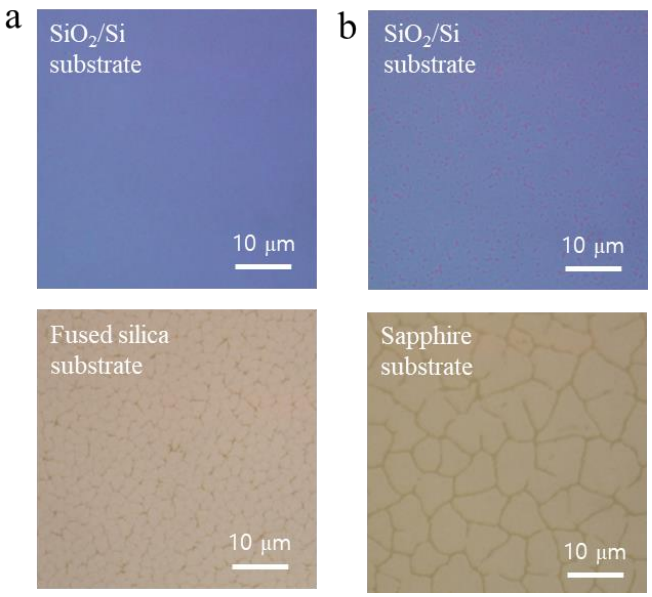

Figure 3.8. Optical images of MoS_2 films grown on a) (top) a standard SiO_2/Si wafer and (bottom) a fused silica wafer in the same growth, and b) (top) a standard SiO_2/Si wafer and (bottom) a sapphire wafer in the same growth.

other fused silica substrates, but we find that most of these either exhibit no nucleation (**Fig. A3.5**, middle panel) or result in films with striation-like features (**Fig. A3.5**, right panel) resulting from the TMD having to grow over ridges in the substrate leftover from poor mechanical polishing.

One important observation about MOCVD growth on fused silica wafers is that it is not possible to grow MoS_2 films with grain size larger than ~ 2 μm. At low nucleation densities, the islands simply start nucleating multilayers before becoming continuous, although the reason for this is not clear. This poses an issue for optical studies that require large grain size material, such as those that will be discussed in Chapter 5. Conveniently, we have found that sapphire substrates, such as the one shown in **Fig. 3.8b** (bottom panel) typically produce significantly larger grain size films compared to SiO_2/Si wafers for the same growth condition (**Fig. 3.8b**, top panel). While the nucleation rate is slower, the growth rate on sapphire is significantly faster. We have observed these general behaviors on sapphire substrates from various suppliers, however, are not all sapphire substrates facilitate monolayer growth. Often times, the MoS_2 domains exhibit dendritic features, such as seen in **Fig. A3.5** (middle and right panels). We find that the best MoS_2 growth on sapphire occurs on wafers purchased from MTI Corporation.

3.5.2 Substrate Surface Cleanliness

Although thermally-oxidized silicon wafers usually provide the highly reproducible growth, any substrate subject to ambient conditions can change over time. One example of this is shown in **Fig. 3.9a**, where the top panel shows a MoS_2 film grown on a few-month-old batch of wafers (a film grown on a newly-opened batch of wafers placed in the same growth is shown for comparison in the bottom panel). The growth on the older wafers is exactly the same in nucleation density and growth rate, but these films exhibit the same pyramid-shaped

nanostructures (white arrows) introduced in Section 3.3, and none of the techniques we applied in that section can resolve the issue in this case. By taking XPS of each of these substrates before growth, we find that the few-month-old batch of wafers (**Fig. 3.9b**, top panel) exhibit not only significantly more surface carbon, but ~1/3 of the carbon is not the aliphatic carbon that is commonly observed on samples that come from an ambient environment (**Fig. 3.9b**, bottom panel).

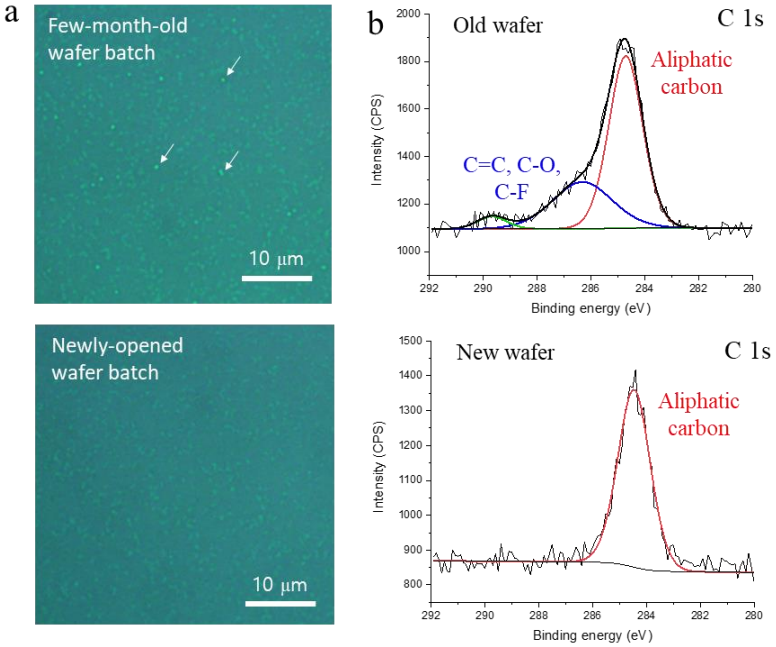

Figure 3.9. a) Optical images of MoS_2 films grown on (top) a new batch of SiO_2/Si wafers, (bottom) a few-month-old batch of similar wafers, both substrates placed in the same growth; and b) C 1s XPS spectra of (top) a new batch of SiO_2/Si wafers (bottom) a few-month-old batch of similar wafers.

The additional carbon peaks on the older substrate can be fit to carbon-carbon double bonds, carbon-oxygen bonds, and/or carbon-fluorine bonds. These carbon species somehow promote the growth of nanostructures on the TMD films. The above study is one example of how the surface of a substrate can have an unexpected impact on material grown, and it is often difficult to pinpoint the substrate as the source of the issues, since there are usually multiple other sources of the same problem in complex CVD processes. While we find that a wafer batch stored in air is fine for 1-2 months for easy-to-grow TMDs such as MoS_2, the surface carbon content could be a limiting factor in the growth of more sensitive materials, such as metallic TMDs (e.g., NbS_2, TaS_2). Storing wafers in vacuum could help, but is space-consuming. It

would seem more prudent to develop a substrate-cleaning procedure to be carried out before each growth, especially since, unlike 2D materials, the surface of bulk materials is easy to clean.

We have tested the efficacy of a few simple wafer-cleaning protocols. General wafer-cleaning processes for device fabrication often suggest sonicating wafers in acetone and isopropanol. As expected, this does not seem effective for producing more reproducible growth surfaces, as seen by the result in **Fig. A3.6**. The sonicated wafer results in a MoS_2 film with the exact same nucleation density and growth rate, except with sparse patches of defective film growth, likely the result of residue left from improper evaporation of the solvent in regions throughout the surface. We have also briefly examined the effect of O_2 plasma cleaning, but the film nucleation on these substrates is quite low, and the resulting growth had more particles on the surface. Because O_2 plasma involves highly-reactive oxygen radical species, the process can sometimes result in deposition of unknown substances (i.e., from the walls of the plasma chamber) onto the surface of wafers, and so this type of process requires much more optimization to produce reproducible results. Surface etching methods that remove the top layer of the substrate, such as KOH or HF, would also not be ideal, since they effect the surface morphology, which is already at its flattest. The most effective method for producing a reproducible growth surface would likely be piranha treatment, which is a highly oxidizing solution of H_2SO_4 and H_2O_2, to decompose any organic matter on the substrate surface without risking additional contamination. However, as mentioned in the previous subsection, although removing the nucleation-inducing species may produce a more reproducible growth surface, it would also require drastically changing the reaction conditions in order to achieve any material deposition, and these conditions may not necessarily result in better quality film growth.

3.6 Reactor Tube Condition

We now discuss the largest source of variation in vacuum deposition processes—the condition of the reactor tube. This is especially problematic in hot-walled deposition reactors, such as those used for CVD and PVD, since any adsorbates on the tube wall will desorb at the high temperatures and redeposit on the growth substrates. (This is as opposed to cold-walled reactors, where only the substrate is heated, so most of the gases just condense onto the side walls and have very low vapor pressure at the low reactor wall temperature.) In solution-phase reactions, cross-contamination between experiments can be avoided by running reactions in single-use vials or, for larger reactions, by etching off the interior layer of glass in a flask using a base bath (mixture of KOH and isopropanol). Unfortunately, quartz tubes for hot-walled vacuum processes are too costly to replace each time and are also too large to safely clean using a base bath. For these reasons, even if one were able to measure exactly the same concentrations of reactants for every growth and ensure that the surface of the substrate was exactly the same, each growth will still look slightly different from the next.

3.6.1 Short-Term Changes from Subsequent Depositions

In a clean CVD reactor (what is meant by "clean" will be described later), the first few reactions will have the largest differences between them, since the condition of the reactor tube is changing dramatically as the walls are being coated with layers of reactants and films of unknown composition. Repeating the same reaction condition many times will result in a progressively more reproducible growth, since the tube walls will reach a sort of "equilibrium" state for that specific temperature and reactant concentration. If one suddenly changes the reaction conditions, the film produced from that change will be different than what would be seen if one had used that changed condition in a cleaner tube. For example, we find that it is not

possible to grow large grain size films after running many reactions using a condition that produce small grain size films, no matter how close the NaCl precursor is moved towards the growth substrates. The way to grow large grain size films is to clean the tube, prepare a thick salt plate with high surface area, and then run another reaction with the NaCl precursor decently close to the substrates during the first growth. This growth will "condition" the reactor tube for large grain size film growth, by coating the walls with nucleation-inhibiting species. Then all of the following reactions will have a grain size larger than average, even if one pulls the salt plate away from the substrates and runs the previous reaction condition that was producing small grain size films.

Any change to the reaction condition throws the tube coating out of equilibrium, so to actually understand the differences between different reaction conditions, it is necessary to repeat the same condition many times successively before making conclusions about the result. Ideally, one would always "reset" the condition of the reactor by cleaning the tube before making large changes to the reaction conditions, so that the system can achieve an equilibrium state that is dominated by the reaction condition of interest. Repeating the same reaction results in films that look progressively more similar and, as explained in Chapter 2.3, progressively more homogeneous. However, there are natural changes in the film morphology that one would expect as the coating on the reactor walls becomes thicker and thicker. First, the nucleation and growth rates become progressively faster, which is expected since the species coating the tube will give reactions in a coated tube a head start. In general, we find that the growth rate in a clean reactor tube is ~10% slower than what was observed immediately before cleaning. Furthermore, the domain size will slowly drop over time, so that after many growths the film will become homogeneous with small grain size.

Ultimately however, the tube will reach a condition where the reaction becomes uncontrollable. The most common consequences of this are shown in **Fig. 3.10**, which are both related to a deviation from the two-dimensional growth mode. A heavily-coated reactor tube will eventually bring back the multilayer pyramid-shaped nanostructures (black spots in **Fig. 3.10a**, top panel) that were discussed in previous sections. At this point, only cleaning the tube will remove these features (**Fig. 3.10a**, bottom panel). Continuing to grow beyond this point will result in films that will grow a second layer before the first layer is complete, as shown in **Fig. 3.10b** (top panel), where the white arrows indicate holes of bare SiO_2 substrate for clarity. After cleaning, the film immediately reverts back to two-dimensional growth, as illustrated by the bottom panel of **Fig. 3.10b**, which shows a complete monolayer MoS_2 film with only sparse bilayer islands.

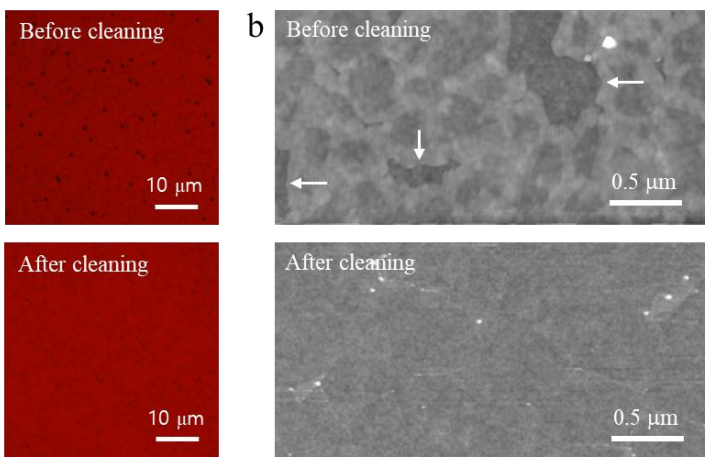

Figure 3.10. Various consequences of growth with a heavily-coated reactor tube. a) Optical images showing (top panel) a MoS_2 film exhibiting pyramid-shaped nanostructures (black spots) on the surface, and (bottom panel) a film grown using the same reaction conditions, immediately after tube cleaning; and b) AFM images showing a MoS_2 film (top panel) exhibiting multilayer growth before the first layer is complete (white arrows indicating bare SiO_2 substrate), and (bottom panel) immediately after tube cleaning.

We know from previous chapters and sections that deviation from the two-dimensional growth mode is typically the result of excess metal precursor. Indeed, we find that flowing more chalcogen precursor during both the ramping and growth stages in a heavily-coated tube can help regain the two-dimensional growth, however, this is only a temporary fix. Developing a proper cleaning procedure is necessary. Certain residues are more easily removed, such as the ionic

species from the alkali metal halide salts, which can be dissolved in ultra-pure water and wiped away using low-lint (cleanroom-grade) wipes. For the non-soluble residues, heating the tube in the presence of ambient oxygen pressure to temperatures higher than the growth temperature oxidizes away carbon-containing species and converts the metallic species to oxides that exhibit much lower reactivity at the growth temperatures.

We further find that leaving the reactor unused for even a short period of time (e.g., a week) will result in the same multilayer growth problems shown in **Fig. 3.10b** upon restarting. Presumably, this is because of continual offgasing of precursors adsorbed in the gas line, which build up in the tube during periods of unuse and the react uncontrollably when the growth is restarted. We find that cleaning the reactor before entering periods of unuse and then cleaning it again before restarting the growth minimizes the impact of this.

3.6.2 Long-Term Changes in Tube Condition

One requirement for two-dimensional growth is that the reactant concentrations should be low, in order to limit the vertical growth rate relative to the lateral growth rate. In this dilute limit, the other gaseous species precent in the reactor, such as small amounts of contaminants or those coating the tube wall, will have significant effects on the film growth. We believe that much of the variation in mechanical properties and surface properties (e.g., surface adsorbates, films adhesion to the growth substrate) of the films are the result of a lack of understanding of the reactor tube coating. For example, we sometimes find that a reaction condition that is regularly used suddenly starts producing films that can no longer be delaminated from their growth substrates. When the tube coating is returned to some equilibrium state (e.g., by doing a rigorous cleaning and then repeating the same condition continually for a long period of time), the samples will usually begin to delaminate again. We do find that reaction conditions that use

very high concentrations of metal precursor appear less susceptible to these short-term variabilities, but the properties of the films produced will be very different in those cases—not only because the reaction is different under high metal flow, but also because such conditions result in a buildup of a thick layer of carbon and oxide on the tube wall.

It turns out that the optical and electronic properties of 2D TMDs are actually more dependent on the reactor tube condition than they are on any specific reaction condition. We know this from our extensive work with Poddar and Zhong, *et al.*,[10] which studied the electrical properties of TMD films using a polymer-free lithography technique. Traditional device fabrication procedures, which change the electrical performance of 2D materials though doping from polymers and solvents and damage from metal deposition, make it impossible to measure the properties of TMD films as-grown. This polymer-free lithography technique enabled the measurement of TMD electrical properties, unaffected by such external factors. By measuring the electrical properties of MoS_2 field-effect transistors over the long-term, we found that consistent (i.e., growth-to-growth) and homogeneous (i.e., in different areas of the film) electrical performance can only be achieved in a heavily-used reactor tube. By this, we mean a tube that has been used for many months and undergone many cleaning cycles. Films grown in a newly-installed reactor tube will exhibit extremely low conductivity and large device-to-device variation. After a long time of use, a semi-permanent tube coating builds up, and the average conductivity of the films increases and roughly saturates (i.e., films grown in older tubes appear to have higher levels of n-doping), with a concurrent reduction in device-to-device variation, unaffected by tube cleaning. When the tube is changed, the film conductivity and homogeneity drop sharply.

From the above study, it may seem ideal to never change the reactor tube, but this is only advantageous for studies that involve device applications, which only use TMD films with very small grain sizes, usually < 200 nm (recall from Section 2.3 that films with smaller grain sizes are more homogeneous over the wafer-scale, which is necessary for large-scale device fabrication). A heavily-used reactor tube loses the ability to grow films with large grain sizes (> 1 μm), no matter low much of the salt precursor is used, or how little chalcogen precursor is used. Basically, the nucleation rate becomes uncontrollable, and attempting to grow large grain size films results in multilayer growth before the films become continuous (see **Fig. 3.11**, first panel). For reactions run at lower temperatures (less than ~550ºC) the problem becomes progressively worse, to the point where even continuous films with small grain size cannot be grown (**Fig. 3.11**, second panel), and even cleaning the tube cannot bring back the two-dimensional growth mode.

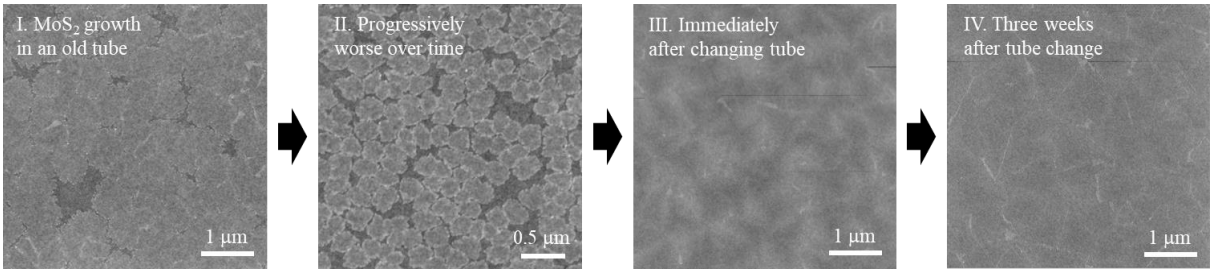

Figure 3.11. AFM images of MoS_2 growths taken at different points in a quartz tube's lifetime when the reactions are run at lower temperatures.

At this stage, the reactor tube should be changed, but this comes with a new set of challenges. Changing the quartz tube does bring back the two-dimensional growth mode and allows for growth of large grain size samples again, but in our work with Lee, *et al.*,[4] we find that TMD films grown in a new reactor tube cannot be stacked layer-by-layer. Although a single layer can be peeled from the substrate, when this layer is placed on another film and peeled, the second films does not come off completely, resulting in a stack with holes. An AFM image of a MoS_2 film grown in a newly-replaced reactor tube is shown in **Fig. 3.11** (third panel). There

appear to be triangular-shaped undulations in the film. However, we if we transfer such a film to a new SiO_2 substrate, the MoS_2 film is actually a flat monolayer, and the undulations are actually on the growth substrate (see **Fig. A3.7**). This roughness of the growth substrate prevents use in applications that require layer-by-layer stacking, since the it does not allow layers from making good contact with one another. Our conclusion is that these tubes are coated with ambiguous contaminants from their manufacturing process, which cannot be removed using a regular cleaning procedure. These contaminants react with the precursors at the growth temperatures and cause unknown morphological changes to the growth substrate.

We have carried out XPS studies of samples grown in a newly-replaced reactor tube, but were unsuccessful in identifying any chemical signature related to these substrate morphology changes. However, we find that if we simply continue growing in the tube, the undulations eventually go away, as can be seen from the AFM image in **Fig. 3.11** (last panel), which was taken from a sample grown three weeks after the tube change. At this point, the tube has been "conditioned", and the films return to being able to be stacked again (although the electrical properties will still be inhomogeneous for a much longer time). We have further investigated numerous procedures for speeding up the process of new-tube-conditioning, and have found that heating a new tube under constant oxygen flow, and then continuing to bake the chamber under carrier gas flow for an extended period of time, helps accelerate this process. We also find that if we run many reactions at higher furnace temperatures (~600ºC) and then return to the lower reaction temperature, the substrate issues are improved, implying that the contaminants can be reacted away at higher temperatures.

One final point is that a new quartz tube is much more sensitive than a conditioned one. If there is some major event that changes the coating of a tube, e.g., the carrier gas flow running out

during the reaction or the furnace heater shutting off suddenly during the growth, the repercussions of these events will be worse in a new tube than in a properly conditioned one. In a conditioned tube, simply performing the routine tube cleaning procedure after some major tube-changing event would return the system back to normal. In an unconditioned tube, however, it seems that excess precursors deposited in the tube react with the foreign species already present in the tube, forming byproducts that have long-standing implications on the growth. For example, we have experienced periods of time where even a new reactor tube would exhibit uncontrolled multilayer growth, or the films would not delaminate from their growth substrates, after a major tube-changing event. When this happens, only extensive cleaning procedures (such as the oxygen-assisted cleaning or high-temperature growths described above) can help return the system back to normal after a long time.

In general, consistently using higher reaction temperatures seems to allow us to circumvent the long-term changes in growth quality described in this subsection, which we typically see for reaction temperatures < 550ºC. When we run reactions at high temperatures for a long time (e.g., ~600ºC), although it quickly becomes impossible to grow large grain size films, the resulting small grain size growths (< 200 nm domain size) are still monolayer and the growth is highly reproducible. High temperature growths still experience increased conductivity over time due to the doping effect from residual species in the tube, but as we saw with the low-temperature growths, the conductivity appears to saturate eventually. Hence, if small grain size films are suitable for a particular application, the most reproducible result will be achieved by using the same tube for a long time and running the reactions at higher temperatures. If grain size control is necessary, then the issues described in this subsection are inevitable. Other issues

associated with reaction conditions for large grain size film growth will be described in the following subsection, as well as in Section 3.7.

3.6.3 Common Contaminations

The previous subsections mainly addressed the consequences of natural precursor buildup in a tube furnace over time. There are, however, a number of sources of foreign contamination common to this MOCVD synthesis. One of these sources was already addressed in the previous section, which was installation of a new reactor tube. Most contaminants, however, build up slowly and degrade the film quality over time, making it difficult to pinpoint the exact source.

One important example is contamination resulting from precursor introduction geometries that involve heating the precursor and gas line. In Section 3.2 (**Fig. 3.2**), we described the three possible introduction geometries. The original MOCVD work used Configuration A[1] (**Fig. 3.2a**, heating only the precursor canister), but we later changed this to Configuration B (**Fig. 3.2a**, heating precursor canister, MFC, and gas line) to improve the reproducibility. Unfortunately, we found that using Configuration B for an extended period of time slowly degrades the sample quality. Initially, only the mechanical stability of the MoS_2 films were affected, and we would find that attempting to stack these films would always result in severe cracking, as seen in the SEM image in the left panel of **Fig. A3.8a**. We test many different reaction conditions, and found that these films had consistently poorer mechanical properties, regardless of growth temperature, grain size, etc. The other properties of the film appeared to be normal, but eventually even the as-grown films began exhibiting nanoscopic morphology changes. These can be seen from the AFM images in the left panel of **Fig. A3.8b**, which show tiny crack-like features in the film and odd pits at the center of each domain arranged in a trefoil-like pattern.

Such a severe degradation in sample quality can only be the result of foreign substances in the reaction, although the source can be many. Since we know from Section 3.2 that $Mo(CO)_6$ actually decomposes as it sublimates at higher temperatures, it is possible that using Configuration A for an extended period of time results in a buildup of unknown chemical species in the MFC and gas line, which begin to offgas into the reactor when the lines are heated upon changing to Configuration B. It is also possible that the foreign species were present from the initial construction of the system (since it is not unheard of to find residues in standard vacuum-grade parts), and these species only started to make their way onto the reactor when we began heating the gas lines. Regardless, we find that upon rebuilding the system in Configuration C, both the film cracking and the pit-like features described in the previous paragraph disappear almost immediately (see **Fig. A3.8a** (right panel) and Fig**. A3.8b** (right panel)). We find that MOCVD systems built in Configuration C are quite stable, even after many years.

In addition to contaminants that come from external sources, it is also important to understand that some contamination can be the result of side reactions that build up after running certain reaction conditions for long periods of time. **Figure A3.9** (left panel) shows an AFM image of a monolayer MoS_2 film, where the edges of the individual domains are raised relative to the centers. We know this film is monolayer because we can transfer it to another substrate and find that the raised features remain in the original substrate, as seen from the right panel of **Fig. A3.9**. Although these features look similar to those described in the previous subsection related to new tube installation (i.e., **Fig. A3.7**), the sources of the undulations seem to be different.

Seeing small undulations on substrates used for growth in this MOCVD method is actually common. This may be due to the intercalation of chemical species underneath the TMD

film during the growth. With many growths, these features become more and more prominent, leading to samples like that shown in **Fig. A3.9**. These surface undulations appear to dominate in reactions that are run at lower temperatures < 550°C and running reaction conditions aimed at growing large domain size TMDs, such as reduced chalcogen flow or increased NaCl, seem to make the issue worse. Although we have not been able to identify the exact nature of the species causing these substrate undulations, we sometimes find the presence of reduced silicon species (i.e., reduced compared to the main SiO_2 peak) in the Si 2p XPS spectra of such films (**Fig. 3.12**). The binding energy indicates this peak possibly corresponds to Si-C.[11] Interestingly, the XPS signatures are only found on the surfaces of the MoS_2 films (black and dark blue lines), not the substrates (light blue and light green lines), and a transfer method that involves polymer/solvents touching the surface actually removes these species (dark green line).

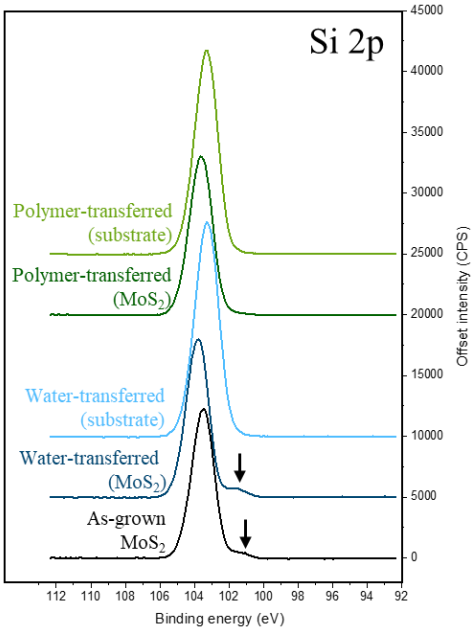

Figure 3.12. Si 2p XPS spectrum of the MoS_2 film from Fig. A3.9a, as-grown (black line), water-transferred to a new substrate (dark blue), and polymer-transferred to a new substrate (dark green). Light blue and light green lines are the Si 2p XPS spectra of the substrates from which the films were removed.

We further find that replacing the tube causes the additional silicon peak to go away, but this cannot be a general solution, since these undulations are so commonly-occurring, and we also know that tube replacement causes other issues. Doing a more rigorous tube cleaning, such as what is done in a new reactor tube (describe in the previous subsection), seems to help "reset" the system. Additionally, since this issue dominates at lower temperatures, running reactions at

higher temperatures for some time may also help. The best practice for dealing with this issue would be not to run reactions for large grain size films for extended periods of time, since those conditions accelerate the problem (running a few reactions is usually fine). Even better would be to keep a separate reactor tube just for running large grain size reactions.

3.7 Limitations of Large Grain Size Films

The previous section touched on one drawback of growing TMD films with large grain size—the reaction conditions required to do that can cause morphological changes in the growth substrate over time. There are numerous other limitations inherent to crystals with large domain size, that limit the applications of these materials. Although larger domain size films, which have a lower density of grain boundaries, may seem like they would exhibit properties closer to those of exfoliated single-crystal TMDs, this is not necessarily the case for 2D films grown using CVD processes. Often times, the case is the opposite: large grain size films frequently exhibit poorer optical, electronic, mechanical properties, and surface properties than films with smaller grain sizes, grown by the same CVD method. Actually, Kang and Xie *et al.* found that the electrical properties of films with 1 μm and 3 μm grain sizes were almost exactly the same, as long as the inter-domain connections have minimal defects.[1] We have also found from our work with Poddar and Zhong *et. al*[10] that small grain size films experience significantly less device-to-device variation.

To understand this seemingly counterintuitive claim, recall that dimensionally-confined material synthesis already requires the use of a very narrow range of reaction conditions. If, on top of that, one also desires to reduce the nucleation density in order to grow large crystals, more "extreme" conditions are necessary, for example, drastically reducing the chalcogen precursor concentration. A reduced chalcogen concentration limits the nucleation, but also now forces the

crystal to grow under a chalcogen-deficient condition, which will likely result in a material with different properties. For this reason, films that appear to be more "crystalline" can actually have a higher density of defects. As indirect evidence for this, we find that larger TMD crystals are more prone to *internal nucleation*, which is nucleation of a bilayer island on the basal plane of a single-crystal monolayer island. From Section 1.3, we saw that multilayer nucleation usually only occurs at the grain boundaries where two islands meet, because the defects known to be present at grain boundaries exhibit a significantly lower energy barrier for heterogenous nucleation. For crystals grown under the extreme conditions that reduce the nucleation density, we often also find random islands of bilayers dotting the inside of a single-crystal TMD domain (e.g., **Fig. 2.9**, middle panel; **Fig. A3.10c**), suggesting that these positions also exhibit a reduced nucleation barrier, implying the presence of defects there.

The consequences of differences in reaction conditions on the defect density of a crystal, which requires atomic-resolution characterization, are not straightforward to measure. Still, we can tell from other metrics of film quality that large grain size TMD films are not ideal for most applications. As an example, **Fig. 3.13a** shows the photoluminescence (PL) spectra of two regions of a MoS_2 film with large grain size (5 μm and 20 μm). The distribution in the PL intensity and peak position is highly variant, and significantly deviate from the expected band gap of 1.9 eV. Films with grain sizes < 1 μm typically exhibit higher PL intensity, with the peak energies closer to the expected value (usually ~1.87 eV), and are much more spatially homogeneous. These differences can be mainly attributed to strain in the films. A large monolayer TMD flake that comes from a bulk crystal is grown sandwiched between other TMD layers, which have the same thermal expansion coefficient, so the lattice contraction from cooling does not produce the same magnitude of strain experienced by monolayer crystals grown

on a different material (e.g., SiO_2). Furthermore, when isolated crystal stitch together to form a film, the film will experience additional strain because of the boundary requirements holding the domains together.

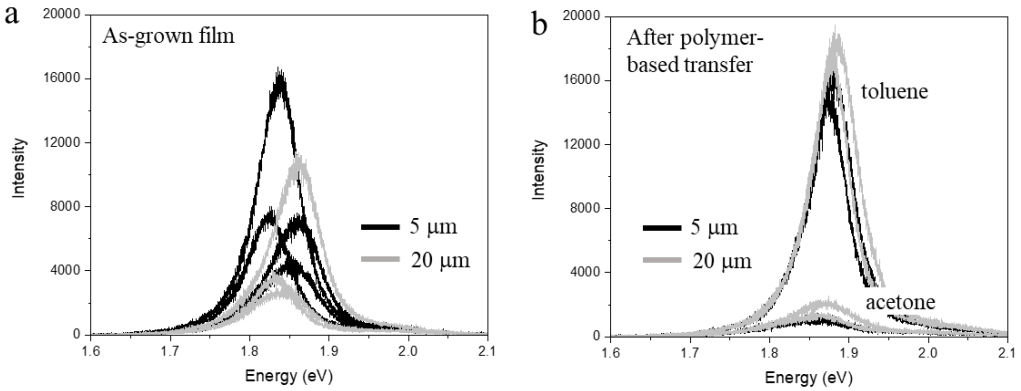

Figure 3.13. a) PL spectra of 5 μm and 20 μm grain size regions of a MoS_2 film, and b) PL spectra of those same regions after transferring to a new substrate using PMMA and removing the polymer in either acetone or toluene.

Indeed, we find that transferring films from **Fig. 3.13a** to a new substrate relives the majority of the strain, causing the spectra of different grain size areas to converge in intensity and position, around same value usually observed for small grain size films (~1.87 eV). These spectra are shown in **Fig. 3.13b**, although the final PL intensity depends on the solvent used to remove the polymer. We can further observe optical inhomogeneities within a single domain when we carry out reflection imaging of MoS_2 films with large grain sizes (see **Fig. A3.10**), where there exist "rings" within a domain that absorb at different energies. This suggests that the chemical nature of a crystal evolves over the course of a reaction, and large crystals, which take longer to grow, are highly subject to these effects. We find that these optical inhomogeneities can actually affect the deposition of molecular layers on the surface of the TMD films, which will be elaborated on more in Section 5.4.

Because of the enormous amount of strain experience by large grain size films, we find that these films cannot be transferred or stacked without damage. We learned this through our

work with Lee *et al.*,[4] where tunnel devices made from stacks of large grain size MoS_2 films were always shorted. **Figure A3.10b** shows SEM images illustrating why this happens—the large grain size films (> 2 μm) completely crack upon transfer, whereas the small grain size films (~200 nm) are perfectly fine. It is also common to find that films with large grain size will contract and wrinkle when delaminated on the surface of water, which is usually not the case for smaller grain sizes. Although small grain size films are generally better for applications that require transfer, some studies will require the transfer of large grain size TMD films, such as the optical measurements described in Chapter 5. For this we found that post-synthetic annealing of as-grown TMD films under vacuum at even low temperatures (~200°C) for a short period of time (few hours) will help improve the mechanical stability of the film. For example, we find that 5 μm grain size films of perylene-modified MoS_2 are significantly less wrinkled upon water transfer if we anneal the MoS_2 film once prior to the deposition of the perylene molecules. The drawback here is that the annealed films do not delaminate completely because even this mild annealing will cause TMD films to have stronger adhesion to the substrate, making them more difficult to peel off for applications that require delamination and stacking.

Even for applications that do not involve film transfer, such as lithography-based device fabrication, small grain size samples are still more ideal because large grain size films can have weaker adhesion to the growth substrate, resulting in device delamination during fabrication. The increased strain levels can be part of the reason for this, but it was also thought that this was because a higher grain boundary density results in more "contact points" where there is stronger chemical bonding to the substrate. After extensive work with Poddar and Zhong *et al.*,[10] however, we now believe that the trend is actually more related to the alkali metal halide precursor, rather than the grain size. We find that small grain size films grown in the presence of

NaCl appear to be different from similar grain size films grown in the absence of NaCl, and that reactions with less alkali metal halide precursor seem to promote stronger substrate adhesion. This could be because high concentrations of the alkali metal halide precursor may result in more intercalated species underneath the film, weakening the adhesion to the substrate. Although this theory is consistent with our observations of large grain size film growth from Section 3.6, more careful study on this needs to be done.

Lastly, we find that giant monolayer TMD crystals (> 20 μm) often exhibit surface inhomogeneities, such as those seen in **Fig. A3.10c**. Here, the ~100 μm WS_2 crystal appears to be covered with sparse bright spots, which also line the edges of the crystal. These features, which could be internal nucleation and/or other adsorbates, can be ignored for most applications. We believe this because, in our work with Mannix and Ye *et al.*,[12] we find that these giant single-crystals can actually be stacked to form layered structures that exhibit lattice reconstruction at the interfaces, which should only be possible for materials that have clean surfaces. Even so, we find that giant TMD crystals sometimes have unpredictable surface properties, with large growth-to-growth variation. This results in reduced reproducibility for extremely surface-sensitive applications, such as the growth of 2D molecular crystals, which will be covered in more detail in the following chapter.

3.8 Summary

In this chapter, we examined various practical limitations in achieving reproducible, high-quality growth of 2D crystals and films. We can see that the growth-to-growth variation in sample properties of vacuum deposition processes is the result of a number of factors, including failures in consistently measuring the concentrations of gaseous reactants, the variation in the surface properties of growth substrates, the presence of spatial and temporal temperature

gradients, and the inability to produce a clean reactor vessel between reactions. There are also effects that limit the applications of these films, such as surface residues or nanostructures promoted by certain reaction conditions or deficiencies inherent to the growth of large crystallites. Some of the examples discussed in this chapter are specific to this MOCVD method, but many of them are general, and will also be applied to the understanding of 2D molecular crystal growth using physical vapor deposition in Chapter 4.

3.9 Appendix

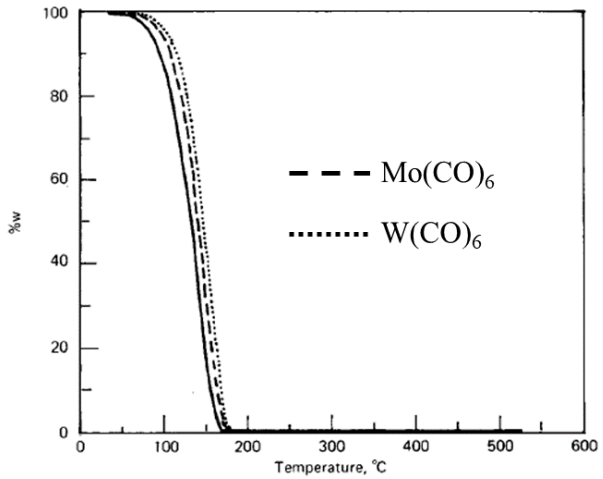

Figure A3.1. Thermogravimetric analysis of $Mo(CO)_6$ and $W(CO)_6$ indicating major weight loss between 100-175°C. Reproduced from Ref. 2.

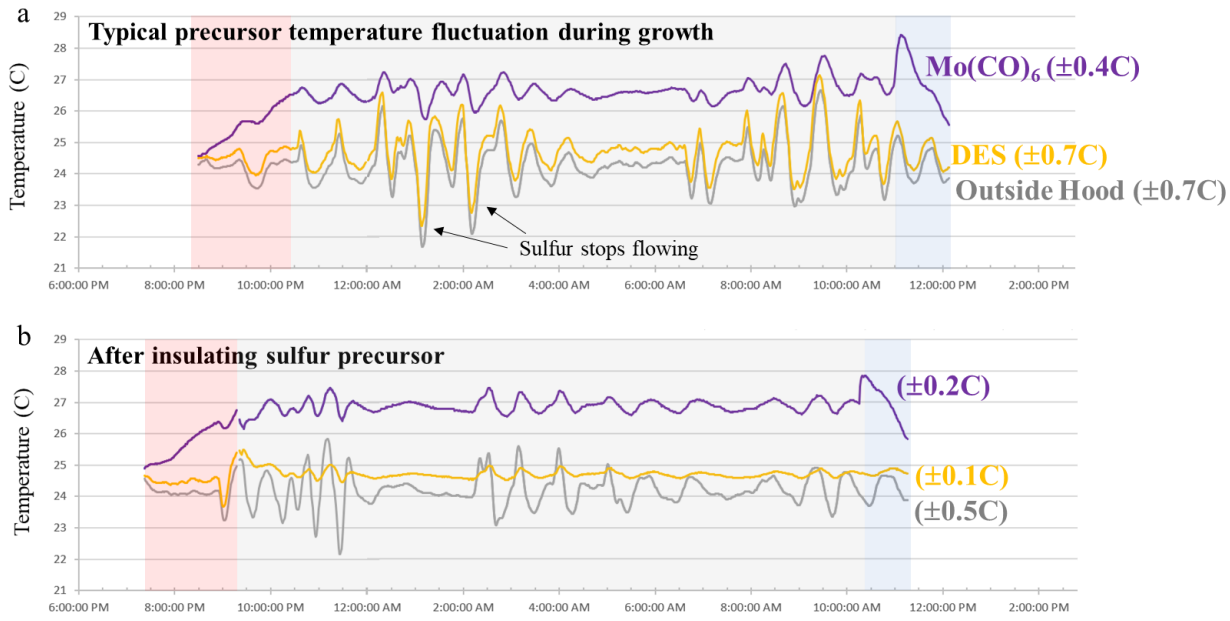

Figure A3.2. a) Temperature fluctuation of precursor canisters (purple line = $Mo(CO)_6$, yellow line = DES during a typical growth, plotted alongside the temperature fluctuation outside the hood (gray line), and b) temperature fluctuations after insulating the DES precursor canister. Red shading indicated the ramping stage, gray shading indicated the growth stage, and blue shading indicates the cooling stage.

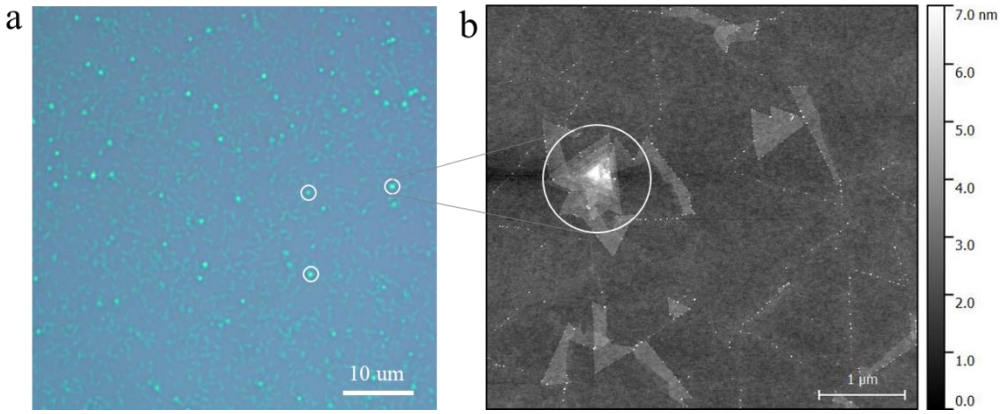

Figure A3.3. a) Optical image of an MoS_2 film showing tall, triangular features on the surface, and b) AFM image indicating that these triangular features are pyramidal nanostructures of multilayer MoS_2.

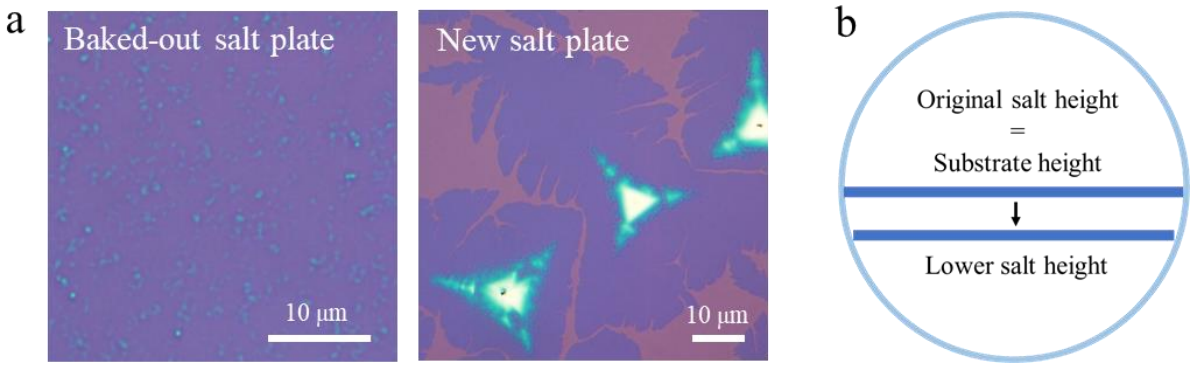

Figure A3.4. a) Optical images of (left) a typical MoS_2 film after the salt plate has been used in many growths and (right) a growth run immediately after, with a newly-made salt plate, and b) Schematic of reactor tube cross-section, illustrating how to prevent excessive reaction of new salt plates by lowering the height of the salt plate slightly below that of the growth substrate.

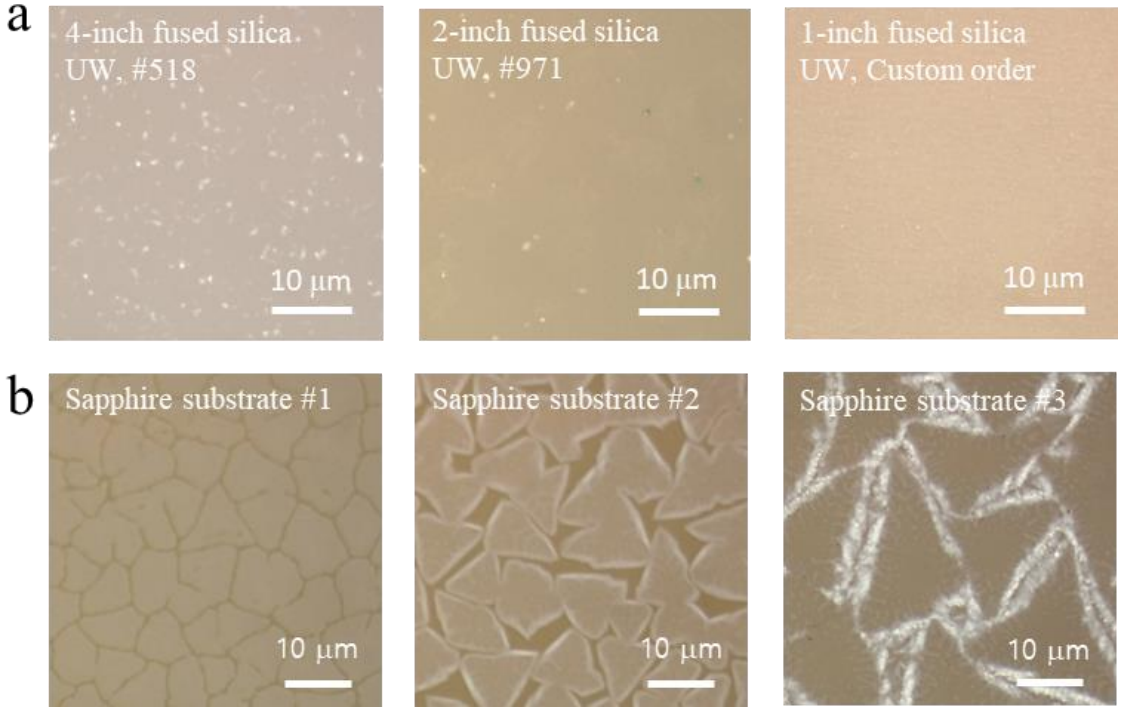

Figure A3.5. Optical images of MoS_2 films grown on a) various fused silica substrates from University Wafer, and b) sapphire substrates from various suppliers.

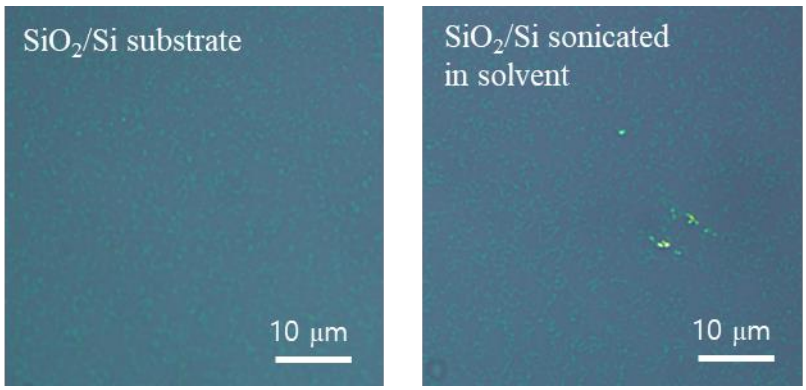

Figure A3.6. Optical images of MoS_2 films grown on a) a standard SiO_2/Si wafer, and b) a SiO_2/Si wafer sonicated in acetone and isopropanol, both substrates placed in the same growth.

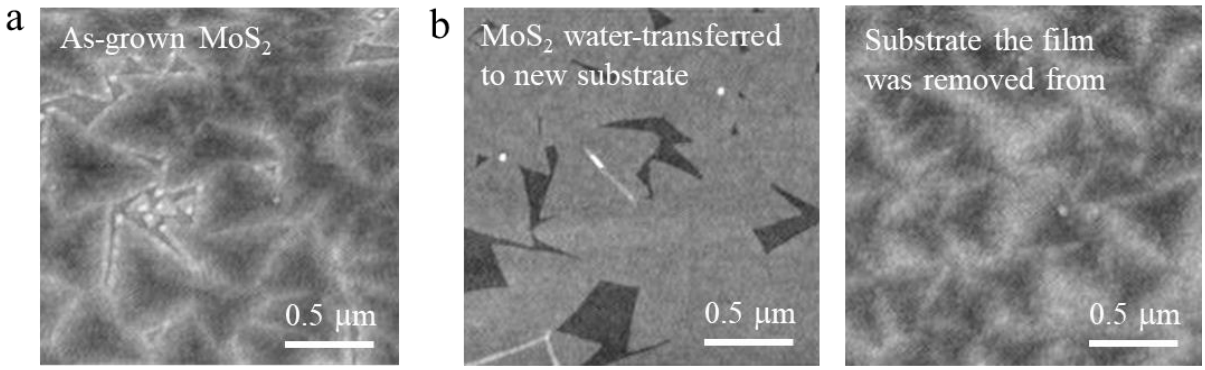

Figure A3.7. a) AFM image of a partial MoS_2 film grown right after installing a new quartz tube, b) AFM image of the sample from (a) after delaminating on water and transferring to a new SiO_2 substrate (left), and of the original substrate from which the film was delaminated (right).

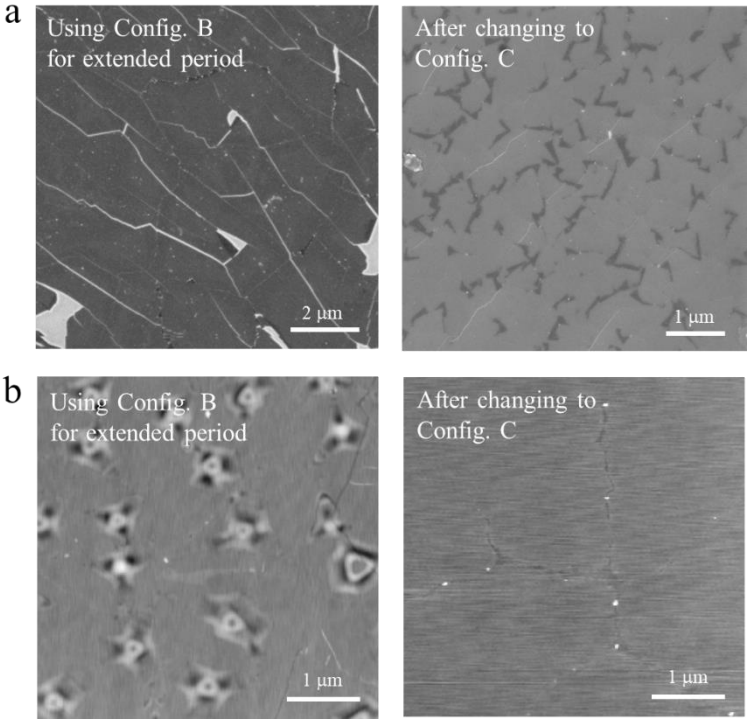

Figure A3.8. a) SEM images of (left panel) a MoS_2 film that was grown using Configuration B and then polymer-transferred to a new substrate, and (right panel) a MoS_2 film grown and transferred shortly after converting the system to Configuration C; and b) AFM image of an as-grown MoS_2 film (left panel) grown using Configuration B for an extended period of time and (right panel) grown after converting the system to Configuration C.

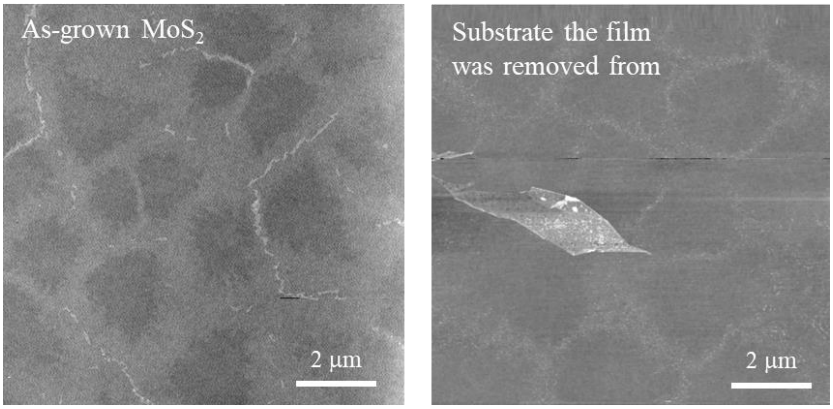

Figure A3.9. a) AFM image of a monolayer MoS_2 film typically seen after running many reaction conditions for large domain size films, and b) AFM image of the original substrate from which the film was removed (right).

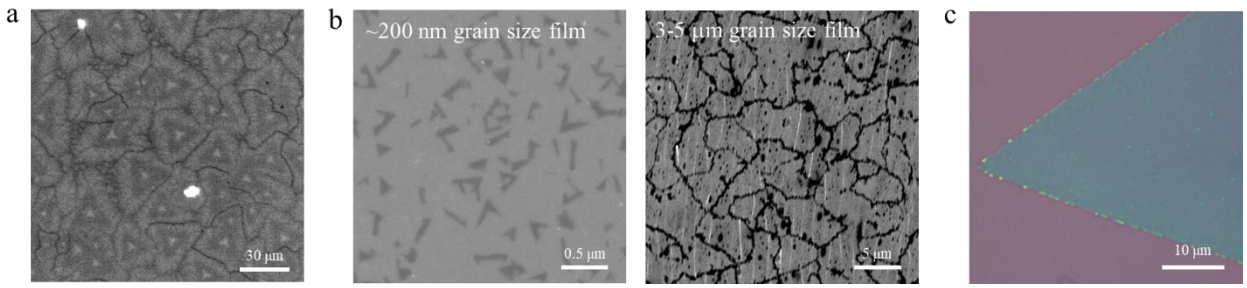

Figure A3.10. Limitations in sample quality of large grain size TMDs. a) Reflection image of a > 20 μm grain size MoS_2 film taken at 660 nm, showing how the absorption within a large MoS_2 domain is shifted when moving from the center outwards, in triangular-shaped rings; b) SEM images of PMMA-transferred MoS_2 films with different grain sizes, showing cracks in transferred films with few-μm grain sizes; and c) optical microscope image of a giant WS_2 crystal showing inhomogeneities on the surface.

3.10 References

(1) Kang, K.; Xie, S.; Huang, L.; Han, Y.; Huang, P. Y.; Mak, K. F.; Kim, C.-J.; Muller, D.; Park, J. High-Mobility Three-Atom-Thick Semiconducting Films with Wafer-Scale Homogeneity. *Nature* **2015**, *520* (7549), 656–660.

(2) Fillman, L. M.; Tang, S. C. Thermal Decomposition of Metal Carbonyls: A Thermogravimetry-Mass Spectrometry Study. *Thermochimica Acta* **1984**, *75* (1–2), 71–84.

(3) Gao, H.; Suh, J.; Cao, M. C.; Joe, A. Y.; Mujid, F.; Lee, K.-H.; Xie, S.; Poddar, P.; Lee, J.-U.; Kang, K.; Kim, P.; Muller, D. A.; Park, J. Tuning Electrical Conductance of MoS_2 Monolayers through Substitutional Doping. *Nano Lett.* **2020**, *20* (6), 4095–4101.

(4) Lee, K.-H.; Chakram, S.; Kim, S. E.; Mujid, F.; Ray, A.; Gao, H.; Park, C.; Zhong, Y.; Muller, D. A.; Schuster, D. I.; Park, J. Two-Dimensional Material Tunnel Barrier for Josephson Junctions and Superconducting Qubits. *Nano Lett.* **2019**, *19* (11), 8287–8293.

(5) Kim, S. E.; Mujid, F.; Rai, A.; Eriksson, F.; Suh, J.; Poddar, P.; Ray, A.; Park, C.; Fransson, E.; Zhong, Y.; Muller, D. A.; Erhart, P.; Cahill, D. G.; Park, J. Extremely Anisotropic van Der Waals Thermal Conductors. *Nature* **2021**, *597* (7878), 660–665.

(6) Donarelli, M.; Bisti, F.; Perrozzi, F.; Ottaviano, L. Tunable Sulfur Desorption in Exfoliated MoS2 by Means of Thermal Annealing in Ultra-High Vacuum. *Chemical Physics Letters* **2013**, *588*, 198–202.

(7) Janisch, D. S.; Lengauer, W.; Dreyer, K.; Rödiger, K.; van den Berg, H. Can We Influence Hardmetal Properties by Sintering in Carbon Monoxide? In *PM Tool Materials*; 2005.

(8) Lei, S.; Wang, X.; Li, B.; Kang, J.; He, Y.; George, A.; Ge, L.; Gong, Y.; Dong, P.; Jin, Z.; Brunetto, G.; Chen, W.; Lin, Z.-T.; Baines, R.; Galvão, D. S.; Lou, J.; Barrera, E.; Banerjee,

K.; Vajtai, R.; Ajayan, P. Surface Functionalization of Two-Dimensional Metal Chalcogenides by Lewis Acid–Base Chemistry. *Nature Nanotech* **2016**, *11* (5), 465–471.

(9) Eichfeld, S. M.; Hossain, L.; Lin, Y.-C.; Piasecki, A. F.; Kupp, B.; Birdwell, A. G.; Burke, R. A.; Lu, N.; Peng, X.; Li, J.; Azcatl, A.; McDonnell, S.; Wallace, R. M.; Kim, M. J.; Mayer, T. S.; Redwing, J. M.; Robinson, J. A. Highly Scalable, Atomically Thin WSe_2 Grown *via* Metal–Organic Chemical Vapor Deposition. *ACS Nano* **2015**, *9* (2), 2080–2087.

(10) Poddar, P. K.; Zhong, Y.; Mannix, A. J.; Mujid, F.; Yu, J.; Liang, C.; Kang, J.-H.; Lee, M.; Xie, S.; Park, J. Resist-Free Lithography for Monolayer Transition Metal Dichalcogenides. *Nano Lett.* **2022**, *22* (2), 726–732.

(11) Watanabe, H.; Hosoi, T. Fundamental Aspects of Silicon Carbide Oxidation. In *Physics and Technology of Silicon Carbide Devices*; Hijikata, Y., Ed.; InTech, 2012.

(12) Mannix, A. J.; Ye, A.; Sung, S. H.; Ray, A.; Mujid, F.; Park, C.; Lee, M.; Kang, J.-H.; Shreiner, R.; High, A. A.; Muller, D. A.; Hovden, R.; Park, J. Robotic Four-Dimensional Pixel Assembly of van Der Waals Solids. *Nat. Nanotechnol.* **2022**, *17* (4), 361–366.

CHAPTER FOUR

Two-Dimensional Molecular Crystal Growth Enabled by

Transition-Metal Dichalcogenide Substrates

4.1 Introduction

In the past few chapters, we have focused mainly on the growth of inorganic two-dimensional (2D) crystals and films, such as transition-metal dichalcogenides (TMDs). The field of inorganic nanomaterials has one limitation from the perspective of new material design and synthesis, which is the ability to systematically grow crystals with properties desired for any particular application. This limitation exists because the structure of covalently- and ionically-bonded crystals are restricted, due to the fact that strong interatomic bonds have relatively narrow requirements for bond distances and angles. Hence, a certain combination of atoms will, for the most part, form one primary stable phase that has its own particular chemical and physical properties and other structures typically cannot be prepared reliably. For example, MoS_2 typically exists in its semiconducting 2H phase. It does have a metallic phase (the 1T phase), but even if this phase can be prepared, it is only metastable.

This is the novelty that molecular materials bring to the field of nanomaterials. First, a molecular unit can be synthesized to have an inherent desired functionality. This can be optical absorption in a particular range of energies enabled by the use of a conjugated core, electronic properties tuned by doner or acceptor groups, or specific chemical activities such as catalysis through the incorporation of metals or redox activity by incorporating redox-active species. Such systematic property tuning is not possible for extended crystal systems, and attempting to modify the properties of an inorganic crystal usually results in the introduction of defects that degrade other properties inherent to the crystal.

Furthermore, modifying the substituents on organic molecules can dramatically change the nature of their intermolecular interactions, so that supramolecular units (i.e., molecular crystals) formed from similar molecular monomers can actually exhibit strikingly different structures (e.g., packing arrangements, densities, etc.).[1–3] These structural differences have ramifications on the physical properties of the molecular solid (for example, solubility, conductivity, absorption, etc.). The structural tunability of molecular crystals is enabled by the fact that the intermolecular forces binding molecular solids are relatively weak (and hence, more "flexible" in nature), and forms the basis for the field of *crystal engineering*—the design of crystals with desired chemical and physical properties by tuning the forces between their building blocks.[4,5]

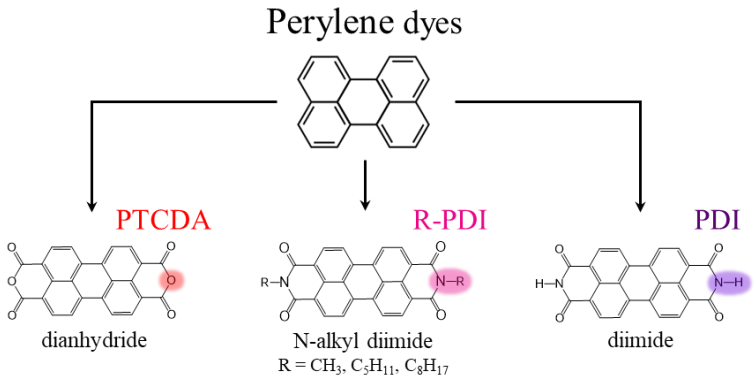

Figure 4.1. Various perylene derivatives that will be used to grow 2D molecular crystals with different responses to polarized light resulting from structural differences brought about by changes in their intermolecular interactions.

We apply the aforementioned approach to the following chapters, using the system shown in **Fig. 4.1**. We pick perylene—a conjugated dye molecule—as the base monomer for its strong visible absorption. We then choose different functional groups to modify the core: anhydrides (**Fig. 4.1**, left molecule; 3,4,9,10-perylenetetracarboxylic dianhydride (PTCDA)), imides (**Fig. 4.1**, right molecule; 3,4,9,10-perylenetetracarboxylic diimide (PDI)), and alkyl-substituted imides (**Fig. 4.1**, middle molecule; e.g., N,N′-dimethyl-3,4,9,10-perylenetetracarboxylic diimide (MPDI), N,N′-dipentyl-3,4,9,10-perylenetetracarboxylic diimide (PPDI), and N,N′-dioctyl-3,4,9,10-perylenetetracarboxylic diimide (OPDI)). Using these

derivatives, we synthesize 2D crystals with unique structures, which exhibit different physical properties, such as polarized absorption.

Although structure-property relationships have been studied extensively in bulk molecular crystals, the same level of design and understanding is difficult to achieve in the limit of atomic thinness, due to two major challenges. The first is the difficulty of synthesizing dimensionally-confined molecular materials over a scale relevant for applicability, and the second is the difficulty of characterizing the structure and properties of interest for single-atom-thick materials. Chapters 4 and 5 will be devoted to the former challenge, which is the large-scale synthesis of 2D molecular crystals (the latter challenge will be addressed in Chapter 6). Actually, the thermodynamically-limited, high-temperature physical vapor deposition (PVD) process introduced in Section 1.5 was based on principles taken from the field of *molecular self-assembly*. In this chapter, we will explain fundamental concepts from this field and use them to develop a self-limiting growth technique for 2D molecular crystals and films, where TMD substrates play a key role.

4.2 Surface-Enabled, Self-Limiting Monolayer Formation

In Section 1.5, we explained the general requirements for forming 2D molecular crystals. These requirements are: 1) an atomically-flat substrate and 2) in-plane vs. out-of-plane anisotropy. We saw from **Fig. 1.13** why van der Waals (vdW) crystals provide ideal surfaces for the formation of molecular monolayers. Actually, bulk vdW crystals have been used for decades in a closely related field, which is molecular self-assembly.[6,7] Molecular self-assembly involves the spontaneous formation of locally-ordered, monolayer molecular films on crystalline surfaces, such as metals, graphite, or bulk TMD crystals. These materials are effectively the same as 2D molecular crystals, but understanding in the field of molecular self-assembly is based on the

principles of *surface adsorption*,[8] rather than crystal growth, since self-assembled monolayers typically have poor crystallinity (i.e., small domain size). Still, there is one key concept we can adapt from this field, which is that self-assembled monolayer formation using solution-based methods is actually *self-limiting*. This is very different from the CVD-based growth processes for monolayer TMDs that are kinetically-limited. Hence, we can use an understanding of molecular self-assembly approaches to inform us on how 2D molecular films can be achieved, and then make modifications to these approaches to improve the crystallinity.

We begin by addressing why traditional molecular crystal growth techniques are not self-limiting. For now, let us ignore the issue of dimensionally and think about bulk crystal growth[9,10] either in solution (using recrystallization techniques) or in vacuum (using physical vapor transport, PVT, techniques). "Growth" is an inherently kinetic process. For example, solution-based recrystallization involves making a saturated solution of the molecule of interest at elevated temperatures and then slowly cooling it.[11] As the temperature drops, the dissolved concentration of the solute exceeds its equilibrium solubility at the lower temperature (i.e., the solution is "supersaturated"), and so a solid will nucleate and grow. If it were possible to cool just a little bit and hold the temperature for a period of time, then the crystal will grow until all of the excess solute in the solution is used up, i.e., until the system has reached equilibrium for that temperature. Since growth only happens when there is some nonequilibrium condition in the system, the longer one can maintain the nonequilibrium state, the larger the crystals will grow. For this reason, cooling slower (i.e., "growing" for longer time) produces larger crystals. The case is even simpler for PVT processes, where a nonequilibrium concentration state is maintained throughout the entire growth process, as the reactor is kept under a temperature

gradient and the quantity of the molecule in the vapor is constantly being replenished via sublimation of the molecular source powder.[12]

We can see why both of the above-mentioned crystal growth processes require kinetic control to limit the crystal size (i.e., since longer growth times produce larger crystals). Same is the case for the CVD growth of 2D TMD crystals. In solution-based molecular self-assembly, however, the molecular crystals only increase in size for a very short period of time, after which the deposition stops. This is because there is no purposefully-sustained period of nonequilibrium (and hence, no sustained period of growth). A molecule is dissolved in a solvent well below its saturation concentration, and the target substrate is dipped inside for a period of seconds to minutes. Molecules deposit on the surface, and then the substrate is pulled out and rinsed to remove any excess. The process is completely room-temperature.

Here, the nonequilibrium factor driving the assembly is the introduction of a new surface. An uncoated surface surrounded by a high concentration of potential adsorbates is a nonequilibrium state (recall the surface energy arguments from Chapter 1). This spontaneous adsorption will only occur if the substrate experiences strong interactions with the molecule of interest. This is because, as introduced in Section 1.5, a large enthalpy change (i.e., very negative ΔH) is required for molecular ordering to be spontaneous, since the reduction in entropy is always working towards an unfavorable (i.e., more positive) free energy change (Eq. 1.2). Molecular materials, however, exhibit much weaker bonding forces than inorganic crystals, and hence, experience a weaker thermodynamic driving force for ordering. This is why, as we explained in **Fig. 1.13**, the substrate plays a key role in molecular monolayer formation—not only is the intermolecular bonding (**Fig. 1.13**, green arrows) important, but the molecule-substrate bonding (**Fig. 1.13**, orange arrows) also contribute to the total enthalpy change of the

system. In the field of surface adsorption, the specific enthalpy change associated with molecule-substrate bonding is called *adsorption enthalpy*,[8] or ΔH_{ads}. Hence, atomically-flat vdW crystals, which will experience maximum vdW forces with a flat-lying molecule, are commonly used in these self-assembly processes.

During a solution-based self-assembly, two processes occur simultaneously—adsorption of the molecule of interest to the substrate and desorption of molecules from the surface back into solution. If the concentration of the solute is high enough, the adsorption rate will overtake the desorption rate, driving deposition onto the surface. As soon as the surface is coated, there is no longer a driving force for growth/deposition. Hence, molecular deposition is self-limiting due to the finite number of adsorption sites on the surface of the substrate. Usually the system equilibrates quickly (i.e., the nucleation and growth phases in solution-based self-assembly are extremely short), and the maximum surface coverage for a given solute concentration is achieved in a matter of seconds to minutes.[6]

From the above discussion, we can see that molecular monolayer formation is thermodynamically-limited in the case of solution-based self-assembly processes, and that having the proper substrate is key in enabling thermodynamically-limited film growth. Although the self-limiting behavior is quite convenient, there are other limitations of solution-based self-assembly methods (which will be fully explained in Section 4.4), which do not make this particular technique ideal for achieving our goal of highly-crystalline, 2D molecular films. As a final note, we will find that it is informative to introduce language from surface adsorption processes such as molecular self-assembly in the remainder of this chapter and throughout Chapter 5. However, this thesis will not molecular adsorption theory in detail, but rather, borrow concepts and point out key similarities.

4.3 Ideal Substrates for Large-Scale Molecular Films

As explained in the precious section, an atomically-flat substate is key to molecular monolayer formation. **Figure 4.2a** shows a scanning tunneling microscopy (STM) image of a self-assembled monolayer domain of Ni(II)octaethylprophyrin (NiOEP) deposited on a crystal of highly-oriented pyrolytic graphite (HOPG),[13] which is a bulk vdW crystal. Over the scale of ~10 nm, the film looks well-ordered. As one zooms out to the 100 nm scale, however, the atomic steps in the HOPG surface that break up the molecular layer become apparent, and so do the holes in the film (**Fig. 4.2b**). Zooming out even further, we can see that the surface of the HOPG substrate, although locally flat, is actually not flat on a technologically-relevant scale (**Fig. 4.2c**). Hence, the self-assembled molecular "film" is not a film at all, but patches of molecules deposited on a heavily undulating, bulk crystal surface. Moreover, a molecular monolayer cannot be removed from its substrate without damage, so the applications of such a material is limited by the ability of its substrate to be integrated with other systems and processes. Additionally, any nanomaterial has little worth sitting on a thick substrate, which will dominate the properties of the combination.

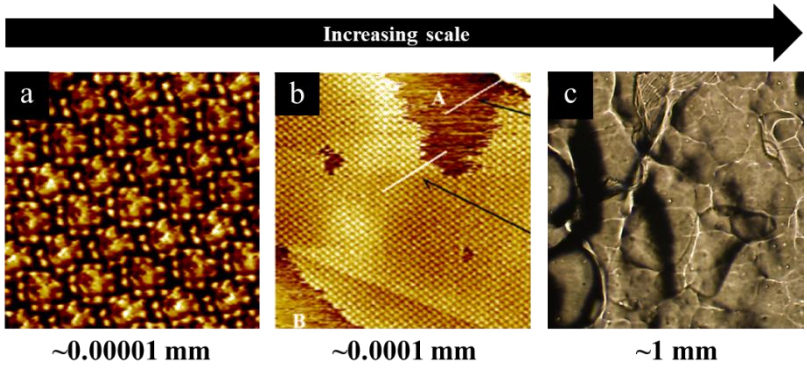

Figure 4.2. Morphology of a 2D molecular film deposited on a bulk van der Waals crystal. a) 8 x 8 nm STM image of Ni(II)octaethylprophyrin deposited on HOPG, b) 70 x 70 nm STM image of Ni(II)octaethylprophyrin deposited on HOPG, and c) 1 x 1 mm optical image of HOPG surface. (a) and (b) reproduced from Ref. 13.

Therefore, although the idea illustrated in **Fig. 1.13b** can be used to grow isolated 2D molecular crystals, bulk vdW substrates are not ideal for scaling up to technologically-relevant molecular films. The ideal substrate would be one that is locally atomically flat, but also macroscopically uniform. We have already spent the past three chapters introducing such a substrate in the—2D TMD films, which we are able to grow as uniform monolayers over the wafer scale[14] (see **Fig. 4.3**). 2D TMD films also have the advantage of processability, i.e., the films can be removed from their substrates to allow the integration of the 2D molecular films into more complex systems and architectures, which will be the topic of discussion in Chapter 7.

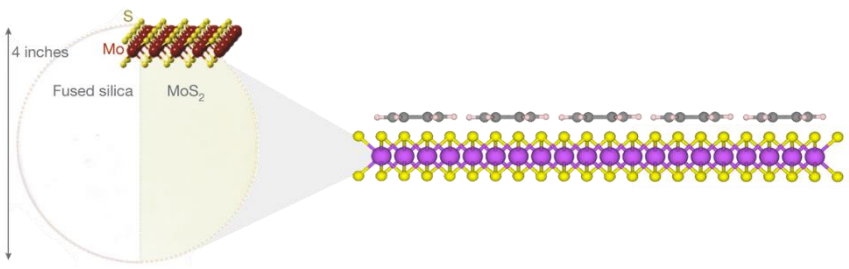

Figure 4.3. Synthesis of 2D molecular crystal films enabled by the deposition onto wafer-scale transition-metal dichalcogenides, which are both atomically-flat and macroscopically uniform. Left panel reproduced from Ref. 14.

4.4 Advantages and Limitations of Various Synthetic Approaches

With the proper choice of substrate selected for our applications, we can now move forward to developing a thermodynamically-limited deposition technique for large-scale growth of 2D molecular crystals and films. Even in the field of molecular self-assembly, there are numerous approaches that can be applied to achieve monolayer formation. We will begin by trying understand the differences between the various approaches. The main techniques used to produce self-assembled monolayers are shown at the left and right extremes of **Fig. 4.4**.

As briefly introduced before, solution-based molecular assembly methods (**Fig. 4.4**, left side) are thermodynamically-driven, where the chemical interactions in the system (i.e.,

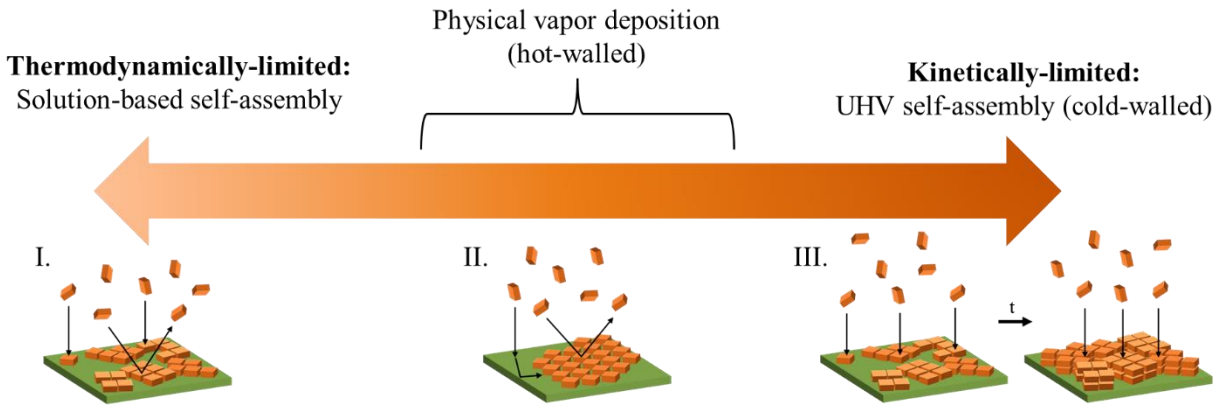

Figure 4.4. Approaches for forming monolayer organic films. At the thermodynamic limit is solution-based assembly (left side) and at the kinetic limit is ultra-high vacuum deposition (right side). The hot-walled physical vapor deposition approach (middle) exists between these two extremes.

molecule-molecule, molecule-solvent, and molecule-surface interactions) dictate monolayer formation. This process is carried out in a closed system, so the total amount of mass in the system stays constant with time. With the right combination of solvent choice and molecule concentration (not too high or too low), the system can equilibrate with a full, single layer of molecules passivating the substrate surface, without additional layers of molecules crystallizing on the surface (**Fig. 4.4**, schematic I). Although this approach is quite quick and technically easy, films tend to have small domain sizes and many holes, since the process is carried out at room temperature where there is little surface diffusion. Even if films are annealed afterwards, there is usually not a drastic improvement in domain size, since the high packing density restricts molecular rearrangement. Furthermore, this approach is limited to molecules with decent solubility, so they cannot be applied to many classes of molecules, including highly conjugated dyes such as perylene. One other consideration is that certain substrates may not be compatible with specific solvents, as is the case with monolayer TMDs, which unpredictably delaminate from their supports in numerous solvents, such as water and methanol. We also know from Chapter 3 how much solvents can affect the optical and electrical properties of 2D materials.

At the opposite extreme is ultra-high vacuum (UHV) deposition (**Fig. 4.4**, right side), where monolayer formation is kinetically-limited. This process is an open system, where there is constant mass transport to and away from the substrate. A crucible containing the molecule of choice is heating to achieve a constant molecular flux, while a shutter blocks the surface of the substrate. When the desired deposition rate is achieved, the shutter is removed, allowing deposition for few to 10s of seconds, and then closed to stop the deposition after a desired amount of time. Although this approach is significantly more expensive and technically challenging to implement, it is actually possible to control the thickness of the molecular film layer-by-layer, by stopping the molecular flux after a certain amount of time (**Fig. 4.4**, schematic III), since UHV conditions allow uniform sublimation (see discussion for **Fig. 4.5** for a more detailed explanation). Furthermore, many molecules can be deposited in this manner since the low-pressure environment promotes molecular sublimation while preventing oxidation during the heating process. Still, pure kinetic control is tricky, and it is often difficult to stop the deposition at exactly the right time to get a full monolayer without adlayers. Because this approach is usually carried out with a room temperature substrate, it also tends to form films with many holes and small domain sizes.

Using our understanding of the two different molecular assembly methods, we have developed a hybrid approach for the growth of highly-crystalline, monolayer films. The advantage of solution-based methods is that the turnover rate is fast, which is ideal for application-driven studies. The deposition rate is also largely self-limiting, convenient for nanomaterial synthesis. Since avoiding solvents is generally better for processes involving 2D materials, an ideal method would be a self-limiting, vacuum-based strategy. Although UHV deposition processes are not self-limiting, one might recognize that if the deposition rate for a

UHV process could be slowed down, then one could achieve the thermodynamically-limited growth regime described in Section 1.5 by simply heating the substrate throughout the deposition. This would also produce more crystalline films. UHV processes, however, are time-consuming and costly because of the extremely low-pressure environment ($P < 10^{-8}$ torr). Furthermore, such ultraclean deposition techniques are actually not necessary for films that will eventually be removed from vacuum for measurement and post-processing.

With our applications in mind, performing the deposition at higher pressures ($P > 10^{-4}$ torr; i.e., low to medium vacuum levels), would dramatically simplify the reactor geometry, significantly increase the turnover rate, and make the system more amenable to scaling up the material growth. Furthermore, implementing temperature control in a higher-pressure environment is actually quite easy—the design of such a reactor is shown in **Fig. 4.5**, which looks similar to a CVD reactor (see **Fig. 2.2**). In this hot-walled PVD approach, a powder of the molecule of choice is loaded into a tube furnace upstream of the target substrate, which in this case is a 2D TMD film. The tube is heated to a target temperature, and the sublimed molecule is carried downstream to deposit on the substrate, before being carried out of the system by vacuum. This approach is actually quite similar to the PVT technique mentioned earlier, which is also carried out in low-vacuum and uses a temperature gradient to crystallize bulk molecular crystals from the vapor phase. The key difference with the PVD process shown in **Fig. 4.5** is that the entire reactor is kept near thermal equilibrium, so that the temperature of the

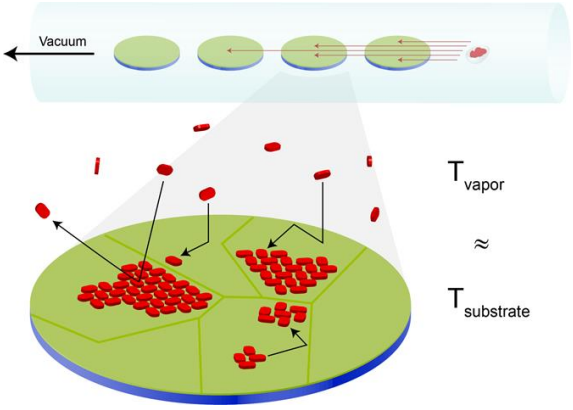

Figure 4.5. Geometry for the physical vapor deposition of 2D molecular crystals onto monolayer TMD films, using a hot-walled quartz tube furnace.

molecular vapor is very close to the temperature of the substrate. This results in a self-limiting deposition rate, despite being an open system where there is constant mass flow to and from the growth substrate. A more detailed understanding of the growth mechanics will follow in the following sections.

Applying the proposed PVD-based deposition approach at high substrate temperatures (i.e., temperatures close to the sublimation temperature of the molecule) would allow us to achieve the thermodynamically-limited deposition regime proposed in Section 1.5. However, this methodology can either land closer to the thermodynamically-limited side or the kinetically-limited side (see **Fig. 4.4**) depending on the working pressure and temperature. The molecular crystals grown in this thesis are deposited closer to the thermodynamic limit, but in order to deposit a wider array of molecular crystals, a slight shift towards the kinetic side will be necessary. We will return to the latter topic in Section 5.6.

4.5 Requirements for Uniform Deposition in Different Vacuum Regimes

To understand why we are specifically interested in PVD in the thermodynamic limit, we need to be aware of the limitations of working in systems that operate under different pressures and temperatures. The effect of pressure is summarized by **Fig. 4.6**. For deposition processes under UHV conditions (i.e., $P < 10^{-8}$ torr; **Fig. 4.6a**), the mean free path (MFP), which is the average distance a molecule can travel before it collides with another molecule and changes its trajectory, is much longer than the distance between the molecular source and the target substrate. This allows uniform, layer-by-layer deposition onto the substrate, where the thickness can be controlled by time, even if it is at room temperature (although we know these films will exhibit poor crystallinity). However, deposition behaviors are very different in medium to low vacuum (e.g., $P > 10^{-4}$ torr for this PVD process), where the MFP << the source-substrate

distance. Depositing on a room-temperature substrate under conditions where the molecules are constantly being scattered by one another (**Fig. 4.6b**) will never result in a complete first layer, no matter how much time is waited. The molecules will deposit as sparse, bulk crystals that increase in size and number with time, and there is no mechanism to control the thickness. This can be seen from the optical images shown in **Fig. A4.1** of NiOEP molecules deposited on a room-temperature MoS_2 substrate using PVD.

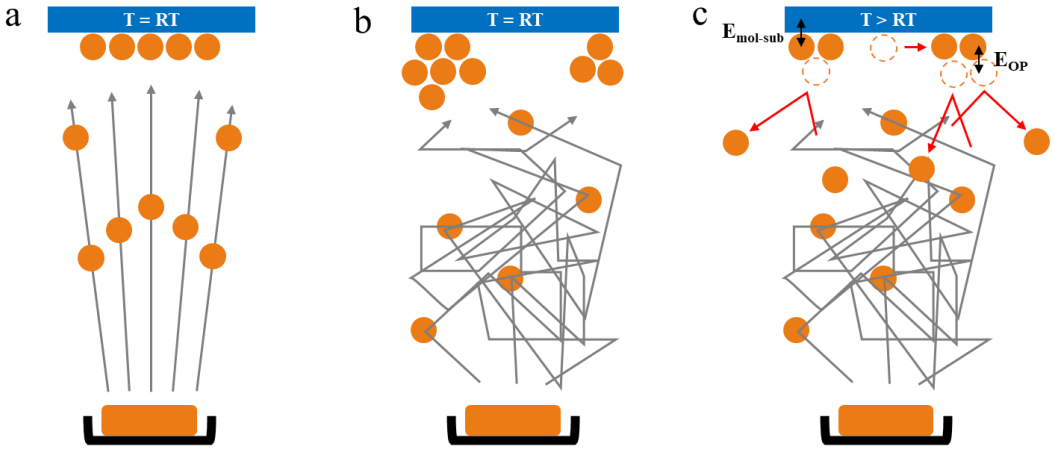

Figure 4.6. Gas-phase molecular deposition in different pressure regimes: a) ultra-high vacuum conditions, b) medium or low vacuum conditions, and c) medium or low vacuum conditions when the substrate is held at elevated temperatures, where $E_{mol-sub}$ is the strength of the interactions between the molecule and the substrate, and E_{OP} is the strength of the out-of-plane interactions

It is possible, though, to achieve thickness control under lower vacuum conditions if the substrate is held at elevated temperatures during the deposition (**Fig. 4.6c**). This approach will only work if the interactions between the molecule and the substrate ($E_{mol-sub}$) are stronger than the out-of-plane interactions between molecules (E_{OP}). If this is the case, then the interactions binding the multilayers will be broken, leaving only the monolayer on the substrate surface. If we recall the thermodynamic arguments in Section 1.5, we can now see the practical reason why an atomically-flat substrate is one of the two conditions for PVD-based 2D crystal growth: the

energetic requirements for monolayer selectivity (i.e., $E_{mol\text{-}sub} > E_{OP}$) will generally be fulfilled within a wide range of temperatures for molecules lying down on an atomically-flat 2D material. However, although using an atomically-flat substrate will help ensure the molecular film is *monolayer*, it has no bearing on the *crystallinity*, or other aspects of the film morphology, such as *surface coverage* or density. (Strictly speaking, this is the case for a "perfect" substrate that is free from surface inhomogeneities, and also assuming there is no epitaxial relationship between the molecular layer and the substrate. In reality, we do find that the substrate can have significant effects on the film morphology, which will be addressed in Sections 5.4 and 5.5.)

For understanding how to promote highly dense and crystalline film morphologies, we recall the second requirement for 2D crystal growth mentioned in Section 1.5—in-plane vs. out-of-plane bonding anisotropy. As we know, the use of elevated substrate temperatures promotes surface diffusion. Because molecules do not reach the surface uniformly under low or medium vacuum conditions, high surface diffusion is a necessity for achieving dense and/or crystalline films. This ensures that no matter where the molecules land, they will have enough energy to either find other molecules to nucleate a new island or attach to an existing island, and eventually all the pinholes in the film will be filled. Since we know from Chapter 2 that the energy barrier for nucleation is much greater than that for adding to an existing island, in general, higher substrate temperatures will usually promote crystal growth, rather than nucleation. One point we want to emphasize is that, at low to medium vacuum levels, high surface diffusion is critical for achieving both high *surface coverage* and high *crystallinity*. This is different from the case of UHV, where it is possible to form a dense film even without surface diffusion, since the lack of molecular scattering results in uniform sublimation at all points across the substrate. This is why a lower vacuum PVD process needs to be carried out at the thermodynamic limit—because

monolayer selectivity and spatial uniformity simply cannot be achieved at higher pressures when the temperature is low.

Unfortunately, there is a major limitation to this high temperature approach. For molecular crystals, which are bound by weak intermolecular forces (IMFs), there is only a small temperature window in which the molecules will stay bound to each other. **Table 4.1** shows the relative strengths of various intermolecular forces that can exist in a molecular crystal.

Intermolecular Forces
van der Waals
π-π interactions
Electrostatic (dipole)
Hydrogen bonding
Halogen bonding

Increasing strength

Table 4.1 Relative strengths of various intermolecular forces.

Ideally, the substrate temperature should be just high enough to break the out-of-plane interactions and allow surface diffusion, but low enough to leave the in-plane interactions intact, as shown in **Fig. 4.7a**. This is only possible, however, if the in-plane vs. out-of-plane anisotropy is sufficiently large (i.e., $E_{IP} >> E_{OP}$). If the bonding anisotropy is weak or if the out-of-plane interactions are stronger than those in-plane ($E_{IP} \lesssim E_{OP}$), the results will be the case shown in **Fig. 4.7b**. Here, temperatures high enough to break E_{OP} also prevent molecules from nucleating new islands or attaching to existing ones, and the result is a surface sparely populated with molecules and small domains.

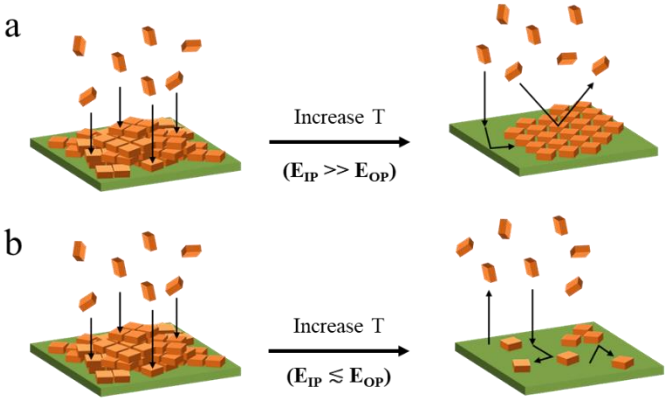

Figure 4.7 The effect of increasing substrate temperature on molecular film morphology under in medium to low vacuum deposition conditions. At low substrate temperatures (left panels), molecules deposit as sparse crystals with non-uniform thickness. a) The result of heating when in-plane intermolecular forces (E_{IP}) are much strong than the out-of-plane intermolecular forces (E_{OP}), and b) the result of heating when the in-plane forces are roughly equal or less than the out-of-plane forces.

In other words, weak bonding anisotropy prevents the formation of crystals or dense films, although the result is technically still "monolayer". This is the behavior we experimentally observe for most conjugated molecules at reactor pressures > 10^{-4} torr, including porphyrins such as NiOEP, where the in-plane forces (vdW forces) are similar in magnitude to the out-of-place forces (vdW forces or pi-pi interactions). Although the molecules can be found on the surface and the surface concentration is self-limiting with time, no clear crystals or film are ever observed (see **Fig. A4.2**). Hence, simply depositing flat-lying molecules sparsely across a surface is quite straightforward as long as the surface is atomically-flat, but forming a *crystal* (or even just a dense film) requires more careful selection of chemical interactions.

From this, it is now apparent the challenges of trying to grow 2D molecular crystals using a more convenient/scalable approach such as low-vacuum PVD. Achieving high coverage in low vacuum requires higher surface temperatures, but higher surface temperatures break weak intermolecular forces. One might guess, however, that molecules with in-plane forces that are significantly stronger than out-of-plane pi-pi interactions, such as hydrogen bonds, could work (see **Table 4.1**). This is the reason for specifically choosing the dianhydride and diimide derivatives of perylene—we find that the bonding anisotropy is large enough to promote 2D crystal growth under medium to low vacuum conditions.

As a final note, although we find that hydrogen-bonding perylenes work quite well for growing highly dense and crystalline molecular films using this PVD processes, this is not general to all hydrogen-bonding systems. Crystals of perylene dianhydrides and diimides are extremely thermally stable because they consist of 6-8 hydrogen bonds per molecule. Other crystals that only have 2-4 hydrogen bonds per molecule, such as hydroxy-substituted porphyrins, also do not form stable films using this PVD approach. Furthermore, smaller arene

derivatives that have less “contact area” with the TMD substrate (e.g., carboxy- or amine-substituted benzenes or indoles), tend to easily sublimate off the surface near the temperature required to break their out-of-plane IMFs. Although it may seem that the utility of this PVD-based approach is extremely limited due to the strict requirements for IMFs, we have used perylene derivatives as a model system to understand the general principles of 2D molecular crystal growth in non-UHV PVD systems. We will show these results in Chapter 5. Then in Section 5.6, we will use this understanding to expand to the growth of 2D crystals will weaker bonding anisotropy, including unsubstituted conjugated molecules such as perylene (**Fig. 4.1**), without resorting to UHV growth techniques.

4.6 Summary

In this Chapter, we took understanding from the field of molecular self-assembly in order to develop a self-limiting gas-phase deposition technique based on hot-walled physical vapor deposition. We see that thermodynamically-limited monolayer formation is heavily reliant on the substrate, which should ideally be an atomically-flat 2D TMD film for the formation of large-scale molecular films. We also realized that self-limiting crystal growth relies on the ability to achieve an equilibrium state, absent of thermal or concentration gradients. Using this idea, while understanding the advantages and limitations of working in lower-vacuum systems, we find that the best way to achieve high-throughput, scalable, deposition of 2D molecular films would be a high-temperature PVD technique, where the molecular source and the substrate are kept at roughly the same temperature. Although we originally introduced this approach as crystal growth in the thermodynamic limit (Section 1.5), we will find in the next chapter that the growth dynamics in this gas-phase system do actually reproduce characteristics of molecular adsorption phenomena such as solution-based self-assembly.

4.7 Appendix

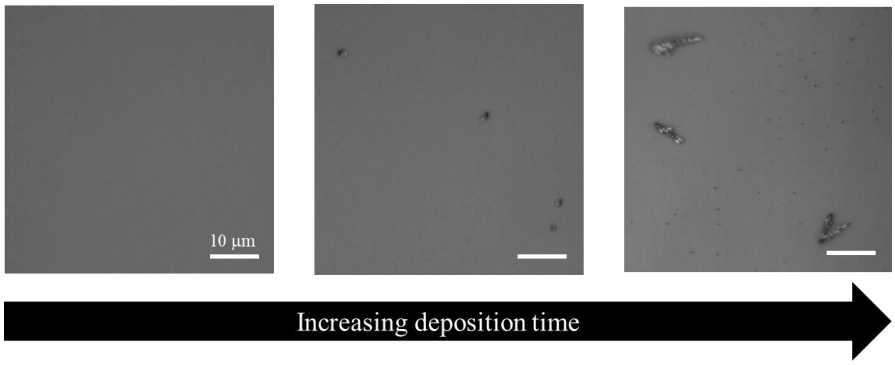

Figure A4.1. Optical images of NiOEP molecular crystals deposited on MoS_2 using PVD with a room-temperature substrate, with increasing deposition time. The temperature of the NiOEP source was maintained at 200°C.

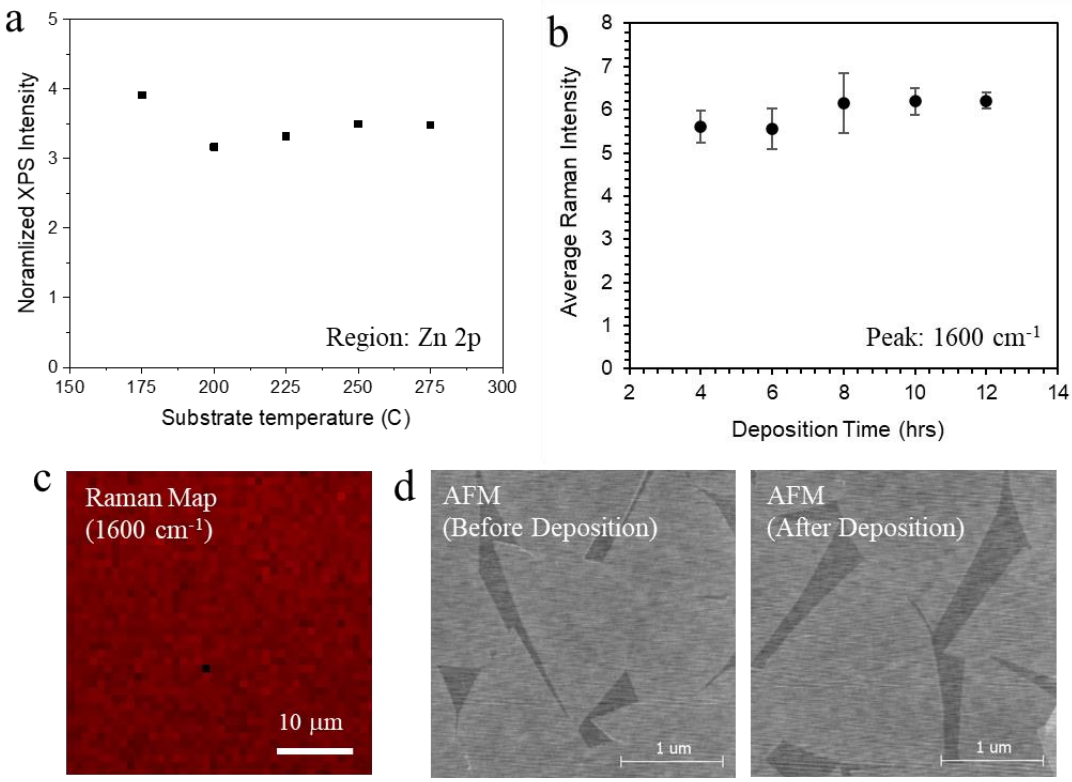

Figure A4.2. Characterization of Zn- and Ni-based octaethylporphyrins deposited on MoS_2 using PVD with a heated substrate, where the OEP source temperature was 200°C. Self-limiting deposition behavior is observed from a) integration of Zn 2p XPS spectra showing a saturation of intensity for substrate temperatures T_{sub} > 200°C and b) integration of OEP Raman peaks showing no significant increase in intensity with deposition time for T_{sub} = 200°C. Although c) Raman mapping indicates the presence of the OEP molecules everywhere, d) AFM before and after deposition shows no morphology or thickness change of the TMD substrate.

4.8 References

(1) Austin, A.; Hestand, N. J.; McKendry, I. G.; Zhong, C.; Zhu, X.; Zdilla, M. J.; Spano, F. C.; Szarko, J. M. Enhanced Davydov Splitting in Crystals of a Perylene Diimide Derivative. *J. Phys. Chem. Lett.* **2017**, *8* (6), 1118–1123.

(2) Balakrishnan, K.; Datar, A.; Naddo, T.; Huang, J.; Oitker, R.; Yen, M.; Zhao, J.; Zang, L. Effect of Side-Chain Substituents on Self-Assembly of Perylene Diimide Molecules: Morphology Control. *J. Am. Chem. Soc.* **2006**, *128* (22), 7390–7398.

(3) De Luca, G.; Pollicino, G.; Romeo, A.; Patanè, S.; Scolaro, L. M. Control over the Optical and Morphological Properties of UV-Deposited Porphyrin Structures. *Chem. Mater.* **2006**, *18* (23), 5429–5436.

(4) Corpinot, M. K.; Bučar, D.-K. A Practical Guide to the Design of Molecular Crystals. *Crystal Growth & Design* **2019**, *19* (2), 1426–1453.

(5) Desiraju, G. R. Crystal Engineering: From Molecule to Crystal. *J. Am. Chem. Soc.* **2013**, *135* (27), 9952–9967.

(6) Schwartz, D. K. Mechanisms and Kinetics of Self Assembled Monolayer Formation. *Annu. Rev. Phys. Chem.* **2001**, *52* (1), 107–137.

(7) Ulman, A. Formation and Structure of Self-Assembled Monolayers. *Chem. Rev.* **1996**, *96* (4), 1533–1554.

(8) Kolasinski, K. W. *Surface Science: Foundations of Catalysis and Nanoscience*, Fourth edition.; Wiley: Hoboken, NJ, USA, 2019.

(9) Wang, C.; Dong, H.; Jiang, L.; Hu, W. Organic Semiconductor Crystals. *Chem. Soc. Rev.* **2018**, *47* (2), 422–500.

(10) Virkar, A. A.; Mannsfeld, S.; Bao, Z.; Stingelin, N. Organic Semiconductor Growth and Morphology Considerations for Organic Thin-Film Transistors. *Adv. Mater.* **2010**, *22* (34), 3857–3875.

(11) *Crystallization: Basic Concepts and Industrial Applications*; Beckmann, W., Beckmann, W., Eds.; Wiley-VCH: Weinheim, Germany, 2013.

(12) Laudise, R. A.; Kloc, C.; Simpkins, P. G.; Siegrist, T. Physical Vapor Growth of Organic Semiconductors. *Journal of Crystal Growth* **1998**, *187* (3–4), 449–454.

(13) Ogunrinde, A.; Hipps, K. W.; Scudiero, L. A Scanning Tunneling Microscopy Study of Self-Assembled Nickel(II) Octaethylporphyrin Deposited from Solutions on HOPG. *Langmuir* **2006**, *22* (13), 5697–5701.

(14) Kang, K.; Xie, S.; Huang, L.; Han, Y.; Huang, P. Y.; Mak, K. F.; Kim, C.-J.; Muller, D.; Park, J. High-Mobility Three-Atom-Thick Semiconducting Films with Wafer-Scale Homogeneity. *Nature* **2015**, *520* (7549), 656–660.

CHAPTER FIVE

Vapor Deposition of Molecular Monolayers near the Thermodynamic Limit

5.1 Introduction

In Chapters 1 and 2, we mainly focused on understanding the growth dynamics of two-dimensional (2D) crystals in kinetically-limited regimes, and how different reaction parameters affected the morphology of the synthesized films. For example, we found that the shape of individual transition-metal dichalcogenide (TMD) crystals can be manipulated by adjusting temperature and metal-to-chalcogen precursor concentration ratios, that the size of domains in a film can be controlled by nucleation-rate-limiting parameters such as chalcogen or salt precursor concentrations, and that the surface coverage of a film is dictated by time. In this chapter, we will see how these same properties are different in thermodynamically-limited growth processes that are surface-assisted, in particular, for the physical vapor deposition (PVD) method we described in Chapter 4.

One could probably already guess that crystal shape in surface-assisted growth is dictated by the shape of the underlying substrate. We will find that the size of the domains (i.e., the crystallinity of the film) is also dominated by substrate-related factors. It is also expected that time should have no effect in thermodynamically-limited processes once the system reaches equilibrium, and so what determines the surface coverage is the parameters that dictate the concentration of the molecular species near the surface of the substrate.

In order to be able to study aspects of film morphology, however, we need to have a high-throughput a methodology for visualizing these properties. For strongly-absorbing dyes, such as the perylene derivatives used in this thesis, a regular optical microscope can actually give us information about the surface coverage of even single-atom-thick films. This does not tell us

anything about the crystallinity though. For that, we make use of a convenient property of crystals, which is *optical anisotropy*. Because most crystals have different structures when viewed along different directions, their optical properties (absorption and refraction) will also differ along different directions. Hence, by shining polarized light, which oscillates in a certain direction, crystals with different orientations will reflect different amounts of light. The result will look like the top-right inset of **Fig. 5.1**, which schematically depicts how anisotropic perylene crystals deposited on an isotropic, polycrystalline TMD substrate (such as MoS_2) would look under polarized light. The same film viewed under unpolarized light would look like the inset in the bottom-right. The exact microscope configuration actually uses two polarizers that are oriented perpendicular to each other to enhance the signal for these atomically-thin films, but the details of this cross-polarized microscopy measurement will be saved for Chapter 6.

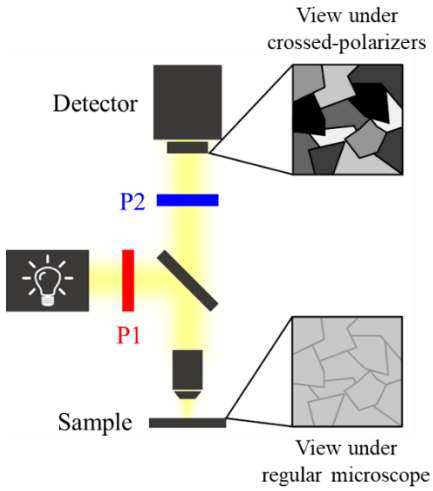

Figure 5.1. Schematic of cross-polarized microscopy setup for visualizing the domain structure of optically anisotropic materials. Top right inset shows how domains of anisotropic molecular crystals deposited on a polycrystalline TMD film would appear under crossed-polarizers, while the bottom right inset shows how the same film would look under a regular (unpolarized) optical microscope.

In this chapter we will use a combination of unpolarized and cross-polarized optical microscopy to investigate the growth of perylene-based 2D molecular crystal and films using hot-walled PVD, with polycrystalline films of monolayer MoS_2 or large single-crystals of monolayer WS_2 as the growth substrates. We begin be studying the effect of basic deposition parameters on surface coverage, followed by more detailed studies of external factors that affect the surface coverage. We will then transition to a discussion of the role of the TMD substrate in

the crystallinity of the perylene-based molecular films, and address the limitations of CVD-grown 2D films for surface-sensitive studies. Finally, we will end with an understanding of how this synthetic approach can be generalized to other molecular systems that have weaker intermolecular forces (IMFs).

5.2 General Deposition Parameters: Effects on Surface Coverage

5.2.1 Substrate-Source Distance

As explained in **Fig. 4.5**, monolayer TMD substrates are placed in the PVD reactor at various distances from a crucible containing a powder of the molecule of interest. Similar to powder CVD processes, distance is used as a proxy for precursor concentration in the absence of flow rate control for low vapor pressure species. For the experiment in **Fig. 5.2**, 3,4,9,10-perylenetetracarboxylic dianhydride (PTCDA, **Fig. 4.1**, left molecule), was deposited on polycrystalline films of monolayer MoS_2 that were grown using the MOCVD method described in Chapters 2 and 3. The entire reactor was heated to T_R = 225°C (same temperature for the molecular powder and the substrates), for a deposition time t_d = 8 hrs, and the total pressure of the reactor during the deposition was P_R = ~0.5 torr. MoS_2 substates located far from the PTCDA powder (i.e, extremely low molecular concentration) show no deposition (**Fig. 5.2a**), but closer

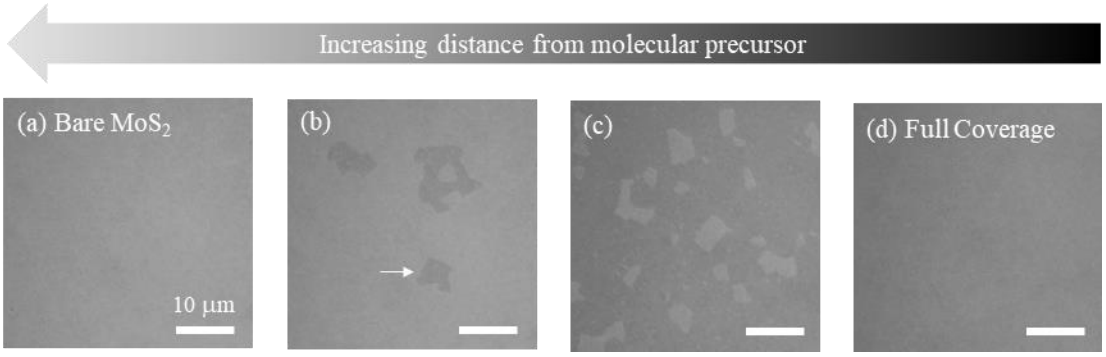

Figure 5.2. Unpolarized optical images showing the distance dependance of the surface coverage of PTCDA on polycrystalline MoS_2 film substrates. White arrow points to a monolayer domain of PTCDA, which appears darker against the MoS_2 background. All scale bars are 10 μm.

substrates begin to exhibit deposition of sparse, few-micron-sized patches of PTCDA (white arrow in **Fig. 5.2b**), which appear darker than the MoS_2 background. Atomic force microscopy (AFM) imaging (**Fig. A5.1**) confirm that the thickness of these domains (~0.4 nm) corresponds to a monolayer of flat-lying PTCDA. The coverage increases moving closer to the PTCDA source (**Fig. 5.2c**) until full coverage is achieved for the substrate sitting directly adjacent to the PTCDA crucible (**Fig. 5.2d**).

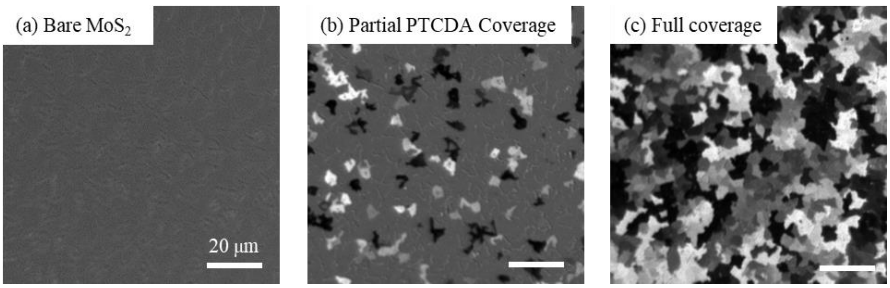

Figure 5.3. Cross-polarized images of PTCDA on polycrystalline MoS_2 films with different surface coverages. All scale bars are 20 μm.

By performing cross-polarized measurements, we find that the "patches" of monolayer PTCDA in **Fig. 5.2b** are actually also single-crystals. This can be seen from the cross-polarized image in **Fig. 5.3b**, where the isolated patches of PTCDA each reflect a single, uniform intensity. For reference, **Fig. 5.3a** shows how a film of bare MoS_2 (i.e., similar to the film in **Fig. 5.2a**) looks like under the same instrumental configuration, and **Fig. 5.3c** shows a PTCDA/MoS_2 film with nearly full coverage (comparable to the film in **Fig. 5.2d**). Although the distance appears to have no consistent effect on the size of individual PTCDA domains (more clearly seen in **Fig. 5.6**), it does have implications on other aspects of the film morphology, which will be covered in Section 5.4.

The surprising inference that can be made from the results shown above is that the crystallinity is independent of the molecular concentration in the vapor, since the average size of the crystals is the same for any source-substrate distance. Instead, we see a domain-by-domain deposition behavior, where single-crystal domains of PTCDA increase in number with

decreasing source-substrate distance. In other words, the *surface coverage* increases with molecular concentration, but *crystal size* is a constant. This is different from what we observe in CVD-based crystal growth, where the absolute crystal size typically decreases down the length of the reactor due to the slower growth rates downstream.

5.2.2 Deposition Time

We can further investigate the effect of molecular concentration by studying the dependance of the PTCDA deposition on time, for a given source-substrate distance. The result of this experiment is given in **Fig. 5.4**, which shows the surface coverage of PTCDA on polycrystalline MoS_2 films for different deposition times, where T_R = 225°C and P_R = 0.5 torr. The furnace ramp time was an additional 30 min in each case, and the reactor was cleaned between each deposition to minimize the effect of external factors. For t_d = 1 hr and 2 hrs, the PTCDA surface coverage is roughly zero (although very sparse PTCDA domains can be found for the 2-hour deposition). Somewhere between t_d = 2 hrs and 4 hrs, however, the coverage jumps to ~90% and stays at that value no matter how long the deposition is continued afterwards. (The percent surface coverages were determined from the unpolarized optical images in **Fig. A5.2**, since it is not straightforward to tell the exact surface coverage from cross-polarized images.) The specific quantity at which the surface coverage saturates is dictated by substrate

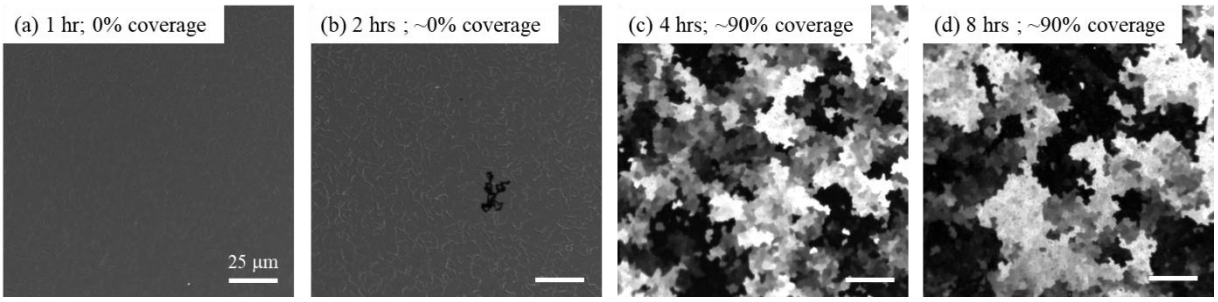

Figure 5.4. Cross-polarized images showing the effect of deposition time on the PTCDA surface coverage of an MoS_2 film. Percent coverage was determined from the unpolarized optical images in Fig. A5.2. All scale bars are 25 μm.

position, reactor temperature, and reactor pressure, all of which contribute to the concentration of the molecular species in the vapor.

From this, we see that our PVD approach indeed exhibits similar characteristics to thermodynamically-limited molecular adsorption phenomena (described in Section 4.2), where the nucleation and growth phases are completed extremely quickly (so that it is not possible to isolate individual domains in their growth phase), and the system saturates at whatever is the "equilibrium surface coverage" for the particular concentration of molecular species near the substrate surface. Recall that the equilibrium surface coverage is the result of a competition between the rate of adsorption of molecules to the surface and the rate of desorption of molecules from the surface. For the experiment in **Fig. 5.2**, the desorption rate is the same for all substrate positions, since the temperature is the same everywhere. Substrates closer to the source, however, experience a higher concentration of molecules in the surrounding vapor, leading to an increased adsorption rate. Hence, this explains why the equilibrium surface coverage increases with decreasing source-substrate distance—because the rate of molecular adsorption increases relative to the rate of desorption.

In the case of this PVD process, we observe a large (> 2 hour) lag in surface coverage, after which the increase is abrupt. This is likely related to the fact that deposition only occurs when a critical concentration of molecular vapor has been achieved, which takes time in a large reactor where molecular species also have to coat the walls of the tube during the first few hours of the deposition (see Section 5.3). Due to external factors that create uncertainty in hot-walled deposition systems (such as cooling), we cannot actually chart the full transition between 2 to 4 hours.

5.2.3 Temperature and Pressure

From the understanding in the previous subsection, we can guess that the molecular surface coverage will depend on rector temperature and pressure, which also affect the local molecular concentration near the substrate surface. **Fig 5.5a** first examines the effect of reactor temperature, T_R, where P_R = 0.5 torr and t_d = 8 hrs. Here, it is important to remember that T_R represents the temperature of the entire system—including the source and substrate (recall from Section 4.1 that the goal is to simulate an equilibrium condition like solution self-assembly methods, not saturate the vapor like PVT processes). The primary consequence of this is that the molecular vapor pressure is also changing with temperature. The substrate was placed a significant distance away from the source in order to have independent temperature readings at both positions, and the reactor was cleaned between each temperature change in order to mitigate cross-contamination.

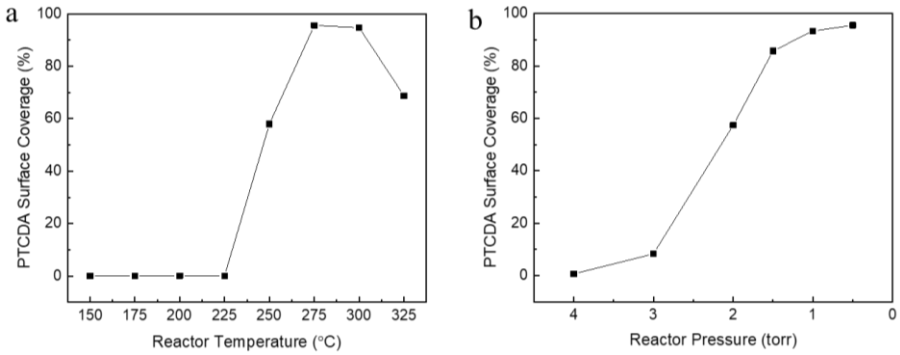

Figure 5.5. Effects of a) reactor temperature (at constant reactor pressure = 0.5 torr), and b) reactor pressure (at constant reactor temperature = 225°C) on the surface coverage of PTCDA on an MoS_2 substrate. Images of the films used for the plots are shown in Fig. A5.3 and Fig. A5.4, respectively.

We find that there is no significant deposition even at T_R = 225°C, indicating that sufficient PTCDA vapor substrate is not generated at these temperatures to deposit on a substrate for this particular source-substrate distance. Between T_R = 225°C and 300°C, the surface coverage steadily increases and then levels off, and at T_R > 300°C, the surface coverage

decreases with increasing temperature. Hence, we can see that below a certain temperature range (~275-300°C), the surface coverage is limited by the molecular vapor pressure (i.e., of the source), while above that it is limited by desorption of molecular species from the substrate surface. The latter observation is consistent with the expectation in **Fig. 1.5**, indicating that we have indeed achieve film deposition in the thermodynamic limit. We further find that the temperatures required to achieve any deposition (> 225°C) are already high enough that the domain size is unaffected by increasing the temperature (see **Fig. A5.3**). We do observe other morphology changes at higher temperatures, which will be covered in Section 5.4. The temperature conditions in **Fig. 5.5a** were only attempted to test the limits of the deposition behavior. Typically, we would not heat these perylene derivatives higher than 250°C, since the relatively high concentrations of oxygen in low vacuum environments risk oxidation.

From **Fig. 5.5a**, we can see that the PTCDA film actually does not achieve 100% surface coverage, even at temperatures where the molecular vapor pressure is high, since those high temperatures also increase the rate of molecular desorption from the substate surface. Hence, one may wonder what is the advantage of keeping the source and substrate at the same temperature. We illustrate the reason for keeping the system in thermal equilibrium in **Fig. 5.6**, where we use our PVD process to deposit monolayer PTCDA on large single-crystal triangles of WS_2. **Fig. 5.6a** shows many holes in the single-crystal PTCDA layer when the source and substrate are at the same temperature, for a specific reactor pressure, P_0. If we use the PVT approach of reducing the substrate temperature (here, less than few 10s of degrees difference), we find that the PTCDA crystal becomes continuous. However, this condition also causes bulk crystallization at the edges of the WS_2 triangles, which we know are highly reactive due to the presence of dangling bonds. Alternatively, we find that if we go back to the equilibrium condition, but this

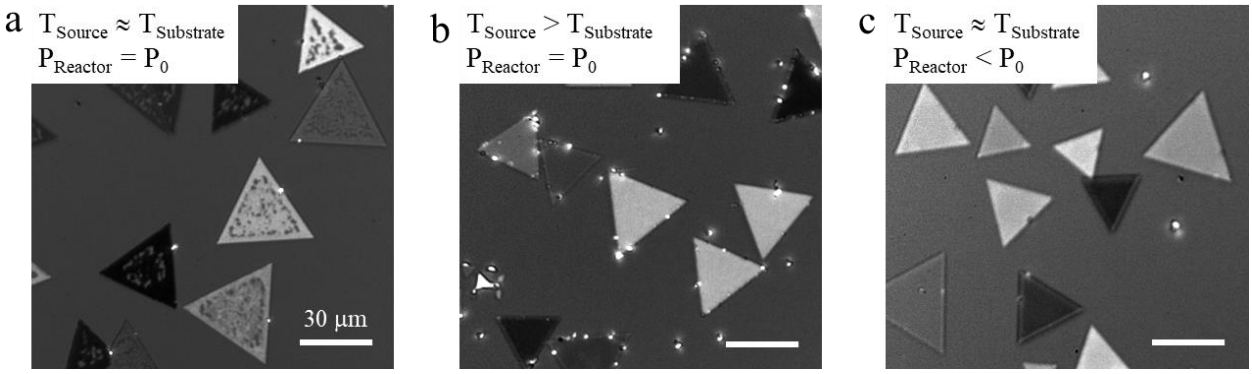

Figure 5.6. Polarized optical images of monolayer PTCDA crystals deposited on triangular, single-crystal WS_2 using this low-vacuum PVD approach. a) The PTCDA film saturates at partial coverage when the deposition is carried out near thermal equilibrium at a particular reactor pressure, P_0, b) using a temperature gradient increases the surface coverage, but results in unwanted bulk crystallization at the edges of the WS_2, and c) using a thermal equilibrium condition, but instead reducing the rector pressure, achieves complete monolayer coverage. All

time reduce the reactor pressure to $P_R < P_0$, the PTCDA film also becomes continuous, except this time without the unwanted bulk crystallization.

We can further chart the effect of the reactor pressure, P_R, on the surface coverage of PTCDA on MoS_2 at constant temperature. Here, the vapor pressure of the molecule is constant (T_R = 225°C), and we are changing is the local concentration of the molecular vapor at the surface of the substrate by flowing different amounts of Ar (i.e., P_R is actually the pressure of the carrier gas, and the vapor pressure of PTCDA is insignificant in comparison). We place the substrate closer to the source in this case, to minimize the effect of temperature gradients, and each deposition is run for 2 hours. The result, shown in **Fig 5.5b**, actually looks similar to an adsorption isotherm,[1] where shape indicates a more complex behavior than the most common isotherms, but data cannot be treated quantitatively due to limitations in measuring the pressure and other issues related to working in hot-walled vacuum reactors (recall Chapter 3).

The x-axis in **Fig 5.5b** is plotted in reverse since decreasing reactor pressure corresponds to an increase in molecular concentration near the surface. At very dilute concentrations, there is no adsorption, but the surface coverage increases almost exponentially with reduced carrier gas

flow, before tapering off at ~95% for P_R ~ 0.5 torr. Once again, we see that the surface coverage saturates at a certain value, and find no clear correlation with domain size. Presumably, going to even lower pressures would allow us to achieve full surface coverage for this same temperature and substrate distance, but 0.5 torr is lowest pressure achievable in this particular vacuum system. Hence, we can see that using reactor pressure to control the surface coverage produces better results than using a temperature gradient. Actually, the bulk crystallization shown in **Fig 5.6b** does not occur when continuous TMD films are used as substrates (due to the lack of exposed edges; also see **Fig. A5.8a**). Still, nonequilibrium deposition conditions are not ideal, since we find that continually running depositions with temperature gradients results in extremely high growth-to-growth variability in the molecular film thickness, while running depositions near thermal equilibrium always results in consistently monolayer films. This aspect will be covered in more detail in the following section.

The findings in this section confirm that we are successfully able to produce a thermodynamically-limited, vapor-based crystal growth technique to deposit monolayer molecular crystals and films in a self-limiting manner, which also exhibits behaviors similar to surface adsorption processes. The major difference, however, between this PVD approach and solution-based adsorption processes is the ability to equilibrate a PVD system at elevated temperatures, which enhances crystallinity and provides another knob for control.

5.3 Detailed Synthetic Strategies on Surface Coverage

Although hot-walled material growth processes are convenient and scalable, the growth-to-growth variation of film properties can be significant, as we saw for CVD processes in Chapter 3. It is quite easy to produce similar-looking TMD films using MOCVD, but these films can have very different physical and chemical properties. Single-component molecular crystal

growth with PVD is much simpler, since there are no chemical changes involved, and hence, no buildup of byproducts that can be detrimental to the film growth. Furthermore, since the product is chemically the same as the starting material, the two will always have very similar physical and chemical properties. Hence, molecular crystal growth is almost the opposite of TMD growth—there is very little variability in the physical and chemical properties, but the *morphological* aspects of the product, such as surface coverage and crystallinity, change dramatically between depositions.

The substrate is one major source of variability (addressed in Section 5.5), but equally important is the condition of the reactor tube. In PVD processes, the coating on the inner walls of the reactor is exactly the same as the product, so there is no way to limit deposition directly onto the growth substrate during ramping and cooling (which was possible for MOCVD). Moreover, the specific thickness distribution of the molecular coating along the length of the reactor depends on how the reactor is cooled, which is difficult to control. Because backflow is significant at these pressure levels (~1 torr), molecules deposited on the reactor downstream will even affect the deposition behavior upstream. Furthermore, since the molecular source must always be loaded directly into the chamber due to its low vapor pressure, even the concentration of molecules from the source depends heavily on factors that are difficult to control, such as the surface area of the powder, the temperature gradient in the reactor, and the heating and cooling rate.

Hence, we find that it is very difficult to make conclusions related to factors affecting surface coverage and crystallinity, besides the basic concepts we introduced in Section 5.2. Still, we will be able to discuss *tendencies* of certain conditions to promote different degrees of surface coverage and crystallinity. Surface coverage will be covered in the remainder of this

section, and crystallinity will be covered in Sections 5.4 and 5.5. Regardless of the film morphology, however, we find that the optical properties of the molecular monolayers are highly reproducible, as will be seen in Chapter 6.

5.3.1 Maintaining Equilibrium for Large-Area Monolayers

In the previous section, we saw that parameters that affect the local concentration of molecular vapor at the substrate surface determine the surface coverage of the molecular crystal. At reasonable temperatures (i.e., < 250°C), the PTCDA system saturates below 100% surface coverage for the lowest reactor pressure (e.g., 0.5 torr), even for the smallest possible source-substrate distance (i.e., directly adjacent to the molecular powder). However, there are ways to achieve fully continuous PTCDA films (such as the one shown in **Fig. 5.2**), in the absence of being able to further reduce the reactor pressure. As we discussed in Chapter 3, the tube environment plays a large role in the growth of films in hot-walled vapor deposition processes, such as CVD and PVD. This is because adsorbates coating the inner surface of the reactor tube will start depositing on the substrates before the actual precursors reach sufficient quantity for reaction/deposition. Hence, running multiple PVD depositions in sequence results in increased deposition, just as doing so for CVD results in an increased reaction rate.

Figure A5.5 illustrates this effect for PTCDA deposited on MoS_2 films, where the surface coverage is tracked for various source-substrate distances for multiple depositions after a tube cleaning (T_R = 225°C, P_R = 0.5 torr, and t_d > 4 hrs). The same deposition conditions were repeated each time, and new MoS_2 substrates were used for every deposition. A substrate 3 inches away from the source exhibits >75% surface coverage for the first deposition, while one located 15 inches away from the source has 0% coverage. However, by the third deposition, even the substrate 15 inches away exhibits 100% surface coverage of PTCDA. **Figure 5.7** shows the

morphologies of such PTCDA films deposited in a fully-coated coated reactor tube at various substrate distances, all of which look extraordinarily similar.

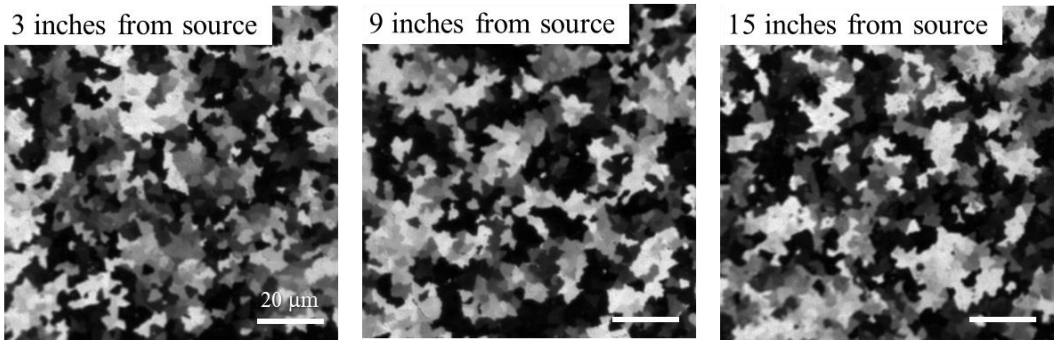

Figure 5.7. Cross-polarized images of PTCDA deposited on MoS_2 films, where the substate was place at various distance from the source. All scale bars are 20 μm.

Such large-scale uniformity in surface coverage is not achievable by kinetically-limited growth processes, as we have seen from Chapter 2 how much carful tuning of reaction conditions is required to produce even a just 4-inch wafer of a TMD with homogeneous surface coverage. We further find that after the molecular deposition reactor is fully coated, the deposition time to full coverage becomes extremely short—less than 30 min—compared to the 4 hours required to achieve surface coverage saturation for similar conditions in a clean reactor. The minimum deposition time is limited by the slow ramp time of the furnace, otherwise we would likely find the time to full coverage to be even shorter. A coated reactor tube is truly in an "equilibrium" state, allowing us to clearly observe a time-independent behavior consistent with a thermodynamically-limited deposition process.

From the above experiments, we can see that extremely uniform, monolayer PTCDA films can be achieved by repeating the same deposition condition many times, similar to our experience with TMD film growth using MOCVD. Unlike MOCVD, however, where running too many reactions results in a deviation from a two-dimensional growth mode, this PVD technique never results in multilayer deposition, no matter how many depositions are run, as long as the same temperature is repeated each time. The reactor tube simply reaches some equilibrium

surface coverage of the molecule of interest. As long as the temperatures used do not cause decomposition of the molecular species, and the purity of the chemical is high, the reactor coating should be similar to the source powder. Indeed, we find that completely removing the PTCDA source from a coated reactor tube still results in significant (albeit lower) surface coverage of the MoS_2 substrates (**Fig. A5.6a**), and the morphology of the films deposited from the tube wall very similar (**Fig. A5.6b**).

We believe that reactor cooling rate is also an important factor for maintaining the deposition equilibrium, but we have not been able to make clear conclusions about the effects of different cooling procedures on the molecular crystal growth (e.g., faster cooling with the furnace lid open, or slower cooling with the furnace lid closed). Overall, however, we find that repeating deposition conditions successively, whatever those conditions are, is one way to increase the surface coverage and improve film homogeneity along the length of the reactor. Unfortunately, though, we find that repeated depositions without reactor cleaning can unpredictability affect other aspects of the film morphology related to crystallinity, which we will discuss in Section 5.5.

5.3.2 Nonequilibrium Conditions for Multilayer Growth

As we have seen, it is not possible to produce observable quantities of multilayers or thick crystals in this PVD process, since the depositions are carried out under conditions of thermal equilibrium. It is possible, however, to achieve few-layer-thick molecular films or bulk molecular crystals, such as those shown in **Fig. 5.8**, by creating a temperature gradient along the length of the furnace. **Fig. A5.7a** shows cross-polarized images of how these different morphologies can be formed. In this experiment, the substrate is held at a constant temperature, and the temperature of the source is increased progressively. Since the reactor is a multi-zone

furnace, there will be a decreasing temperature gradient from the source to substrate, so the substrate is kept at a sufficient distance to ensure that the temperature is the intended value. If the substrate is set to 225°C, then monolayer PTCDA films can be achieved for source temperatures up to 255°C (**Fig. A5.7a**, first panel), resulting in films that look like **Fig. 5.8a**, first panel. If the source temperature is increased by 15°C (**Fig. A5.7a**, second panel), then few-layer PTCDA films, such as those shown in **Fig. 5.8a**, second panel, are produced. Increasing the source temperature by another 15°C (**Fig. A5.7a**, third panel) results in the deposition of bulk TCDA crystals, such as those shown in the third panel of **Fig. 5.8a**.

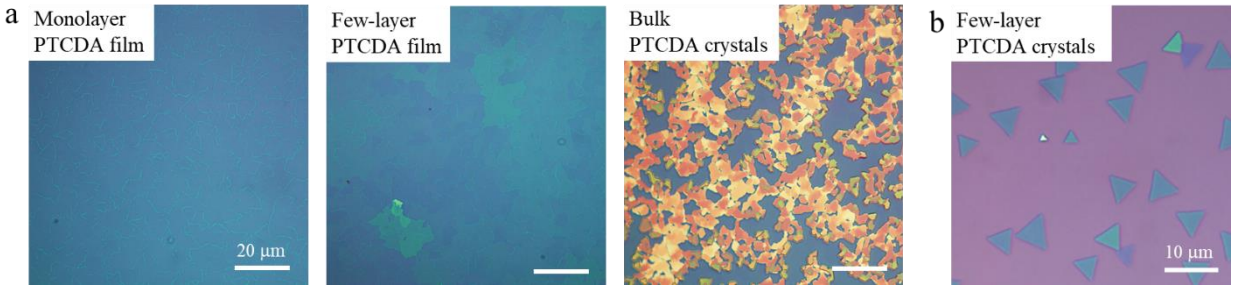

Figure 5.8. Optical images of a) PTCDA deposited on MoS_2 films where the PTCDA deposits as monolayer (first panel), few-layer (second panel), and thick bulk crystals (third panel); and b) Few-layer thick single-crystals of PTCDA deposited on single-crystal WS_2 triangles. All scale bars in (a) are 20 μm.

Of course, the deposition in the middle panel of **Fig. 5.8a** is not layer-by-layer, which would require ultra-high vacuum conditions, but the size of the different-thickness regions is large enough for fundamental studies. Probably a more practical way of producing few-layer-thick molecular crystals would be to use single-crystal WS_2 as the growth substrate, since we know from **Fig. 5.6** that this produces single-crystal PTCDA. Such few-layer PTCDA crystals are shown in **Fig. 5.8b**, where WS_2 triangles with different colors correspond to different thicknesses of PTCDA. It is worth noting that these few-layer crystals are likely not composed of flat-lying PTCDA. It has been observed in other studies that the first layer of a molecular crystal

deposited on a 2D material surface lies flat, but the molecules in subsequent layers stand on-end,[2,3] as they would on a rougher substrate (e.g., **Fig. 1.13a**).

As a final note, although the use of temperature gradients can produce molecular films with different thicknesses, repeating deposition conditions that use nonequilibrium conditions does not always produce the same thickness, since the reactor tube coating is constantly evolving. Furthermore, changing between deposition temperatures after running a growth with a temperature gradient produces extremely unpredictable results. An example of this is shown in **Fig. A5.7b**. The first panel shows a monolayer film of PTCDA on MoS_2, where the substrate was kept slightly below the source temperature of 300°C. The following deposition was run with the source and substrate at the same, lower temperature of 225°C. This resulted in thick, bulk crystals of PTCDA (**Fig. A5.7b**, second panel), as the excess molecular deposits on the tube wall from the thermal gradient was deposited on the substrate. That same condition (T_R = 225°C) was then repeated for the third deposition, and the result returned to monolayer thickness (**Fig. A5.7b**, third panel), indicating that the tube returned to its equilibrium coating for the 225°C temperature. Increasing the reactor temperature usually poses less issues, since the molecular coating on the reactor is thinner than would be produced at the higher temperatures, but decreasing temperature from the preciously-used condition typically results in excessive crystallization.

5.4 Substrate Contributions: Surface Distribution and Crystallinity

We previously saw in Section 3.5 the large effects that substrates can have on the nucleation density and crystal morphology of TMD materials. Hence, it is not unexpected to see similar behaviors for the deposition of molecular crystals. However, in the case of TMD growth, the substrates are commercially-purchased, highly-standardized silicon or glass wafers. This

molecular deposition uses TMD film substrates that are grown in-house, which are subject to all of the variabilities described in Chapter 3. Still, we can use our knowledge of MOCVD-grown TMD films to develop some understanding of how 2D molecular crystals grow in this thermodynamically-limited deposition process, even in the absence of a "perfect" substrate.

5.4.1 Surface Coverage Distribution

In Sections 5.2 and 5.3, we discussed how that the major factors that determine surface coverage are the deposition parameters that affect the molecular concentration in the vapor. However, the *distribution* of the surface coverage of the films shown in those sections was conveniently ignored. We will now explain some of those features in this subsection. We start by looking at the simplest case, which is a single-crystal TMD substrate. **Fig. 5.9** shows the morphology for PTCDA deposited on large, isolated single-crystal islands of WS_2. If the deposition is carried out in a clean reactor, the result typically looks like the left panel of **Fig. 5.9**. We can first see that the molecular domains are always single-crystal within a single WS_2 island. Observations related to crystallinity will be saved for the following subsection. The other important observation here is that the PTCDA molecules appear to deposit from the edges of the WS_2 islands, inward. Knowing nothing about the studies in the previous two sections, one might naively assume that what is happening here is that the molecules landing on the surface simply have

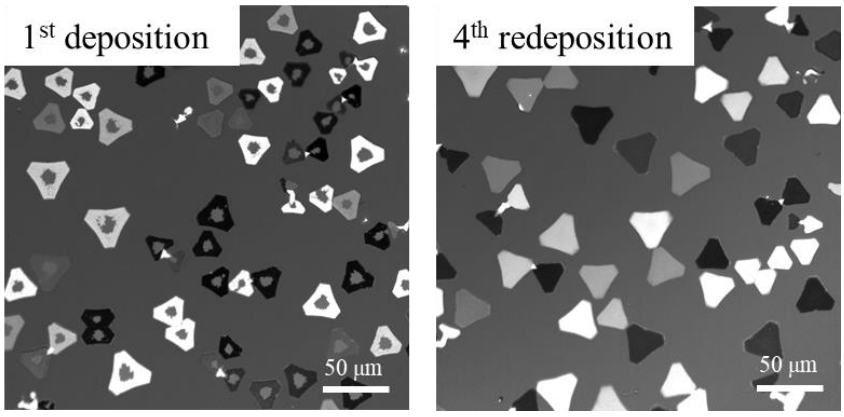

Figure 5.9. Cross-polarized images of PTCDA deposited onto large single-crystal islands of WS_2 in a newly-cleaned reactor (left image) and after heating off the PTCDA and redepositing it another three times (right image).

extremely long diffusion lengths at these high temperatures, and do not nucleate until they reach the edge.

If this were happening, then in the case of kinetically-limited crystal growth, one would expect the growth rate to be the same for each PTCDA crystal, and so smaller WS_2 islands should exhibit greater percent surface coverage. We can see that this is not the case, however, since the "width" of the PTCDA crystals (i.e., from the edge of the WS_2 island to the crystal growth front) is generally smaller for smaller WS_2 islands, and most islands exhibit similar PTCDA surface coverage between 80-90%, regardless of size. Furthermore, the surface coverage for these single-crystal substrates also does not increase with time, so the situation is definitely more complex than simple crystal growth from the edge.

Even we think about this phenomenon from a thermodynamically-limited standpoint, a high surface diffusion mechanism still cannot explain the observations. This is because the rate of adsorption to the surface depends on the *local* number of open adsorption sites and surface concentration of the molecular species. If molecules that adsorbed to the middle always diffused away to the edges, then the central region would still be out of equilibrium, and more molecules would continue adsorbing until the center achieved the equilibrium surface coverage. However, we see that while the edges of the WS_2 islands (here, roughly 80-90% of the area from the outside, inwards) saturate at nearly 100% surface coverage, the central regions (i.e., 10-20%) of the islands saturate at ~0% coverage, suggesting two different states of equilibrium surface coverage. These observations of spatially-inhomogeneous deposition of PTCDA suggest that there are differences between the properties of the center of WS_2 islands and the edges. If every region on a substrate was the same, then the percent surface coverage at any given region on the substrate should be equal, and the result should look more like the PTCDA crystals in **Fig. 5.6a**.

We find that this result is not the typical behavior, though. Most WS_2 crystals result in deposition similar to **Fig. 5.9** (left panel).

We can investigate this phenomenon further by taking the same substrate, heating off the PTCDA crystals in another reactor, and redepositing the PTCDA in the original (uncleaned) reactor with the same deposition conditions used previously (note this is slightly different from the experiments in **Fig. A5.5**, where a new MoS_2 substrate was used each time). If we perform this heating and redeposition repeatedly, then by the 4^{th} deposition, that same WS_2 sample now exhibits 100% surface coverage of PTCDA (**Fig. 5.9**, right panel). To understand what we are seeing, we return to the surface adsorption terminology introduced in Section 4.2. On a "perfect" substrate, every adsorption site should have the same ΔH_{ads}. In "real" materials, however, this quantity can vary significantly, due to surface inhomogeneities. As a result, some adsorption sites on a surface experience lower desorption rates, due to stronger binding to the adsorbate (i.e., more negative ΔH_{ads}). These sites will become occupied under "milder" deposition conditions, such as lower molecular concentration, because more molecules will stay bound for a given adsorption rate. We know from Section 5.3 that repetitive depositions increase the concentration of the molecular species in the vapor, which increases the adsorption rate relative to the desorption rate. At these higher rates of molecular adsorption, the central regions of the triangles now exhibit the same percent surface coverage as the edges. Hence, the experiment in the right panel of **Fig. 5.9** is consistent with our hypothesis of surface variation in the adsorption enthalpy.

Of course, this raises questions about the source of such substrate inhomogeneities. To further examine these effects, we attempt deposition on substrates with various morphologies. **Fig. 5.10a** shows cross-polarized images of a partially-merged film of large MoS_2 islands, before

depositing PTCDA. The left panel image, which is taken at the typical wavelength that that we use to image PTCDA films (560 nm), shows a very uniform MoS_2 surface within the roughly-triangular single-crystal domains. However, when the same film is imaged near the A exciton of MoS_2 (650 nm), we can see triangular inhomogeneities in the center of each single-crystal domain, where the absorption appears to be slightly red-shifted (**Fig. 5.10a**, right panel).

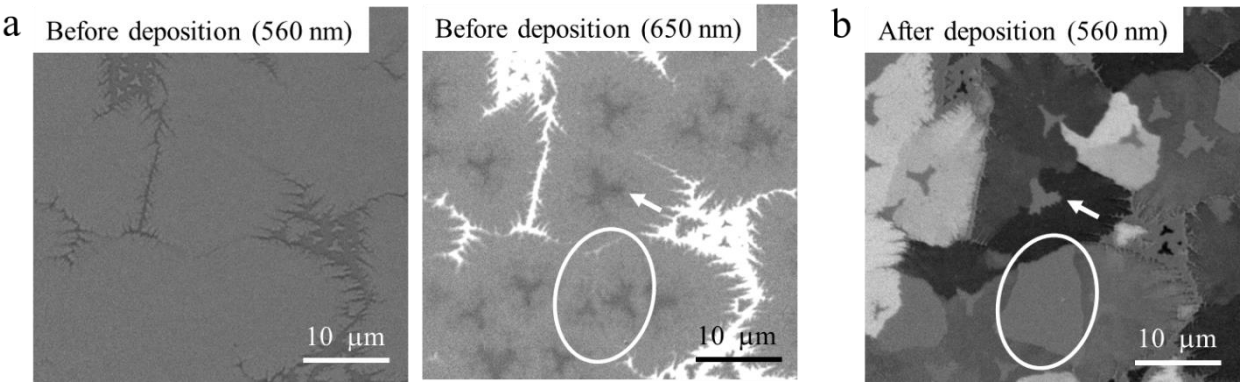

Figure 5.10. a) Cross-polarized images of a partially-connected films of large MoS_2 triangles before the deposition of PTCDA. The left image is taken at the wavelength where PTCDA exhibits a polarized response, and the right image is taken at the A exciton of MoS_2. b) Cross-polarized image of the same area after the deposition of PTCDA, taken at the same wavelength as the left image in (a). White arrow indicates a hole in the center of a PTCDA domain, and white circle indicates whole MoS_2 domains not covered with PTCDA.

When we deposit PTCDA onto these partially-grown films, we find observe two things. First, we find that PTCDA does not adsorb well to these regions, leaving holes in the exact shape of the triangular inhomogeneities (**Fig. 5.10b**, white arrow). This behavior is similar to the WS_2 islands in **Fig. 5.9**, except now we can see some correlation to a property of the underlying substrate. We previously discussed the optical inhomogeneities in large TMD crystals in Section 3.7 (**Fig. A3.10a**), where we find that the band gap varies from the center of the island, moving towards the edge. As explained before, large single-crystal TMDs are grown by applying extreme reaction conditions for extended periods of time. Hence, it is not unexpected for regions of a crystal that are grown later (i.e., the outer regions) to exhibit different properties than regions grown first, which were subject to those extreme conditions for longer (i.e., the center).

In this case, it appears the central region is experiencing more tensile strain (hence, reduced band gap), but the optical change could also be due to a difference in defect density in the different regions.

The second observation is that, in these partially-connected films, we also find that some random MoS_2 domains are completely uncovered by PTCDA (**Fig. 5.10b**, white circle). This behavior is different from the isolated WS_2 islands from **Fig 5.9**, where we typically do not observe random islands with zero surface coverage. We can see a difference in the PTCDA adsorption to these two types of void regions (i.e., completely bare MoS_2 domains and bare regions in the center of a mostly-covered MoS_2 domain), by taking a film such as the one shown in **Fig. 5.10b** and placing it back in the reactor to continue the deposition. Here, we do not heat off the PTCDA before the second deposition, which is slightly different from the experiment in **Fig. 5.9**. By doing this, we see that the completely bare MoS_2 domains are completely filled upon repeating the deposition (**Fig. A5.8b**, white circles), but the triangular regions only become partially filled (**Fig. A5.8b**, white arrows). We also see that the PTCDA continues depositing as the same orientation inside existing PTCDA domains, even though the same condition produces smaller domain size deposition on the fully-uncovered MoS_2 domains.

We can make a number of inferences from the experiments in **Fig. 5.10** and **Fig. A5.8**. The observations related to crystallinity we will leave for the following subsection. In terms of the surface coverage change, we see that there are numerous “classes” of substrate regions with different affinities for the molecular absorbate. In a partially connected film, some TMD domains exhibit a significantly lower binding affinity than others (i.e., circled domains). Then within a single domain, the central region exhibits and even lower binding affinity. The former

regions can be filled by a deposition condition with a slightly increased molecular concentration, but the central regions require an even higher concentration to achieve fill coverage.

One straightforward way to explain this difference in the adsorption behavior can be related to strain in the TMD substrate. We saw that the central regions in **Fig. 5.10** appear to be strained relative to the outer regions of the crystal. This could be due to height variation of the MoS_2 film due to intercalation of chemical species underneath the films during growth (such as we saw in **Fig. A3.9**). The driving force for adsorption will be much weaker on a surface that is not flat, due to the weaker interactions between the molecule and the substrate. It is also possible that the strain is completely in-plane (i.e., the entire island is actually flat), since strained crystals can be found to exhibit different adsorption properties,[4,5] although the effect of the strain in these cases (i.e., whether the binding affinity increases or decreases) seems to be highly system-specific. This in-plane strain difference can also explain why random domains within the film have different adsorption properties, while domains that are isolated or mostly isolated do not exhibit this behavior.

If we carry on our analysis to completely continuous TMD films, we can clearly see two extreme morphologies of the molecular deposition. The first is a "domain-by-domain" deposition behavior (originally pointed out in **Fig. 5.3**), where certain MoS_2 domains require higher concentrations of the molecular species in the vapor in order to achieve full surface coverage (**Fig. 5.11**, left panel). The MoS_2 films used in **Fig. 5.11** are overgrown, so that the domain boundaries are clearly visible from the multilayers that line the domain boundaries (i.e., bright white lines in the images). The other extreme is the "edge-first" deposition, where triangular voids are left at the centers of the individual MoS_2 domains, but the coverage of every domain is roughly the same. We find that two different MoS_2 films placed side-by-side in the same

deposition can exhibit these two completely different behaviors (see **Fig. A5.9**), but even for the same MoS_2 film, there is variation depending on the deposition conditions. For example, the edge-first deposition seems to be promoted at higher reactor temperatures (e.g., **Fig A5.3f**) and higher reactor pressures (e.g., **Fig A5.4a** and **Fig A5.4b**). The predictability of what conditions promote which morphology is low, however. Actually, the MoS_2 films in **Fig. 5.11** originate from the same MOCVD growth, and the difference was that the substrate in the left image was placed much closer to the PTCDA source. The substrate in the right image was located closer to the downstream edge of the heating zone, where the temperature and reactor coating are less predictable. Usually however, we see a mixture of the edge-first and domain-by-domain deposition behaviors on a single substrate, as we saw in **Fig. 5.10**.

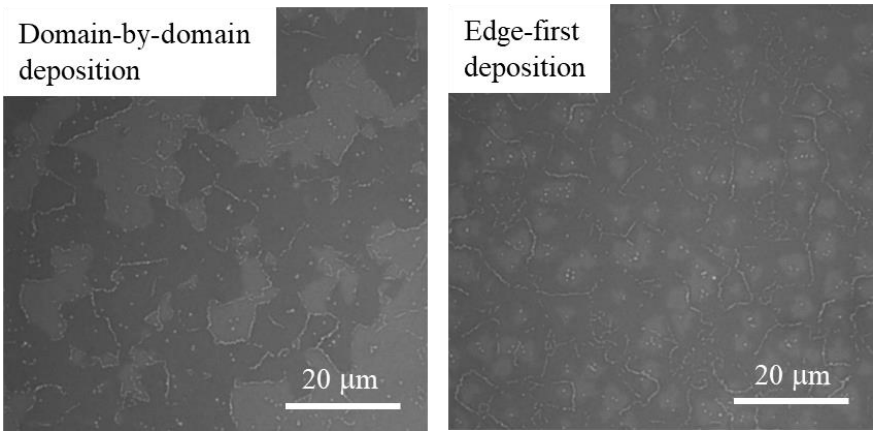

Figure 5.11. Two extreme morphologies of PTCDA deposition on continuous MoS_2 films.

Another way to think about these adsorption differences is in terms of surface energy. Regions of the substrate with higher surface energy will experience a more negative ΔH_{ads} upon molecular binding, and hence, will be passivated first. For example, defect sites have higher surface energy than the basal plane of a TMD crystal, and so one possibility is that regions of a TMD film with more vacancies could promote increased molecular deposition. This possibility, however, is not very straightforward to prove, since it is difficult to tell defect distribution without atomic-resolution measurements. A third possible cause for the domain-to-domain or

intra-domain variation in adsorption properties is the presence of surface residues, which we know are products of the MOCVD growth. If some adsorption sites are already occupied by surface contamination, then the molecular species cannot occupy those sites unless the ΔH_{ads} for the molecule exceeds the ΔH_{ads} for the adsorbed species.

From Chapter 3, we know that patches of carbon are distributed across the surfaces of these TMD films, which cannot be removed by any surface treatment. However, since we are indeed able to produce continuous films of PTCDA that are only the thickness of a single atom (by AFM), we can assume that the PTCDA molecules are actually able to kick the carbonaceous adsorbates off the TMD surface (although this may not be the case for molecular crystals with weaker interactions with the substrate). If the PTCDA crystals were depositing on top of the carbon layers, we would expect the molecules to instead stand on their sides, since, as previously mentioned, other PVD-based deposition studies have found that depositing a second layer of molecules on a flay-lying layer of molecules results in the second layer standing up.[2,3] Still, we do sometimes observe what appears to be the presence of amorphous residues in the void regions of PTCDA films. An example of this is shown in **Fig. A5.10**, where AFM imaging shows the centers of the MoS_2 domains to be taller than the surrounding area, but Raman mapping confirms that there is no PTCDA in those central regions. This data appears to support the hypothesis that existing adsorbates on the surface of these TMD films can cause variation in the surface coverage distribution.

To summarize, we can now have some idea why the surface coverage vs. reactor pressure plot in **Fig. 5.5b** appears to exhibit a more complex adsorption behavior than the most basic adsorption models. We find that different regions of TMD films exhibit different adsorption enthalpies, for the possible explanations given above, and that this behavior is largely due to

factors that are not straightforward to observe or predict. We will see in Section 5.5, however, how certain surface processing procedures can actually reduce this domain-to-domain or intra-domain variability in the surface coverage distribution.

5.4.2 Crystallinity and Interdomain Communication

Until now, we have largely ignored the topic of crystallinity related to these 2D molecular films. In understanding this topic, we will again start with the simplest case, which is a single-crystal TMD substrate. In the previous sections, we saw that we could grow single crystals of monolayer PTCDA that are few 10s of microns in size, by using single crystal WS_2 or MoS_2 substrates. These domain sizes are already extraordinarily large for 2D organic crystals, which usually exhibit domain sizes of few 10s of nm to a few microns for solution-based or ultra-high vacuum synthesis methods (both at room temperature). **Fig. 5.12** illustrates how far we can push the crystallinity of monolayer molecular crystals deposited using this high-temperature PVD method, which shows a 175 μm crystal of PTCDA deposited on a giant single-crystal triangle of monolayer WS_2. To the best of our knowledge, this it the largest reported single-atom-think molecular crystal (the previous record being a few 10s of microns[6]). Although there are sparse pinholes in the PTCDA layer (which could be fixed by tweaking some deposition parameters), it is surprising that the crystal maintains its orientation at this large scale. The ability to grow such large single-crystals usually implies the presence of an epitaxial relationship between a

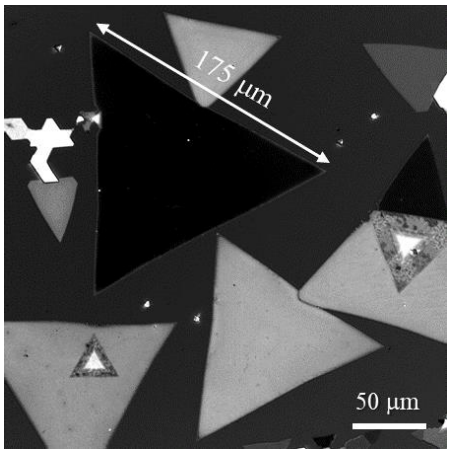

Figure 5.12. Cross-polarized image of giant 2D molecular crystals of PTCDA deposited on giant single-crystal islands of WS_2.

molecular layer and its substrate, but experiments shown later in this subsection indicate that this may not necessarily be the case here.

One interesting point to note with these giant single-crystals is that, due to the three-fold symmetry of the WS_2 crystal and the two-fold mirror symmetry of the PTCDA crystal, one would actually expect that a single TMD domain could have up to 6 different orientations of PTCDA, even in the presence of an epitaxial relationship.[7] However, we find that the PTCDA is a single orientation in most cases, besides a few exceptions that will be described in Section 5.5. This is curious because it seems to imply that either the crystal grows from only one nucleation point, or that all the other crystals break down at some point and add to one particular island. The latter case is also odd, since multiple nuclei are still expected in Ostwald ripening processes.

Since the nucleation and growth phases occur extremely rapidly in this PVD process, it is not possible to isolate a crystal mid-growth to investigate this behavior carefully. However, we have seen some examples of PTCDA growth on WS_2 at higher reactor pressures, where we find that the PTCDA grows out from only one of the three corners of the WS_2 islands (i.e., darker patches in **Fig. A5.11**). This does seem to indicate the possibility of a single nucleation point, but more controlled studies regarding pressure dependance in these systems is required. What may be another insightful experiment would be to use even larger single-crystal TMD substrates, to see at what point the coherence in the orientation of the PTCDA is lost. Unfortunately, we cannot go past the crystal size shown in **Fig. 5.12** because that is the limit to how large we can grow single-crystal TMDs on amorphous substrates (i.e., SiO_2). TMDs films grown epitaxially on sapphire would be the next step toward understanding the mechanism of the formation of these giant single crystals.

Figure 5.13 shows how the crystallinity of PTCDA domains is affected by the presence of grain boundaries, as individual TMD islands merge together to form a film. The left panel shows a cross-polarized image of PTCDA deposited on MoS_2, which is imaged near the A exciton of MoS_2 (660 nm) to roughly indicate the orientations of the partially-merged MoS_2 islands and the positions of the domain boundaries where they meet. Then, we can image the same area at a higher energy where the PTCDA crystals exhibit their polarized response (560 nm), in order to see the relationship. The image in the right panel of **Fig. 5.13** is false-colored so that different orientations of PTCDA crystals exhibit a unique color, where the rotational relationship between the orientations follows the RGB color wheel (see **Fig. 5.14** for scale bar; details of image processing explained in Chapter 5). By carefully inspecting this image, we can see that, not only is the PTCDA single-crystal within an isolated island of MoS_2, but that the molecular domains seem to break their crystallinity across the boundaries where MoS_2 islands merge (white arrows point to groups of merged MoS_2 islands).

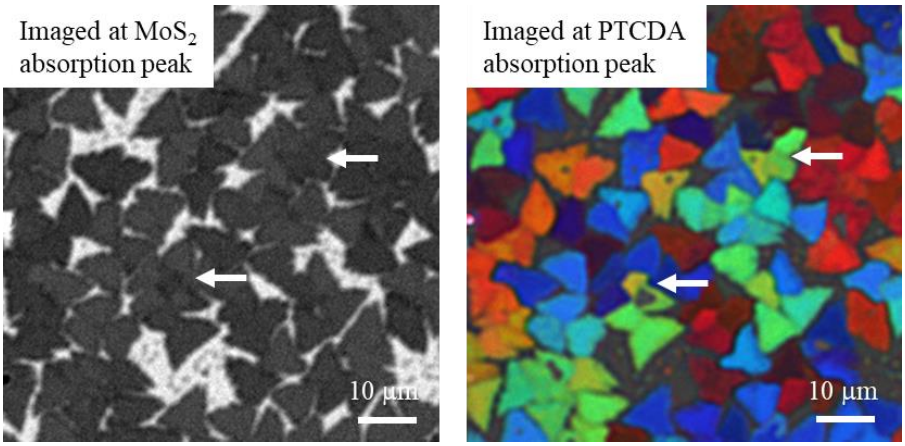

Figure 5.13. Effect of substrate domain boundaries on the crystallinity of PTCDA films. Cross-polarized images of film of PTCDA deposited on partially-merged MoS_2 islands, taken at the A exciton of MoS_2 (660 nm; left image), and taken where the PTCDA exhibits a polarized response (560 nm; right image). Domains in the right image are color-coded to show the relative rotations of individual PTCDA domains (scale bar in Fig. 5.14, inset). White arrows point to some groups of completely-merged MoS_2 islands.

These observations again appears to support the existence of epitaxy, but it could also indicate that the PTCDA molecules are simply not able to easily diffuse over domain boundaries, forcing them to form domains within the confines of a single MoS_2 crystal. The latter would not be entirely surprising, given that we find that the domain boundary regions in these MOCVD-grown TMD films even experience different interactions with the AFM tip during imaging measurements, which can be sometimes picked up as a height difference or other times as a simple a phase difference. Whether the main contribution to these differences at the domain boundaries is physical (i.e., real height difference due to intercalated species) or chemical (related to defects) is unclear.

We continue to investigate this behavior by comparing the molecular deposition on slightly-partial and fully continuous, polycrystalline MoS_2 films. In this experiment we actually deposit monolayer crystals of 3,4,9,10-perylenetetracarboxylic diimide (PDI; **Fig. 4.1**, right panel), but the deposition behaviors of PDI and PTCDA are similar. Both films in **Fig. 5.14** are cut from the same MoS_2 substrate, except the left panel was from slightly downstream in the MOCVD reaction, where we know the growth rate is slightly slower, resulting in a partial film. Aside from the continuity, both MoS_2 films are otherwise identical, including in domain

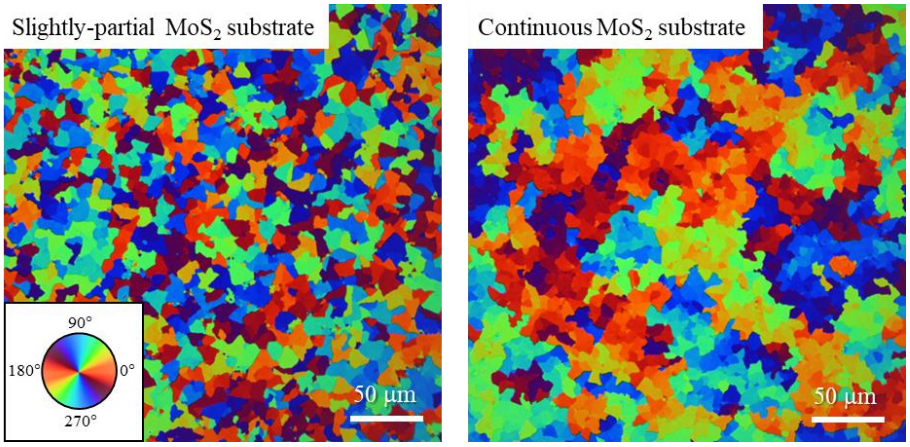

Figure 5.14. False-colored, cross-polarized images of PDI deposited on MoS_2 films with the same domain size, but different levels of continuity: slightly-partial MoS_2 (left image) and continuous MoS_2 (right image). PDI domains are color-coded to show their relative rotations (scale bar in the bottom left inset).

size. The images are also false-colored to show the relative orientations of the PDI domains, according to the color wheel in the bottom left inset. Although the slightly-partial MoS_2 film exhibits the same randomly-oriented PDI domains that we have seen throughout this chapter (**Fig. 5.14**, left panel), as soon at the MoS_2 film becomes continuous, the orientations of neighboring PDI domains suddenly appear to be correlated (**Fig. 5.14**, right panel). Each individual PDI domain is still similar in size to the underlying MoS_2 domains, but neighboring domains seem to communicate and reoriented themselves to be within few 10s of degrees, despite molecules appearing not to be able to diffuse across domain boundaries. If we do careful optical characterization of these correlated molecular films (e.g., polarized reflectance measurements such as those discussed in Chapter 6), we find that their optical responses are no different from the randomly-oriented films. Moreover, these "superdomains" even exist in extremely overgrown MoS_2 films (**Fig. A5.12**, right panel), suggesting that the molecular domains can communicate underneath MoS_2 bilayers, possibly through intercalation.

Because we know that the orientation of MoS_2 domains grown on SiO_2 substrates is random (e.g., recall **Fig. 1.6**), the results in **Fig. 5.14** (right image) seem to suggest the absence of epitaxy in these molecule-TMD systems. Unfortunately, we have found it extremely difficult to pinpoint the mechanism by which these superdomains form, but we have noticed some tendencies. We first point out that we believe the superdomains are mainly the result of the deposition conditions, rather than being caused by to the substrate, since even two TMD substrates with similar morphologies can produce either the correlated or uncorrelated behaviors (**Fig. A5.12**). We also find that the correlated behavior is actually the *natural* tendency for PTCDA. This could indicate that PTCDA crystals exhibits stronger total IMFs than the other perylene derivatives, which could promote rearrangement and rotation of the molecular domains

as they interact strongly across a TMD domain boundary. We rarely see this behavior in PDI, and have never observed it in the molecular crystals of the alkyl-PDI derivatives. More discussion on this topic will be given in Section 6.2.

Generally, we find that the only way to consistently achieve "random" PTCDA deposition is to use a partial TMD film (like the experiment in **Fig. 5.14**, left panel). However, there are a number of deposition-related factors that reduce the communication distance in these polycrystalline molecular films. The first is that the size of superdomains tend to decrease with increasing source-substrate distance, as shown in **Fig. A5.13**. although the origin for this is not clear. We further find that repeatedly depositing PTCDA on the same MoS_2 film (i.e., same experiment as **Fig. 5.9**) causes a loss in the communication between domains. This can be seen in **Fig. 5.15**, where the same area is imaged after each heating and deposition cycle (white arrow

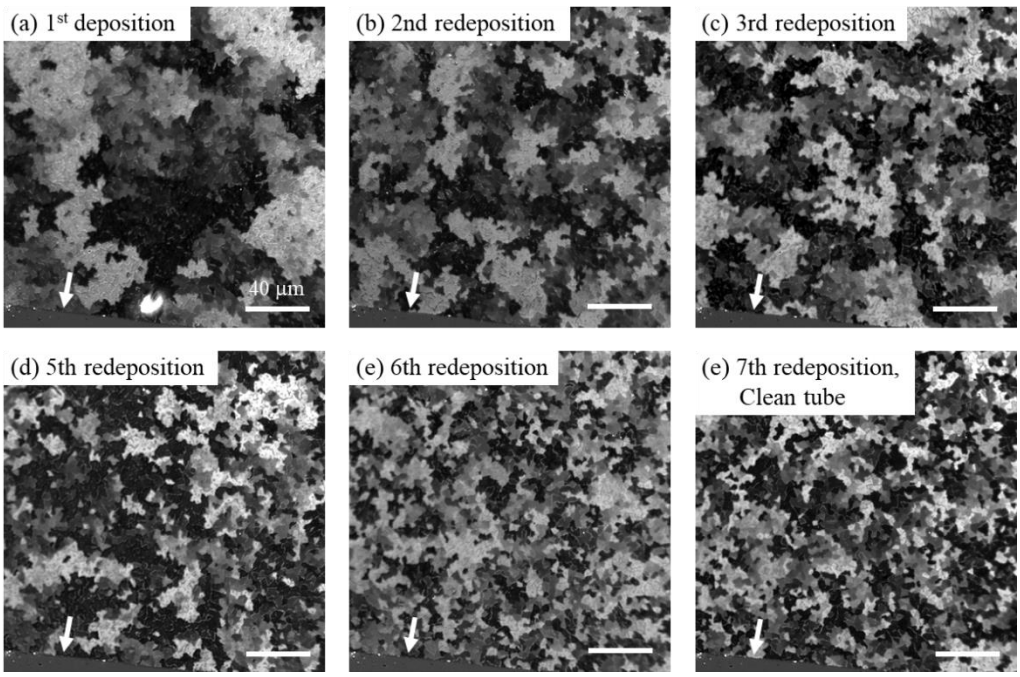

Figure 5.15. Cross-polarized images of PTCDA deposited on the same area of a MoS_2 substrate, after repetitive cycles of heating off the PTCDA and redepositing it. The seventh redeposition was carried out after cleaning the reactor tube. White arrows point to a scratch in the film for refence, and all scale bars are 40 μm.

points to a scratch in the film, for reference). If we inspect the film carefully, we can see that the individual PTCDA domains retain their original size after many redeposition cycles—the only change is that fewer neighboring domains have similar orientation.

Even if the reactor is cleaned (**Fig 5.15e**), we can see that the morphology of the PTCDA domains remain significantly less correlated than the first deposition (**Fig 5.15a**), which was also carried out in a clean reactor. Furthermore, a new MoS_2 substrate placed in the same deposition as **Fig 5.15e** does indeed exhibit more correlated behavior (**Fig. A5.14**). This is not too surprising, since we know from Chapter 3 that temperature cycling continuous TMD films releases strain, presumably by changing the film morphology. So, although we do not believe that any particular TMD substrate *promotes* correlated molecular deposition, we find that morphology changes in the substrates can obstruct this behavior.

This interdomain communication phenomenon is extremely spatially-dependent, exhibiting rapid changes on the local (millimeter) scale that are largely devoid of any trend. After testing many deposition conditions in trying to elucidate the origin of this behavior, we find that it is limited by our ability to control the reactor tube environment. For example, in a well-cleaned reactor tube with a newly-refilled PTCDA source, repeating multiple depositions, each time using new MoS_2 substrates, (e.g., similar to the experiment in **Fig. A5.5**) typically results in reduced interdomain communication (**Fig. A5.15**, middle and bottom rows). By "well-cleaned", we mean that molecular adsorbates are completely removed by heating the tube at high temperatures (e.g., 500°C) under oxygen flow. However, we can instead clean the tube by flowing large amounts of carrier gas (Ar) at the same high temperatures. This "cleaning" pushes most of the molecular adsorbates downstream, but still leaves a small amount coating the tube, as well as significant quantities deposited upstream and downstream of the heating zone.

Performing a PTCDA deposition in this tube environment significantly increases the proportion of the resulting film that exhibits this correlated behavior.

We find that the first deposition carried out after performing the latter cleaning process (i.e., with high carrier gas flow) actually produces greater molecular surface coverage than the first deposition in a completely clean reactor tube, implying that the molecular residues left over from the cleaning process are indeed affecting the growth of the molecular films. It is possible that this cleaning process leaves a different morphology of PTCDA deposits on the reactor tube, which can have different sublimation properties compared to the source, and that these deposits produce the correlated behavior of the molecular film. To reproduce this more controllably, it would be worth testing annealing the PTCDA source under different temperature and carrier gas flow conditions and then seeing how these processed powders affects the resulting 2D crystal growth. Dissolving the molecules in different solvents could be another way to change the morphology of the source crystals. It is also possible that the formation of superdomains simply requires better control of molecular concentration during the nucleation stage, so having a very small number of molecules coating the reactor can limit the deposition of too many nuclei during furnace ramping. To test this, however, would more clever experimental strategies.

5.5 Synthetic Strategies for Reducing Morphology Variation

As mentioned throughout this chapter, certain characteristics of the film morphology in this 2D molecular crystal growth can sometimes be quite unpredictable. For example, the first, second, fourth, and fifth PTCDA depositions in **Fig. A5.15** follow trends that were described in previous sections, but the third deposition randomly exhibits significantly reduced domain size and obstructed interdomain communication. It is unclear whether the cause of these sporadic deviations are the result of substrate surface effects or factors related to the reactor environment,

but we generally find that both of these aspects are extremely important for producing highly crystalline molecular domains. For example, **Fig. 5.16a** shows very different behaviors from two WS_2 substrates placed side-by-side in a PTCDA deposition in a coated reactor tube—one polycrystalline and one single-crystal. The difference between the two WS_2 substrates is that the left was grown with 25% reduced carrier gas flow compared to the WS_2 substrate in the right panel. The result of the PTCDA deposition suggests that these two samples have significantly different surface properties, which results in a loss of coherence for the PTCDA crystals in the left panel, possibly due to the presence of more surface residues from MOCVD processes at reduced carrier gas flow. In general, we find that polycrystalline MoS_2 substrates exhibit significantly less variability than single-crystal WS_2 substrates with similar domain size, likely due to the large differences in the growth conditions used to produce these two different TMD morphologies.

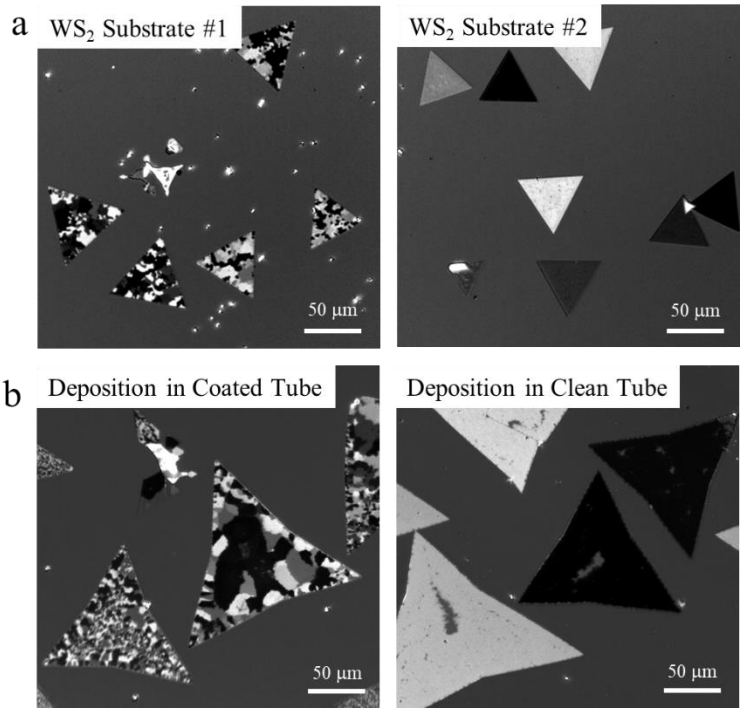

Figure 5.16. Cross-polarized images of PTCDA deposited on a) two WS_2 substrates grown using different MOCVD conditions, and b) WS_2 substrates from the same MOCVD growth, where the PTCDA was deposited in a coated reactor tube (left panel) or a newly-cleaned reactor tube (right panel).

Although variation in molecular crystallinity resulting from the MOCVD growth is an important factor to consider, it is a one that is largely unavoidably and not straightforward to

predict. Interestingly, a substrate similar to the one shown in the left panel of **Fig. 5.16a** can still enable single-crystal PTCDA growth if the deposition is performed in a newly-cleaned reactor tube. This can be seen from the images in **Fig. 5.16b**, where a WS_2 growth that gives polycrystalline PTCDA deposition in a coated reactor tube produces single-crystal (albite partial) PTCDA domains in a newly-cleaned tube. This polycrystallinity of PTCDA is typically only seen in TMD islands with very large domain size (as expected from the discussions in chapter 3), and the larger the TMD domain size, the more difficult it is to achieve single-crystal molecular deposition. From this, we can see that reactor tube cleaning is critical for producing large single-crystals of PTCDA, although it causes a drop in the surface coverage.

Recall from Section 5.4 that an epitaxial relationship between PTCDA and WS_2 substrate could produce up to six different orientations of PTCDA on a single WS_2 island. Yet, for well-controlled deposition conditions, we usually only see one orientation of PTCDA. Using the polycrystalline PTCDA film in **Fig. 5.16b**, we can analyze the intensities of each PTCDA domain and plot the number of pixels that correspond to a given intensity value. This histogram is given in **Fig. A5.26a** (bottom panel), with a histogram for a similar-sized area of PTCDA deposited on a polycrystalline MoS_2 film given in **Fig. A5.26b** (bottom panel), for comparison. In both cases, the PTCDA orientations corresponding to the dark domains will be overrepresented, for reasons that will become clear in Chapter 6, but the rest of the histogram should be relatively flat if there are roughly an equal number of domains with any given orientation. This is indeed that case for the PTCDA on the MoS_2 film, as expected, since the randomness of the underlying MoS_2 domains would still result in an equal number of each PTCDA orientation, even in the case of epitaxy. What is intriguing it that the histogram of the polycrystalline PTCDA on the WS_2 actually exhibits 5-6 peaks, suggesting an orientational

preference. More analysis is needed here to draw any conclusion related to epitaxy, but taking this data with the other epitaxy-related evidences from the previous section suggests that the answer may not simply be one or the other (i.e., it is possible that there is significant dependance on the substrate and the depositions conditions). A technique like low-energy electron diffraction (LEED) would be required to clearly determine the nature of the relationship between the TMD material and the molecular layer.

Returning to our discussion about methodologies to promote more reproducible molecular crystal morphologies, we find that some of the variability associated with deposition on large single-crystal TMD islands can be reduced by performing many cycles of deposition, heating off the molecular crystals, and redepositing. This experiment is similar to the one shown in **Fig. 5.15**, except now we see how the morphology evolves within a single-crystal domain. The results are shown in **Fig. 5.17**, where the same WS_2 islands are imaged each time. We see

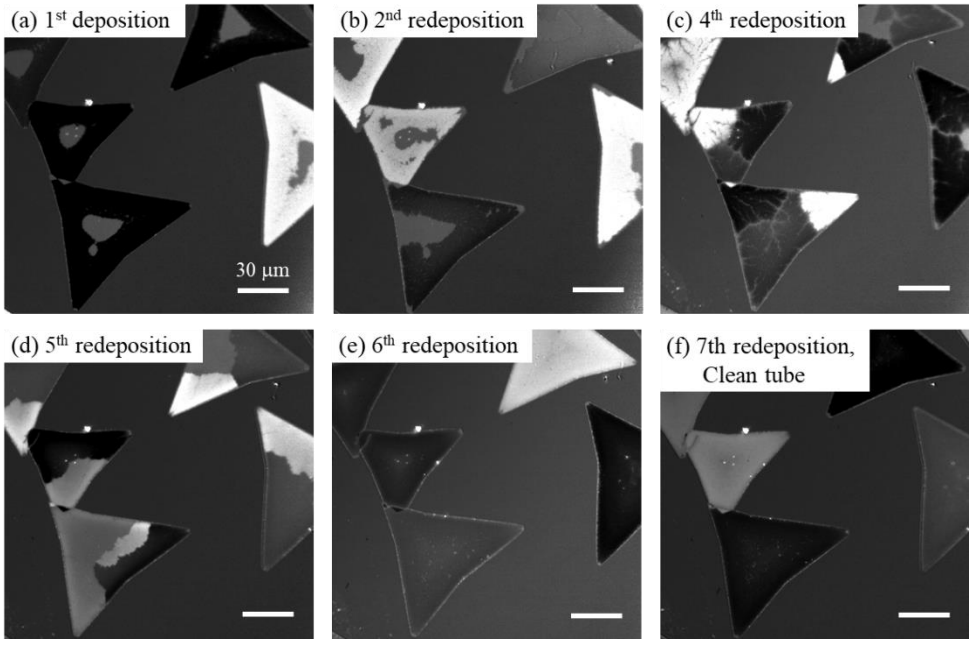

Figure 5.17. Cross-polarized images of PTCDA deposited on the same WS_2 substrate, after repetitive cycles of heating off the PTCDA and redepositing it. The 7th redeposition was carried out after cleaning the reactor tube. All scale bars are 30 μm.

that deposition in a newly-cleaned reactor (**Fig. 5.17a**) gives partially-covered WS_2 islands with single-crystal PTCDA domains, and that the coverage increases after multiple cycles of redeposition, achieving full coverage by the fifth deposition. What is interesting here is that, while the fourth and fifth redepositions are polycrystalline, the sixth returns to being single-crystal. Then, even when the reactor tube is cleaned for the seventh deposition (**Fig. 5.17f**), the same WS_2 crystals now exhibit full coverage.

We should remember that the difference between this experiment and what was shown in **Fig. 5.16b** is that the same exact substrate is being used repetitively in **Fig. 5.17** (as opposed to new substrates cut from same WS_2 growth in **Fig. 5.16b**). If a new substrate was placed in the same deposition as **Fig. 5.17e**, the result would highly likely be polycrystalline. Essentially, we find that repetitive depositions on large single-crystal TMD substrates can help improve the likelihood of achieving single-crystal molecular deposition, which could be due to the displacement of surface adsorbates by the PTCDA molecules over time. Furthermore, these repetitive heating cycles seem to reduce the spatial inhomogeneity that exists in the center of the TMD island, so that the center of the domains now exhibit the same precent coverage (i.e., 100%) as the edges, for a condition where the centers previously exhibited no coverage. So, although repetitive heating of polycrystalline MoS_2 films reduces interdomain communication between neighboring molecular crystals (i.e., **Fig. A5.15**), we find that this same process actually improves *intra*domain crystallinity. Looking carefully, however, we can see that the islands in **Fig. 5.17f** still do exhibit some inhomogeneous optical contrast in their centers, although we are not sure if this originates from the PTCDA layer or the WS_2 layer. This particular effect is highly substrate-dependent (e.g., not present in Fig. 5.9 or Fig. 5.16), but we have not done much more in studying the origin.

Another that can be employed to improve the reproducibility of 2D crystal growth on these TMD substrates is by applying different solvent treatments to dissolve surface residues leftover from the MOCVD growth. Actually, all of the molecular depositions we presented in this chapter were carried out on TMD substrates treated by rinsing the surface with methanol, isopropyl alcohol (IPA), and then drying off the solvent under a stream of nitrogen. We do this because we know from Chapter 3 that sodium-containing residues are common surface contaminants from our MOCVD process, and that a polar solvent is required to remove them. IPA is used to follow the methanol because methanol by itself contains trace contaminants that to leave significant quantities of residues upon drying from a surface. We blow the IPA directionally off the surface in order to minimize trace contaminants left from the IPA evaporation.

One might expect that removing surface adsorbates from the substrate would increase the surface coverage the molecular crystals, but we actually find that using this solvent-cleaning process actually results in significantly reduced surface coverage of PTCDA (**Fig. 5.18b**) compared to the as-grown films (**Fig. 5.18a**). Furthermore, if the IPA is instead allowed to evaporate from the surface of the substrate at the end of the cleaning process, then the surface coverage of the deposited PTCDA is reduced even further (**Fig. 5.18c**). These results suggest that

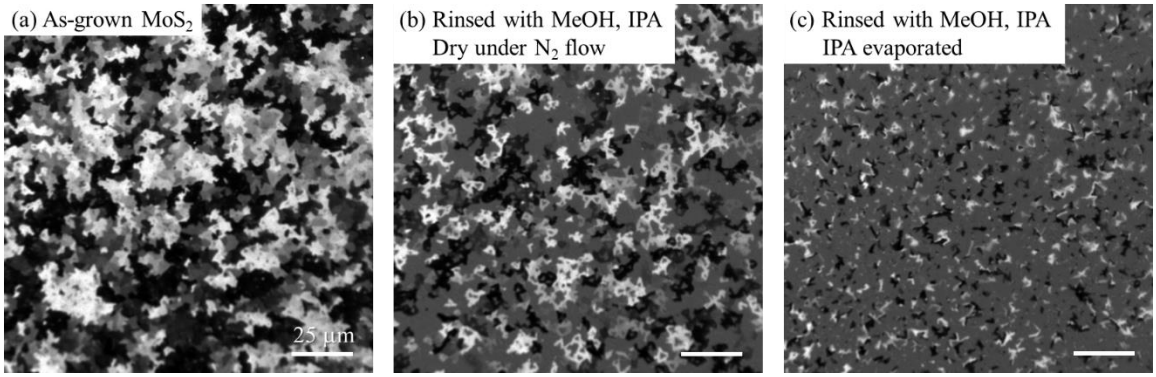

Figure 5.18. Effect of different MoS_2 surface treatment processes on the surface coverage of the subsequent PTCDA deposition. All scale bars are 25 μm.

the solvents effect the deposition more than the sodium-containing residues from the MOCVD growth, possibly by leaving unidentifiable residues on the surface that are not even removed at the high temperatures used to deposit the molecular crystals. This would be consistent with our discussions in Chapter 3, where we mentioned how simple solvent treatments appear to cause doping effect in 2D TMD devices.

Although it may seem from the data in **Fig. 5.18** that leaving the TMD substrates as-is might be the better option to achieve high surface coverage, we find that not removing the sodium residues from the substrates actually leads to inconsistent deposition behaviors. For example, we sometimes find that using as-grown MoS_2 film substates results in molecular crystals that are actually smaller than the MoS_2 domain size—a behavior that we do not normally observe for these continuous films. This effect is most significant in the deposition of the alkylated derivatives of PDI, such as N,N′-dimethyl-3,4,9,10-perylenetetracarboxylic diimide (MPDI; **Fig. 4.1**, middle panel), and can be seen in **Fig. A5.17a** where the solvent-treated sample has only partial surface coverage but clearly larger crystal size. We therefore always opt for the surface treatment, but it would be worth testing different solvent systems to see their effects on the morphologies of the molecular crystal films in terms of surface coverage, interdomain communication, and domain size.

The final source of variation in the molecular crystal growth is the morphology of the SiO_2 support on which the TMD substrate was grown. As we described in Section 5.4, we think the cause of the "edge-first" deposition behavior seen in **Fig. 5.11** could be the surface roughness in the SiO_2 resulting from to intercalated compounds during the MOCVD growth (i.e., Chapter 3). Hence, transferring the TMD film can remove effects related to the SiO_2 support morphology, allowing us to observe the contribution of the TMD substrate alone. Furthermore, sometimes the

TMD needs to be transferred to a different substrate in order to perform some characterization later. For example, most of the cross-polarized measurements in Chapter 5 require the films to be on a transparent substrate, such as fused silica.

If we used a polymer-based transfer process, such as the one typically used to stack TMD films,[8] the PTCDA (not unexpectedly) deposits with extremely small domain size, and the surface coverage appears to drop significantly (**Fig. A5.17b**, right panel). If the MoS_2 film is instead transferred by delaminating on the surface of water and then scooping onto the target substrate, the resulting molecular deposition (**Fig. A5.17b**, left panel) appears deceptively similar in morphology to an un-transferred film (minus the inevitable large cracks and wrinkles from the transfer process). We know, however, from Chapter 3 that transferring large domain size TMD films (by any method) results in nanoscopic cracking of the individual domains, which cannot be seen under regular optical measurements (**Fig. A3.10b**). It turns out that these cracks block the diffusion of molecules across the film surface, resulting in a slightly smaller molecular crystal size, as well as crystals that are less round in shape. Hence, we find that the most consistent way to achieve 2D molecular crystal growth is to actually use the TMD substrate on the SiO_2 support on which it was originally grown, and then just modify the deposition parameters to make up for any surface coverage variation resulting from nonuniformities in the SiO_2 support. Any substrate transfer is best done after the molecular crystal deposition.

5.6 Expanding to Systems with Weaker Intermolecular Forces

As mentioned to at the end of Chapter 4, this high-temperature PVD process works well for molecular systems with strong IMFs, such as the anhydride and imide derivatives of perylene. **Figure 5.19** shows a side-by-side comparison of cross-polarized images of various hydrogen-bonding perylene derivatives deposited on polycrystalline MoS_2 films. The domain

sizes of the perylene crystals are different in each case due to the MoS_2 substrates used, but very similar film morphologies can be produced in all cases. The major difference between the molecules in **Fig. 5.19** would be the total strength of their intermolecular forces in the crystals that they form (more details on the crystal structures will be given in Chapter 6).

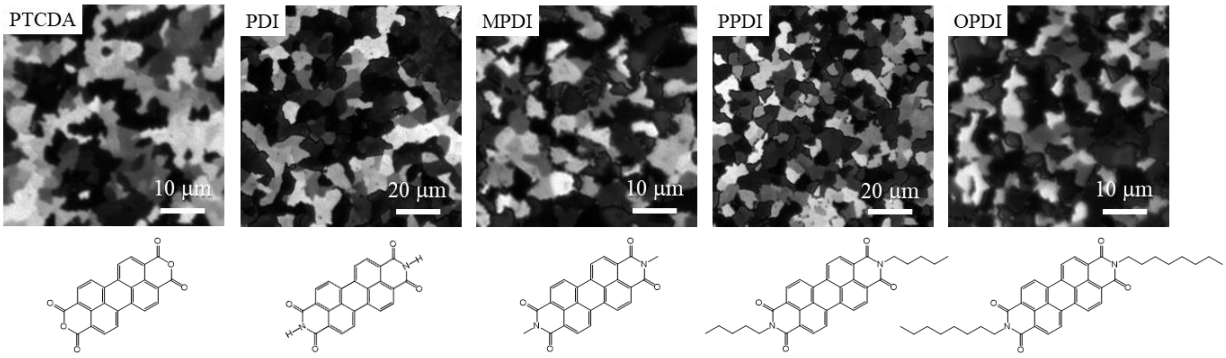

Figure 5.19. Cross-polarized images of molecular crystals of various perylene derivatives deposited on polycrystalline MoS_2 films. The structure of each derivative is given below the image.

Even without knowing the structures of these various molecular crystals, it appears that the binding energies of the crystals is greatest for PTCDA, followed by PDI, followed by the MPDI derivatives. One reason for this theory was already mentioned, which is that communication between neighboring molecular crystals is stifled in systems with weaker IMFs. So although PTCDA typically produces films with "superdomain" structure, this is extremely difficult to achieve in PDI, and we have never observed this behavior in the alkyl-PDI derivatives. We also find it extremely easy to grow large single-crystals of PTCDA, but this is more difficult for PDI, and even more difficult for the alkyl-PDI derivatives.

Another observation suggesting that the other perylene derivatives form more weakly-bound crystals is that they produce drastically-reduced surface coverage compared to PTCDA. Presumably, this is because the high temperatures necessary to achieve uniform deposition in this PVD technique break weaker intermolecular bonds. For example, we find that although PTCDA can achieve full surface coverage of the substrate at $P_R = 0.5$ torr by repeating the deposition a

few times (to coat the reactor tube), using a similar reactor geometry for PDI typically results in a surface coverage saturation around 75-90%. To achieve full coverage of monolayer PDI, we actually have to greatly increase the surface area of the source and place the target substrate extremely close to the PDI source crystals. Then, full coverage can be achieved after many repetitive depositions. The alkyl-PDI derivatives are even more challenging—the system typically saturates at a surface coverage between 50-75% in even a heavily-coated reactor tube, and usually attempting to further increase the molecular concentration (i.e., by increasing the surface area of the source or implementing a small temperature gradient) results in a drop in the domain size of the alkyl-PDI crystals. Actually, we find that the process for cleaning the reactor tube (i.e., using the high-carrier-gas-flow cleaning process described at the end of Section 5.4) is critical for achieving full coverage of the alkyl derivatives with decent crystal size.

Although we can achieve full coverage for the other perylene crystals by carefully applying the strategies discussed in the Sections 5.4 and 5.5, there is a limit to the effectiveness of these approaches. Such strategies do not work for crystals composed of smaller molecular species or those bound by extremely weak van der Waals (vdW) forces in-plane. There is a more systematic way to deposit these weakly-bound 2D crystals, and that is by reducing the reactor pressure. From the understanding in **Fig. 4.6** and the experimental data in **Fig. 5.5**, we can infer that the pressure of the deposition environment will dictate the temperature required to achieve uniform, monolayer coverage. At higher pressures (here, ~10^{-1} torr), higher temperatures are required for unform deposition (i.e., 200-300°C), which is only compatible with molecular crystals that are very thermally-stable (i.e., experience stronger IMFs). Most molecular species will never achieve full surface coverage under these conditions, so moving to lower reactor

pressures is key to enabling deposition at lower temperatures, to grow crystals with weaker IMFs.

Due to limitations in our reactor setup, we are not able to attain lower pressures to test this theory, but we have found a recent work that does achieve 2D films of molecular crystals with purely vdW bonding in-plane.[3] This study also uses a hot-walled PVD reactor, but with high vacuum conditions (~10^{-6} torr) and lower substrate temperatures (~40°C) to achieve 2D crystals of tetracene, albeit with (expectedly) smaller domain size. Unfunctionalized tetracene is an extreme case of a molecule with very weak bonding anisotropy (actually, the out-of-plane IMFs are stronger than the in-plane forces). If monolayers of tetracene can be achieved at pressure of 10^{-6} torr (as opposed to the 10^{-1} torr used in our system), then many other functionalized molecular systems, such as porphyrins, should be possible to deposit as 2D crystals, even without having to reach such low reactor pressures (and definitely going to ultra-high vacuum is not necessary). Lower reactor pressures and temperatures presumably make the system more kinetically-limited (i.e., more time-dependent), but provides an extra tuning knob to grow decently-sized 2D molecular crystals that cannot be achieved in the thermodynamic limit.

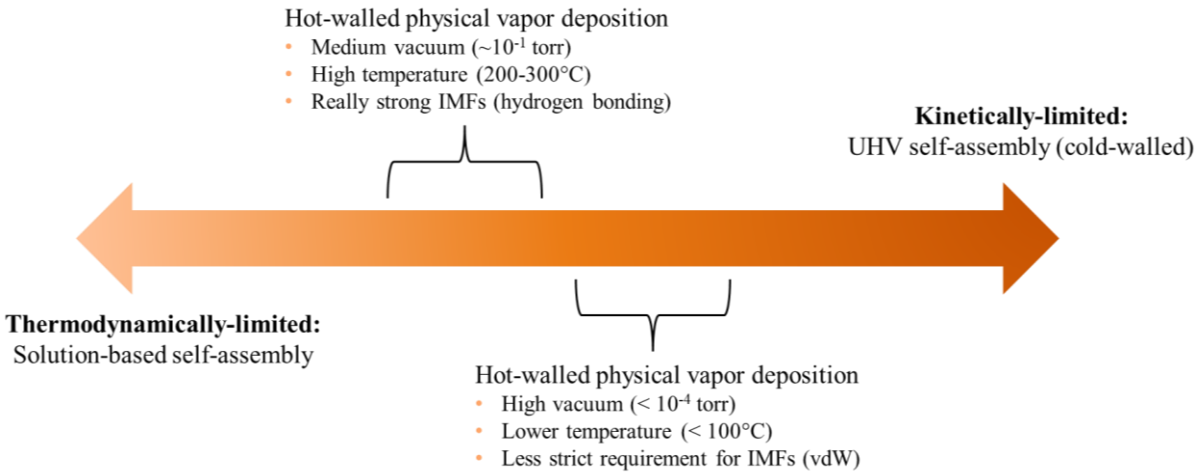

Figure 5.20. Three main approaches for forming monolayer organic films, where this hot-walled physical vapor deposition approach can exist closer to the thermodynamically-limited side or the kinetically-limited side depending on the working pressure and temperature.

Our ideas are summarized in **Fig. 5.20** (a revised version of **Fig. 4.4**), where we can now see how this hot-walled PVD process can be operated either closer to the thermodynamically-limited side or the kinetically-limited side by adjusting the pressure and temperature regimes.

5.7 Summary

We have seen from the data in this chapter that it is possible to deposit highly crystalline, 2D molecular films that exhibit monolayer coverage over the inch-scale by using this thermodynamically-limited PVD process. Similar to adsorption phenomena, the surface coverage of the molecular films is dictated by the deposition parameters that affect the concentration of the molecular species near the surface of the substrate (i.e., reactor temperature, reactor pressure, and source-substrate distance). Maintaining the deposition at thermal equilibrium is key to producing high-surface-coverage monolayers over large areas. We further find that the surface coverage distribution and crystallinity of these molecular films are dominated by the TMD growth substrate. By carrying out certain substrate processing procedures, we can produce giant 2D molecular crystals that are only a single atomic thick but larger than 100 microns. Although our studies have only looked perylene derivatives, we can apply our understanding of the growth mechanics of these crystals to learn how to grow 2D crystals with weaker intermolecular forces—by reducing the pressure and temperature of the deposition environment and carrying out the deposition slightly closer to the kinetic limit.

5.8 Appendix

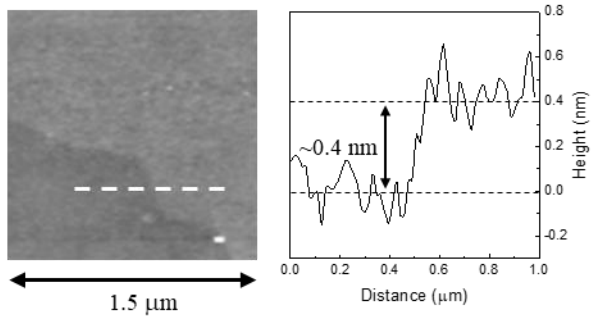

Figure A5.1. AFM image (left) and linescan (right) of a PTCDA molecular crystal confirming monolayer thickness.

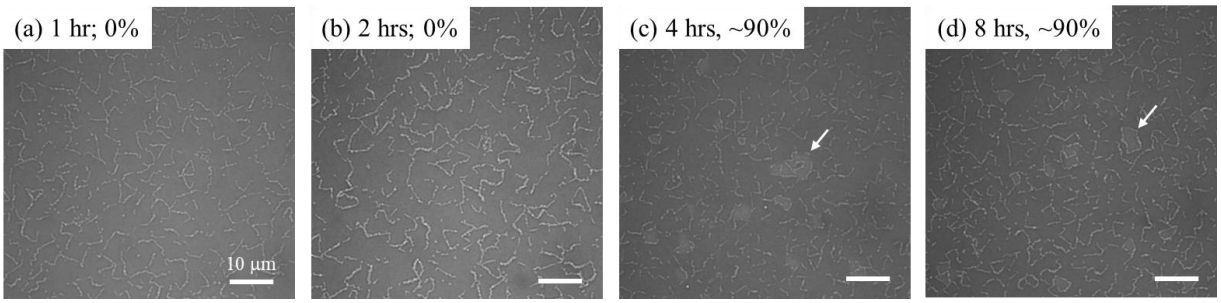

Figure A5.2. Unpolarized optical images of the same films from Fig. 4.11, showing the surface coverage of PTCDA on MoS_2 films with different PTCDA deposition times. White arrows indicate areas of bare MoS_2 substrate, for clarity. All scale bars are 10 μm.

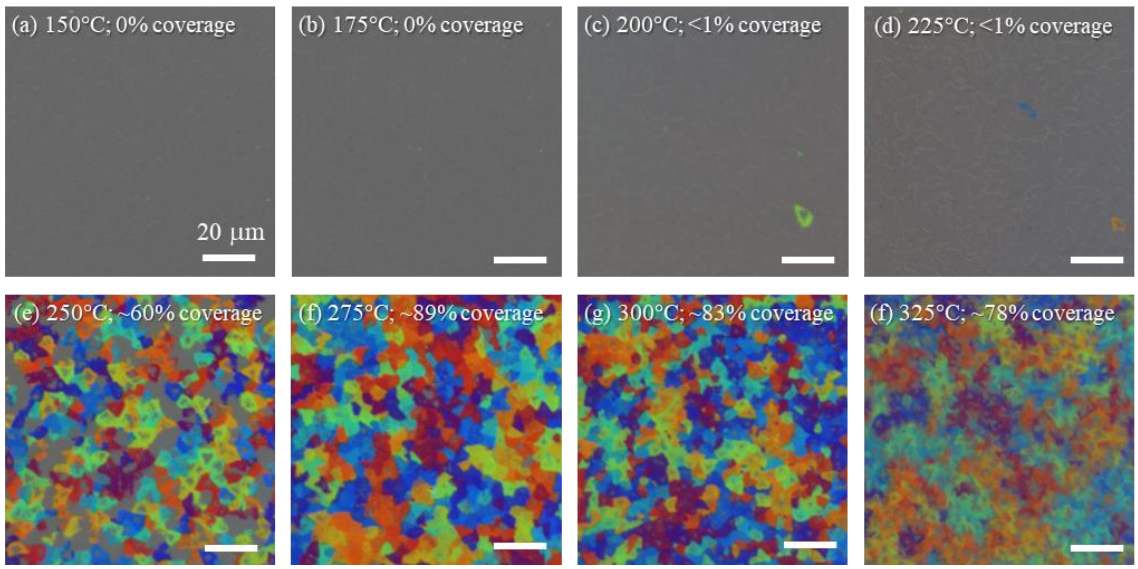

Figure A5.3. False-color cross-polarized images of the films plotted in Fig. 5.5a, showing the temperature-dependance of the PTCDA surface coverage, where the gray area indicates the bare MoS_2 substrate and each color represents a single orientation of PTCDA. See Chapter 6 for image processing details. All scale bars are 20 μm.

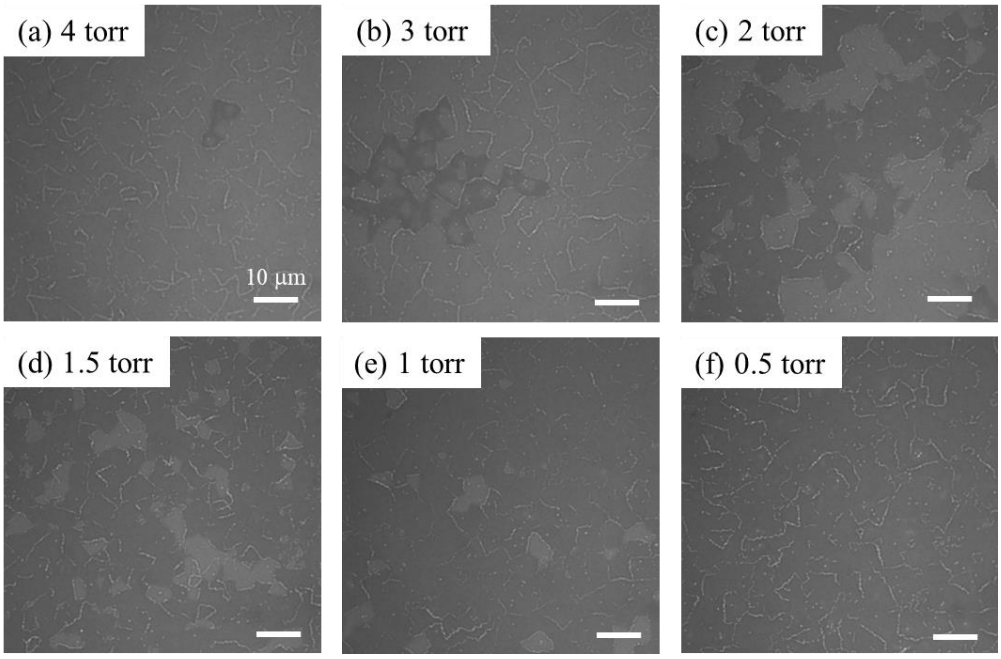

Figure A5.4. Optical images of films plotted in Fig. 5.5b, showing the pressure-dependance of PTCDA (dark regions) deposited on MoS_2 films (lighter regions). All scale bars are 10 μm.

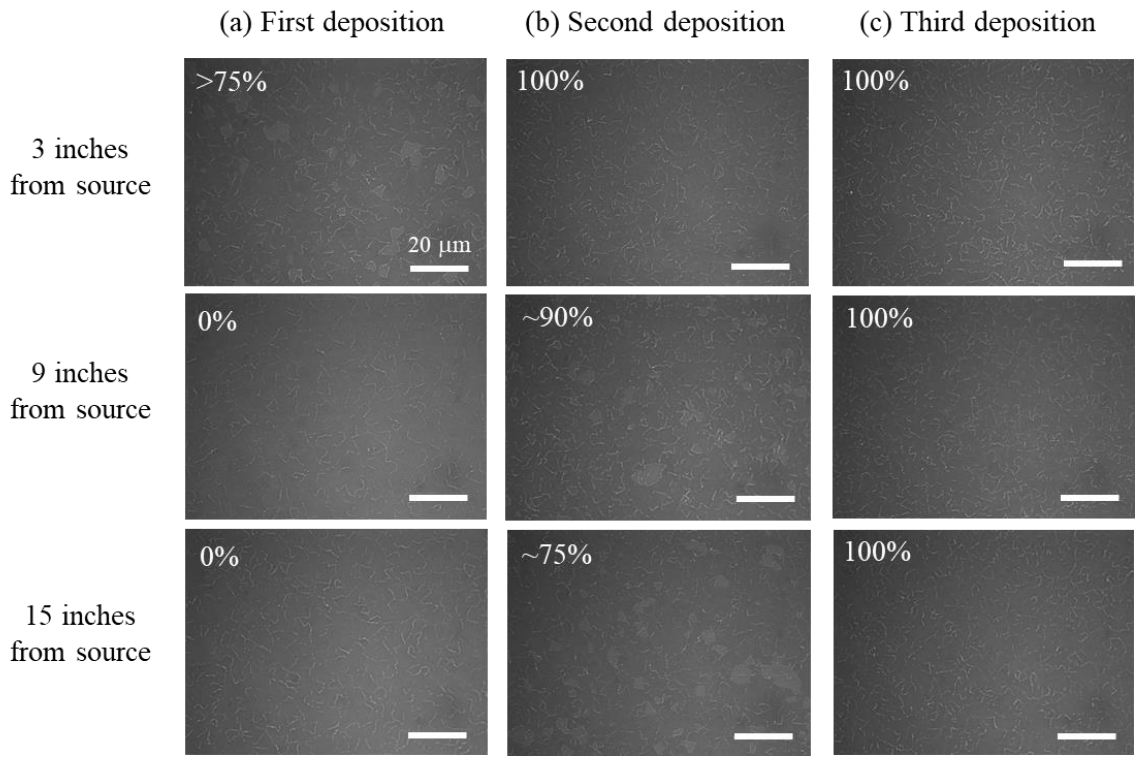

Figure A5.5. Optical images of subsequent depositions of PTCDA (lighter areas) deposited on MoS_2 films (darker areas) after reactor tube cleaning, where the substrates were placed at various distances from the source (increasing distance going down). Lighter patches indicate areas of bare MoS_2 substrate, and approximate surface coverages of PTCDA are listed in the top left corners of each image. All scale bars are 20 μm.

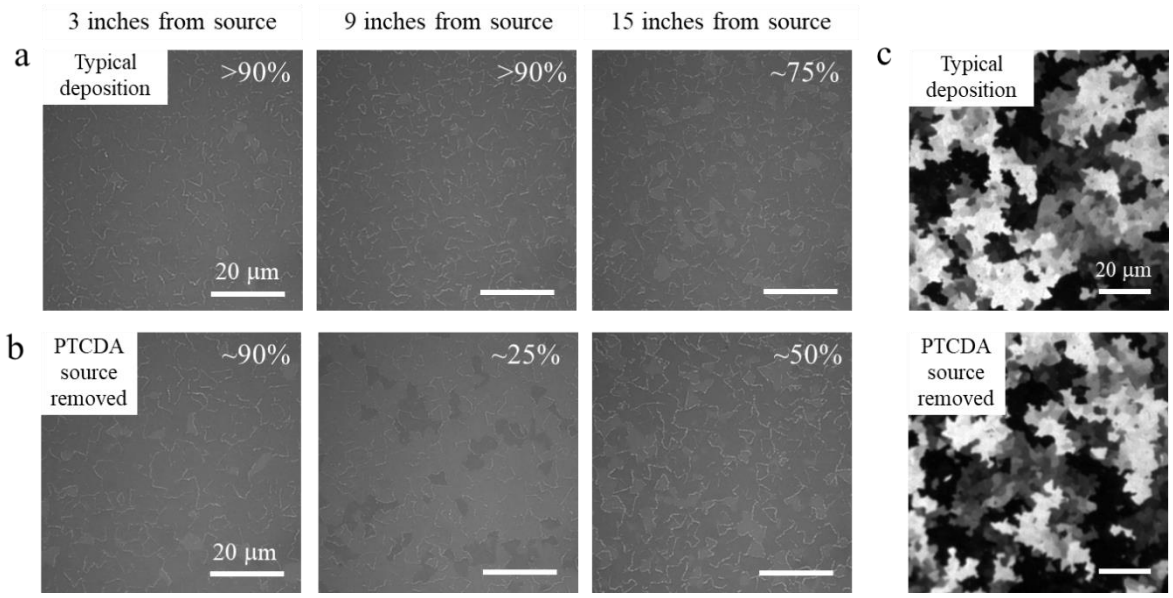

Figure A5.6. Optical images of PTCDA (lighter areas) deposited on MoS_2 films (darker areas) where the substrates were placed at various distances from the source (increasing distance going right), where (a) shows the coverage for one specific deposition condition, and (b) shows the coverage of that same condition repeated, except with the PTCDA source removed from the reactor. Approximate surface coverages of PTCDA are listed in the top right corners of each image. (c) shows cross-polarized images of the films shown in the first panels of (a) and (b). All scale bars are 20 µm.

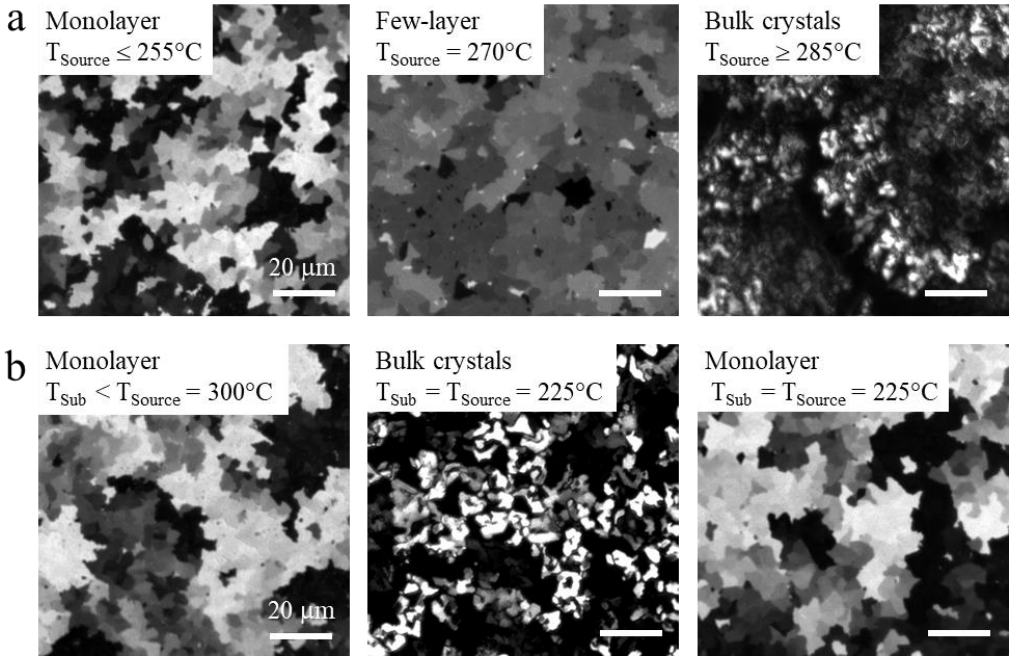

Figure A5.7. Cross-polarized images of subsequent deposition of PTCDA onto MoS_2 film, where different temperature gradients were used. a) The substrate was kept at 225°C, while the source temperature was increased, left to right. b) A temperature gradient was used (first panel), followed by a change to thermal equilibrium (second panel), which was repeated for a second time (third panel). For clarity, the thickness of the PTCDA is indicated in the top left of each image. All scale bars are 20 µm.

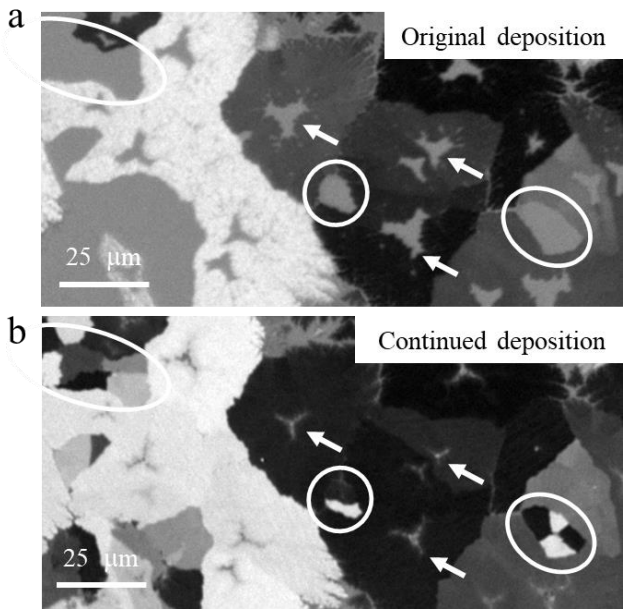

Figure A5.8. a) PTCDA deposited onto a partially-connected film of large MoS_2 triangles, and b) the same are after being put back into the reactor to continue depositing PTCDA. White arrows indicate holes in the center of PTCDA domains, and white circles indicate whole MoS_2 domains that were not covered with PTCDA in the original film.

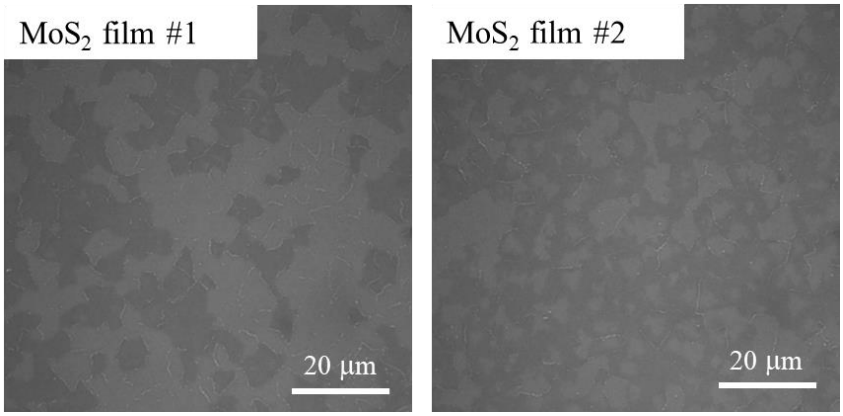

Figure A5.9. Two different MoS_2 substrates placed side-by-side in the same PTCDA deposition, where the left substrate predominately exhibits the domain-by-domain deposition behavior, and the right substrate predominately exhibits the edge-first deposition behavior.

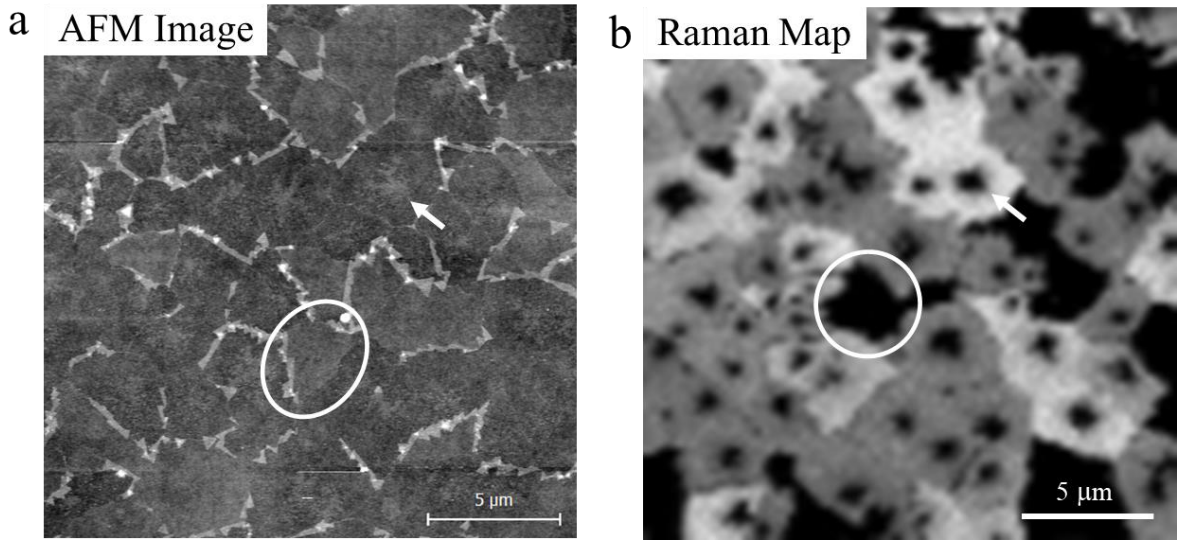

Figure A5.10. a) AFM image of a film of PTCDA deposited on an (overgrown) MoS_2 film, where the centers of the MoS_2 domains appear raised (white arrow) and some other MoS_2 domains appear taller than the surrounding area (white circle). b) Raman map of the film from (a) indicating that the raised features are actually areas void of PTCDA (hence, no Raman signal) and suggesting that the raised features in (a) are actually amorphous surface residues existing inside and between the PTCDA domains.

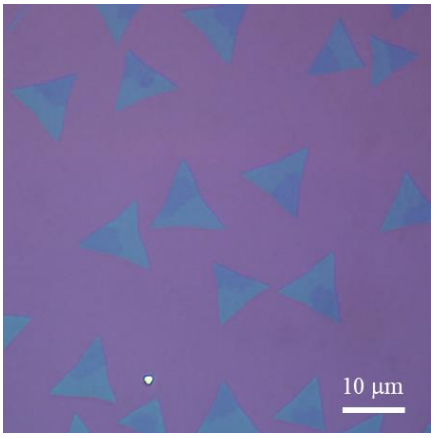

Figure A5.11. Optical image of PTCDA deposited on single-crystal islands of WS_2, where the PTCDA crystals (darker patches) appear to grow out from a single corner of each island.

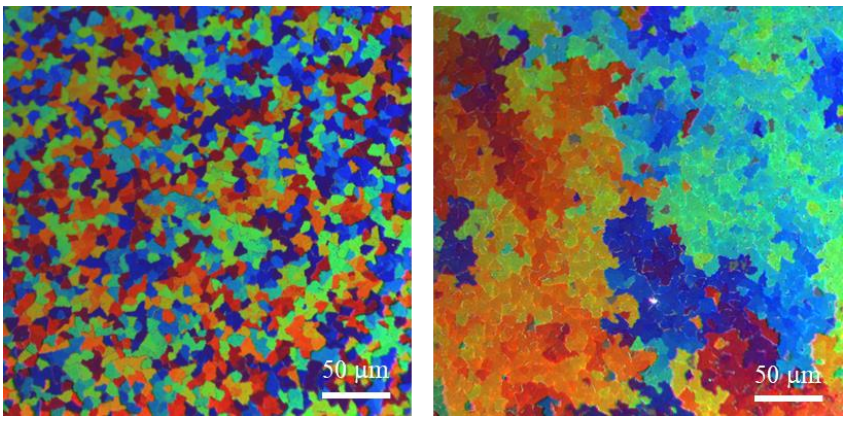

Figure A5.12. False-colored, cross-polarized images of two PTCDA depositions onto overgrown films of MoS_2, exhibiting uncorrelated (left image) and correlated (right image) domain distributions. Domains are color-coded to show the relative rotations of individual PTCDA domains (scale bar in Fig. 5.14, inset).

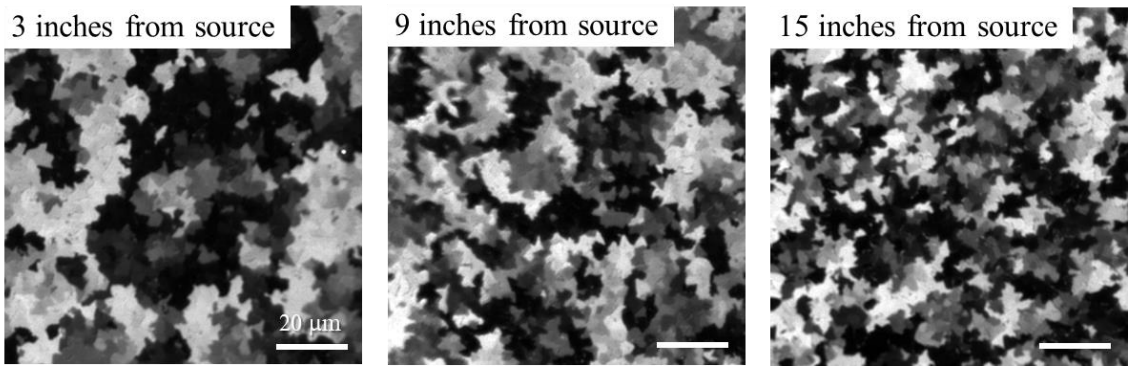

Figure A5.13. Cross-polarized images of PTCDA deposited on MoS_2 substrates placed at various distances from the source, showing a reduction in interdomain communication with increasing distance. All scale bars are 20 μm.

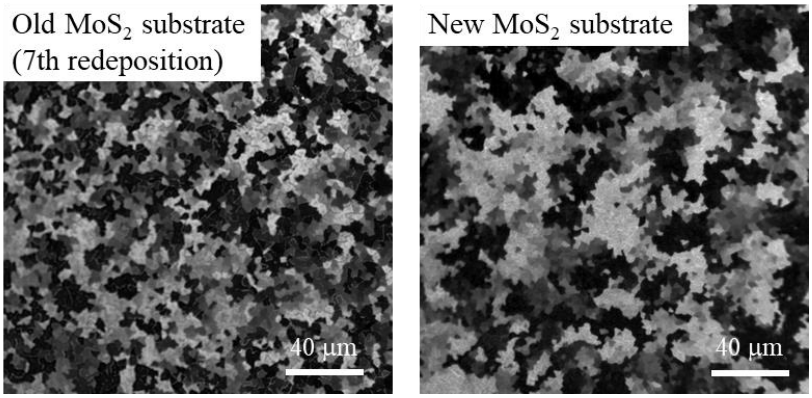

Figure A5.14. Cross-polarized images of PTCDA deposited on two MoS_2 substrates placed in the same deposition, where the left substrate was reused multiple times, and the right substrate was a new MoS_2 film.

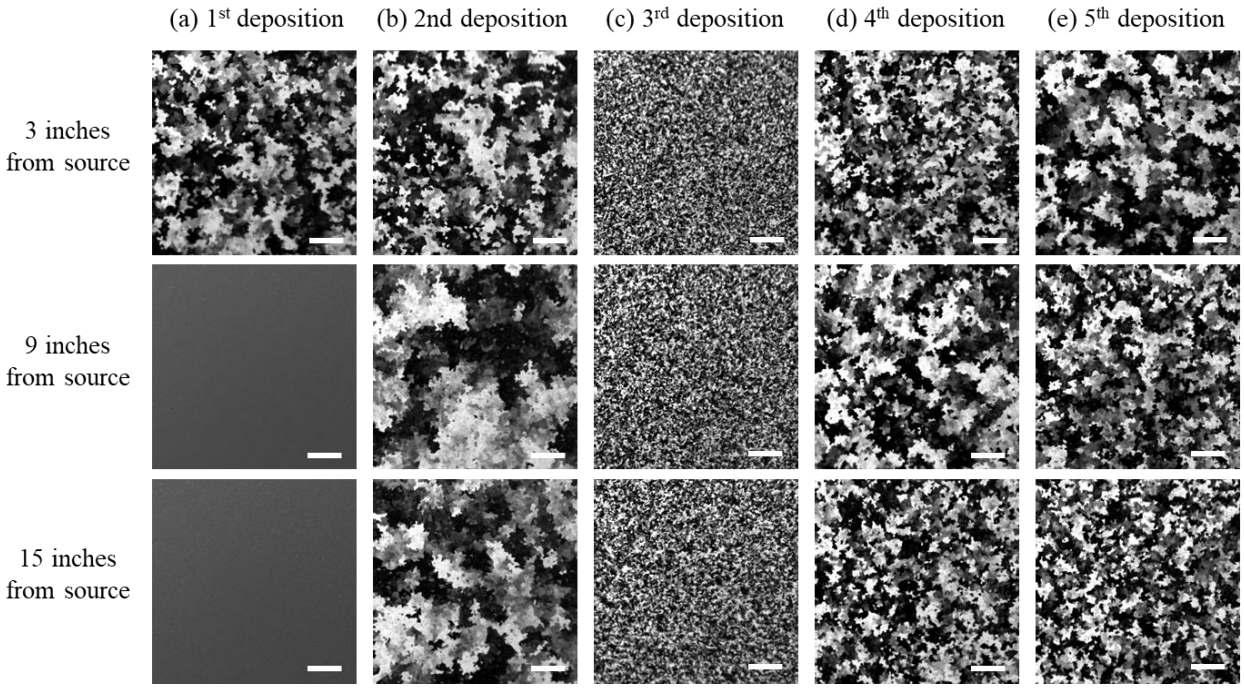

Figure A5.15. Cross-polarized microscope images of PTCDA films deposited on MoS_2 substrates placed at different distances to the source (rows), where the same deposition condition was repeated multiple times (columns) to track the change in PTCDA film morphology. The first deposition was carried out in a newly-cleaned reactor tube, and new MoS_2 substrates were used for each deposition. All scale bars are 30 μm.

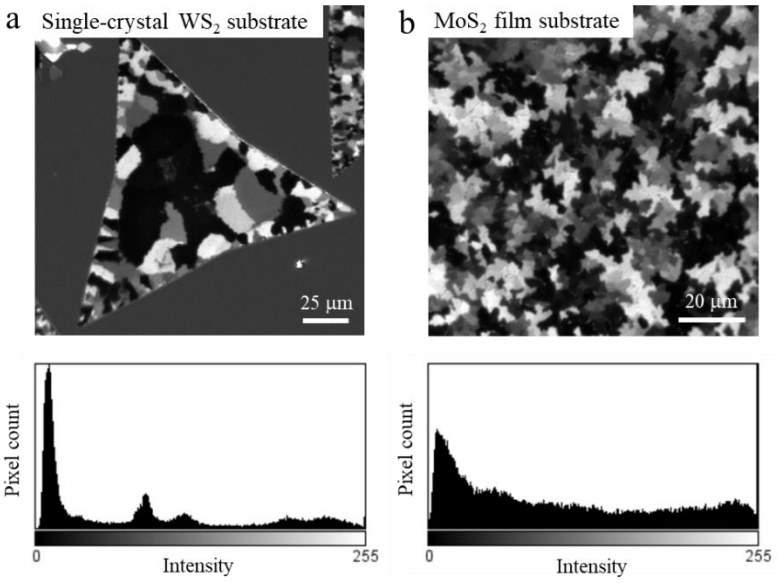

Figure A5.16. a) Cross-polarized microscope image of a single-crystal island of WS_2 that resulted in polycrystalline PTCDA deposition (top panel) and histogram showing the pixel area of the PTCDA film that correspond to a given intensity value, i.e., different orientations of PTCDA (bottom panel). b) Cross-polarized image of polycrystalline PTCDA deposited on a polycrystalline MoS_2 film (top panel), and similar histogram (bottom panel) to what was plotted in (a).

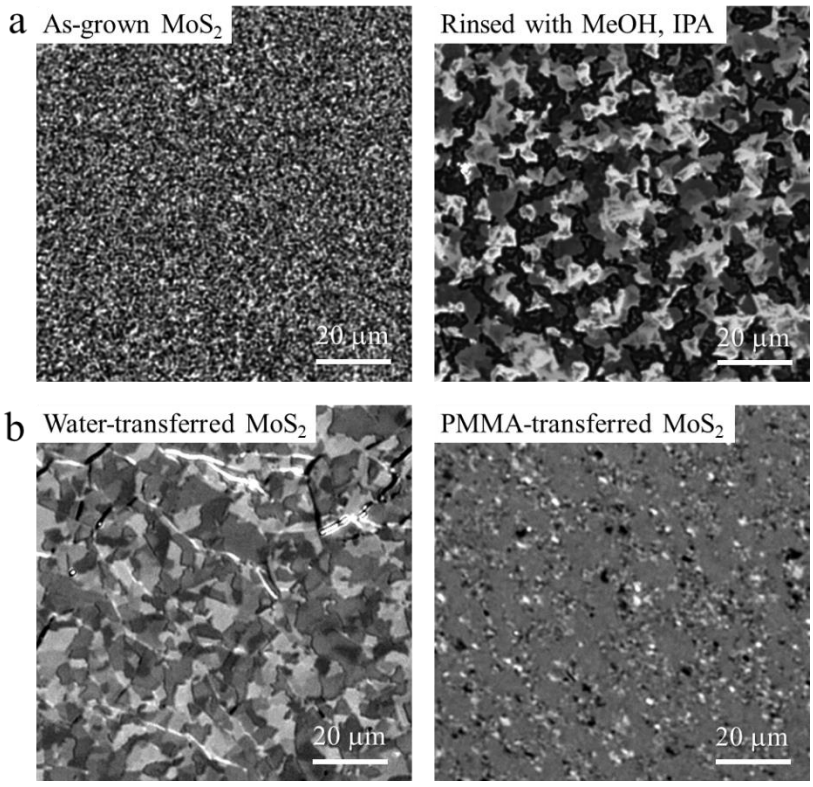

Figure A5.17. a) Effect of MoS_2 surface treatment on the morphology of the subsequent MPDI deposition, and b) effect of water-transfer (left panel) or polymer-transfer (right panel) of MoS_2 on the morphology of the subsequent PTCDA deposition.

5.8 References

(1) Kolasinski, K. W. *Surface Science: Foundations of Catalysis and Nanoscience*, Fourth edition.; Wiley: Hoboken, NJ, USA, 2019.

(2) Wu, B.; Zhao, Y.; Nan, H.; Yang, Z.; Zhang, Y.; Zhao, H.; He, D.; Jiang, Z.; Liu, X.; Li, Y.; Shi, Y.; Ni, Z.; Wang, J.; Xu, J.-B.; Wang, X. Precise, Self-Limited Epitaxy of Ultrathin Organic Semiconductors and Heterojunctions Tailored by van Der Waals Interactions. *Nano Lett.* **2016**, *16* (6), 3754–3759.

(3) Koo, S.; Park, I.; Watanabe, K.; Taniguchi, T.; Shim, J. H.; Ryu, S. Extraordinary Photostability and Davydov Splitting in BN-Sandwiched Single-Layer Tetracene Molecular Crystals. *Nano Lett.* **2021**, *21* (15), 6600–6608.

(4) Ni, J.; Wang, W.; Quintana, M.; Jia, F.; Song, S. Adsorption of Small Gas Molecules on Strained Monolayer WSe2 Doped with Pd, Ag, Au, and Pt: A Computational Investigation. *Applied Surface Science* **2020**, *514*, 145911.

(5) Homann, K.; Kuhlenbeck, H.; Freund, H.-J. N2 Adsorption and Dissociation on Thin Iron Films on W(110). *Surface Science* **1995**, *327* (3), 216–224.

(6) Zhao, H.; Zhao, Y.; Song, Y.; Zhou, M.; Lv, W.; Tao, L.; Feng, Y.; Song, B.; Ma, Y.; Zhang, J.; Xiao, J.; Wang, Y.; Lien, D.-H.; Amani, M.; Kim, H.; Chen, X.; Wu, Z.; Ni, Z.; Wang, P.; Shi, Y.; Ma, H.; Zhang, X.; Xu, J.-B.; Troisi, A.; Javey, A.; Wang, X. Strong Optical Response and Light Emission from a Monolayer Molecular Crystal. *Nat Commun* **2019**, *10* (1), 5589.

(7) Marchetto, H.; Schmidt, T.; Groh, U.; Maier, F. C.; Lévesque, P. L.; Fink, R. H.; Freund, H.-J.; Umbach, E. Direct Observation of Epitaxial Organic Film Growth: Temperature-Dependent Growth Mechanisms and Metastability. *Phys. Chem. Chem. Phys.* **2015**, *17* (43), 29150–29160.

(8) Kang, K.; Lee, K.-H.; Han, Y.; Gao, H.; Xie, S.; Muller, D. A.; Park, J. Layer-by-Layer Assembly of Two-Dimensional Materials into Wafer-Scale Heterostructures. *Nature* **2017**, *550* (7675), 229–233.

CHAPTER SIX

Structure-Property Relationships of Two-Dimensional Molecular Crystals

6.1 Introduction

Understanding how intermolecular interactions influence crystal structures is critical for designing and synthesizing molecular materials with desirable chemical and physical properties. In Chapter 4 we mentioned two challenges in engineering the structure-property relationships of 2D crystals, which are extremely difficult to synthesize and characterize due to their atomic thinness. We already addressed synthetic approaches that allow us to achieve single-atom-thick molecular crystals of various perylene derivatives over the wafter-scale, with crystal sizes in excess of 100 microns. In this chapter, we will address the second challenge by developing a set of hyperspectral microscopy techniques that allow us to characterize the polarized optical responses of ultrathin crystals while simultaneously providing information about the film morphology and crystal structure.

In Section 5.1, we briefly introduced the concept of optical anisotropy, wherein a material responds differently to light of different linear polarizations. In **Fig. 6.1** we illustrate this origin of this phenomenon more clearly. Polarized light is composed of an electric field that

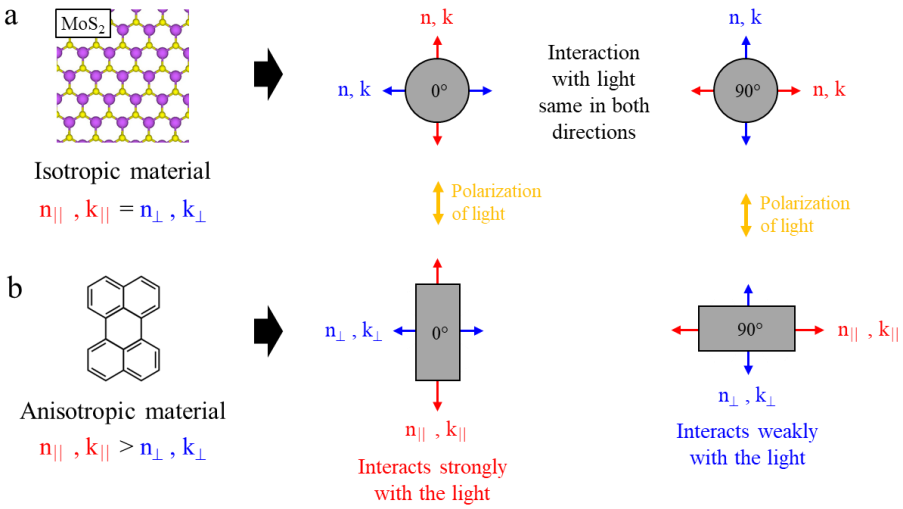

Figure 6.1. How a) an isotropic crystal such as MoS_2, and b) and anisotropic crystal such as perylene, of different orientations interact with polarized light.

oscillated in one direction (we are ignoring the magnetic field since most common materials are not magnetic). We represent the way in which this electric field responds to a material by using optical constants, such as the complex index of refraction, which are properties specific to a given direction along the material that also depend on the wavelength of the light. An optically anisotropic material is one that exhibits different complex refractive indices along different directions.

The complex refractive index, $N = n + ik$, has a real part, which is simply referred to as the refractive index, n, and an imaginary part, which is the extinction coefficient, k.[1] The (real) refractive index tells us how much a light is slowed down when passing through the material, which corresponds to a phase shift in the light wave. The extinction coefficient is indicative of how much light is attenuated by the medium, corresponding to a loss of intensity, usually through absorption. If n and k are the same along two orthogonal axes of a crystal (here, we are referring to these as the parallel, $||$, and perpendicular, $\perp$, axes), such as shown in **Fig. 6.1a**, then the reflection and transmission of polarized light from this material will be the same no matter how this crystal is oriented with respect to the polarization direction of the light. This is the case for 2D TMD materials with hexagonal symmetry, including MoS_2 and WS_2.

Most molecular crystals, however, are anisotropic in their shape. For this reason, the optical constants along the longer axis, or "major axis" (here, $n_{||}$ and $k_{||}$), are larger than those along the shorter axis, or "minor axis" (here, $n_{\perp}$ and $k_{\perp}$), as shown in **Fig. 6.1b**. More specifically, in the visible range that will be investigated in this thesis, $k_{\perp} = 0$ for perylene. This is because the absorption of a molecule at a particular wavelength is always polarized along one specific axis, which happens to be the long axis of perylene for the visible range (the short axis absorbs at much shorter wavelengths—in UV).[2] For the refractive index, on the other hand, both

$n_{||}$ and $n_{\perp}$ will generally be nonzero across the entire spectral range, although the values are expected to be extremely small for a single-atom-thick crystal. Throughout this thesis, we will always choose the major axis of the crystal to be the axis where we observe polarized light to experience the greatest refraction and absorption, and the minor axis to be exactly orthogonal to that. It is important to recognize, however, that this major axis is actually the major axis of the crystal's *unit cell* and does not necessarily coincide with the major axis of the constituent molecule. This happens when there is more than one molecule in the unit cell, in which case, the major axis of the crystal is determined by the directions of the major axes of all constituent molecules in the unit cell, as we will see later in this chapter.

The property of a material that experiences different (real) refractive indices in orthogonal directions, such as the one shown in **Fig. 6.1b**, is referred to as linear birefringence (LB), which is calculated as $n_{\perp} - n_{||}$. The corresponding anisotropic property for the absorption coefficient is called linear dichroism (LD), or $k_{\perp} - k_{||}$. Optically anisotropic materials exhibit one or both of these properties. The consequences of this differential refraction and absorption along different directions is that an incoming light wave of a given polarization will experience a polarization change when passing through a material that exhibits LB and/or LD. The extent to which the polarization is changed depends on the angle that the major and minor axes of the crystal make relative to the polarization direction of the incident light. Therefore, by changing the structure of a crystal, we can change the way that crystal interacts with polarized light.

In this chapter, we will show how the various functionalized derivatives of perylene introduced in Chapters 4 and 5 form 2D crystals with unique structural characteristics, which manifest as large differences in their polarized optical properties. We will start by investigating the structure of each crystal using nanoscale imaging and diffraction techniques and extend that

to visualizing the structure of the domains on the film-scale using various microscopy measurements based on polarized light. We further explore the spectral responses of the 2D crystals in the visible regime and correlate their macroscopic polarization-dependent properties to their nanoscopic crystal structures. We will also touch on our preliminary efforts in trying to extract values for the optical constants of these 2D molecular crystals from the polarized microscopy data.

6.2 Structural Characterization of Molecular Monolayers

6.2.1 Film Thickness

When characterizing the thickness of polycrystalline films, we want to know both the thickness of each individual crystal, as well as the average thickness over a larger scale. **Figure 6.2** shows an atomic force microscopy (AFM) image of a monolayer MoS_2 film before and after the deposition of PTCDA. The bright lines in the image of the bare MoS_2 film (left panel) indicate the edges of individual MoS_2 domains. This happens because the AFM tip interacts differently with the defect-rich domain boundaries than it does with the basal plane of the MoS_2, allowing us to sometimes trace out the edges where domains meet. After the deposition of a (partial) PTCDA film, we can see that some areas of the film have increased in height uniformly (right

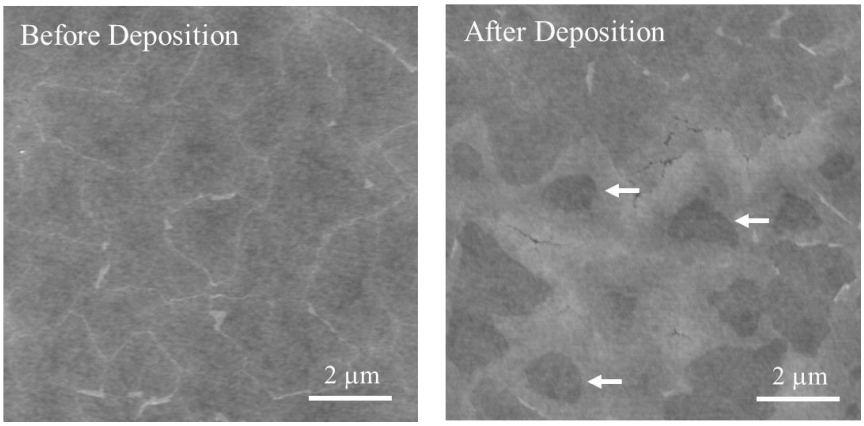

Figure 6.2. AFM of an MoS_2 films before (left) and after (right) PTCDA deposition. The darker regions in the right panel correspond to areas void of PTCDA, and the white arrows point out holes in some PTCDA domains.

panel). Using the aforementioned observation that the bright lines indicate MoS_2 domain boundaries, we can see that this particular film exhibits both the edge-first and domain-by-domain deposition behaviors (described in Chapter 5), where some MoS_2 domains have holes in the center that are void of PTCDA (white arrows), while others are completely uncoated with PTCDA (top region of image). We have seen from **Fig. A5.1** that line profiles across these PTCDA domains confirms that they are all monolayer, with a thickness of ~0.4 nm, indicating that the perylene molecules are lying flat on the TMD substrate. A MoS_2 film fully-coated with PTCDA looks completely uniform, indistinguishable from a bare MoS_2 film.

While AFM measurements give clear information about local crystal thickness, we would ideally like to know how uniform the thickness is over the films scale. We can do this by creatively applying a measurement usually used to determine the lattice spacings of bulk crystals—grazing-incidence wide-angle x-ray scattering (GIWAXS). Previous works have used GIWAXS to measure the d-spacing of TMD films prepared using a layer-by-layer stacking technique.[3] We can perform a modified version of this process, depicted in **Fig. 6.3a**, by first depositing molecular films (pink) on many TMD monolayers (green) and then stacking those on top of each other to make a hybrid superlattice of alternating TMD and molecular layers. We can further alter the number of

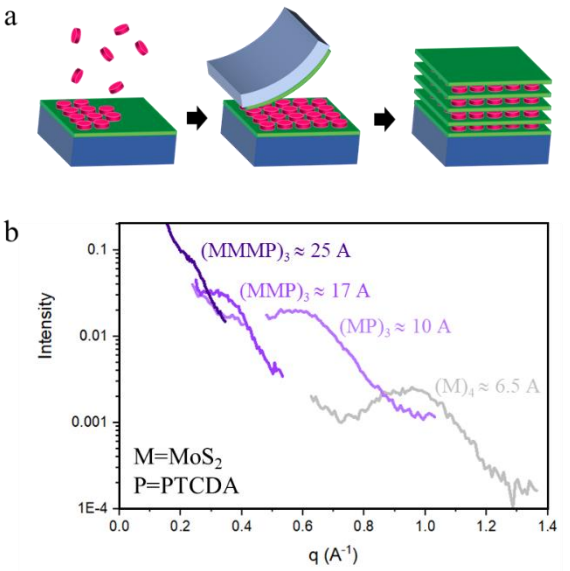

Figure 6.3. a) Process for the formation of PTCDA/MoS_2 superlattices via deposition on MoS_2 followed by stacking, and b) GIWAXS of PTCDA/MoS_2 superlattices composed of one molecular layer sandwiched between one, two, or three MoS_2 layers (purple lines), with a pure MoS_2 superlattice shown for comparison (gray line).

TMD layers in each stack, forming superlattices consisting of one TMD and one molecular layer, two TMDs and one molecular layer, or three TMDs and one molecular layer. By comparing the integrated GIWAXS signal of these various superlattices (**Fig. 6.3b**, purple lines) with a pure MoS_2 superlattice (**Fig. 6.3b**, gray line), we can see how much the d-spacing of MoS_2 increases from the presence of a single PTCDA layer (i.e., here, we are measuring the distance between the planes of Mo atoms in the direction normal to the basal plane of the stack). The results in **Fig. 6.3b** indicate that the average thickness of the molecular film over the millimeter-scale measurement area is ~3.5 Å, consistent with the AFM measurements and indicating that the molecular films are indeed of uniform, monolayer thickness.

6.2.2 Molecular Ordering

In order to gain information about the local ordering of our 2D molecular crystals, we perform scanning tunneling microscopy (STM) measurements. These measurements were carried out using an Omicron VT-UHV AFM/STM with the assistance of Nathan Guisinger at the Center for Nanoscale Materials at Argonne National Lab. We have tried numerous sample preparation procedures for the STM measurements, and the procedure that gave the best result is as follows. The molecular crystal films were deposited on MoS_2 grown on SiO_2/Si, using the normal procedures. A 200 nm film of Au(111) on Mica (purchased from Phasis) was loaded into the UHV chamber and subjected to many cycles of Ar sputtering (20 min, 6.0×10^{-6} mbar) followed by annealing (20 min, 500°C). This substrate was then unloaded from the UHV chamber, and the molecular crystal/MoS_2 film was immediately transferred onto the surface using the water-based transfer method, in order to keep the surface of the film as clean as possible. The sample was then immediately loaded back into the UHV chamber. Molecular-resolution images typically cannot be achieved unless the sample is annealed overnight at 80-

100°C. Although we are able to image at room temperature, the imaging is significantly easier at low temperatures (55 K).

In general, the imaging is extremely challenging, even when using the sample preparation procedures described above. One reason for this is the presence of surface adsorbates, which is difficult to avoid given that the samples that are not directly prepared in UHV. Minimizing the amount of time that the film sits out of vacuum appears to help, which is why we perform the water transfer and sample loading as soon as possible once the film is removed from the deposition chamber. In working with Yu and Chang, *et al.*,[4] we also learned that the image quality of solution-processed 2D metal-organic frameworks can be drastically be improved even without annealing after loading into the STM chamber, simply by keeping the sample under UHV conditions for many days. Although all the STM data present in this thesis were taken in UHV, we have also devoted much time to ambient STM imaging of these molecular films. Unfortunately, we were never successful in imaging the molecules. Since we find that it is actually possible to image bare MoS_2 in air with some difficulty, we think that the issue in ambient imaging of the molecules is mainly due to the instability of the molecular films—i.e., the molecules or other surface adsorbates continually being pushed around and building up on the STM tip. On UHV instruments, we are able to clean the tip using large pulses of bias voltage, which appears to be necessary for achieving molecular-resolution images.

The formation of nanoscale bubbles in the molecule/TMD film from the transfer process is another big issue with the STM imaging. This effect is largely unpredictable, since it likely depends on the surface properties of the MoS_2 film, which as we know from Chapter 3 are difficult to control. Any factors that affect the interface properties between the MoS_2 and the Au could also contribute to the bubbling, including contaminants present in the transfer water or

residues on the Au/Mica before the transfer. We do have evidence that using freshly-annealed Au/Mica seems to help this issue, which is given in **Fig. A6.1**. **Fig. A6.1a** shows a large-scale STM image of a MPDI/MoS_2 film water-transferred to Au/Mica that was used newly-opened from the manufacturer, but not sputter-annealed or H_2 flame-annealed immediately before transfer. If we compare this to the PTCDA/MoS_2 film in **Fig. A6.1b**, which was sputter-annealed with Ar immediately before transfer, we see that the film sample exhibits significantly less bubbling, with >100 nm flat regions. Although there were other differences between the preparation procedures of these two samples, we believe from other transfer processes that we have tried that the major difference here is that cleaning the Au surface immediately before transfer helps remove organic residues, allowing for the TMD film to better "wet" the surface and hence minimize bubble formation. Avoiding the transfer step altogether would be ideal, but this is difficult since it would require the direct growth of the TMD film on an ultraflat, high-temperature-stable, electrically conducting substrate that also has very large terrace sizes.

Figure 6.4a shows the molecular-resolution STM images of our PDI, MPDI, and PTCDA films, with the unit cells overlaid in the bottom-left of the images. The corresponding fast Fourier transfer (FFT) patterns of the corresponding images are shown in **Fig. 6.4b**. We can see that the structures of each crystal are quite different, despite being formed from similar monomers. The crystal structures are reproduced more clearly in **Fig. 6.5**. The molecular crystals exhibit three very distinct structures: brick wall for PDI, canted for MPDI, and herringbone for PTCDA. These phases are among those commonly observed for monolayers of perylene derivatives deposited on bulk materials in ultrahigh vacuum.[5,6] The noteworthy differences between these three types of ordering are summarized in **Table 6.1**, with the full lattice parameters tabulated in **Table A6.1**.

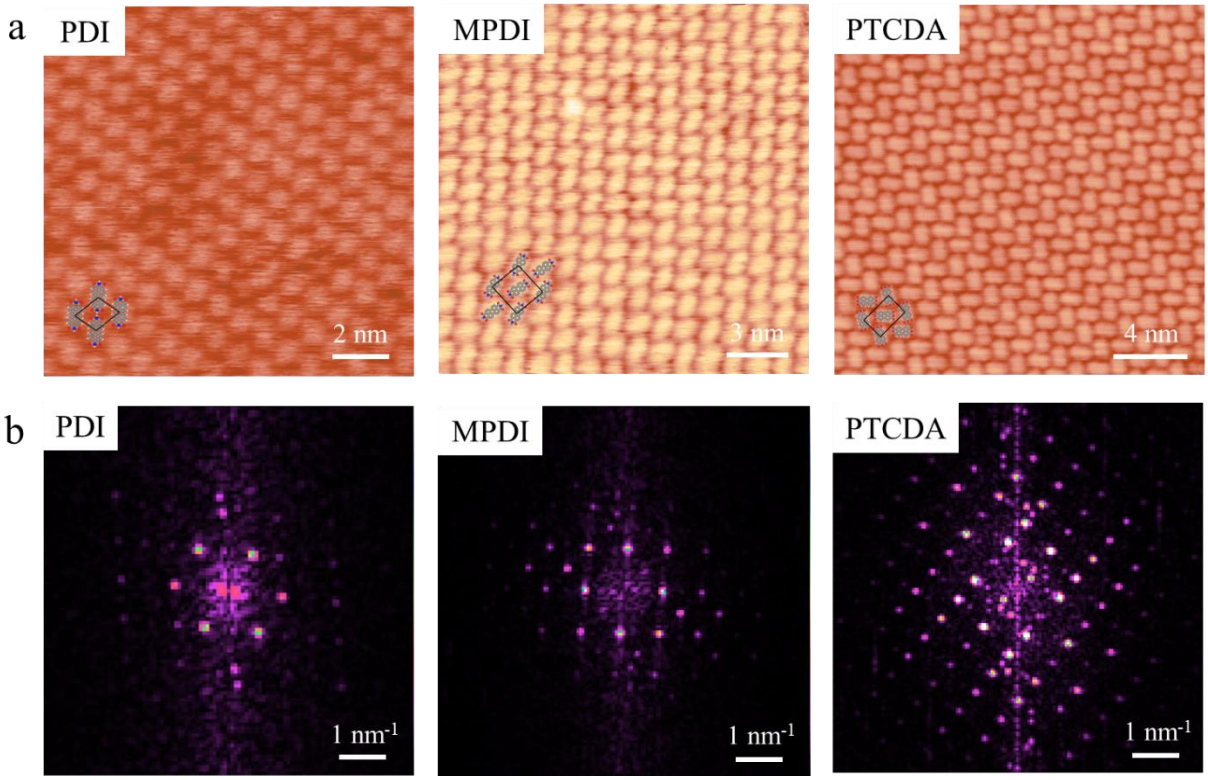

Figure 6.4. a) Molecular-resolution STM images of PDI, MPDI, and PTCDA molecular crystals deposited on MoS_2 taken in constant current mode, and b) FFTs of the images in (a). Unit cell of each crystal is overlaid on the STM images in (a). Imaging conditions were as follows: for PDI, V_{bias} = -1 V and current setpoint = 100 pA; for MPDI, V_{bias} = +2 V and current setpoint = 100 pA; and for PTCDA, V_{bias} = -0.8 V and current setpoint = 50 pA.

From our STM measurements, as well as the optical studies presented later in the chapter, we find that each molecular crystal film appears to form as largely a single phase, which are the phases depicted in **Fig. 6.5**. The phases that we observe for each molecule appear to be among the more stable phases for that particular functionalized derivative. For example, we can start by considering the defining structural difference between these three crystals, which is the angle between the molecules, γ (indicated with blue arrows on the schematics in **Fig. 6.5**). We can see that the molecules in the PDI domains all have their long axes pointed in the same direction (γ = 0°), while half of the molecules in the MPDI and PTCDA domains are angled differently, with γ ≈ 29° for MPDI and γ ≈ 72° for PTCDA.

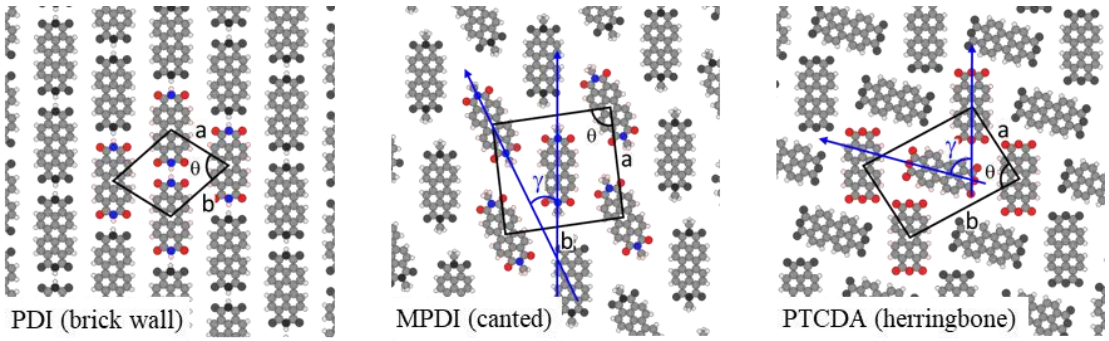

Figure 6.5. Schematics of the unit cells of PDI, MPDI, and PTCDA molecular crystals.

	PDI	MDPI	PTCDA
Phase	Brick wall	Canted	Herringbone
Packing density (molecules/nm^2)	0.99	0.77	0.87
Angle between molecules, γ	0°	29°	73°
Molecules per unit cell	1	2	2

Table 6.1. Structural features of the PDI, MPDI, and PTCDA molecular crystals.

For PTCDA, the herringbone phase, which is characterized by the nearly-perpendicular (i.e., end-to-side) orientation between molecules, is the most commonly observed in STM studies. This is because the strong **O**···H-C hydrogen-bonding tries to maximize the number of oxygen atoms near the hydrogens on the perylene core.[7] For PDI, a more parallel orientation is preferred, since the **N**-H···O=C hydrogen bonds require the hydrogen atom on the nitrogen to be close to the corner oxygens.[7] Thus, these molecules more commonly form the canted or brick-wall structures. Although the brick-wall (i.e., end-to-end) structure is thought to be less stable than the canted phase,[5] that is the structure we observe. We will note, however, that the STM images are not so clear in the case of PDI, so it is possible that the molecules could be tilted at some small γ that is not observable from the FFT analysis. For MPDI, both the end-to-end and end-to-side structures are impeded by the presence of the bulky methyl groups, and the molecules are forced into a canted structure that allows at least some hydrogen-bonding between the between the oxygen atoms and the core hydrogens.

Another noteworthy observation is that the packing density of the crystal domains is different, being the greatest for the PDI, followed by PTCDA, and then MPDI. The low density

of MPDI is expected, since the bulkier methyl groups prevent closer packing of the molecules. The final distinguishing structural characteristic between these three films is the number of molecules per unit cell. This is a natural consequence of this molecular tilting, since only parallel molecules, such as is the case with PDI, can have a single-molecule unit cell. The canted and herringbone phases of MPDI and PTCDA both contain two molecules.

Hence, we can see that small differences in the structures of functionalized perylene molecules can drastically impact the nature of their intermolecular forces, promoting different types of packing inside the crystal. Each of the characteristics listed in **Table 6.1**—packing density, angle between molecules, and number of molecules per unit cell—plays a unique role in determining the macroscopic optical response of these molecular crystal films, as we will see in Section 6.6.

6.3 Techniques for Visualizing Morphologies of Polycrystalline Films

6.3.1 Raman Mapping

Any characterization technique that used a polarized excitation can be used to observe the morphology of optical anisotropic materials. Raman mapping is one way to visualize the morphology of a polycrystalline film while simultaneously collecting chemical information about the system. This is because crystals with different orientations will absorb the polarized laser to different extents, leading to a stronger Raman signal for domains with the stronger absorption. By sweeping the laser over an area of the film and taking a spectrum at each point, we can identify a single-crystal domain as one with a uniform Raman response. Hence, this measurement can serve as an indirect observation of the LD of a material. Of course, thicker crystals will also produce stronger Raman signals, so this technique is only useful in cases where

the thickness of the film is constant, which is the case for 2D materials such as the molecular crystals studied in this thesis.

Figure 6.5a shows a Raman (point) spectrum of a monolayer PTCDA crystal on MoS_2, taken with a Horiba confocal Raman microscope with a 532 nm excitation. The peaks marked with green stars correspond to the MoS_2 Raman peaks, the blue star marks the primary Si Raman feature, and the PTCDA Raman peaks can be identified by the reference spectrum of bulk PTCDA in the upper right inset (bulk spectrum was taken with a 475 nm excitation, to avoid overlap with the photoluminescence features). From these spectra, we can conclude that the 2D crystals we have deposited are indeed PTCDA and that the deposition process does not oxidize or chemically change the molecules during heating. We have further confirmed that the MoS_2 is also not oxidized during the deposition by performing x-ray photoelectron spectroscopy (XPS) measurements before and after PTCDA deposition (see Chapter 7, **Fig. 7.2**).

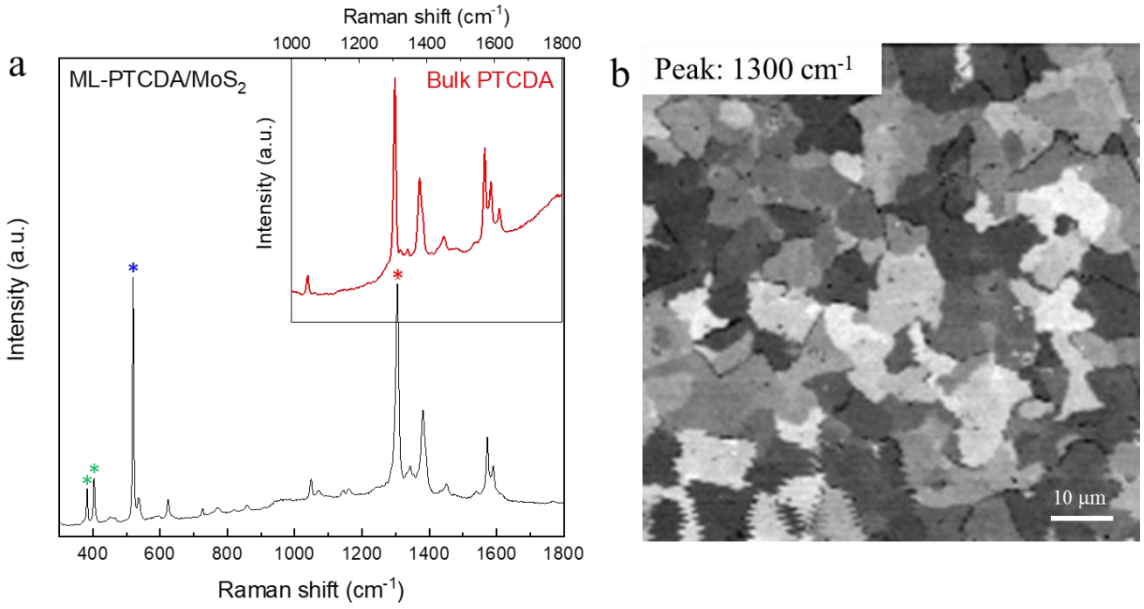

Figure 6.6. a) Raman spectrum of a monolayer PTCDA crystal on MoS_2 (black line), with the spectrum for bulk PTCDA given in the inset (red line). Green stars mark the Raman peaks for MoS_2, blue star for Si, and red star for the PTCDA Raman feature used to generate the map in part (b), and b) Raman map of a monolayer PTCDA film on MoS_2, imaged using the Raman mode at 1300 cm^{-1}.

We can further chart the spatial change in the intensity of the strongest Raman feature at 1300 cm^{-1} (indicated with a red star) by rastering the laser (~1 μm spot size) over the sample, with a step size of 0.5 μm. This data is shown in the 80 x 80 μm Raman map in **Fig. 6.5b**. The morphology of the film looks similar to what we observed throughout Chapter 5—single-crystal patches of PTCDA that are few to 10 μm in diameter. We can perform similar measurements to confirm the chemical nature and morphology of the MPDI and PDI molecular crystal films, which are shown in **Fig. A6.2** and **Fig. A6.3**, respectively.

Although Raman mapping is a convenient technique for simultaneously collecting chemical and structural information about a crystalline film, measurements that involve raster scanning take an extremely long time to collect a single image (~40 minutes for the map in **Fig. 6.5b**), and are subject to drift and other types of interference over such long time scales, which can be seen from the jaggedness in the bottom left of **Fig. 6.5b**. Furthermore, Raman spectroscopy involves the measurement of the inelastic scattering of photons, which are events that occur with low probability, and consequently, produce low signal. For this reason, the measurement requires the use of high-power lasers, which actually degrade molecular materials (either due to sublimation or oxidation of the molecules), resulting in a loss of Raman signal over time. Since our crystals are only one molecule thick, we actually find that the same area cannot be mapped twice using Raman.

6.3.2 Configurations for Polarized Microscopy

A higher-throughput and less destructive method for visualizing polycrystalline films of optically-anisotropic materials is through the use of reflection-based microscopy techniques. Reflectance measurements are more direct manifestations of absorption and refraction phenomena compared to scattering or emission techniques, where the polarization dependance is

only related to the absorption (i.e., LD) and cannot give any insight into the LB of the material. Furthermore, the signal intensity is strong enough to use a lower-power lamp source, enabling imaging without film degradation, and the wide-field nature of the measurement allows for extremely short measurement times—on the order of second to minutes. Lamp-based imaging techniques also allow changing of the excitation wavelength, λ, allowing us to build a complete understanding of a material's light-matter interactions in a significant range of energies (in our case, visible wavelengths). The particular approach implemented here is a variation of cross-polarized microscopy, which is widely used to observe materials with anisotropic optical properties such as liquid crystals,[8,9] bulk molecular crystals,[10–12] and anisotropic 2D materials.[13] Our specific instrumental geometry is described in **Fig. A6.4**.

Figure 6.7 illustrates the general working principles behind cross-polarized microscopy. An unpolarized light source is passed through a polarizer and shone on the surface of an optically anisotropic film sitting on an isotropic substrate. The substrate, which is much thicker than the film, reflects the majority of the incident light, reducing its intensity but maintaining its polarization (i.e., large vertical arrows → smaller vertical arrows). Because the film is optically anisotropic, it causes a polarization change in a small portion of the reflected light due to the LD and/or LB of the film (i.e., large vertical arrow → thinner, rotated arrows). By passing the light through a second polarizer (called the "analyzer") that is oriented exactly perpendicular to the first polarizer, we can filter out all of the light that did not experience a polarization change.

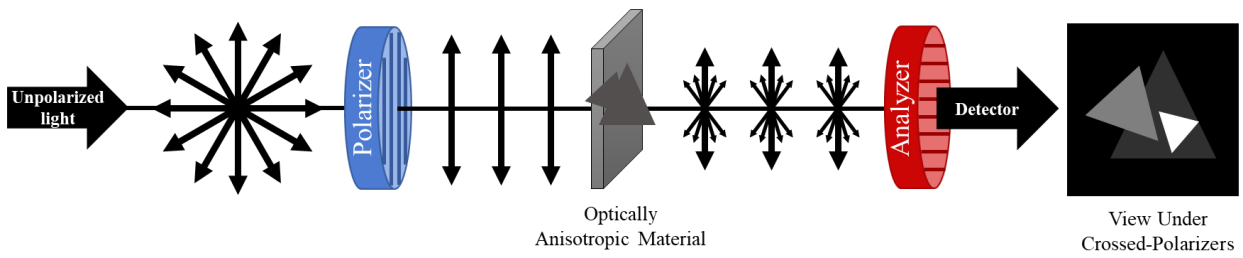

Figure 6.7. Working principles of cross-polarized microscopy.

Because domains in the film will rotate the incident light by different amounts depending on the angles of their major/minor axes, each will project different intensities onto the analyzer. The result is that domains that caused more change to the incident light polarization appear brighter, while those that caused no change (including the substrate) appear dark. As alluded to earlier, the measurement approach we mainly apply in this thesis is a *variation* of this cross-polarized technique described above. Actually, we apply a combination of three different instrumental geometries in order to build a thorough understanding of the polarized optical responses of our various 2D crystals and relate that to their structural properties. The three geometries—single-polarizer, crossed-polarizer, and titled-analyzer—are described in **Fig. 6.8**.

A single-polarizer reflectance measurement (**Fig. 6.8a**) is actually the traditional geometry for visualizing molecular crystals and polymer films and measuring their optical constants.[14–16] This setup is the same as is shown in **Fig. A6.4**, except without the analyzer. Here, polarized light is shone on the sample, and everything reflected back is detected. The approach works well for materials that are significantly thicker than the substrate, but, as introduced in **Fig. 6.7**, the light reflecting by an atomically-thin film is dominated by the substrate on which the film is supported. For example, let us suppose that we shine s-polarized light on a film of 2D molecular crystals deposited on a TMD that sits on a fused silica substrate. The orientation of the polarizer (P) is given by the direction of the red arrow in **Fig. 6.8a** (left panel), and the angle that the major axis of a molecular crystal domain makes with the polarizer is θ_c. We define a clockwise rotation of the crystal to be a positive θ_c.

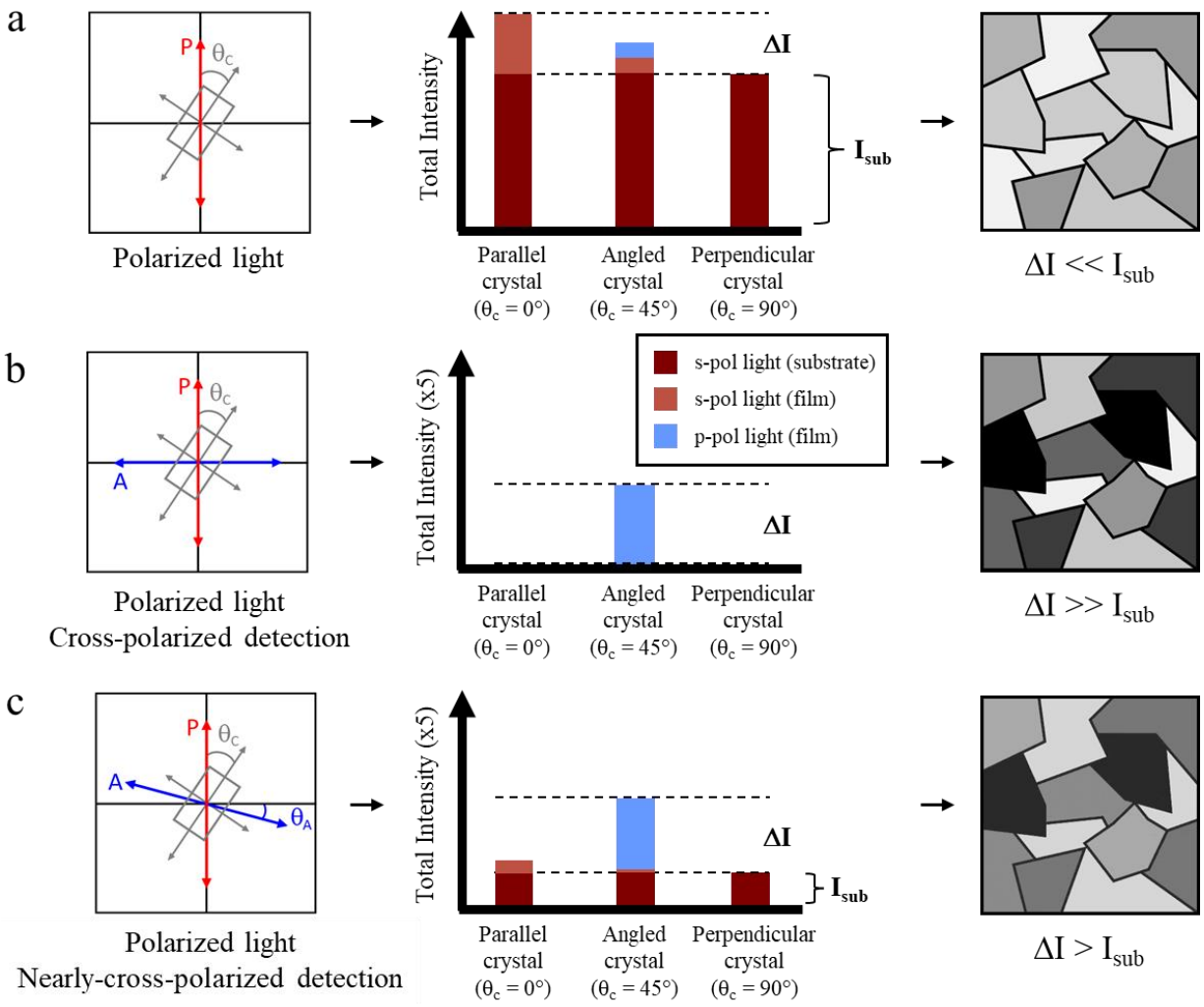

Figure 6.8. Understanding the origin of the optical contrast from optically anisotropic films viewed under a) a single-polarizer geometry, b) a cross-polarized geometry, and c) a tilted-analyzer geometry. Red arrows indicate the orientation of the polarizer, blue arrows indicate the orientation of the analyzer, and gray arrows indicate the orientations of the major and minor axes of the molecular crystal unit cell. The schematic graphs illustrate the contribution of both the isotropic substrate (I_{sub}) and the anisotropic crystal (ΔI) to the total detected intensity, with the s-polarized contributions depicted in red, and the p-polarized contributions depicted in blue. The magnitude of the optical contrast is determined by the ratio of anisotropic response, ΔI, to the isotropic background, I_{sub}.

Note that θ_c is the major axis of the *unit cell*, and so it is not necessarily aligned with the major axis of any single molecule when there is more than one molecule in the unit cell.[14] This is more clearly illustrated in **Fig. A6.5**, which relates the major and minor axes of the unit cells for PDI, MPDI, and PTCDA crystals (from the STM images in **Fig. 6.4**) to the major and minor axes

of their constituent molecules based on the angles between them. We will also make one oversimplification in describing our three instrumental setups: although we will find later that these molecular crystals exhibit both LD and LB, we will ignore the refraction along the major and minor axes of the crystals for most of this chapter (since we already know the absorption to be the dominant contribution to the response). We will also assume, for the description in **Fig. 6.8**, that the absorption is polarized along the major axis, since we know that the minor axis does not absorb at the wavelengths that we will use later in our experimental studies. For this reason, we define θ_c with respect to the major axis only.

The middle panel of **Fig. 6.8a** schematically depicts the reflected intensities (in a single-polarizer configuration) from crystal domains with different orientations (i.e., different θ_c), broken down by the various contributions to their total intensities (see color key in the middle panel of **Fig. 6.8b**). Because the major axis interacts with the light (i.e., through absorption), light polarized exactly along the major axis experiences an intensity change. As a result, a crystal with its major axis exactly parallel to the light polarization ($\theta_c = 0°$) reflects a small amount of the s-polarized light (light red bar), while the substrate reflects a large amount of s-polarized light (dark red bar). Because the minor axis does not absorb light at these wavelengths, a crystal with its major axis exactly perpendicular to the light polarization ($\theta_c = 90°$) reflects none of the s-polarized light.

If the major axis is oriented at any other angle ($0° < \theta_c < 90°$), then we can break up the incident light into two orthogonal vectors oriented along the major and minor axes of the crystal. The component of the light oriented along the major axis will experience an intensity change, while the component along the minor axis will not. Summing these two vectors back up results in a vector that is rotated with respect to the original light wave. In other words, a material that

has different extinction coefficients (k) for the major and minor axes changes the polarization of linearly polarized light, and the extent of the polarization change depends on θ_c. Hence, the resulting reflection from these domains contains a mixture of both s-polarized light and p-polarized light (light blue bar), with the maximum amount of p-polarized light produced from $\theta_c = 45°$. Although we are ignoring the birefringence here, a material that has different refractive induces (n) along the major and minor axes also changes the polarization of light, but it does so by causing a greater phase shift (not intensity change) of one of the light vectors compared to the other. Superimposing the two waves back up in this case changes the linearly polarized light into elliptically polarized light, and the extent of this polarization change also depends on θ_c. This effect is also detectable by polarized optical microscopy techniques, but for our material it is just overwhelmed by the polarization change from the absorption. A useful resource for understanding more about the origin of both these phenomena can be found here.[17]

In all three regimes of θ_c described above, the substrate contributes the same amount of s-polarized light to the total intensity (I_{sub}). The magnitude of the *contrast* that we perceive from the film depends on the ratio of the intensity difference between the brightest and darkest domains (ΔI) and the intensity contribution from the substate, I_{sub}, which includes both the TMD and the SiO_2 substate on which the TMD was grown. Hence, we can see that the light from the substrate floods the detector (i.e., $\Delta I << I_{sub}$) and so the contrast between domains appears weak in this instrumental geometry, as illustrated by the third panel of **Fig. 6.8a**.

As we know from our discussion of **Fig. 6.7**, however, as long as the substrate is isotropic, we can filter out the light reflected from it by using an analyzer, since the substrate reflection is fully s-polarized while the film has both s-polarized and p-polarized contributions. This cross-polarized geometry is explained in more detail in **Fig. 6.8b**, where the orientation of

the analyzer (A) is indicated by the blue arrow in the first panel. To be clear, the amount of light actually reflected by the sample is exactly the same as in **Fig. 6.8a**, but now the detection side is cutting out all of the s-polarized light. The magnitude of the blue bars in the middle panels of (a) and (b) is exactly the same, but the schematic graph in (b) is "multiplied" to see the bar more clearly. From **Fig. 6.8b** (middle panel), we can see that light polarized either along the major or minor axes (i.e., $\theta_c = 0°$ or $\theta_c = 90°$), which experienced no polarization change, shows no response in a cross-polarized geometry. Meanwhile, the crystal oriented at exactly 45° degrees now exhibits the maximal signal response, since it produces the maximum amount of p-polarized light. Because now $I_{sub} \approx 0 << \Delta I$, the contrast between domains visualized in a cross-polarized geometry is extremely high (**Fig. 6.8b**, third panel).

The drawback to cross-polarized imaging is that >99.9% of light is cut out by the analyzer, including the s-polarized light from the film that also contributed to ΔI. This leads to extremely poor signal-to-noise in studies of atomically-thin crystals, such as our single-atom-thick perylene crystals. We can strike a balance between cutting out the isotropic substrate response and letting though enough light for decent signal-to-noise by rotating the analyzer slightly, to allow a bit more light to hit the detector. This nearly-cross-polarized detection, which we will henceforth refer to as a "tilted-analyzer" geometry is described in **Fig. 6.8c**, where θ_A is the angle at which the analyzer is "tilted" with respect to the cross-polarized (i.e., orthogonal) position (the instrumental setup is the same as is shown in **Fig. A6.4**). We define a clockwise rotation of the analyzer to be a positive θ_A. The graph drawn in the middle panel of (c) is on the same scale as the graph in (b). Here, we are letting through a small amount of the s-polarized light reflected from both the film and the substrate, slightly increasing I_{sub} relative to ΔI. This

results in a lower contrast image (**Fig. 6.8c**, right panel), but the total intensity hitting the detector is higher (i.e., greater total signal-to-noise).

As we continue to tilt the analyzer towards the polarizer, the projection of the s-polarized components of the reflected light onto the analyzer continues to increase, while the projection of the p-polarized light concurrently decreases. If we rotate the analyzer 90° (i.e., parallel to the polarizer), the result would be very similar to that of **Fig. 6.8a**, except now all the p-polarized light (blue bar) is filtered out. We typically use a small analyzer tilt from a few to 10°, depending on the particular molecular crystal under investigation (the reasoning for choosing specific values will become clear later in the chapter). There are a few literature examples of titled-analyzer measurements on ultrathin materials,[18,19] although in these cases the anisotropy was mainly from LB, not LD.

6.4 Tilted-Analyzer Microscopy Measurements

6.4.1 Effect of θ_A on the θ_c-Dependent Reflectance

The graphs drawn in the middle panels of **Fig. 6.8** are not meant to be quantitative, but simply guides to illustrate relationships between the reflected intensities for domains visualized in different instrumental geometries. For example, the perylene crystals all exhibit C_2 symmetry, and correspondingly we expected the reflectance of the crystal in the single-polarizer geometry (**Fig. 6.8a**) to be maximum at 0° and decrease monotonically as the crystal is rotated to 90° (i.e., also a two-fold rotational symmetry in the reflectance signal). However, adding an analyzer changes what is detected, and so in the cross-polarized configuration (**Fig. 6.8b**), we expect the maximum reflectance to be at 45° and decrease monotonically from 45° to 90° (i.e., a four-fold rotational symmetry). Then, in the tilted-analyzer geometry, we should expect to see some transition between these two responses.

We can confirm the above expectations experimentally by tracking the intensity of a single PTCDA domain for all rotation angles (i.e., θ_c) under these different instrumental configurations. The results are shown in **Fig. 6.9**. We plot the data as the optical contrast, C, between the film under study and its support substrate, calculated as:

$$C = \frac{I_{film} - I_{sub}}{I_{sub}} * 100 \qquad \textbf{Eq. 6. 1}$$

where I_{film} is the reflected intensity from the molecular crystal plus TMD, and I_{sub} is the reflected intensity from the bare SiO_2 substrate on which the TMD was grown.

We can see from **Fig. 6.9** that the single-polarizer configuration indeed produces the expected two-fold rotational symmetry (green line), while the cross-polarized configuration produces the expected four-fold rotational symmetry (black line). The tilted-analyzer geometry is slightly more complicated. As the analyzer is rotated, the contrast of all domain rotations decreases (as expected), but some decrease faster than others. In the cross-polarized configuration, domains with $\theta_c = 0°$ and $\theta_c = 90°$ exhibit the minimum response, while $\theta_c = +45°$ and $\theta_c = 135° = -45°$ exhibit equal, maximal responses. If the analyzer is rotated clockwise (CW; i.e., positive θ_A), the $\theta_c = -45°$ domain decreases until it becomes the minimum reflected intensity, with $\theta_c = +45°$ still being maximum (blue line in **Fig. 6.9**). If instead the analyzer is rotated counterclockwise (CCW; i.e., negative θ_A), the behavior flips, and the $\theta_c = +45°$ domain will decrease in intensity until it exhibits the minimum reflectance, while $\theta_c = +45°$ remains maximum (red plot in **Fig. 6.9**). We believe that this "flipping" of intensities upon rotating the analyzer through zero originates from the fact that some of the domains rotate the polarization of the light CW (such as the $\theta_c = +45°$ domain), while others rotate the polarization CCW (such as

the θ_c = -45° domain). Thus, rotating the analyzer CW increases the projection of the light from the θ_c = +45° domain onto the analyzer, resulting in an increased signal, while the same rotation decreases the projection of the light from the θ_c = -45° domain (which was rotated in the opposite direction), resulting in a reduction of the signal from that domain. The case is the opposite when the analyzer is rotated CCW.

In either case though, the intensities of two of the four lobes in the cross-polarized data (black line) decrease rapidly and eventually disappear, resulting in a two-fold rotation dependence at some large enough θ_A (the exact value at which this occurs depends on the strength of the anisotropy for the particular material, but is <10° for our perylene-based crystals). These "symmetry transitions" can be seen more clearly in **Fig. A6.6a**, which plots similar data as **Fig. 6.9** except for PDI, and includes many more values of θ_A from 0° (crossed polarizers) all the way to 90° (parallel polarizers). For small increases in θ_A, the reflected intensities of the θ_c = 0° and θ_c = 90° domains remain equal as the analyzer is rotated in either direction, with their magnitudes somewhere between those of θ_c = +45° and θ_c = -45°. As θ_A goes to 90° (i.e., parallel polarizers),

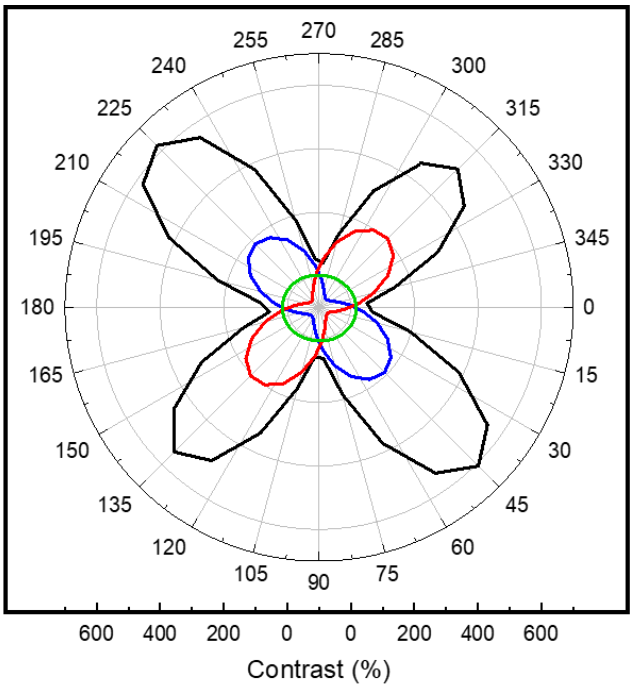

Figure 6.9. Contrast vs. θ_c for a PTCDA domain imaged under different instrumental configurations, showing how the relative intensities between domains evolve as the detection is changed. At θ_c = 0°, the polarizer is aligned with the major axis of the crystal. Green line is single-polarizer, black line is cross-polarizers, and red and blue lines are tilted-analyzer, where θ_A = -3° for the red and θ_A = +3° for the blue.

$\theta_c = 0°$ slowly transitions to becoming the maximum reflectance, and $\theta_c = 90°$ to the minimum reflectance, while the intensities of $\theta_c = +45°$ and $\theta_c = -45°$ converge. Although we have not plotted the parallel-polarizer result in **Fig. 6.9**, this looks almost exactly like the single-polarizer (green) plot (see **Fig. A6.6b** for a direct overlay of parallel polarizer and single polarizer rotation data).

Figure A6.7 further provides images of the PDI/MoS_2 film from which the data in **Fig. A6.6** was taken, where domains with $\theta_c = -45°$, 0°, +45°, and +90° are circled. This data shows more concretely how the film response changes various instrumental configurations and with different θ_A. We also want to note one curious feature that we observe in images taken at very small θ_A (less than a few degrees). For the images in **Fig. A6.7a** and **A6.7b** with $\theta_A < \pm 3°$, we can see that the boundaries between some domains (indicated with pink arrows) appear particularly prominent or dark. The effect is seen for all three molecular crystals, but the θ_A "threshold" to see it varies—these features will be wiped out at smaller θ_A for crystals with weaker anisotropy (e.g., we observe these lines at larger θ_A for PDI, which has a stronger anisotropic response than PTCDA, as we will see later in this section). The boundaries seem to be darker when domains with certain orientations meet, such as domains with θ_c close to +45° and -45°, although we have not carried out the analysis to conclude this definitively. One thing we can say about these features, however, is that they appear to dominate at θ_A for which the rotation dependence (i.e., contrast vs. θ_c) is *not monotonic* with a 90° rotation. In other words, it seems that we see this behavior when the imaging geometry give a four-fold rotational symmetry, but not when it gives a purely two-fold rotational symmetry. Although it is not clear why, the observations above seem to point out that these features appear to be promoted by conditions where we observe sharp changes in the contrast vs. θ_c.

One final general observation is that, for a certain range of θ_A, the domains with the lowest reflected intensities actually reflect *less light than the bare substrate* (i.e., the domains exhibit *negative contrast*). This can be seen more clearly in **Fig. A6.6b** and will also be obvious in the spectroscopy data in Section 6.6. From our calculations on the expected response from anisotropic crystals view in a tilted-analyzer geometry (not shown here), we believe this negative contrast is due to interference between light waves reflecting off the multiple interfaces in the sample—the molecular crystal, TMD, and substrate.

6.4.2 Choosing the Proper Measurement Conditions

We can see from the data in **Fig. 6.9** and **Fig. A6.6** that, depending on the instrumental configuration, domains with different θ_c will appear brighter or darker. We can make several general observations about the three instrumental geometries for polarized microscopy. In the single-polarizer configuration, we are detecting all of the light from the sample (film plus substrate), which includes both the s-polarized and p-polarized responses. If an analyzer is oriented parallel to the polarizer, we can selectively filter out the light that changed polarization through interaction with the film (i.e., remove the p-polarized response). Because the single-polarizer contrast is nearly identical to the parallel-polarizer contrast (**Fig. A6.6b**), it is clear that the data in the single-polarizer configuration is *dominated by the s-polarized response* of the sample. This makes sense, since the p-polarized response of the film is extremely small compared to the combined s-polarized reflectance of the film plus the substrate (recall **Fig. 6.8a**). If we orient the analyzer exactly perpendicular to the polarizer, we are now filtering out the light that did not change polarization though interaction with the sample (i.e., the s-polarized light). Hence, the cross-polarized data is *dominated by the p-polarized response* of the film.

Furthermore, the single-polarizer configuration provides good signal-to-noise with weak optical contrast, while the crossed-polarized configuration provides strong optical contrast with poor signal-to-noise. Because of the atomically-thin nature of 2D molecular crystals, we perform most measurements in the tilted-analyzer configuration to balance these two effects, where the optical contrast increases with decreasing θ_A and signal-to-noise increases with increasing θ_A. The important thing to remember is that the relative intensities between domains will change at different analyzer rotations, so it is not as straightforward to identify which domain has its major axis aligned with the polarizer (which would simply be the brightest domain in a conventional single-polarizer measurement). Still, the data in **Fig. 6.9** and **Fig. A6.6** show that can relate the intensity at any θ_A back to the standard single-polarizer configuration. Hence, a similar understanding can be gained regardless of the instrumental geometry, provided that θ_A and θ_c are tracked properly.

In these measurements, our criteria for choosing θ_A is that it should be large enough for the system to exhibit a two-fold rotational symmetry, such as shown in **Fig. 6.9** where $\theta_A = +3°$ or -3° for PTCDA. We do this for two reasons. The first is because all of the crystals in our study have C_2 symmetry, so we would expect the properties of the crystal to be invariant upon a 180° rotation. Furthermore, data collected in the four-fold symmetry regime (or any transition regime between the two symmetries) will show four unique crystal domains as having same reflected intensity. This degeneracy drops to two domains in the two-fold regime, which can be easily broken using some straightforward image processing techniques (described in the following subsection). The second reason is because conventional LD measurements of molecular crystals are taken in a single-polarizer geometry, which exhibits a two-fold rotational symmetry (although for that configuration there is a monotonic intensity decrease from $\theta_c = 0°$ to $\theta_c = 90°$,

while in the tilted-analyzer configuration the monotonic decrease is actually between $\theta_c = 45°$ and $\theta_c = 135°$). By doing this, we can make analogies between data taken in our unconventional instrumental configuration to data taken under the more well-known configuration, which will do in Sections 6.5 and 6.6.

Lastly, we point a few important things about the selection of θ_A and the excitation wavelength (λ). The minimum θ_A required to see a two-fold rotational symmetry is material-dependent. For example, for PDI on MoS_2 on fused silica, which we will later see is the most optically-anisotropic of the molecular crystals in our studies, θ_A needs to be at least $\pm 7°$ at λ = 585 nm (where PDI experiences the strongest anisotropic optical response). In comparison, a value of $\theta_A = \pm 1.5°$ is required to see the two-fold behavior for PTCDA—the least anisotropic crystal in our studies—at λ = 555 nm (where PTCDA exhibits its strongest response). This difference is related to how the optical response in the four-fold regime is dominated by p-polarized light from the film, while the two-fold regime is dominated by s-polarized light. Crystals with greater optical anisotropy produce more p-polarized light, and hence require larger amounts of "background" (s-polarized) intensity from the substrate in order to transition from the four-fold symmetry regime to the two-fold regime. This also depends on the excitation wavelength, since optical constants vary spectrally. For a specific θ_A, certain λ where the optical anisotropy is high can exhibit four-fold symmetry, while regions of the spectrum are already in the two-fold regime.

The support substrate also affects decisions of θ_A and λ. We find that using wafers of 300 nm SiO_2/Si results in exceptionally good contrast and signal-to-noise, presumably due to the fact that the light passes through the film multiple times on this nontransparent support and because the signal at certain energies can be enhanced due to interferences with other light waves from

internal reflections within the substrate. These internal reflections are a double-edged sword, however, convoluting the peaks in optical spectra, as well as changing the rotation dependance (i.e., θ_c dependance) at certain energies (this will be seen more clearly later from **Fig. A6.8**). Therefore, we perform many of our imaging and rotation measurements on SiO_2/Si wafers, but all of our spectroscopy measurements are carried out on transparent, fused silica wafers, minimizing the effect of the substrate at the cost of some signal.

6.4.3 Single-Wavelength Imaging

Now that we have an instrument suitable for studying the polarized optical properties of these atomically-thin systems, we can apply this to our 2D perylene crystals. **Figure 6.10a** shows an image of a PTCDA molecular crystal film deposited on monolayer MoS_2 grown on a SiO_2/Si substrate. The film is viewed in a tilted-analyzer geometry (with θ_A = -3°), using a 565 nm

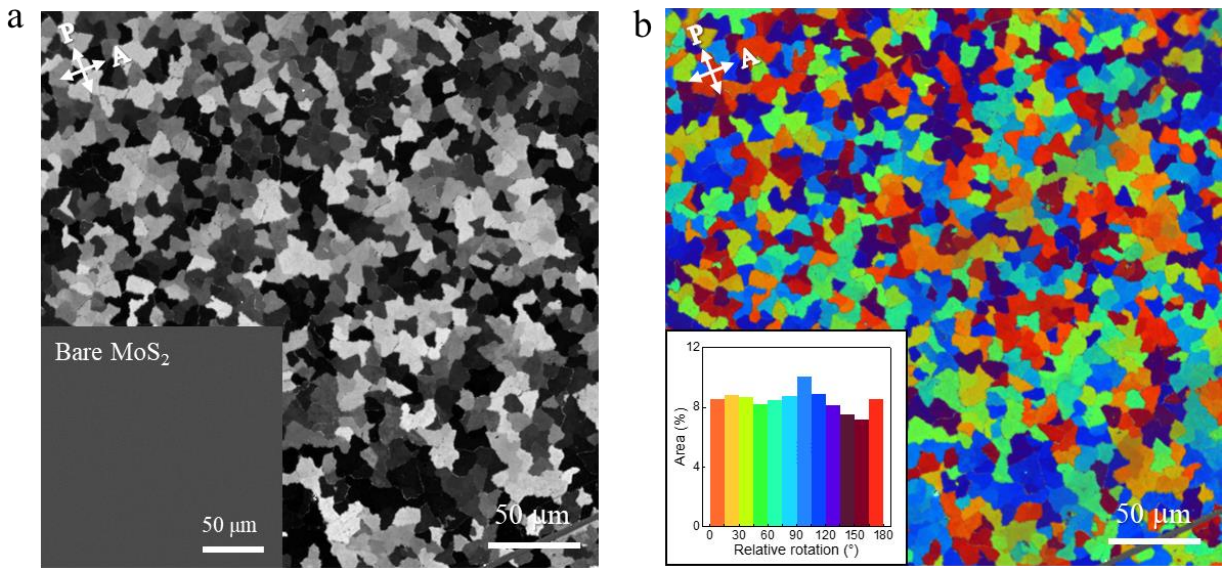

Figure 6.10. a) Image of a film of PTCDA on MoS_2, taken in a tilted-analyzer geometry with λ = 565 nm and θ_A = -3° (main panel), with an image of a bare MoS_2 film, taken under the same conditions, shown in the inset. b) False-color image showing the relative rotations of PTCDA domains for the same image shown in (a), produced by RGB-stacking three images of (a) that taken at film rotations of 0°, 45°, and 90°. Inset shows a histogram of the percent area of the film with crystals of different rotations, using the same color-coding as the false-color image. The directions of the polarizer and analyzer are indicated in the top left.

illumination, with the directions of the polarizer and analyzer given in the top left corner. 565 nm was chosen as the imaging wavelength because it is where PTCDA molecular crystals exhibit the strongest polarized response on this substrate. A bare monolayer MoS_2 film (also taken at 565 nm) exhibits a uniform response due to its lack of in-plane anisotropy (**Fig. 6.10a**, inset), while the PTCDA/MoS_2 film shows patches of irregularly-shaped domains with different reflected intensities.

We can use our imaging technique to confirm that each domain is of identical thickness (i.e., monolayer) by rotating the entire sample (for fixed positions of the polarizer and analyzer) and tracking the intensities of the individual PTCDA domains. **Figure 6.11a** shows a section of the film from **Fig. 6.10a** taken at different sample rotations from 0° to 180° in 45° intervals, and **Fig. 6.11b** compares the full rotation dependence of many PTCDA domains in this film. The orange and blue stars mark the brightest and darkest domains in the 0° film, respectively. We can see from the plot in **Fig. 6.11b** that the darkest and brightest domains have a relative rotation of 90°, and that all domains exhibit two-fold rotational symmetry, returning to the same intensity

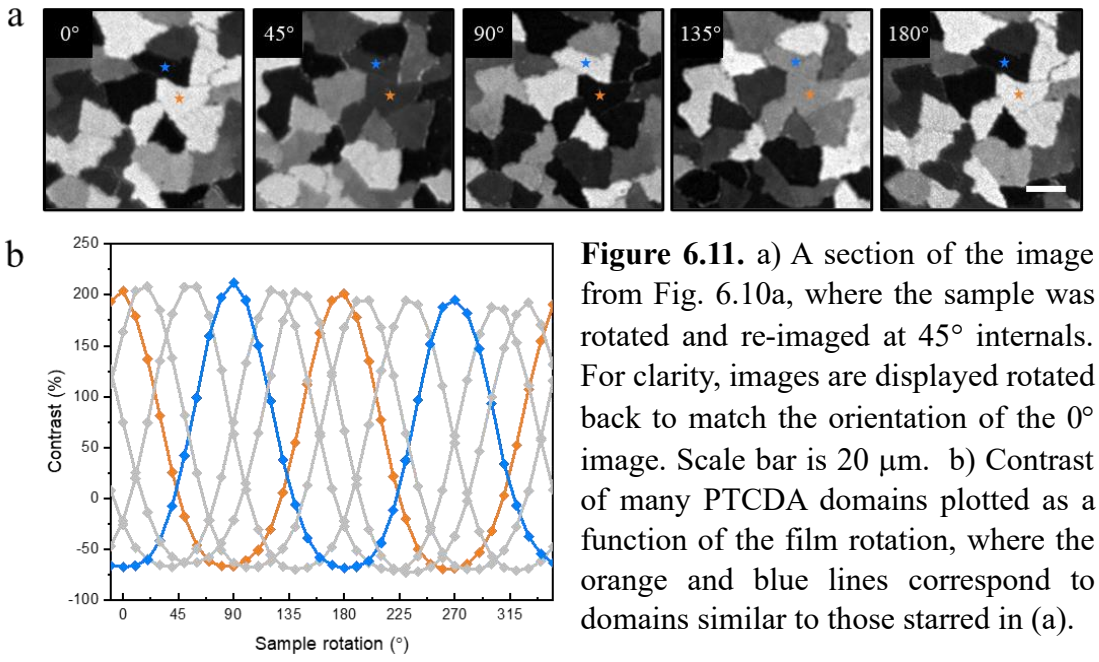

Figure 6.11. a) A section of the image from Fig. 6.10a, where the sample was rotated and re-imaged at 45° internals. For clarity, images are displayed rotated back to match the orientation of the 0° image. Scale bar is 20 μm. b) Contrast of many PTCDA domains plotted as a function of the film rotation, where the orange and blue lines correspond to domains similar to those starred in (a).

after a 180° rotation. The two-fold symmetry is consistent with our expectation for imaging in a tilted-analyzer geometry, and we can identify the brightest domain (orange) to have θ_c = -45° (or alternatively, +135°) and the darkest domain (blue) to have θ_c = +45°, based on our analysis in **Fig. 6.9**. Since the domains exhibit identical minima and maxima, we can assume the film to be of uniform thickness (crystals with different thicknesses would exhibit different maximum reflected intensities).

There is one important technical point to understand related to the collection of a dataset like that shown in **Fig. 6.11b**. Theoretically, the rotation dependance of identical domains should be equal, but in practice, it is quite difficult to observe this behavior. In fact, if we take the same domain, move it to different locations in the field of view, and measure its contrast vs. θ_c at each location, we find that the data actually exhibit different minima and maxima. This is because the polarization of the incident light beam is not spatially uniform. This means that the domains near one edge of the beam "feel" a slightly different θ_A than domains at the opposite edge. Since we know from **Fig. 6.9** and **Fig A6.6** that the rotation response changes significantly with θ_A, the rotation curves will appear asymmetric if the domain being measured is not at the same point in the beam throughout the entire rotation (indeed, the peaks at sample rotations >180º in **Fig. 6.11b** do appear be somewhat smaller in magnitude). This effect gets worse as θ_A goes to 0º. Therefore, when taking any quantitative data in a cross-polarized or tilted-analyzer geometry, it is necessary make sure that 1) the domains being measured are close to one another (within ~100 μm), and 2) the domains should be placed at the center of rotation of the rotation stage (to minimize the spatial shift as the sample is rotated).

Another observation from the images in **Fig. 6.11a** is that the reflected intensities from domains with different rotations are not all unique. For example, the two starred domains give

different responses in the first image, but if the sample is rotated 45° or 135°, the intensities converge and the domains can no longer be distinguished. This is a natural consequence of the 2-fold symmetry of the system. In order to break this degeneracy, we can compile the information from three black-and-white images taken at different film rotations by RGB-stacking them. This processing is similar to traditional color photography, except using different polarizations instead of different color filters. The result is shown in **Fig. 6.10b**, where the first image (0°) from **Fig. 6.11a** was assigned to the red channel, the second image (45°) was assigned to the green channel, and the third image (90°) was assigned to the blue channel. In the composite image, all of the unique domain orientations (i.e., having relative rotation between 0° and 180°) correspond to a unique color, with their rotational relationships following the RGB color wheel. The color scale is shown in the histogram in the inset. Here, the domains with θ_c close to 0° are represented in green, corresponding to the "45°" bin in the relative rotation histogram, and the θ_c = -45° and θ_c = +45° domains are represented in the same orange and blue used in **Fig. 6.11**.

The image processing described in the above paragraph for **Fig. 6.10b** was the same methodology used to generate the false-colored images from Chapter 5. This allows us to visualize the size and angular distribution of domains in our molecular crystal films. A number of observations can be made from the image in **Fig. 6.10b**. In this particular film, the orientations of the PTCDA domains appear to be randomly distributed. This can be confirmed by the histogram in Fig. 2d, inset, which shows a similar number of domains falling within each bin having 15° width. We can also measure the mean width of the PTCDA domains (~20 μm in this film), which we know from Chapter 5 to be decided by the domain size of the underlying MoS_2.

We can extend this imaging measurement to the other perylene-based molecular crystals, as shown in **Fig. 6.12**. The molecules were deposited on MoS_2 films with similar domain size, and the resulting films were transferred (using a water-based transfer method) onto a fused silica substrate for imaging. Each image was taken at the wavelength where that particular crystal exhibits its maximum polarized response on this substrate. The images in the top row (**Fig. 6.12a**) are the original black-and-white images, while the bottom row (**Fig. 6.12a**) shows the RGB images of the same areas. We used $\theta_A = -7°$ in all cases, where all crystals exhibit a two-fold rotational symmetry comparable to **Fig. 6.10b**, and so the color scales of the RGB images in **Fig. 6.12b** are similar to **Fig. 6.10b**, inset. The images are presented on the same intensity scale for comparison (in contrast to **Fig. 5.19**, where the images were autoscaled to compare only the morphologies of the films). The generally morphology of all of the films look similar, with the strength of the polarized optical response being the main distinguishing factor. The PPDI and OPDI films are not shown here, but exhibit a response very similar to the

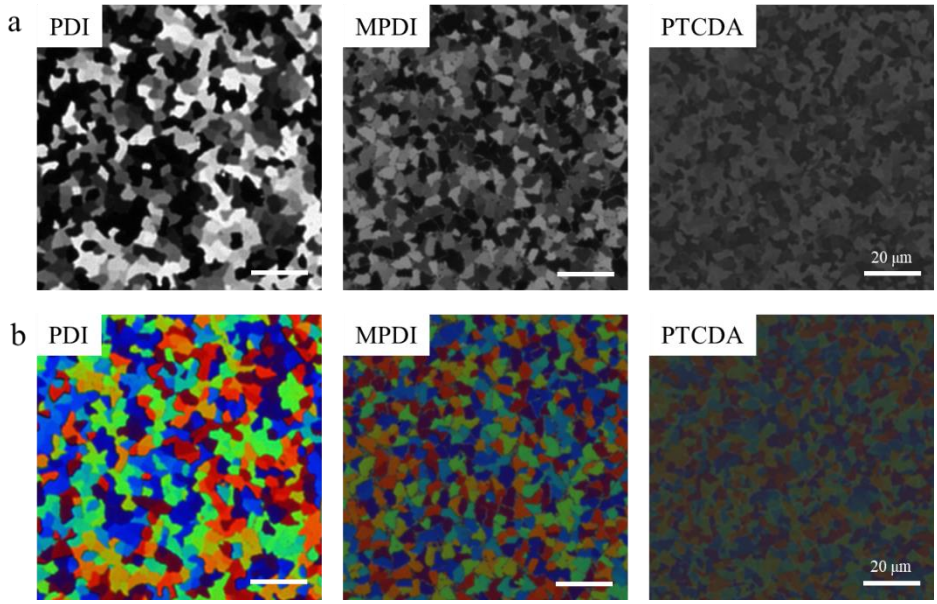

Figure 6.12. Tilted-analyzer images of various molecular crystal films on MoS_2, which were transferred to fused silica substrates. a) Original images taken and $\theta_A = -7°$, where $\lambda = 580$ nm for PDI (left panel), $\lambda = 570$ nm for MPDI (middle panel), and $\lambda = 555$ nm for PTCDA (left panel). b) False-color images of the films from (a). All scale bars are 20 μm and images are presented on the scale intensity scale for comparison.

MPDI film. We can see that although the PTCDA film gives a decent polarized response (**Fig. 6.10**), it is actually the weakest among all the molecular crystals in our study. PDI exhibits the strongest response, and the alkyl-PDI derivatives are in between.

From our discussions in the previous subsection, we know that a stronger optical contrast (i.e., greater difference between the reflectance of the brightest and darkest domains) in these polarized microscopy measurements corresponds to a larger optical anisotropy of the crystal unit cell, which can originate from linear dichroism and/or linear birefringence. It is interesting that the MPDI crystals exhibit a stronger polarized optical response than the PTCDA crystals, since we know from Section 6.2 that the PTCDA crystals actually have more molecules per unit area. This, combined with the fact that the molecular base (perylene) is the same in each case, the large difference in anisotropy presumably comes from the other structural differences between the crystals that we observed in the STM measurements. We investigate this further by analyzing the full spectral response of each crystal in the following sections.

6.5 Traditional Absorption and Reflectance Measurements

6.5.1 Unpolarized Absorption

We begin by establishing the optical properties of each molecular film without paying heed to the orientation of individual crystals. The full unpolarized absorption spectra of PTCDA, MPDI, and PDI deposited on MoS_2 films on fused silica substrates are shown in **Fig. 6.13** (colored lines). The spectra are taken from a 5x5 mm area using a conventional Cary UV/vis spectrophotometer. Using the spectrum of a bare MoS_2 film (gray line) as a reference, we can identify the two lowest-energy features at ~675 nm and ~625 nm (labelled M_A and M_B) and the highest energy feature at ~425 nm (M_C), which are identical in both position and intensity in all four spectra, to be the A, B, and C excitons of the MoS_2 substrate, respectively. The two

remaining peaks (P_1 and P_2), which span the region where the MoS_2 is spectrally flat (500-600 nm), can therefore be attributed to the perylene molecules. These absorption features, which correspond to the first two vibronic bands of the S_0-S_1 transition of perylene, exhibit a 30-50 nm bathochromic shift relative to their positions in solution[20–22] (indicated by black arrows in **Fig. 6.13**). This shift is consistent with literature reports of monolayer molecular films deposited on 2D materials[23,24].

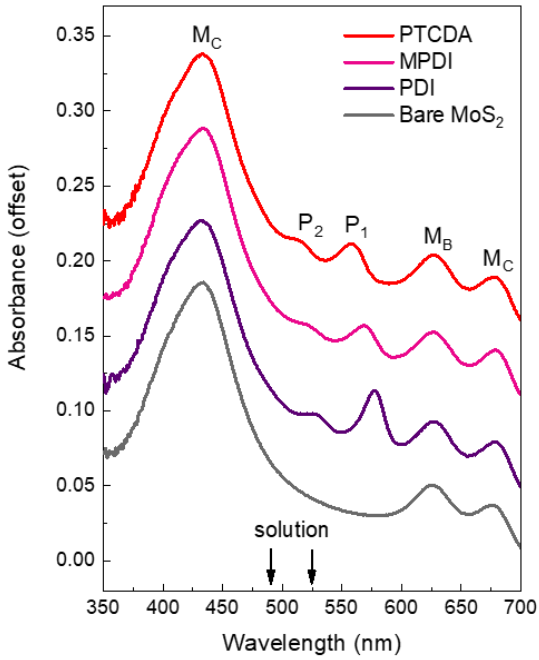

Figure 6.13. Unpolarized absorption spectra (vertically offset) of molecular crystal films deposited on MoS_2 grown on fused silica substrates (PTCDA = red line, MPDI = pink line, PDI = purple line), with a spectrum of bare MoS_2 shown for comparison (gray line). M_A, M_B, and M_C correspond to the A, B, and C excitons of MoS_2, respectively, and P_1 and P_2 indicate the first two vibronic bands of perylene.

Although the absorption spectra of the three perylene-modified MoS_2 films are quite similar overall, two differences can be seen. The first is a small spectral shift of ~10 nm between the absorption bands of the three molecular layers, with the absorption maximum, P_1, around 580 nm for PDI, 570 nm for MPDI, and 560 nm for PTCDA. It is difficult to know if the origin of this shift is related to the differences in the intermolecular interactions of the molecules in each crystal, or if it is just an inherent property of the monomers. This uncertainty is because absorption peaks in solution can shift by small amounts depending on interactions with the solvent, and so we cannot confirm the exact peak positions since the spectra cannot be taken in the same solvent due to solubility issues. In bulk molecular crystals, however, we do know that absorption peaks shift significantly depending on

the film structure,[21,25] due to strong interactions with the many surrounding molecular layers. Our 2D crystals should all be experiencing very similar dielectric environments (air on one side, MoS_2 on the other), and it is unclear if the small in-plane differences in the intermolecular interactions can cause these shifts. The shape of the absorption features of our 2D molecular crystals also look surprisingly similar to the solution spectra, implying a lack of intermolecular charge transfer (not expected for flat-lying molecules without pi-stacking).

The second difference between the spectra is the total strength of the absorption features of each molecular film, which is the greatest for PDI, followed by PTCDA, and then MPDI. We can directly compare the integrated absorption of each molecular films since the monomers have similar extinction ratios.[20] The above-stated trend for the density of each film is consistent with our density calculation from the STM data (**Table 6.1**), reinforcing our observation that the differences in the anisotropy observed in **Fig. 6.11** cannot simply be explained by the packing densities of the three crystals.

6.5.2 Single-Polarizer Reflectance

The optical data we have seen until now suggest that that large differences between the polarized optical responses of PDI, MPDI, and PTCDA should originate from the differences in their crystal structures. To begin establishing these structure-property relationships, we can start with the simplest instrumental geometry—the single-polarizer configuration (**Fig. 6.8a**). **Figure 6.14** shows polarized reflectance spectra of molecular crystal films of PDI, MPDI, and PTCDA on deposited on MoS_2, which was water-transferred to a fused silica substrate. These spectra were obtained by performing hyperspectral imaging measurements, where we take a series of images across the visible spectrum (475-700 nm), at a step size of 5 nm with a 5 nm bandwidth

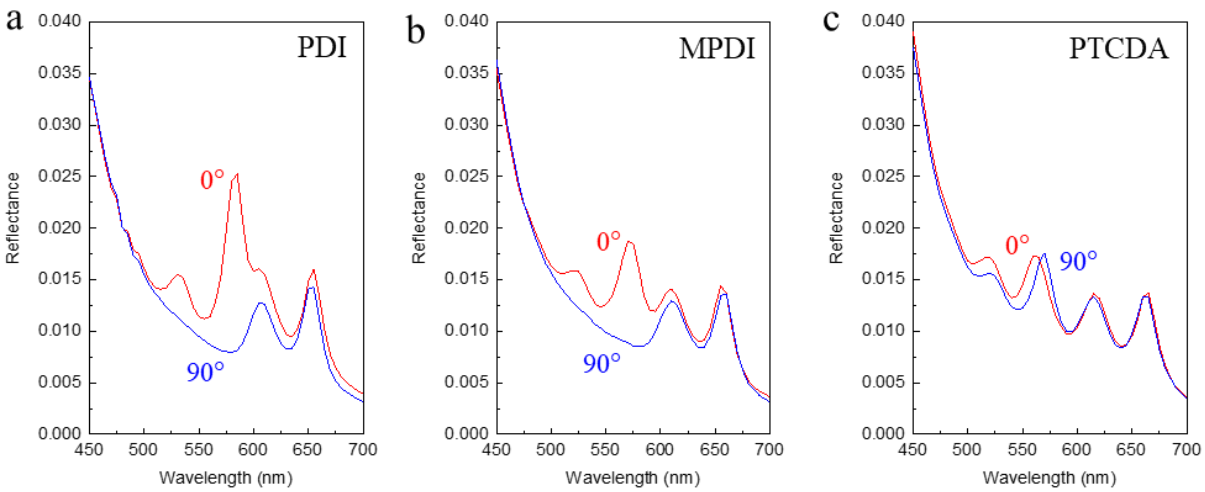

Figure 6.14. Single-polarizer reflectance spectra of a) PDI, b) MPDI, and c) PTCDA films deposited on MoS_2 and transferred to fused silica substrates, shown for $\theta_c = 0°$ (red lines) and $\theta_c = 90°$ (blue lines).

illumination. We integrate the reflected intensity within an individual domain and calculate the reflectance by dividing by the total light intensity at each wavelength.

The red spectra represent the brightest domain in each film, and the blue spectra represent the darkest domain in each film. We find that in all cases the darkest domain is rotated 90° with respect to the brightest, and all other angles follow a monotonic trend in between. This is consistent with our expectation from **Fig. 6.8a**, and confirms that $\theta_c = 0°$ for the brightest domain, and $\theta_c = 90°$ for the darkest domain. Using the unpolarized absorption spectra in **Fig. 6.13** as references, we can assign the two lowest energy peaks in the spectra to the A and B excitons of MoS_2 and assume that the increasing tail on the high-energy side results from the C exciton. Of the two remaining peaks, their positions coincide with what we observed for the first two vibrational states of the first electronic transition of each crystal. Although the unpolarized absorption spectra of MPDI showed a lower peak intensity compared to PTCDA, the single-polarizer reflectance of the $\theta_c = 0°$ for MPDI is actually than that of PTCDA, which is also consistent with the tilted-analyzer images in **Fig. 6.12**. PDI is still gives the strongest response in the case of all three measurements.

The reflectance spectrum of PDI (**Fig. 6.14a**) is straightforward to understand, since the case is similar to **Fig. 6.1b**. The absorption of the crystal is maximum when the polarization of the light is parallel to the major axis of the crystal, and minimum when the light is perpendicular to the major axis. Because the absorption features completely go away for $\theta_c = 90°$, we can assume that the minor axes of both the PDI unit cell does not absorb. This makes sense, since the unit cell of PDI consists of only one molecule, and each transition dipole moment of a molecule is polarized along only a single molecular axis (in this case, the long axis of the molecule). Hence, we do not expect the minor axis of the PDI crystal to absorb, since it coincides with the short (non-absorbing) axis of the molecule.

For MPDI (**Fig. 6.14b**), however, there is no axis of the unit cell that coincides with an axis of the component molecules, since the molecules in the unit cell are not parallel to each other. By this logic, it seems we would not expect *zero absorption* for $\theta_c = 90°$ for MPDI, although that is what we appear to see. We can understand better what we should expect by looking at the case of PTCDA (**Fig. 6.14c**), which also has more than one molecule in its unit cell. The $\theta_c = 90°$ domain in the single-polarizer reflectance spectra for PTCDA does not exhibit zero absorption, although it is still the *minimum absorption* at wavelengths shorter than ~570 nm. At ~570 nm, there occurs an isosbestic point, after which the $\theta_c = 0°$ domain actually exhibits the minimum absorption.

From **Fig. 6.14c**, it appears that the PTCDA crystals absorb at different energies depending on the polarization of the incident light, whereas the absorption features for PDI and MPDI occur at the same energies regardless of crystal rotation. This is actually a well-known phenomenon in the field of molecular absorption, called Davydov splitting. The phenomenon of polarization-dependent molecular absorption, was first studied in the context of aggregation of

molecular dyes in solution[26–28]. A monomer of a dye molecule absorbs at a certain energy in solution. Due to the poor solubility of dyes however, the monomers will aggregate above a critical concentration threshold, resulting in superstructures of strongly-interacting molecules. Depending on the angles between the molecules in the aggregate, their transition dipole moments will couple. This coupling can be "attractive" (i.e., positive to negative) or "repulsive" (i.e., positive to positive or negative to negative), resulting in a splitting of the absorption state into one lower energy and one higher energy state, compared to the isolated monomer in solution.

We can extend this concept to molecular crystals, by treating a bimolecular unit cell as a dimer,[14,25,29] as illustrated in **Fig. 6.15a** with PTCDA. The transition dipole moments of the two inequivalent molecules in a bimolecular unit cell can either couple attractively to produce a lower energy state with a certain polarization direction (red arrow) or repulsively to produce a

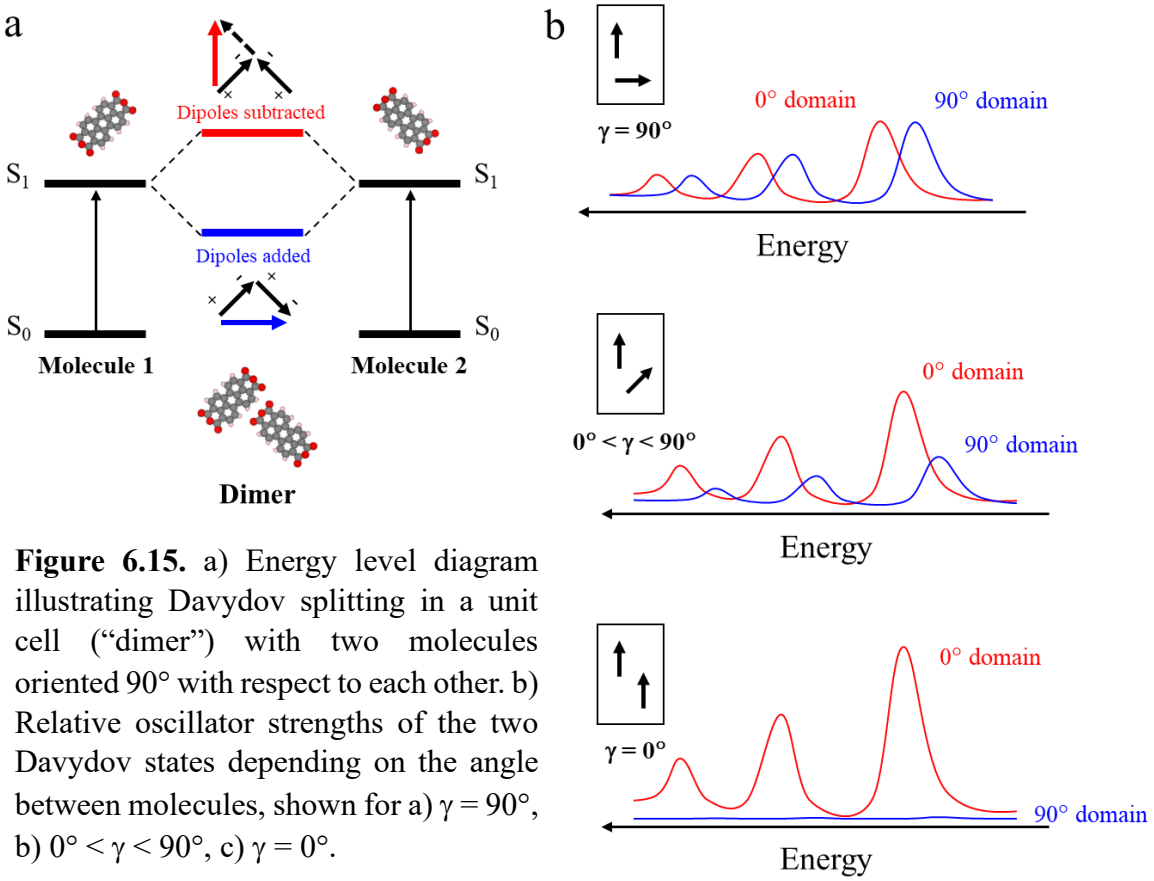

Figure 6.15. a) Energy level diagram illustrating Davydov splitting in a unit cell ("dimer") with two molecules oriented 90° with respect to each other. b) Relative oscillator strengths of the two Davydov states depending on the angle between molecules, shown for a) $\gamma = 90°$, b) $0° < \gamma < 90°$, c) $\gamma = 0°$.

higher energy state with its polarization rotated 90° relative (blue arrow). Because the two Davydov states absorb light of orthogonal polarizations, the state that is excited can be change by either changing the polarization of the incident light or rotating the crystal 90°, such as the behavior we saw with PTCDA in **Fig. 6.14c**. For a crystal where the molecules are oriented exactly 90° relative to each other, the oscillator strength will be split equally between the two Davydov components, as illustrated in **Fig. 6.15b** (top panel). As the angle between the molecules (γ) increases. The intensity of one of the components decreases while the other increases (**Fig. 6.15b**, middle panel), until one component becomes zero for parallel molecules (i.e., a single-molecule unit cell, such as PDI; **Fig. 6.15b**, bottom panel). The depictions in **Fig. 6.15b** shows some very general behaviors of crystals with bimolecular unit cells, but the peak energies and relative intensities in real systems will generally be more complex. This is because strong interactions between molecules causes usually the dimer spectrum to exhibit other changes from the monomer spectrum, including peak position, peak shape, and peak intensity.[27]

Going back to the experiment data (**Fig. 6.14**), is it unclear what is the relative intensities between the two Davydov states for our PTCDA crystal. Since our STM data show that $\gamma = 72°$, we should expect one state to exhibit greater oscillator strength, but it is a difficult to tell since the contrast between domains in the single-polarizer configuration is weak. We would also expect the MPDI to exhibit a behavior similar to the middle panel of **Fig. 6.15b**, but there does not appear to be any Dvaydov splitting in the experimental data (**Fig. 6.14b**). We will revisit these observations in our tilted-analyzer spectroscopy measurements below, which exhibit much stronger contrast. Another observation we will revisit is the small offset in the reflectances of the 0° and 90° molecular domains at the A and B excitons of MoS_2, which is below the band gap of

the molecules. This offset increases from PTCDA to MPDI to PDI, but the signal in this single-polarizer configuration is too low to tell definitively.

6.6 Linking Structure to Properties

To form a better understanding of the optical properties of these atomically-thin crystals, we can use the tilted-analyzer geometry described in previous sections to take the fill spectral response. Here, we want to distinguish between two types of properties: the spectral dependance and the polarization dependance. We will first try to understand the interactions of the 2D crystals with light of different energies in terms of the intrinsic optical properties of the molecular monomers. We will then use the structure of the molecules in each crystal to understand the interactions the crystals with light of different polarizations.

6.6.1 Tilted-Analyzer Spectroscopy

Figure 6.16 shows the spectral responses of films of PDI, MPDI, and PTCDA crystals with different relative rotations deposited on MoS_2 grown on a fused silica substrate. These spectra were obtained by again performing hyperspectral imaging measurements (5 nm step size, 5 nm bandwidth), but this time in a tilted analyzer geometry. Here, we are using θ_A = -7°, in order to achieve a monotonic relationship between the reflected intensity and domain rotation (θ_c) as the crystal is rotated 90°. We plot the spectral responses in terms of surface differential reflectance, using the relation:

$$\frac{\Delta R}{R} = \frac{R_{sam} - R_{sub}}{R_{sub}} \qquad \textbf{Eq. 6.2}$$

where R_{sam} is the reflected intensity from a film sitting on some support substrate and R_{sub} is the reflected intensity from the bare substrate, both quantities measured at a particular wavelength. **Fig. A6.8** shows what similar spectra look like on a SiO_2/Si substrate, where,

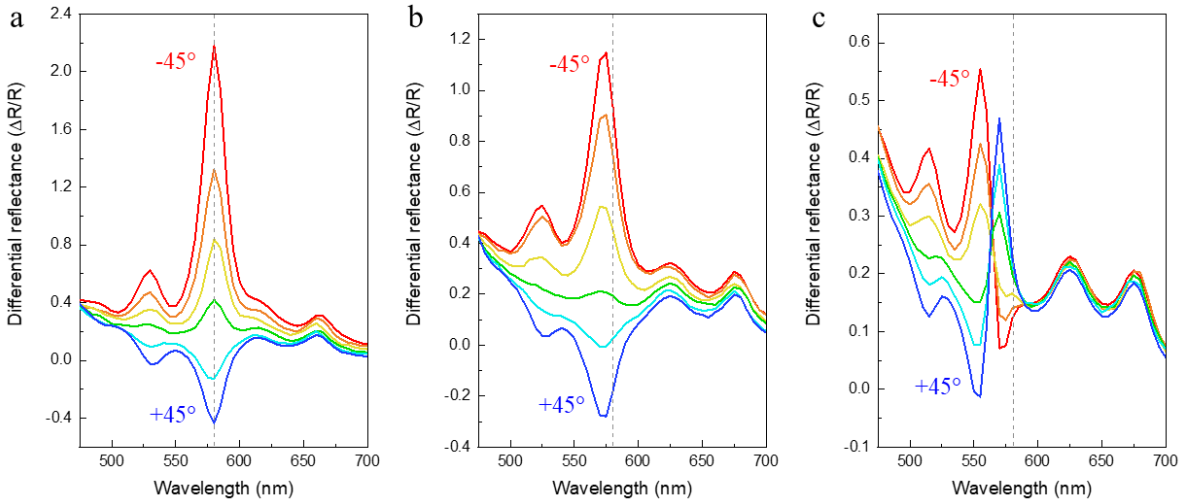

Figure 6.16. Differential reflectance spectra of many crystal domains in films of a) PDI, b) MPDI, and c) PTCDA deposited on MoS_2 grown on fused silica substrates, taken in a tilted-analyzer geometry with θ_A = -7°. Red lines correspond to θ_c = -45°, blue lines to θ_c = +45°, and other colors represent domains with rotations in between. Dashed gray line at λ = 580 nm is to emphasize relative peak positions.

although the signal is much stronger, the positions of the peaks are unclear and the monotonic nature of the intensity change is not maintained over the entire spectral range in the PDI and MPDI films the internal reflections in substrate. (Note: this technically the same as the "contrast" data reported in Section 6.4, but we are changing to a more standard terminology used specifically in spectroscopic studies.) Images taken at a few select wavelengths for all five molecular crystal films studied in this thesis (including PPDI and OPDI) can be found in **Fig. A6.9**.

Similar to the single-polarizer reflectance spectra in **Fig. 6.13**, we show the domain with the overall brightest response in red, and the domain with the overall darkest response in blue (these domains correspond to θ_A = -45° and θ_A = +45°, respectively, in the tilted analyzer geometry). The dashed gray line at λ = 580 nm is to emphasize relative peak positions. The differential reflectance spectra show multiple peaks and valleys. We attribute the valleys (i.e., negative reflectance relative to the substrate) to the interference of the film response with the

substrate response (as explained previously in Section 6.4), and so we will only focus on the positive features in our analysis. We can see that the reflection maxima are slightly shifted to lower energies from PDI (580 nm) to MPDI (570 nm) to PTCDA (555 nm), and that the value of the maximum differential reflectance decreases in the same trend—roughly halving from PDI to MDPI to PTCDA. The images in **Fig. 6.11** were taken at these strongest reflection peaks.

With the much stronger contrast from the reduced substrate background, see that the spectral responses decrease monotonically over the entire visible range for PDI and MPDI as the crystals are rotated 90° (**Fig. 6.16a** and **Fig. 6.16b**). The PPDI and OPDI films give very similar optical responses to that of the MPDI film (**Fig. A6.10**). This monotonic behavior is consistent with the single-polarizer reflectance spectra of PDI and MPDI (**Fig. 6.14a** and **Fig. 6.14b**), as expected for a crystal whose major axis is being rotated with respect to some polarized illumination. For PTCDA, which exhibited an extremely weak response in the single-polarizer geometry, we can now clearly see that the change in the reflected intensity is also monotonic upon a 90° rotation, but that the domains reverse their relative intensities (see images in **Fig. A6.9a**) about two isobestic points at 565 nm and 590 nm.

6.6.2 Monomer Optical Properties to Spectral Response

Using the observations from **Fig. 6.16**, we can identify the different sources of anisotropy that contribute to the spectrally-varying optical contrast of our perylene-based 2D crystals. To quantify the anisotropic response, we calculate the reflection anisotropy between two perpendicular directions (*a* and *b*) for a single domain as a function of wavelength:

$$RA = 2 * \frac{R_a - R_b}{R_a + R_b} \qquad \textbf{Eq. 6. 3}$$

where we choose R_a to be the reflected intensity from the brightest domain at 550 nm and R_b to be the reflected intensity from the same domain rotated 90° (i.e., darkest domain). The reflection anisotropy spectra for PDI, MPDI, and PTCDA on MoS_2 films grown on fused silica are shown in **Fig. 6.17** (colored lines), overlaid with the unpolarized absorption spectra (gray lines) of the same film. (Note: the axes for the unpolarized spectra are not shown in the plot.)

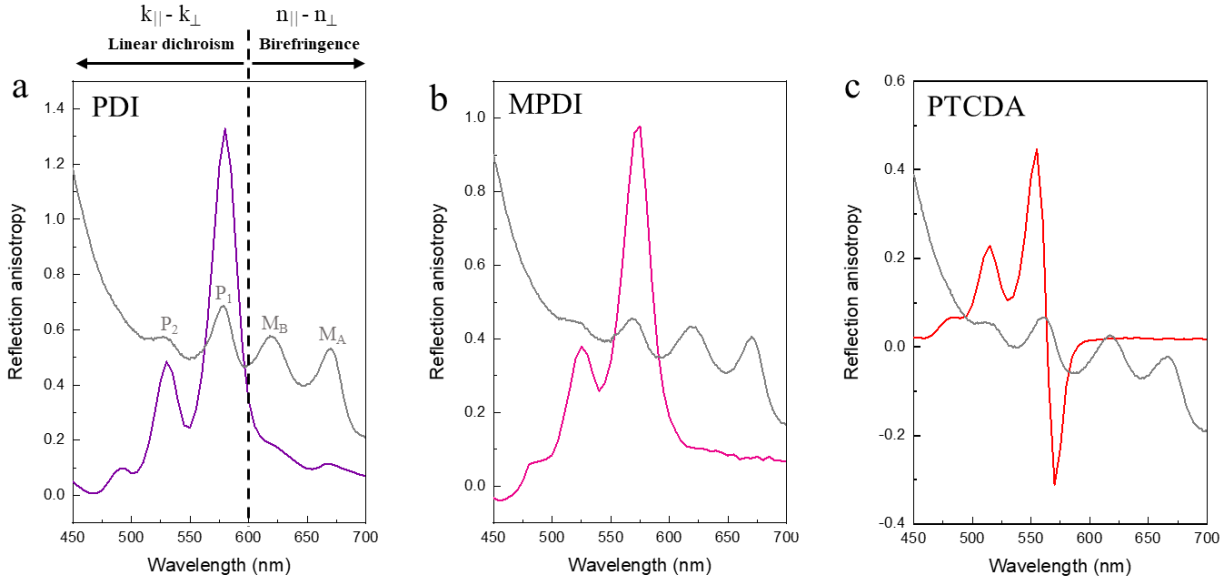

Figure 6.17. Reflection anisotropy spectra (colored lines) of a) PDI, b) MPDI, and c) PTCDA deposited on MoS_2 grown on fused silica substrates, taken in a tilted-analyzer geometry with θ_A = -7°. The unpolarized absorption spectra of the same films is overlaid (gray lines; axis not shown), where M_A and M_B are the A and B excitons of MoS_2 and P_1 and P_2 are the molecular absorption bands. The vertical dashed line is to indicate the transition between the linear-dichroism-dominated and the birefringence-dominated regimes of the optical anisotropy.

We see that the two strongest peaks in the reflection anisotropy spectra (above ~600 nm) directly coincide with the molecular absorption bands P_1 and P_2. In the case of PTCDA, the reflection anisotropy peak that corresponds to P_1 is split into two features with different signs, indicating a flip in the magnitudes of the response for the two perpendicular axes (we will return to these features in the following subsection). We note that there also appears to be a third peak in the anisotropy spectra of each film ~475 nm that may correspond to the third vibronic band of the perylene molecules. This transition was too weak to be observed in the unpolarized

absorption spectra in **Fig. 6.13**. The anisotropy drops sharply below the HOMO-LUMO gap of the perylene molecules (λ ~ 600-700 nm). Thus, we can conclude that the strong, spectrally-varying anisotropic response at wavelengths shorter than 600 nm originates largely from the linear dichroism of the molecular film, i.e., the differential absorption ($k_{||} - k_{\perp}$) between the two perpendicular (major and minor) axes of the crystal domains.

Below the HOMO-LUMO gap of the molecules (λ > 600 nm), however, the anisotropy is still nonzero—falling to a relatively spectrally-invariant constant for all three films. We previously saw this in the single-polarizer reflectance spectra in **Fig. 6.14**, and it can also be seen in the differential reflectance spectra in **Fig. A6.9**, where the images taken at 650 and 700 nm exhibit very weak but nonzero contrast. In this regime, only the MoS_2 absorbs, which we can see from the overlaid unpolarized absorption spectra (i.e., peaks M_A and M_B). However, since we know that the hexagonal lattice of MoS_2 begets an isotropic response to in-plane polarized light, the MoS_2 cannot explain the nonzero anisotropy. We therefore attribute this below-gap anisotropic response to the birefringence of the molecular films. Although the molecular crystal layers are only ~0.3 nm thick, the tilted-analyzer geometry allows us to clearly observe this small phase shift from the difference in the refractive indices ($n_{||} - n_{\perp}$) between the major and minor axes of the crystals, which is strongest for PDI and weakest for PTCDA.

One noteworthy observation here is that the below-gap anisotropy for PDI appears to peak at the A and B excitons of MoS_2 (this can also somewhat be seen in the spectrum for MPDI). Since θ_A was the same in all three cases, these peaks cannot be simply due to light from the MoS_2 leaking through the analyzer, otherwise they would show up in equal strength in the MPDI and PTCDA spectra. This could imply that there is some interaction with the molecular film and the TMD substrate that manifests as a change in the optical response of the molecular

crystal at the TMD absorption peaks, but more measurements need to be done to understand this fully.

6.6.3 Crystal Structure to Polarized Response

We saw in the previous subsection that the spectral behavior of the three perylene crystals are quite similar, since these properties originate from the intrinsic optical properties (i.e., n and k) of the molecular base, which is the same in all cases. The polarization-dependent behavior, however, is determined by the structure of each crystal, which we know to be different between the three. We return to our discussion of the peak corresponding to the lowest energy absorption feature of PTCDA, which is actually split into two components between the θ_c = -45° and θ_c = +45° domains, respectively (**Fig. 6.16c**). This is due to Davydov splitting, as previously introduced in our discussion of the single-polarizer reflectance data in **Fig. 6.14**, where the bimolecular unit cell of PTCDA results in a splitting of the oscillator strength into higher and lower energy states that absorb at orthogonal polarizations. Furthermore, if we look at the reflection anisotropy of the split peaks (**Fig. 6.17c**), it now appears that the two Davydov states do indeed exhibit different oscillator strengths ($|RA| \approx 0.45$ at 555 nm and $|RA| \approx 0.3$ at 570 nm) with the higher-energy state being stronger in this case. This is consistent with our expectation, since $\gamma \neq 0°$ for PTCDA. The MPDI film, which also exhibits a bimolecular unit cell, still seems to lack Davydov splitting features, even in the tilted-analyzer geometry.

For a clearer comparison between the three crystals, **Figure 6.18a** overlays the differential reflectance spectra (colored lines; taken at θ_A = -3°) of the θ_c = -45° domains for each crystal, plus the θ_c = +45° domain of PTCDA (i.e., lower Davydov component). The gray lines shows the spectrum of a bare MoS_2 film taken under the same instrumental conditions, for comparison. Using the structures of each unit cell presented in **Fig. 6.18b**, we can now fully

understand the large difference in the anisotropic responses between the three perylene-based films we saw in the images in **Fig. 6.12**. The strongest response, which peaks between 555-580 nm, originates from the linear dichroism of the molecular crystals. We can see that anisotropy at these energies is greatest for the PDI film (**Fig. 6.18a**, purple line). This is because PDI crystals have largest number of oscillators oriented in the same direction, due to the molecules being aligned parallel ($\gamma = 0$; **Fig. 6.18b**, top panel) and the crystal having the highest packing density (**Table 6.1**). The PTCDA film exhibits the weakest overall contrast (**Fig. 6.18a**, red lines) as a result of the large value of γ and a bimolecular unit cell (**Fig. 6.18b**, bottom panel) that leads to a division of the oscillator strength between two Davydov components. Although the MPDI film (**Fig. 6.18a**, pink line) has the smallest density, the anisotropy is still stronger than PTCDA, due to the smaller angle between molecules (**Fig. 6.18b**, middle panel) and lack of Davydov splitting. It is not clear why the MPDI crystals lack Davydov splitting features. This seems to imply that the molecules in the unit cell interact very

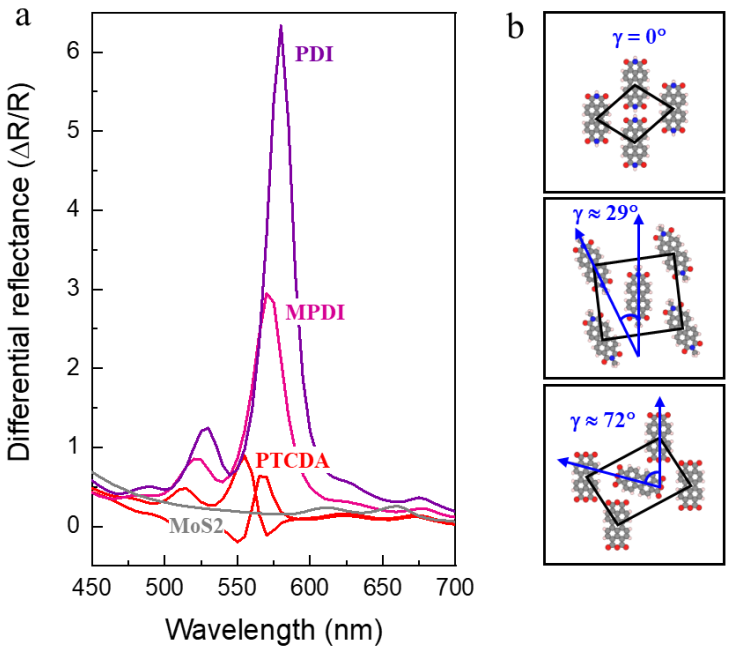

Figure 6.18. a) Overlaid differential reflectance spectra of PDI on MoS_2 (purple; θ_c = -45°), MPDI on MoS_2 (pink; θ_c = -45°), PTCDA on MoS_2 (red; θ_c = -45° and +45°), and bare MoS_2 (gray) taken with θ_A = -3°, all on fused silica substrates. b) Unit cells of the three molecular crystals, where the top panel is for PDI, middle panel is for MPDI, and bottom panel is for PTCDA.

weakly with each other, possibly due to the large distance between them caused by the bulky methyl groups.

As a final note, we can see from **Fig. 6.18** that cross-polarized microscopy is extremely sensitive to structural anisotropy resulting from the packing density and angles of the molecules. Hence, domains that have the same contrast maxima (and same spectral anisotropy) are likely to have the same structure. We can now see clearly that the data in **Fig. 6.11b** imply that the phase of individual domains in our molecular films is highly pure. Such uniformity is unexpected for molecular monolayers, which typically deposit in a mixture of phases as a result of their highly reversible in-plane bonding.[5] We attribute this uncanny structural uniformity in our systems to our high-temperature deposition process, which weeds out most weakly-bound structures, promoting the formation of only the most thermally-stable crystal structure.

6.7 Calculation of Optical Constants for 2D Molecular Crystals

We find that the datasets collected in Sections 6.4-6.6 (both the rotation dependance and the spectral dependance) are highly reproducible for a given instrumental geometry. Hence, the natural next step would be to try to take the optical data and quantitatively extract some property of these 2D molecular crystals, such as their optical constants (i.e., n and k). Although fitting reflectance data is relatively straightforward for bulk materials, it is challenging for materials whose thickness is far less than the wavelength of the light, since the light will be experiencing some "averaged" optical constants—between the ultrathin layer in question and the materials on top and below it (on our case, air on top and MoS_2 and SiO_2 below). There has been significant effort to develop models to calculate the optical constants of two-dimensional films.[30] Our case, however, is even more complicated, for two reasons. First, our system consists of *two* atomically-thin layers (molecular crystal and TMD), and second, measuring the polarized

reflectance of 2D molecular crystals requires an unconventional instrumental geometry (i.e., cross-polarized microscopy) in order to achieve sufficient optical signal. Because of the latter point, even if we use existing 2D models for the optical constants, we still have to account for the effect of our instrumental geometry on the reflected intensity. As it turns out, the cross-polarized geometry adds additional variables that need to be accounted for to quantitatively fit the data.

To understand why this is the case, we can consider what we would expect to happen to the optical contrast (or differential reflectance) as we transition from the conventional (single-polarized) geometry to the cross-polarized geometry. The experimental data was previously shown in **Fig. A6.6**, where we see that the contrast increases as θ_A goes to 0º. Recall that the reason the contrast increases is because we are filtering out the s-polarized light from the isotropic substrate in favor of detecting the p-polarized light from the molecular crystal, where the optical contrast is reported in relation to the reflected intensity of the bare substate: $C = (I_{film} - I_{sub}) / I_{sub}$ (**Eq. 6.1**). There is one inconsistency here: because the substrate reflects no p-polarized light, at exactly $\theta_A = 0º$ we would expect I_{sub} to be zero. Hence, we would actually expect $C \rightarrow \infty$ as $\theta_A \rightarrow 0º$, which is clearly not the case experimentally (**Fig. A6.6**). Experimentally, the isotropic substrate still reflects a small amount of light at $\theta_A = 0º$. So even if we develop a model to calculate n and k from I_{film}, we still need to incorporate an equation for I_{sub} in order to relate the model to our measured optical contrast. Since I_{sub} is clearly is not following a behavior we would expect at $\theta_A = 0º$, we have to conclude that there is another variable present in these cross-polarized measurements that is unaccounted for, and causes the experimental data to deviate significantly from any simple model.

We have come across only one study in the literature that addresses the issue we have presented above.[18] This study found that the nonzero reflectance of the isotropic substrate in a

cross-polarized configuration is the result of birefringence from the objective lens, which is even present in objectives that are supposedly "strain-free". Linearly-polarized waves passing through the objective are slightly phase-shifted relative to one another, resulting in elliptically-polarized light that has a small projection onto the analyzer at $\theta_A = 0^o$. This birefringence from the instrumental components is not significant in conventional transmittance and reflectance measurements (single-polarized or even parallel-polarized) because those measurements are focused on detecting light from the sample that does not change polarization state (recall **Fig. 6.8a**). The small polarization change introduced by the objective is insignificant in comparison to the desired signal. Cross-polarized microscopy, however, focuses on the detection of the small amount of the light that *changed polarization*, and so the small polarization change induced by the objective is significant in comparison.

The study mentioned above[18] introduces a parameter for the objective birefringence, η, which is a positive or negative number determined by fitting the experimentally-measured reflectance from the isotropic substrate at a small value of θ_A. They are then able to quantitatively fit for the *dielectric anisotropy*, $\Delta\varepsilon$ (i.e., the difference in the dielectric constants along the major and minor axes), of a films of organic adsorbates on graphene. The reason that they fit for $\Delta\varepsilon$ and not for the absolute dielectric constants is due to a completely separate issue—even ignoring the effects of objective strain, there are already too many variables and not enough equations to fit them. A conventional measurement would have four variables and four equations: with the variable being the optical constants along the major axis ($n_{||}$ and $k_{||}$) and minor axis ($n_{\perp}$ and $k_{\perp}$) and the equations being the reflectance and transmittance for light polarized along the major axis ($R_{||}$ and $T_{||}$) and minor axis ($R_{\perp}$ and $T_{\perp}$). We only have the cross-polarized reflection signal, i.e., $C_{||}$ and $C_{\perp}$. Thus, the study we are referencing derived an

equation for the optical contrast in terms of the difference between the dielectric constants of the axis: $\Delta\varepsilon' = \varepsilon'_{||} - \varepsilon'_{\perp}$ and $\Delta\varepsilon'' = \varepsilon''_{||} - \varepsilon''_{\perp}$.

We worked extensively with the assistance of Myungjae Lee to try to apply the equation derived in Ref. 18 to our system of 2D molecular crystal on TMD. To do this, we measured the contrast (or differential reflectance) for domains with different θ_c at various θ_A between +10º and -10º (i.e., like taking a vertical slice of the data presented in **Fig. A6.6**). **Fig. A6.11** plots the experimental data corresponding to the contrast vs. θ_A for a film of PTCDA/MoS_2 for θ_c = +45º and θ_c = -45º (the two domains that have the brightest and darkest responses, respectively, in a tilted-analyzer geometry). The data was take at 565 nm. Unfortunately, even with inclusion of the objective birefringence, we could not find any combination of $\Delta\varepsilon'$ and $\Delta\varepsilon''$ that fit both the θ_c = +45º and θ_c = -45º domains using the equation given in the paper. Although we found it possible to fit any single domain very well (see **Fig. A6.11a**, red line), the same values for $\Delta\varepsilon'$ and $\Delta\varepsilon''$ could not reproduce the other θ_c (**Fig. A6.11a**, black line). Basically, we have seen that our molecular crystals flip their relative intensities as the analyzer is rotated through θ_A = 0º, and that the maximum contrast at positive and negative θ_A are equal (**Fig. 6.9**, red and blue lines). The model from Ref. 18, however, predicts that that the "flipping" point should occur at $\theta_A \neq 0$º and that the maximum contrast is weaker on one side of the analyzer (**Fig. A6.11a**, black and red lines). In other words, the model does not reproduce the θ_c-dependance of the contrast, although it can reproduce the θ_A-dependence.

Interestingly, we found that it is possible to simultaneously fit all θ_c if we make one change to the equation: we allow the domains to experience different *signs* for the objective birefringence parameter, η (**Fig. A6.11b**, black and red lines). The data fits extremely well if we choose η to be positive for domains with $0º < \theta_c < 90º$ and negative for domains with $90º < \theta_c <$

180º (or -90º < θ_c < 0º). This change that we made to achieve the fit in **Fig. A6.11b** is clearly nonphysical, since the direction of the phase shift of the light from the objective is independent of anything related to the film under study. Furthermore, the values of Δε' and Δε" produced from this fit were unrealistic—the real part (Δε') was much greater than the imaginary part (Δε"), which is unlikely considering we already know that from **Fig. 6.17** that the anisotropy in our molecular crystals is dominated by absorption. Even after checking the entire derivation, however, we could never identify any approximation used by the authors (although there were many approximations) that could explain why changing the sign for η allowed the fit to be possible. We do know that the main difference between the system from Ref. 18 and our system is that our molecules are absorbing, while the molecular adsorbates studied in the reference were not. Although we are not sure now this could cause the difference, it could be tested by repeating the contrast vs. θ_A experiment, except using an excitation below the band gap of the molecules (the below-gap response for PTCDA is too weak for this, but it may be possible to do the experiment with PDI).

We decided to put the equation from Ref. 18 aside and try to develop our own model to fit the data, using fewer approximations. To do this, we decided to start with the simplest picture: ignore the atomically-thin nature of the films and treat each layer of the sample as a separate (bulk) material. We used Fresnel's equations to define the relationship between the reflectance and the optical constants (n and k) and simply added together the reflectance from each of the four interfaces, plus one internal reflection in the SiO_2 layer (as illustrated by the paths of the black arrows in **Fig. 6.19a**). We then used the Jones Matrix method to calculate the final reflectance through crossed-polarizers, also incorporating a term for the objective birefringence (measured experimentally). Because we still had the issue of two many variables, we decided to

input the bulk optical constants for PTCDA ($n_{P||}$, $k_{P||}$, $n_{P\perp}$, $k_{P\perp}$) and the optical constants for monolayer MoS_2 (n_M and k_M) into the equation, and then fit for **a***n_P, **a***k_P, **b***n_M, and **b***k_M, where a and b are constants. We fit these two variables manually since we did not make any approximations in the math, which made an analytical solution infeasible.

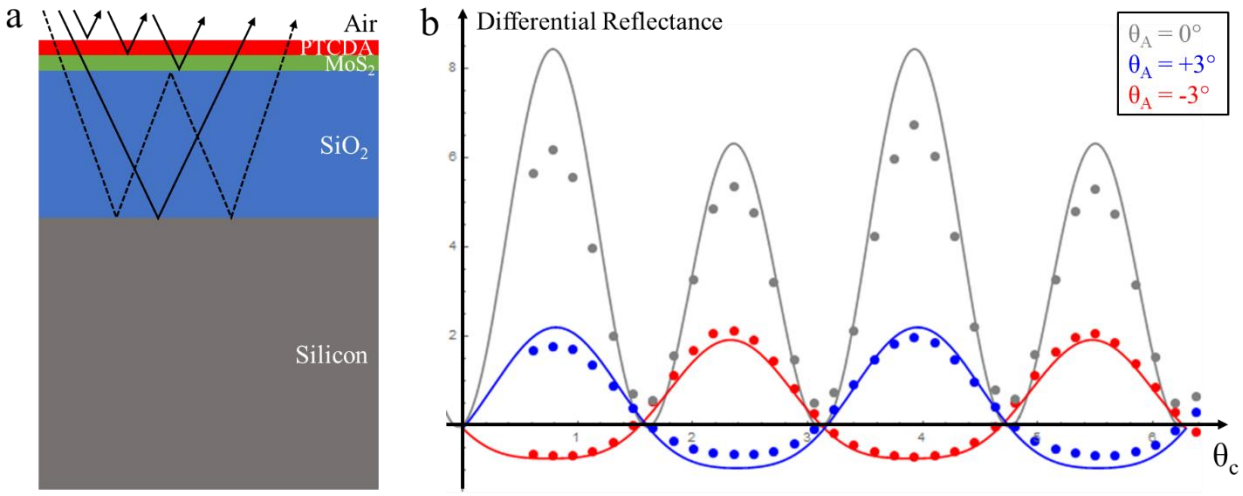

Figure 6.19. a) Diagram illustrating of the structure of a PTCDA/MoS_2 film on SiO_2/Si, where the black arrows indicate the reflections from each interface that were considered in our calculation (four interfaces = solid arrows plus one internal reflection in the SiO_2 = dashed arrow). b) Differential reflectance (contrast) vs. domain rotation from $\theta_c = 0^o$ to $\theta_c = 360^o$ for a domain with the film structure shown in (a), measured for three analyzer tilt angles $\theta_A = 0°$ (gray), +3° (blue), and -3° (red) at λ = 565 nm. The points correspond to the experimental data (taken at 565 nm) and the lines are the corresponding fits.

The results of the fit are shown in **Fig. 6.19b**, where we simultaneously fit the differential reflectance (contrast) vs. θ_c for PTCDA/MoS_2 (on SiO_2/Si) for $\theta_A = 0^o$ (gray), $+3^o$ (blue), and -3^o (red). The points correspond to the experimental data (taken at 565 nm) and the lines are the corresponding fits. From this, we found a = 0.6 and b = 1.2. The results seem reasonable, given they are not too far from the literature values. Furthermore, if we calculate $\Delta\varepsilon$ from our fitted values of n and k, we find that the imaginary part of $\Delta\varepsilon$ is significantly larger than that of the real part (as expected). Hence, we see that the values are more realistic than what we obtained from the equation in Ref. 18. This indicates that there was indeed some approximation made in the derivation in Ref. 18 that does not apply to our system.

Although our model is oversimplified, the results are already promising. Still, we would need to improve our calculation further before we can trust the accuracy of the fitted values. To start, we should measure the optical constants of our monolayer MoS_2 using an independent measurement, to either remove those variables or get a narrower range for them. We should then find a way to independently fit n and k for the molecular crystal (rather than restrict them to be equal fractions of their bulk values) but that would require one more equation. We did come across one study that tried to address this issue by measuring the optical contrast of black phosphorous on both a SiO_2/Si substrate and a fused silica substrate to obtain four equations, and then fitting these equations for the same four optical constants.[13] This study was carried out with parallel polarizers, but we could consider implementing a similar approach for our crossed-polarized calculation (although the equation would be complex).

6.8 Summary

In this chapter, we used a combination of structural characterization and spectroscopy measurements to investigate the relationship between the nanoscopic structures of 2D perylene-based crystals and their macroscopic optical responses. AFM, GISAXS, and STM measurements show that we are able to produce single-atom-thick molecular crystals of perylene derivatives over the film scale. Furthermore, each of these crystals exhibit unique in-plane nanoscopic ordering—different densities, angles between molecules, and number of molecules per unit cell—which are direct consequences of the small structural differences between the molecules that modify their intermolecular forces. Because the unit cells are optically anisotropic, we visualized the structure and morphology of the molecular films over a larger scale using imaging measurements based on polarized illumination, such as Raman mapping and reflectance microscopy. We further studied the differences in the spectral response of each crystal with

polarized light by varying the incident light energy in the visible regime, using an unconventional cross-polarized spectroscopy technique, supplemented by conventional absorption and reflectance measurements. Through this, we are able to understand both how the intrinsic optical properties of the molecule (i.e., linear dichroism and linear birefringence) influence the crystal's interactions with different light energies, as well as how the structure of the unit cell influences the crystal's interactions with different light polarizations. Although we were unsuccessful in fitting our cross-polarized optical data to the best existing model in literature, we were able to extract ballpark values for the optical constants of a PTCDA/MoS_2 film by using the full form of the equation obtained using the Jones matrix method.

6.9 Appendix

	PDI	**MDPI**	**PTCDA**
Phase	Brick wall	Canted	Herringbone
a (nm)	0.96	1.55	1.25
b (nm)	1.12	1.68	1.85
θ (°)	69.6	85.8	85.7
γ (°)	0	29.0	72.7

Table A6.1. Complete set of lattice parameters for the PDI, MPDI, and PTCDA molecular crystals, where a, b, θ, and γ are defined in Fig. 6.5.

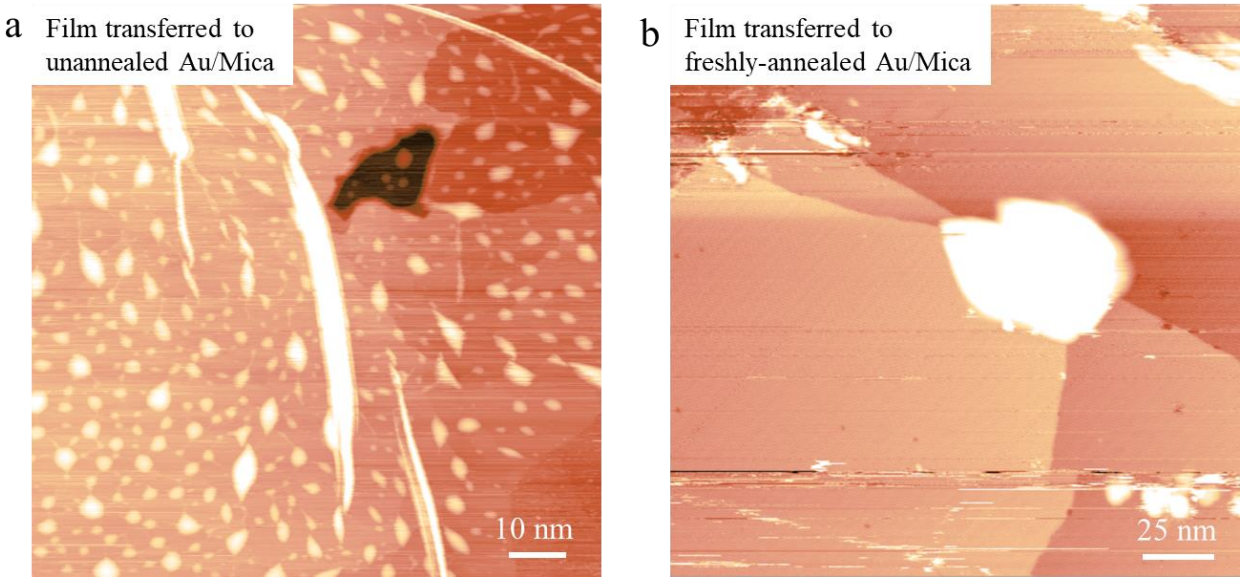

Figure A6.1. Effect of Au surface cleaning on the morphology of water-transferred molecule/TMD films for STM. a) A 100 x 100 nm image of a MPDI/MoS_2 film transferred to a Au/Mica substrate that was newly-opened from the manufacturer's packaging, but otherwise used immediately, and b) a 200 x 200 nm image of a PTCDA/MoS_2 film transferred to a Au/Mica substrate that was Ar sputter-annealed immediately before transfer.

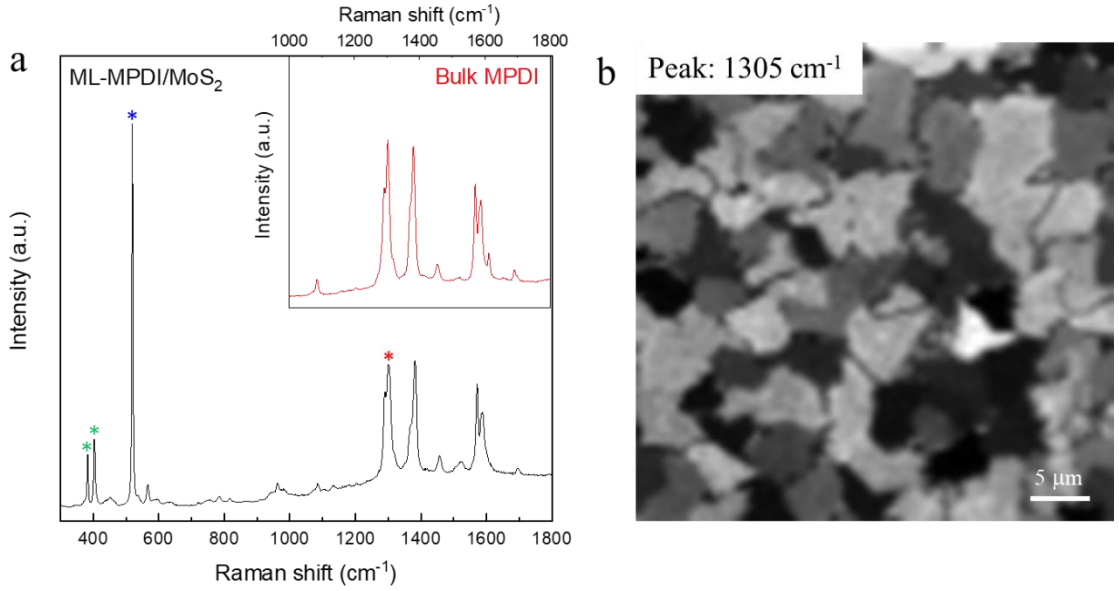

Figure A6.2. a) Raman spectrum of a monolayer MPDI crystal on MoS_2 (black line), with the spectrum for bulk MPDI given in the inset (red line). Green stars mark the Raman peaks for MoS_2, blue star for Si, and red star for the MPDI Raman feature used to generate the map in part (b), and b) Raman map of a monolayer MPDI film on MoS_2, imaged using the Raman mode at 1305 cm^{-1}.

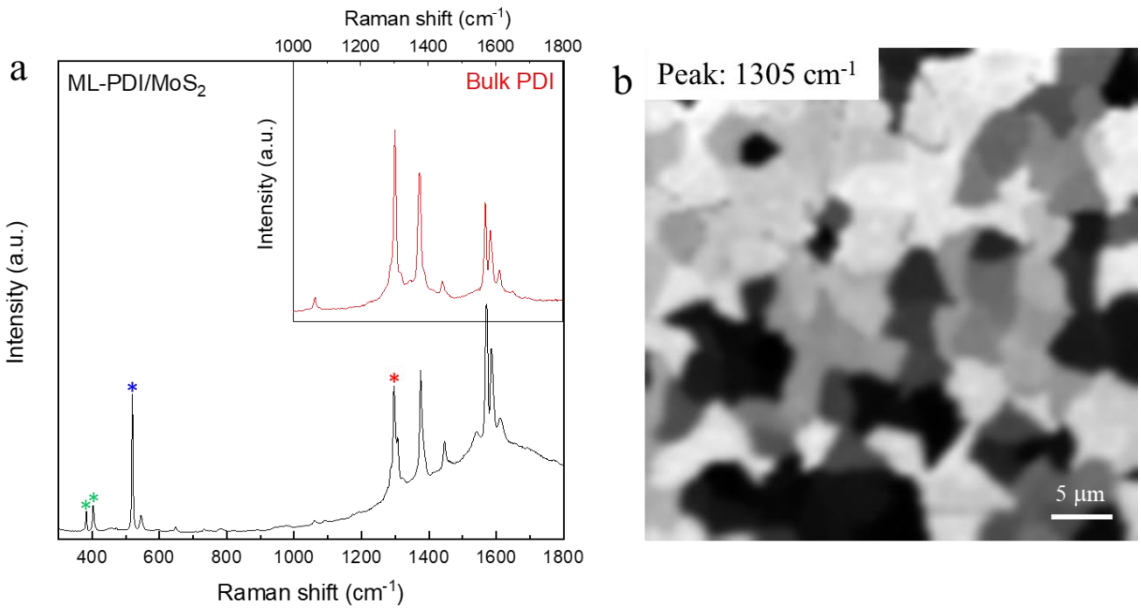

Figure A6.3. a) Raman spectrum of a monolayer PDI crystal on MoS_2 (black line), with the spectrum for bulk PDI given in the inset (red line). Green stars mark the Raman peaks for MoS_2, blue star for Si, and red star for the PDI Raman feature used to generate the map in part (b), and b) Raman map of a monolayer PDI film on MoS_2, imaged using the Raman mode at 1305 cm^{-1}.

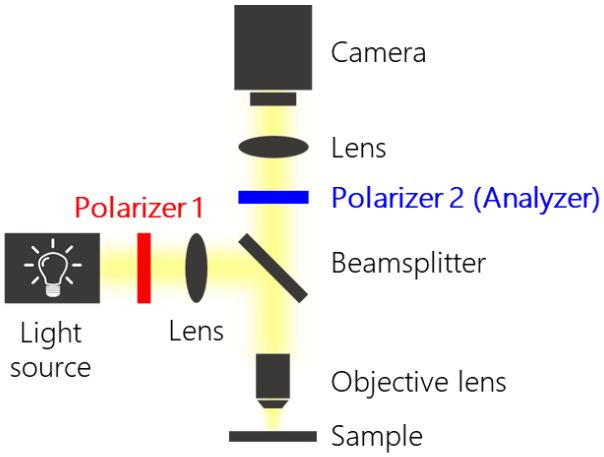

Figure A6.4. Instrumental setup for tilted-analyzer microscopy measurements. The optical components used on the instrument are as follows: Xenon lamp illumination source (Hamamatsu, L2174-01) with monochromator (Optical Building Blocks), 1500 grit diffuser (Thorlabs, DGUV10-1500), broadband polarizers (Thorlabs, LPVISE100-A), f = 30 mm achromatic lens (Thorlabs, AC254-030-A-ML), 10R-90T beamsplitter (Thorlabs, BSN10R), 20x strain free objective lens (Olympus, UPLFLN-P), f = 200 mm tube lens (Thorlabs, ITL200), CMOS camera (pco.edge).

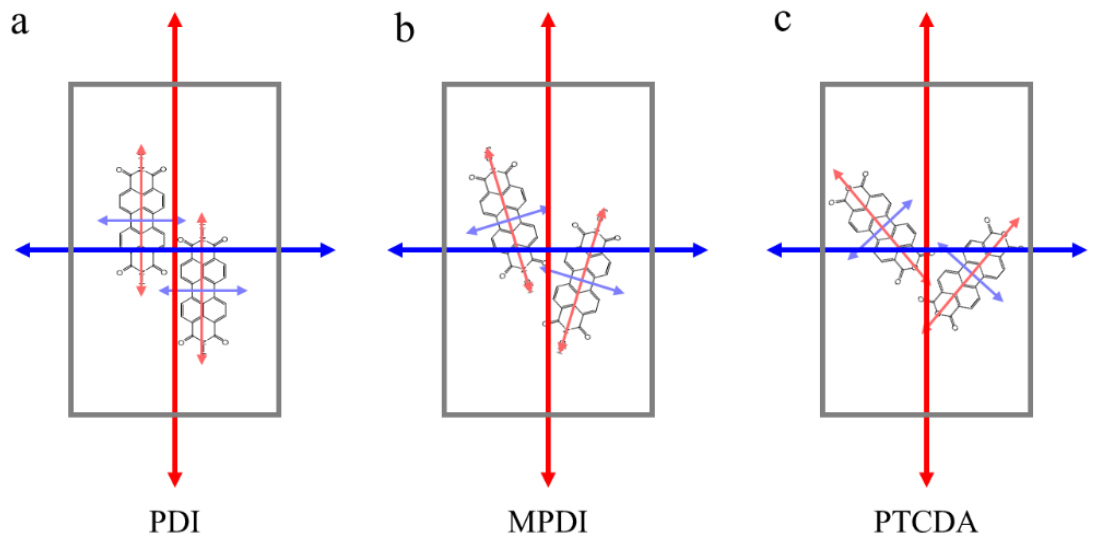

Figure A6.5. Schematics illustrating the expected relationship between the major and minor axes of the crystal's unit cell (large red and large blue arrows, respectively) to the major and minor axes of the constituent molecules (small red and small blue arrows, respectively) for a) PDI, b) MPDI, and c) PTCDA.

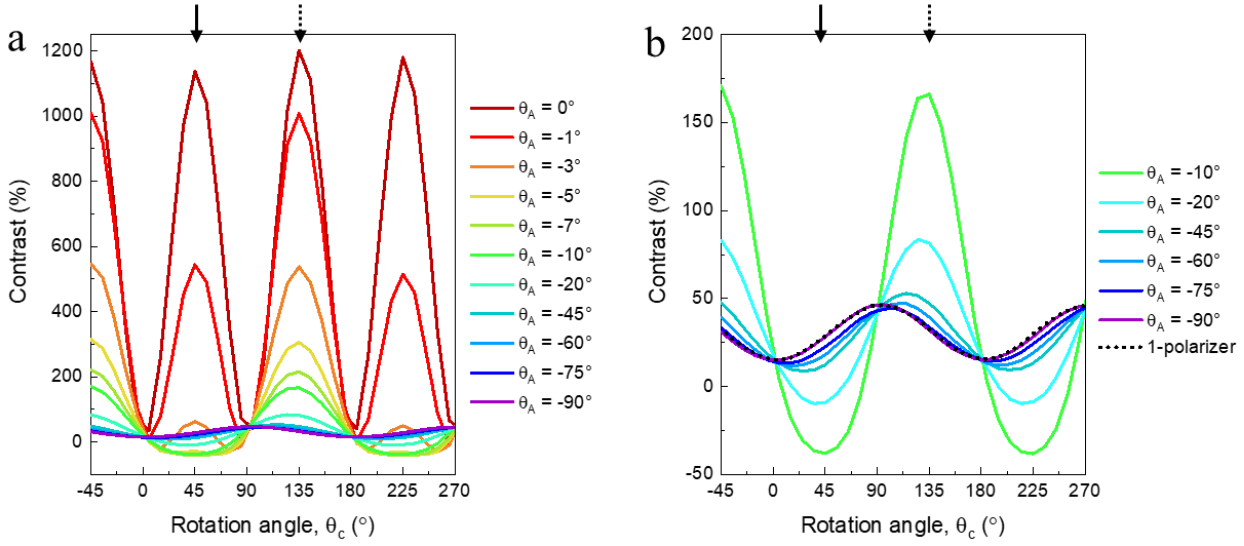

Figure A6.6. How the contrast vs. θ_c for a PDI domain (deposited on MoS_2 grown on a Si/SiO_2 substrate) evolves as the analyzer is rotated counterclockwise, from being exactly cross-polarized (i.e., $\theta_A = 0°$) all the way to parallel polarizers (i.e., $\theta_A = 90°$). The full range of data is given in (a), while (b) zooms in on the data for $\theta_A > -10°$, adding one more plot where the analyzer was completely removed (i.e., single-polarizer configuration; dotted black line). The solid black arrows point to the $\theta_c = +45°$ orientation, and the dashed black arrows point to the $\theta_c = -45° = +135°$ orientation, to emphasize their rapidly diverging responses as θ_A is changed.

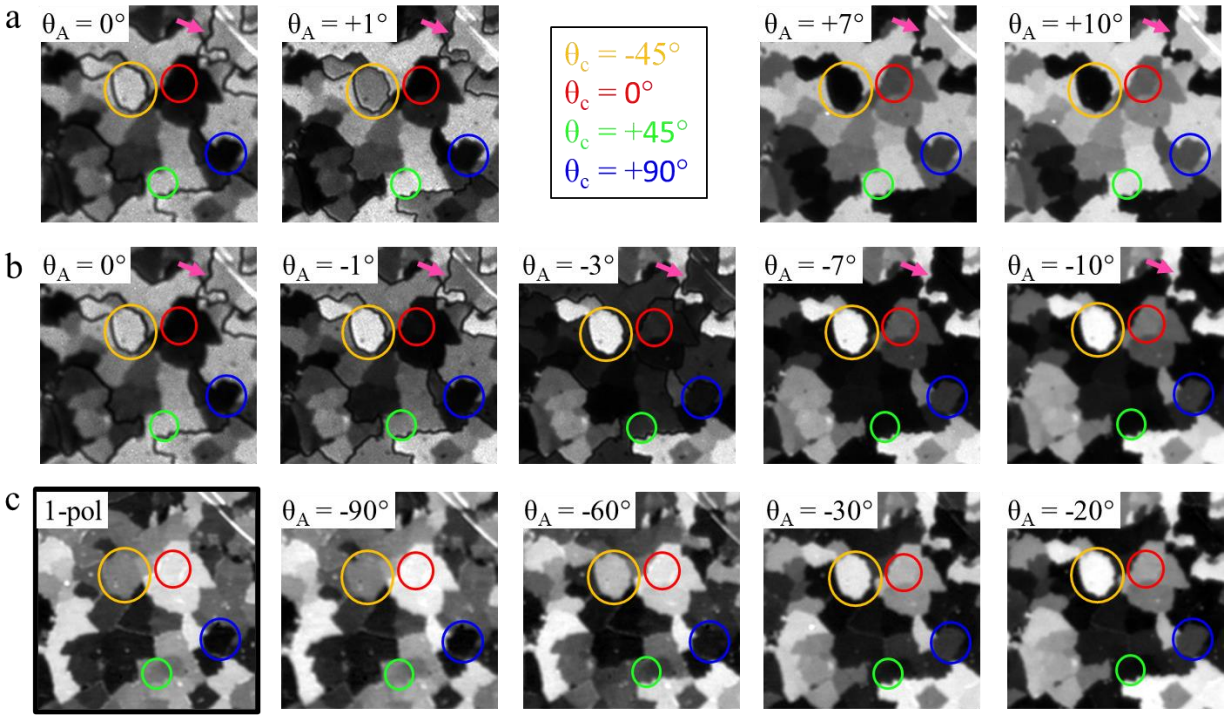

Figure A6.7. How the image of a PDI film (deposited on MoS_2 grown on a Si/SiO_2 substrate) changes with instrumental geometry, where a) shows the effect of rotating the analyzer CW, b) shows the effect of rotating the analyzer by the same amount CCW, and c) shows what happens at very large θ_A. The single-polarizer image (first panel in (c)) is outlined with a black box. The θ_c = -45°, 0°, +45°, and +90° are circled in yellow, red, green, and blue, respectively, and the θ_c = -45° domain was the one used to collect the rotation data in Fig. A6.6. The pink arrows point to a boundary between two domains that appears especially dark in the images where θ_A is close to 0° but disappears at larger θ_A.

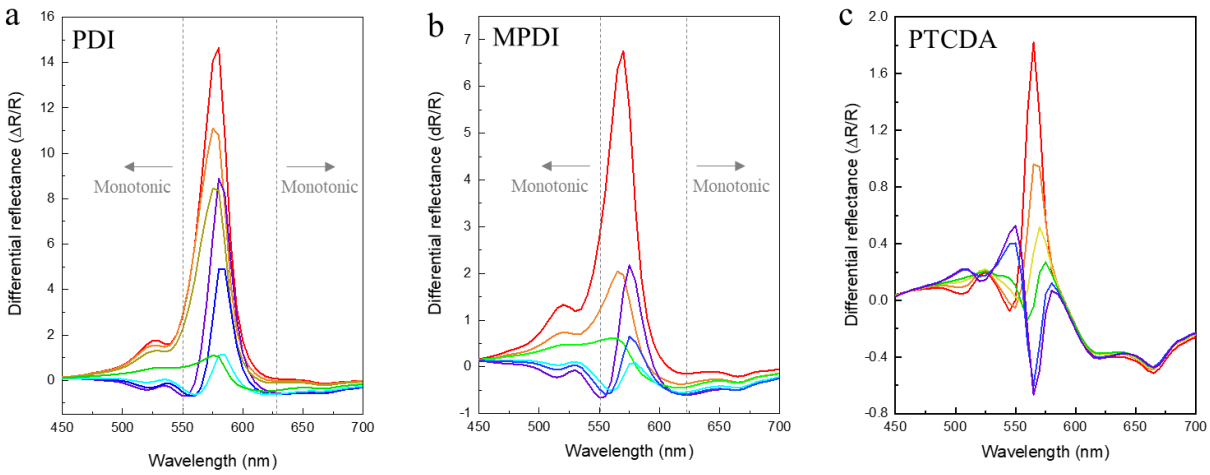

Figure A6.8. Differential reflectance spectra of many crystal domains in films of a) PDI, b) MPDI, and c) PTCDA deposited on MoS_2 grown on SiO_2/Si substrates, taken in a tilted-analyzer geometry with θ_A = -3°. Although the PTCDA spectra exhibit a monotonic intensity change with crystal rotation over the entire visible range, the PDI and MPDI spectra only exhibit this behavior at $\lambda < 550$ nm and $\lambda > 625$ nm.

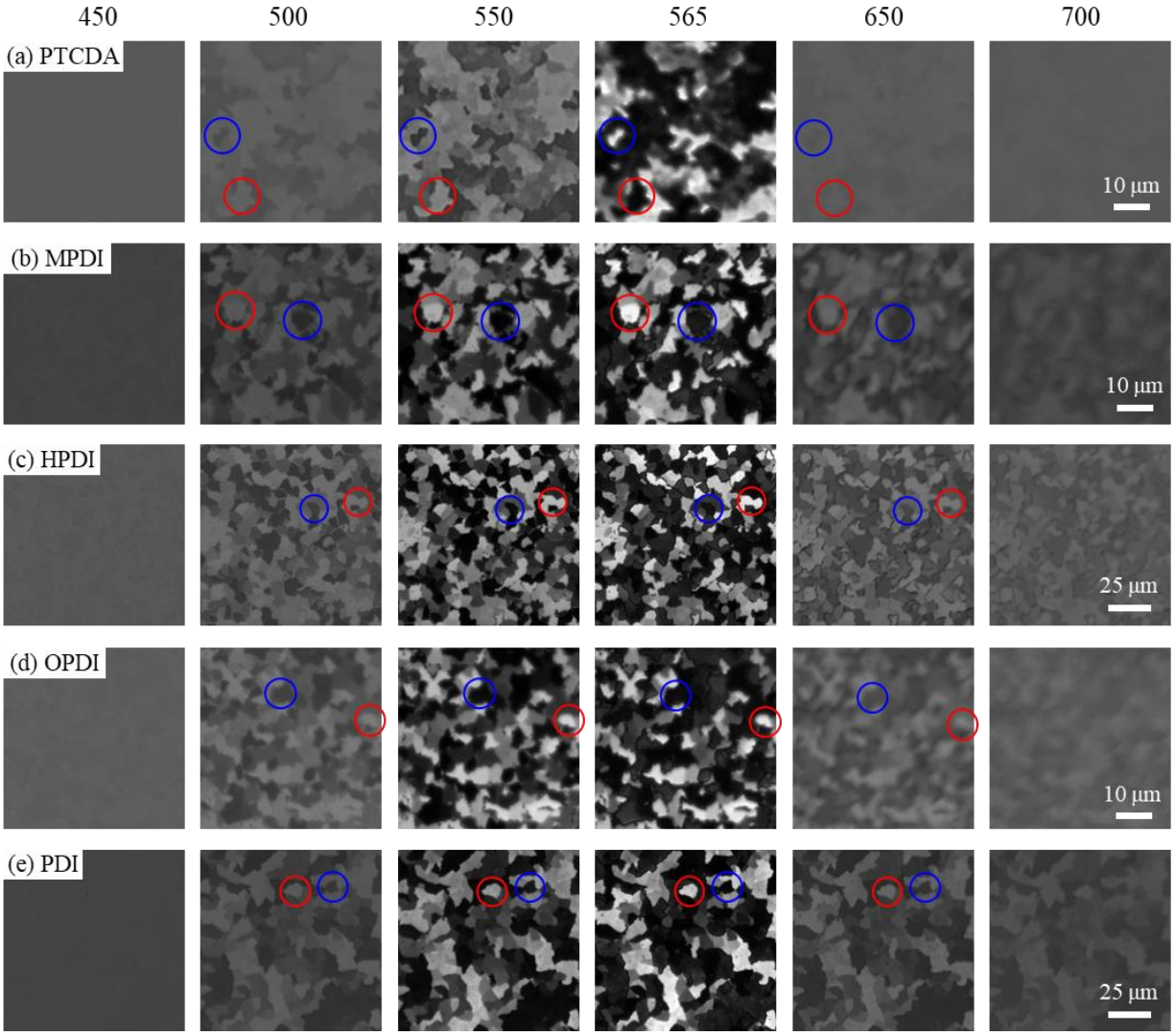

Figure A6.9. Snapshots of the image spectra of the various molecular crystals studied in this thesis, deposited on MoS_2 grown on SiO_2/Si. The images are all taken at θ_A = -3°, with the wavelengths of the images listed at the top of the figure. Red circles indicate the domains with the brightest overall response (similar to the red spectra in Fig. 6.16 and Fig. A6.10), and blue circles indicate the domains with the darkest overall response (similar to the blue spectra in Fig. 6.16 and Fig. A6.10). For the PDI derivatives, MPDI (b), HPDI (c), OPDI (d), and PDI (e), the domains retain their relative intensities over the entire spectral range. For PTCDA (a) the intensities of the two domains flip between 550 and 565 nm.

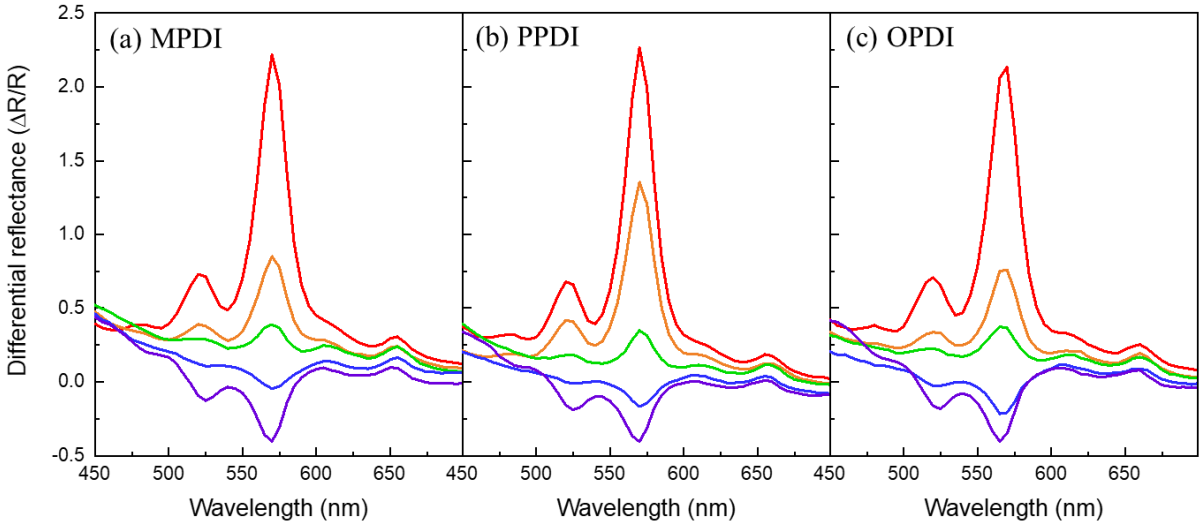

Figure A6.10. Differential reflectance spectra of many crystal domains in films of a) MPDI, b) PPDI, and c) HPDI deposited on MoS_2 grown on fused silica substrates, taken in a tilted-analyzer geometry with θ_A = -3°. All spectra are shown in the same scale.

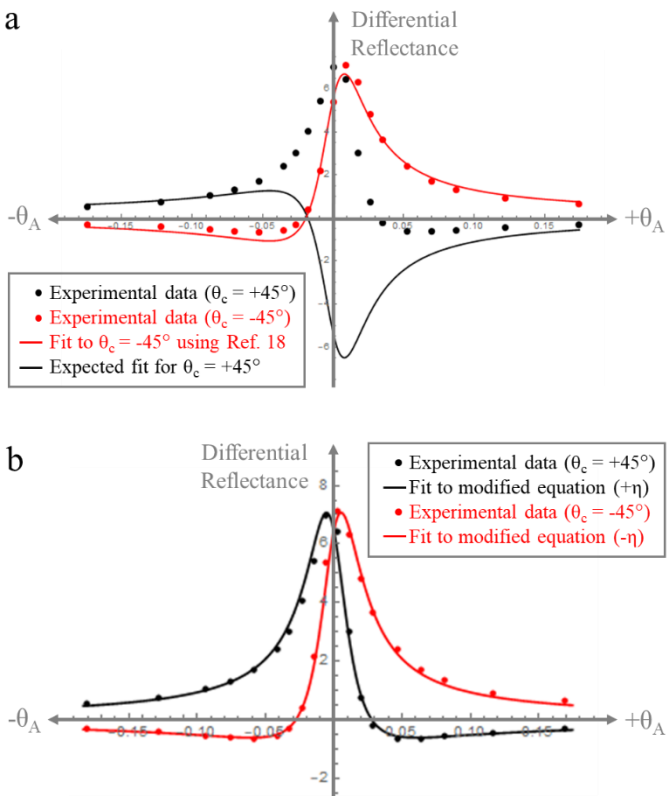

Figure A6.11. Differential reflectance (contrast) vs. analyzer tilt angle for two domains of PTCDA/MoS_2 (on SiO_2/Si) with θ_c = +45º (black points) and θ_c = -45º (red points), measured from θ_A = -10° to θ_A = +10° at λ = 565 nm. a) Red line: Fit for Δε' and Δε" for the θ_c = -45º domain using the equation from Ref. 18. Black line: what the same equation predicts should be the response for the θ_c = +45º domain if the values of Δε', Δε", and η from the red fit are reinput into the equation and θ_c in the equation is manually changed to +45º. b) Fit for Δε' and Δε" obtained using a modified version of the equation from Ref. 18, where η was allowed to change signs depending on θ_c (|η| was measured to be 0.017). +η was used for the θ_c = +45º domain (black line) and -η was used for the θ_c = -45º domain (red line), resulting in Δε' = 12.5 and Δε" = 5 for both domains, but these values are likely nonphysical.

6.10 References

(1) Saleh, B. E. A.; Teich, M. C. *Fundamentals of Photonics*, 2nd ed.; Wiley series in pure and applied optics; Wiley Interscience: Hoboken, N.J, 2007.

(2) Casamayou-Boucau, Y.; Ryder, A. G. Extended Wavelength Anisotropy Resolved Multidimensional Emission Spectroscopy (ARMES) Measurements: Better Filters, Validation Standards, and Rayleigh Scatter Removal Methods. *Methods Appl. Fluoresc.* **2017**, *5* (3), 037001.

(3) Kang, K.; Lee, K.-H.; Han, Y.; Gao, H.; Xie, S.; Muller, D. A.; Park, J. Layer-by-Layer Assembly of Two-Dimensional Materials into Wafer-Scale Heterostructures. *Nature* **2017**, *550* (7675), 229–233.

(4) Zhong, Y.; Cheng, B.; Park, C.; Ray, A.; Brown, S.; Mujid, F.; Lee, J.-U.; Zhou, H.; Suh, J.; Lee, K.-H.; Mannix, A. J.; Kang, K.; Sibener, S. J.; Muller, D. A.; Park, J. Wafer-Scale Synthesis of Monolayer Two-Dimensional Porphyrin Polymers for Hybrid Superlattices. *Science* **2019**, *366* (6471), 1379–1384.

(5) Mura, M.; Silly, F.; Briggs, G. A. D.; Castell, M. R.; Kantorovich, L. N. H-Bonding Supramolecular Assemblies of PTCDI Molecules on the Au(111) Surface. *J. Phys. Chem. C* **2009**, *113* (52), 21840–21848.

(6) Schmidt, A.; Schuerlein, T. J.; Collins, G. E.; Armstrong, N. R. Ordered Ultrathin Films of Perylenetetracarboxylic Dianhydride (PTCDA) and Dimethylperylenebis(Dicarboximide) (Me-PTCDI) on Cu(100): Characterization of Structure and Surface Stoichiometry by LEED, TDMS, and XPS. *J. Phys. Chem.* **1995**, *99* (30), 11770–11779.

(7) Swarbrick, J. C.; Ma, J.; Theobald, J. A.; Oxtoby, N. S.; O'Shea, J. N.; Champness, N. R.; Beton, P. H. Square, Hexagonal, and Row Phases of PTCDA and PTCDI on Ag−Si(111) × ***R*** **30°**. *J. Phys. Chem. B* **2005**, *109* (24), 12167–12174.

(8) Kim, D. W.; Kim, Y. H.; Jeong, H. S.; Jung, H.-T. Direct Visualization of Large-Area Graphene Domains and Boundaries by Optical Birefringency. *Nature Nanotech* **2012**, *7* (1), 29–34.

(9) Arslan Shehzad, M.; Hoang Tien, D.; Waqas Iqbal, M.; Eom, J.; Park, J. H.; Hwang, C.; Seo, Y. Nematic Liquid Crystal on a Two Dimensional Hexagonal Lattice and Its Application. *Sci Rep* **2015**, *5* (1), 13331.

(10) Fesenko, P.; Rolin, C.; Janneck, R.; Bommanaboyena, S. P.; Gaethje, H.; Heremans, P.; Genoe, J. Determination of Crystal Orientation in Organic Thin Films Using Optical Microscopy. *Organic Electronics* **2016**, *37*, 100–107.

(11) Rivnay, J.; Jimison, L. H.; Northrup, J. E.; Toney, M. F.; Noriega, R.; Lu, S.; Marks, T. J.; Facchetti, A.; Salleo, A. Large Modulation of Carrier Transport by Grain-Boundary Molecular Packing and Microstructure in Organic Thin Films. *Nature Mater* **2009**, *8* (12), 952–958.

(12) Vrijmoeth, J.; Stok, R. W.; Veldman, R.; Schoonveld, W. A.; Klapwijk, T. M. Single Crystallites in "Planar Polycrystalline" Oligothiophene Films: Determination of Orientation and Thickness by Polarization Microscopy. *Journal of Applied Physics* **1998**, *83* (7), 3816–3824.

(13) Mao, N.; Tang, J.; Xie, L.; Wu, J.; Han, B.; Lin, J.; Deng, S.; Ji, W.; Xu, H.; Liu, K.; Tong, L.; Zhang, J. Optical Anisotropy of Black Phosphorus in the Visible Regime. *J. Am. Chem. Soc.* **2016**, *138* (1), 300–305.

(14) Austin, A.; Hestand, N. J.; McKendry, I. G.; Zhong, C.; Zhu, X.; Zdilla, M. J.; Spano, F. C.; Szarko, J. M. Enhanced Davydov Splitting in Crystals of a Perylene Diimide Derivative. *J. Phys. Chem. Lett.* **2017**, *8* (6), 1118–1123.

(15) Cocchi, C.; Breuer, T.; Witte, G.; Draxl, C. Polarized Absorbance and Davydov Splitting in Bulk and Thin-Film Pentacene Polymorphs. *Phys. Chem. Chem. Phys.* **2018**, *20* (47), 29724–29736.

(16) Tanaka, J. Electronic Absorption Spectra of Molecular Crystals. *Prog. Theor. Phys. Suppl.* **1959**, *12*, 183–210.

(17) Szilágyi, A. *EMANIM: Interactive Visualization of Electromagnetic Waves*; 2019. URL: https://emanim.szialab.org/index.html

(18) Gallagher, P.; Li, Y.; Watanabe, K.; Taniguchi, T.; Heinz, T. F.; Goldhaber-Gordon, D. Optical Imaging and Spectroscopic Characterization of Self-Assembled Environmental Adsorbates on Graphene. *Nano Lett.* **2018**, *18* (4), 2603–2608.

(19) Hattori, Y.; Kitamura, M. Crystal Orientation Imaging of Organic Monolayer Islands by Polarized Light Microscopy. *ACS Appl. Mater. Interfaces* **2020**, *12* (32), 36428–36436.

(20) Engel, E.; Schmidt, K.; Beljonne, D.; Brédas, J.-L.; Assa, J.; Fröb, H.; Leo, K.; Hoffmann, M. Transient Absorption Spectroscopy and Quantum-Chemical Studies of Matrix-Isolated Perylene Derivatives. *Phys. Rev. B* **2006**, *73* (24), 245216.

(21) Ferguson, A. J.; Jones, T. S. Photophysics of PTCDA and Me-PTCDI Thin Films: Effects of Growth Temperature. *J. Phys. Chem. B* **2006**, *110* (13), 6891–6898.

(22) Scholz, R.; Kobitski, A. Yu.; Kampen, T. U.; Schreiber, M.; Zahn, D. R. T.; Jungnickel, G.; Elstner, M.; Sternberg, M.; Frauenheim, Th. Resonant Raman Spectroscopy of 3,4,9,10-Perylene-Tetracarboxylic-Dianhydride Epitaxial Films. *Phys. Rev. B* **2000**, *61* (20), 13659–13669.

(23) Zhao, H.; Zhao, Y.; Song, Y.; Zhou, M.; Lv, W.; Tao, L.; Feng, Y.; Song, B.; Ma, Y.; Zhang, J.; Xiao, J.; Wang, Y.; Lien, D.-H.; Amani, M.; Kim, H.; Chen, X.; Wu, Z.; Ni, Z.; Wang, P.; Shi, Y.; Ma, H.; Zhang, X.; Xu, J.-B.; Troisi, A.; Javey, A.; Wang, X. Strong Optical Response and Light Emission from a Monolayer Molecular Crystal. *Nat Commun* **2019**, *10* (1), 5589.

(24) Sun, B.; Xu, X.; Zhou, G.; Tao, L.; Xinran, W.; Chen, Z.; Xu, J.-B. Observation of Strong *J*-Aggregate Light Emission in Monolayer Molecular Crystal on Hexagonal Boron Nitride. *J. Phys. Chem. A* **2020**, *124* (37), 7340–7345.

(25) Hestand, N. J.; Spano, F. C. Expanded Theory of H- and J-Molecular Aggregates: The Effects of Vibronic Coupling and Intermolecular Charge Transfer. *Chem. Rev.* **2018**, *118* (15), 7069–7163.

(26) Coates, E. Aggregation of Dyes in Aqueous Solutions. *Journal of the Society of Dyers and Colourists* **1969**, *85* (8), 355–368.

(27) Kistler, K. A.; Pochas, C. M.; Yamagata, H.; Matsika, S.; Spano, F. C. Absorption, Circular Dichroism, and Photoluminescence in Perylene Diimide Bichromophores: Polarization-Dependent H- and J-Aggregate Behavior. *J. Phys. Chem. B* **2012**, *116* (1), 77–86.

(28) Ji, C.; Lai, L.; Li, P.; Wu, Z.; Cheng, W.; Yin, M. Organic Dye Assemblies with Aggregation-induced Photophysical Changes and Their Bio-applications. *Aggregate* **2021**, *2* (4).

(29) Schwoerer, M.; Wolf, H. C. *Organic Molecular Solids*; 2008.

(30) Li, Y.; Heinz, T. F. Two-Dimensional Models for the Optical Response of Thin Films. *2D Mater.* **2018**, *5* (2), 025021.

CHAPTER SEVEN

Working Towards Integration: Ongoing Experiments and Future Directions

7.1 Introduction

Advancements in the field of crystal engineering have accelerated the development of molecular solids for electronics and optoelectronics,[1–3] applied optics,[4,5] pharmaceuticals,[6] and color applications.[7] Molecular thin films, in particular, have found use as both active components in displays technologies (e.g., liquid crystals) and flexible electronics (e.g., organic semiconductors), as well as support layers in such thin-film device structures. In trying to understand how to take any starting material and incorporate it into a useful technology, we can use the example of silicon. There are four stages of processes required to build electronic systems: synthesis of high-quality crystals, modification of the material via doping or metal/oxide deposition, pattering of the different layers into device structures, and integration with other components to produce functional technologies.

In this chapter, we will discuss preliminary work we have done in expanding our 2D molecular crystal platform in the areas of synthesis, modification, patterning, and integration. We will examine the limitations that we have experienced and suggest ideas for process improvement. We will further show the potential for these materials to be used in electrochromic device applications.

7.2 Synthesizing Complex Molecular Solids

With the understanding of this 2D molecular crystal deposition process that we have developed using the perylene-based molecular systems, we can think about extending this technique to more diverse or complex materials. In Section 5.6 we already discussed how reducing the reactor pressure to high vacuum levels ($< 10^{-4}$ torr) and lowering the substrate

temperature (< 100ºC) would enable the deposition of 2D molecular crystals with even very weak intermolecular forces, such as porphyrins or unfunctionalized organic semiconductors like pentacene. This approach could also enable the growth of 2D crystals of low molecular weight molecules (< 300 g/mol), such dyes that absorb in UV or even non-conjugated species like

The motivation to synthesize these different kinds of materials is not only to expand our library of organic 2D materials but can also provide a platform to study low-dimensional excitonic phenomena. The confinement of the molecules in-plane drastically simplifies their spectroscopic properties, hence making them ideal for developing fundamental understandings that were previously only possible though computation. We saw in Chapter 6 how changing the structure of a crystal by altering the functional groups on the molecule significantly impacts even its steady-state absorption. Although there is still much to explore in these systems, one could also consider how the properties of a crystal would change different if we kept the same functional groups and instead increased the size of the conjugated core. This could be studied by comparing crystals of perylene, terrylene, and quaterrylene, which are all of similar shape, but differ in size by roughly a naphthalene unit.[8]

It would also be interesting to explore the properties of crystals with more than one species, such as other molecules[9] or metals[10], incorporated into the lattice—i.e., mixed 2D molecular solids. Although such materials, which have been demonstrated by ultra-high vacuum deposition, are notorious for their poor crystallinity, it may be possible to produce larger bicrystals by first synthesizing large 2D crystals of perylene derivatives and then introducing the other species in a second step. In other words, these 2D molecular crystals could be used as a "template" to synthesize crystalline forms of traditionally poorly-crystalline materials. Along this vein, we have found that if we partially-deposit a film of one molecule, such as PTCDA, on

MoS_2 (**Fig. A7.1a**) and then put that film into a reactor to deposit a different molecule, such as PDI, using the same temperature, the final film (**Fig. A7.1b**) will be solely composed of molecule two (as a monolayer), but the morphology will be different than if we were to directly deposit PDI onto a clean MoS_2 film. In other words, the second deposition will retain some "memory" of the film of molecule one, as seen from the existence of localized regions of large and smaller PTCDA domains in **Fig. A7.1b**.

Although we have not actively attempted to grow mixed-molecular crystals by depositing two molecules at the same time, we have accidently realized some promising results related to this while attempting a completely different experiment, which was the synthesis of 2D crystals of 1,4,5,8-naphthalenetetracarboxylic dianhydride (NTCDA). For this, we cleaned a tube that was previously used for MPDI deposition and loaded NTCDA (97% purity) into the reactor. **Fig. 7.1a** shows the cross-polarized image (θ_A = -3º, λ = 550 nm) of one of the first few depositions onto an MoS_2 film. There appear to be two types of molecular domains: the domains labelled

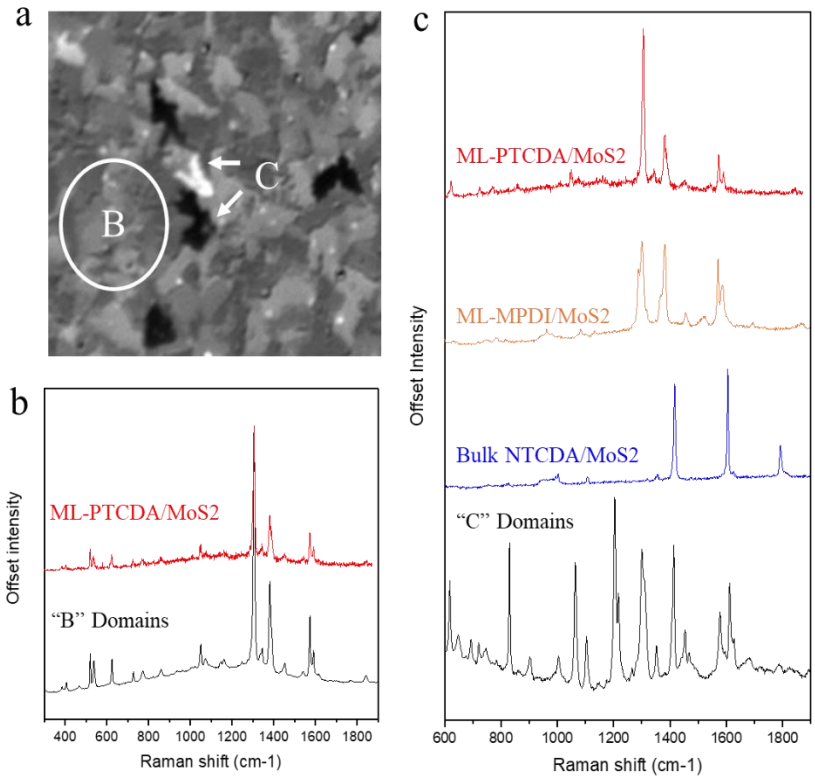

Figure 7.1. a) Cross-polarized image of a molecular film deposited on MoS_2, where the molecular source was NTCDA (97% purity), but traces of MPDI were likely left in the tube from previous depositions. Two types of molecular domains are seen, labelled "B" and "C". b) Raman spectrum of a "B" domain (black), overlaid with spectrum of monolayer PTCDA for reference (red). c) Raman spectrum of a "C" domain (black), overlaid with spectra of monolayer PTCDA, monolayer MPDI, and thick NTCDA crystals, for reference.

"B", which cover most of the area and exhibit a weakly polarized response, and the domains labelled "C", which are fewer in number and exhibit a much stronger response. Both types of domains appear to be single-crystal.

If we take full spectra of these molecular domains, we find that the "B" domains exhibit Davydov splitting, and the response appears strikingly similar in peak intensity and position to that of monolayer PTCDA crystals (**Fig. A7.2b**) and are too low in energy to be NTCDA. This observation is odd, considering that this particular reactor tube was never used for the deposition of PTCDA. However, Raman spectra of these domains, shown in **Fig. 7.1b** alongside a reference spectrum of monolayer PTCDA, appear to support the conclusion that these crystals are PTCDA. This suggests that the NTCDA source power likely contained PTCDA impurities, and possibly even other molecular species.

Knowing this, we now turn to the "C" domains. The peak positions and intensities in the cross-polarized spectra of the "C" domains (**Fig. A7.2c**) closely resemble that of monolayer MPDI crystals (also to low in energy to be NTCDA). Although this appears to be the result of trace amounts of MPDI remaining in the tube from previous experiments, the Raman spectra show that these crystals are actually more complex than just MPDI. **Fig. 7.1c** shows the Raman spectrum of "C", alongside the spectra for monolayer PTCDA, monolayer MPDI, and thick NTCDA crystals (since we do not yet have a reference for monolayer). The Raman spectrum of the "C" domains has significantly more features than any of the pure materials, implying that these crystals are a combination of more than one molecular species, likely among PTCDA, MPDI, and NTCDA. Combined with the fact that the domains appear to be micron-scale single-crystals, this appears to demonstrate the feasibility of synthesizing mixed 2D molecular crystals

with this deposition technique, although more thorough characterization would be necessary to confirm the structure and composition.

7.3 Modification, Patterning, and Integration

7.3.1 Post-Synthetic Modification

Once we have built a library of 2D films, the next step would be to modify those films post-synthesis to incorporate some desired properties that could not be achieved through direct growth. This is analogous to depositing metals or oxides on the surface of silicon. Unlike traditional inorganic crystals like silicon however, the surfaces of inorganic 2D materials are free of dangling bonds, making them highly unreactive to chemical functionalization. As a result, the only way to directly and uniformly functionalize 2D films is to create defects on the surface prior to functionalization. In general though, modifying the surface of any material creates defects at the interface during functionalization—for example, by physically damaging the surface through the deposition[11] or by chemically bonding to surface species changing the valency.[12] For thick materials, these changes at the interface are not significant compared to the volume of the functionalized material. In the limit where the material becomes atomically thin, however, these surface defects begin to dominate the optical and electronic properties of the system. Hence, by covalently functionalizing a 2D material, we are completely changing the characteristics of the material that we cared about in the first place.

Herein lies the advantage of these 2D molecular films: we have seen throughout this thesis that these molecular films can be deposited on 2D inorganic films (such as TMDs) under relatively mild conditions without significantly changing the properties of the inorganic material, which is possible because the interactions between the two layers are weak van der Waals (vdW) forces. Thus, the molecular layer can be used as a scaffold or “sacrificial layer” to functionalize

the surface of inorganic 2D films. Given that organic films are also compatible with a huge body of carbon reaction chemistry (most of which would have no reactivity with a inorganic surface), this provides limitless potential for post-synthetic functionalization. This could include the attachment of catalysts, biomolecules, receptors for sensing, or other active species that would be useful to integrate into device technologies, using the inorganic layer for switching and/or signal communication.

There are already a number of examples of organic functionalization in the literature that take advantage of the organometallic chemistry of monolayers of porphyrins and phthalocyanines to attach small functional groups,[13,14] as well as other studies that use perylene derivatives to seed the growth of ultrathin and uniform oxides on inorganic 2D materials using atomic layer deposition (ALD).[15,16] Furthermore, if the molecular layer is highly dense and ordered like the 2D molecular crystals synthesized in this thesis, then any subsequent functionalization should have high density, reproducible surface spacing, and be tightly bound. These properties are not achievable for methods that try to directly adsorb large (and not flat) macromolecules to inorganic surfaces, which results in sparse and nonuniform adsorption where the species are weakly abound.

In addition to using these molecular films to build up complex layers on an inorganic 2D film, we can also consider depositing a layer of molecules with some specific reactivity, and then triggering that reactivity post-deposition to change some aspect of the molecular film itself. For example, we can imagine depositing a film of the molecular component of a metal-organic framework (MOF), removing the film from the deposition chamber, and then reacting it with the metal component to possibly produce a more crystalline MOF that can be produced by direct

synthesis in solution (i.e., again using the molecular film as a "template", as briefly mentioned in the previous section).

Although we have not attempted experiments like these directly, we have made some observations related to this while performing stability-test experiments of PTCDA films deposited on MoS_2. **Fig. A7.3a** shows a cross-polarized image (λ = 550 nm) of a nearly continuous film (deposition temperature ≈ 200ºC), where the red circles indicate holes in the centers of the PTCDA domains. After heating the film in air (on a hot plate) at progressively increasing temperatures, we find no morphology change in the film annealed up to 250ºC for a total of three hours (**Fig. A7.3b**). After another hour of annealing up to 300ºC, the holes at the centers of the PTCDA domains become slightly enlarged, indicating sublimation of the molecules from the exposed edges of the crystals (**Fig. A7.3c**).

Although we know the molecular film indeed sublimes off the surface at much lower temperatures in vacuum, when annealed in air well above the original deposition temperature, the film morphology looks nearly identical to the pre-annealed state. However, if we take x-ray photoelectron spectroscopy (XPS) measurements of a PTCDA film deposited on MoS_2 on a SiO_2 substrate before and after annealing in air for 1 hour at 150 ºC, we find that there are actually chemical changes occurring in the film even at these mild annealing conditions. **Fig. 7.2a-e** show the XPS spectra of the Mo 3d, S 2p, C 1s, O 1s, and Si 2p regions (respectively) for the PTCDA/MoS_2 film before and after annealing (solid black and solid red lines, respectively), with the spectra of a bare MoS_2 film before and after annealing (dashed black and dashed red lines, respectively) shown for comparison. The spectra are calibrated by setting the C 1s peak to 284.8 eV and shift all spectra for the same sample by the corresponding amount.

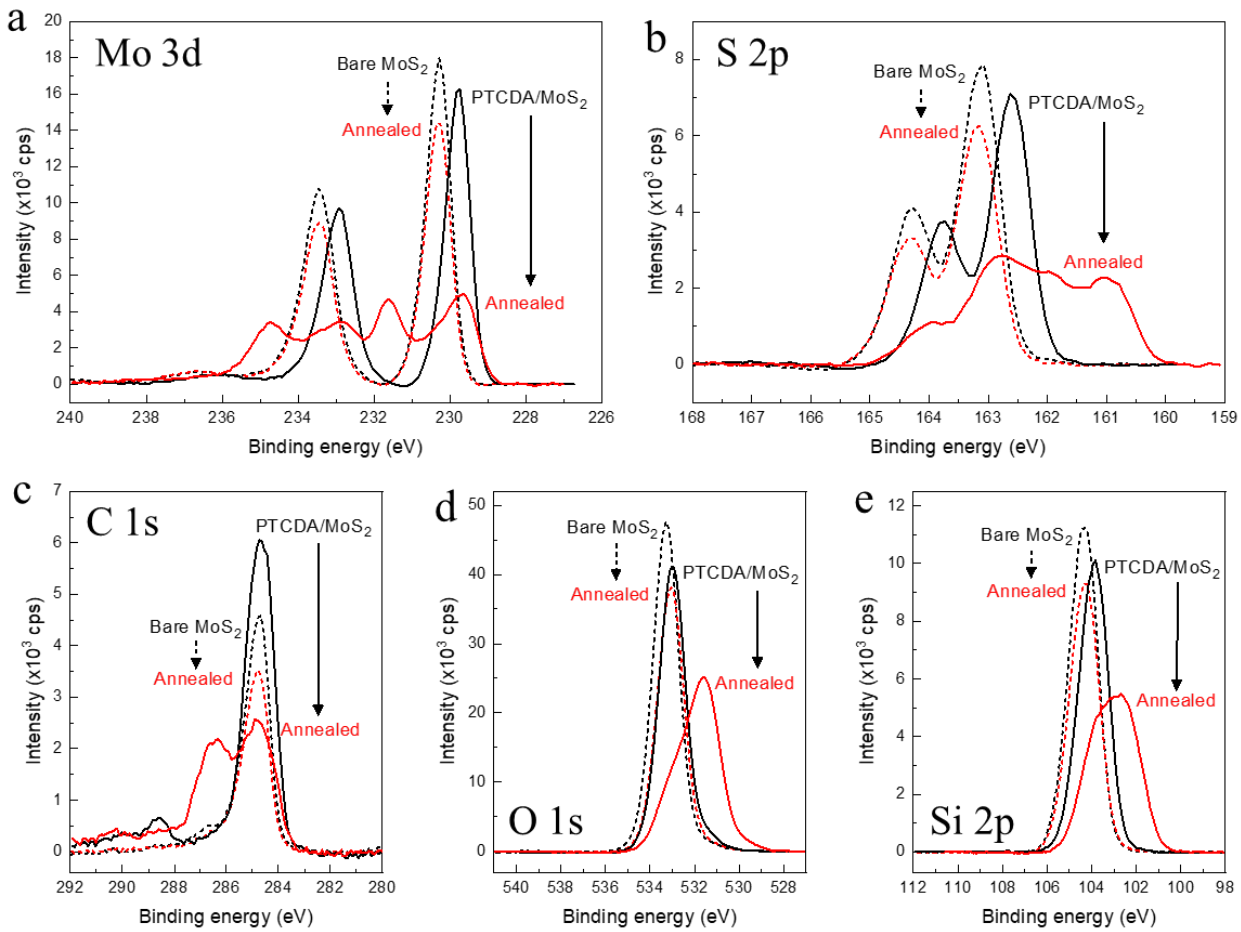

Figure 7.2. XPS spectra of a MoS_2 film on a SiO_2/Si substrate before (dashed black line) and after (dashed red line) annealing at 150ºC for 1 hr, alongside the XPS spectra of a film of PTCDA on MoS_2 (also sitting on a SiO_2/Si substrate) before (solid black line) and after annealing (solid red line) at the same conditions. Spectra of the a) Mo 3d, b) S 2p, c) C 1s, d) O 1s, and e) Si 2p regions are shown.

First, we see that the deposition of the PTCDA (dashed black lines → solid black lines) causes a roughly -0.5 eV shift in the binding energies of the Mo 3d and S 2p electrons (**Fig. 7.2a** and **Fig. 7.2b**). The direction of the shift is consistent with the physisorption of a species that donates electron density to the MoS_2 film, and the relatively large magnitude of the shift implies that the flat-lying molecular crystals experience sizable interactions with the TMD substrate. We also see that the deposition itself does not cause any chemical change to the MoS_2, such as oxidation (Mo oxide peak ~236.5 eV, **Fig. 7.2a**). The C 1s spectrum acquires a new features between 288.5-290 eV after deposition, corresponding to the C-O and C=O bonds of PTCDA,

and there does not appear to be significant change to the O 1s or Si 2p spectra (**Fig. 7.2d** and **Fig. 7.2e**; since these signals largely originate from the SiO_2 substrate).

Upon annealing the bare MoS_2 film in air at 150 ºC (control; dashed black lines → dashed red lines), there appears to be no significant change in any of the XPS regions (including the oxidation state of Mo). However, performing the same process on the PTCDA/MoS_2 film (solid black line → solid red line) appears to convert a significant portion (roughly 1/3 to 1/2) of the Mo-S bonds to other species, where the Mo becomes more oxidized (**Fig. 7.2a**) and the S becomes more reduced (**Fig. 7.2b**). Furthermore, a similar proportion of the C 1s bonds become more reduced (**Fig. 7.2c**) and the O 1s bonds more oxidized (**Fig. 7.2d**). These binding energy shifts are all 1-2 eV—large enough for us to conclude that this is likely chemisorption—i.e., changes in chemical bonding taking place. Interestingly, the Si 2p spectrum (**Fig. 7.2e**) also shows a significant reduction in oxidation state. This is quite odd, considering that Si is only present in the SiO_2 wafer, which is not only highly unreactive but is also separated from the PTCDA by a layer of MoS_2 (i.e., how could the PTCDA be causing such a large change in the Si oxidation state without directly interacting with those atoms). Although careful fitting of the XPS data and supplementary characterizations would be needed to fully understand the nature of the changes occurring here, this is just one example of how a post-synthetic modification procedure (i.e., heating in the presence of oxygen) can be used to chemically change these molecular films.

7.3.2 Patterning and Redeposition

An important characteristic for technological integration is the ability to pattern a thin film over a large scale and incorporate different materials in the removed areas. There are two ways to go about pattering these molecular films: patterning the substrate before deposition or direct patterning of the molecular layer after deposition. The former approach is only possible

because, as we saw in Chapters 4 and 5, the deposition of these 2D molecular crystals is surface-assisted (i.e., changing the morphology of the substrate changes the morphology of the molecular crystal). For this case, the ideal scenario would be to start with a wafer-scale, single-crystal TMD film and pattern that into arbitrary shapes using a polymer-free patterning method. The resulting molecular deposition should be single-crystal, as we have seen with the WS_2 triangles, except now taking whatever shape was defined by the patterning template. This idea is schematically depicted in **Fig. 7.3a**.

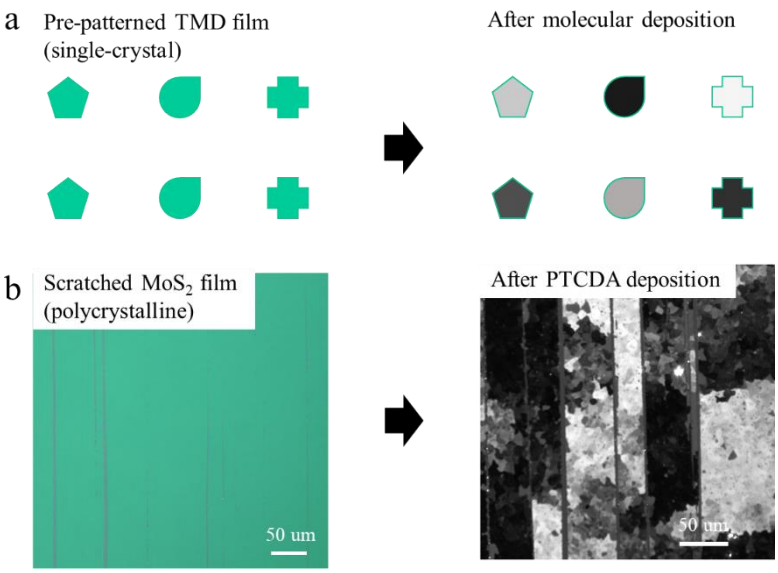

Figure 7.3. Deposition of molecular crystals onto TMD substrates patterned into arbitrary shapes a) schematically illustrated with patterned single-crystal TMD substrates, and b) shown experimentally for a "patterned" polycrystalline TMD film.

In the absence of having single-crystal TMD films, we have tried an alternate version of the experiment proposed above, using polycrystalline MoS_2 films. We saw in Chapter 5 that the molecular crystal domains can sometimes communicate across the domain boundaries of a polycrystalline TMD film, resulting in "superdomains" with individual crystal orientations within ±10º of the average. Although this "bandwidth" results in a reduced overall anisotropy, it is still narrow enough to see a significant difference between superdomains with different average orientations. **Fig. 7.3b** shows a proof-of-concept demonstration of this, using a polycrystalline MoS_2 film that was scratched to mimic clean "patterning". After PTCDA

deposition, we can clearly see superdomains with coherence length between 50-100 μm, which change orientation abruptly at the vertical scratches.

Because the above patterning approach also involves removal of the TMD substrate, it does not allow for the deposition of other molecular films after the patterning (such as what is possible in the photolithography of inorganic materials). This could be achieved, however, if it were possible to selectively pattern the molecular film (after deposition), leaving the TMD substrate intact. Since photolithographic methods are not compatible with most molecular species (due to dissolution of the entire film by the solvents/photoresists), we have tried selective-area patterning of the molecular layer by numerous alternative methods. First, we find that it is not possible to use a pick-up based patterning technique (such as the one used by Mannix and Ye *et al*.[17] to pattern pixels of MoS_2) to selectively pick up the molecular layer. We find that the TMD film is always removed together with the molecular film, indicating that the interaction of the molecular layer with the TMD film is (not unexpectedly) stronger than the interaction of the TMD film with the SiO_2 support wafer.

We have also tried using the laser-based patterning method developed by Poddar and Zhong, *et al*.[18] Although Zhong and Chang, *et al.* showed that this process works for the patterning of room-temperature-synthesized monolayer porphyrin-based metal-organic frameworks deposited on TMD films,[19] we have had no success in patterning our perylene-based molecular films or even adlayers of porphyrin molecules also deposited at elevated temperatures under vacuum. We find that either the molecular film remains intact, or the molecular and TMD films are ablated together (i.e., no selective patterning achieved). This could be due to the enhanced stability of molecular materials deposited under elevated temperature and reduced pressure conditions. However, since we know that the molecular layer can be sublimed off the

TMD film by annealing under vacuum, it may be possible to achieve laser-based patterning if the process is performed under vacuum.

If a clean and effective selective patterning technique for the molecular film is achieved, we can take the next step towards producing films with spatially varying compositions, via deposition and patterning of a first molecular layer, followed by redeposition of another in the areas removed. This has already been demonstrated with numerous inorganic 2D materials grown via CVD processes[20–22], but is only possible if the first material is stable under the conditions required to deposit the second material. An example of this would be choosing the second material to be one with a significantly lower deposition temperature compared to the first (such as MoS_2 and graphene). This is tricky for molecular materials since they are much less thermally stable.

Still, we took a quick attempt at this experiment using PDI and PTCDA. Since we do not have a process for selective-area molecular patterning, we started with a partially-deposited PDI film on MoS_2. A cross-polarized image (λ = 550 nm) of the partial PDI film, which was deposited at a temperature of 235ºC, is shown in **Fig. 7.4a**, where the red arrows point to some void areas for clarity. We then changed the molecular

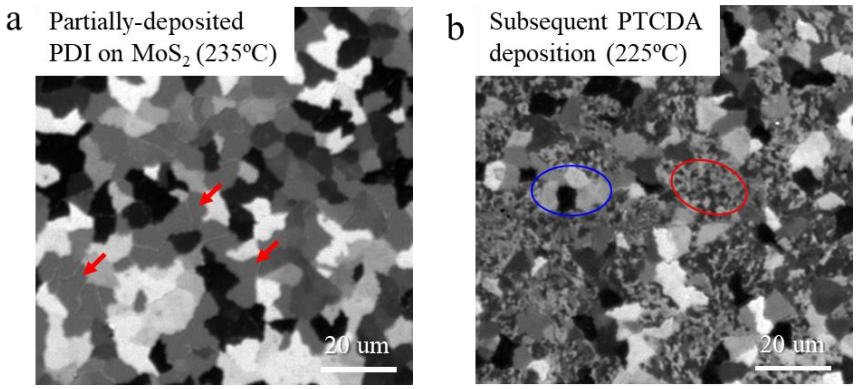

Figure 7.4. a) A partial film of PDI deposited on MoS_2 at 235ºC, where the red arrows point to areas of bare MoS_2, and b) the result of taking the film from (a) and performing a subsequent deposition of PTCDA at 235ºC, where the small domains in the red circle are pure PTCDA and the large domains in the blue circle are something other than pure PDI or pure PTCDA.

precursor to PTCDA, put the film back into the reactor, and deposited PTCDA at the same pressure, but a slightly lower temperature of 225ºC. The resulting film is shown in **Fig. 7.4b**. In the image, we see two kinds of domains: one set (circled in blue) with domain size similar to that of the initial PDI sample, and another set (circled in red) with much smaller domain size and weaker reflectance at this wavelength (550 nm).

By taking a full spectrum (not shown), we can identify the small domains as indeed being PTCDA, confirming that we can successfully redeposit another molecule in the void area of the first film. It is interesting though, that the second molecular deposition produced domains with smaller size than the original (i.e., smaller domain size than the underlying MoS_2). The large domains, however, give a very broad spectral response not consistent with either PDI or PTCDA. This suggests that the temperature reduction for the second deposition was not enough to keep the PDI from sublimating, resulting in mixed domains of PTCDA and PDI that are not well-ordered. Although we have yet to try larger temperature differences between the first and second depositions, there is a limit to how low the temperature for the second deposition can be before the second molecule starts to also deposit on top of the first. Another possible approach could be to use similar temperatures but deposit the first material at much lower pressures. This would likely require the first material to be deposited at orders of magnitude lower pressures than what is achievable with the current reactor geometry (i.e., 0.5 torr), but is definitely feasible.

7.3.3 Stacking and Transfer

One of the major advantages of growing these molecular crystals on TMD substrates is that the TMD film serves as a removable support. After modification and patterning, this allows for integration of the molecular film with other systems and technologies, something that was not possible for traditional molecular monolayers deposited on bulk crystalline materials (i.e., **Fig.**

4.2). We saw one example of this in **Fig. 6.3** (**Section 6.2**), where PTCDA films deposited on MoS_2 were stacked together using a polymer-supported transfer method[23] to form hybrid superlattices with different compositions. We can also realize much thicker films using the automated stacking technique developed in our work with Mannix and Ye *et al*.[17] Furthermore, we know that, as long as the molecular films are deposited at decently low temperatures (a few hundred ºC), the films can be delaminated from their wafer support by simply floating them on the surface of water. This allows them to be cleanly transferred to another surface, without the use of a support polymer (also **Section 6.2**).

One can imagine taking the aforementioned transfer experiments a step further, by stacking different kinds of molecular crystals with each other or with other inorganic 2D materials, enabling the formation of "artificial solids" whose properties are designed with atomic-scale precision in a bottom-up fashion. This idea was originally conceived for inorganic 2D materials (i.e., "materials by design"),[24] incorporating atomically-thin organic building blocks provides us with a huge library of optical, electrical, and chemical properties that were previously inaccessible in the all-inorganic systems.

The preliminary demonstrations in **Section 6.2** both used polycrystalline molecular films, but we can also envision performing this processing with single-crystal films, which we can grow over a scale of 100s of μm (**Fig. 5.12**). Using single-crystal starting materials allows us to specifically build crystals with designed polarized responses. This is conceptually demonstrated in **Fig. 7.5**, for single-crystal PTCDA monolayers deposited on single-crystal WS_2 triangles. Stacking two crystals that have their major axes aligned (**Fig. 7.5a**) produces another optically anisotropic crystal, i.e., responds differently to light of different linear polarizations. Although the total amount of reflected light will be greater for the stacked crystal, the magnitude of the

optical anisotropy will decrease with increasing thickness. This occurs because 1) the much-weaker birefringence (anisotropic refraction) will start to dominate the reflectance signal over the dichroism (anisotropic absorption) in thicker films and 2) each stack also adds a layer of WS_2, which increases the proportion of the isotropic background progressively with every layer (recall **Fig. 6.8**). Since, however, these molecular crystals already absorb a large proportion of light at their absorption maxima (a few percent), it is likely not necessary to produce very thick crystals, especially in the context of atomically-thin device structures.

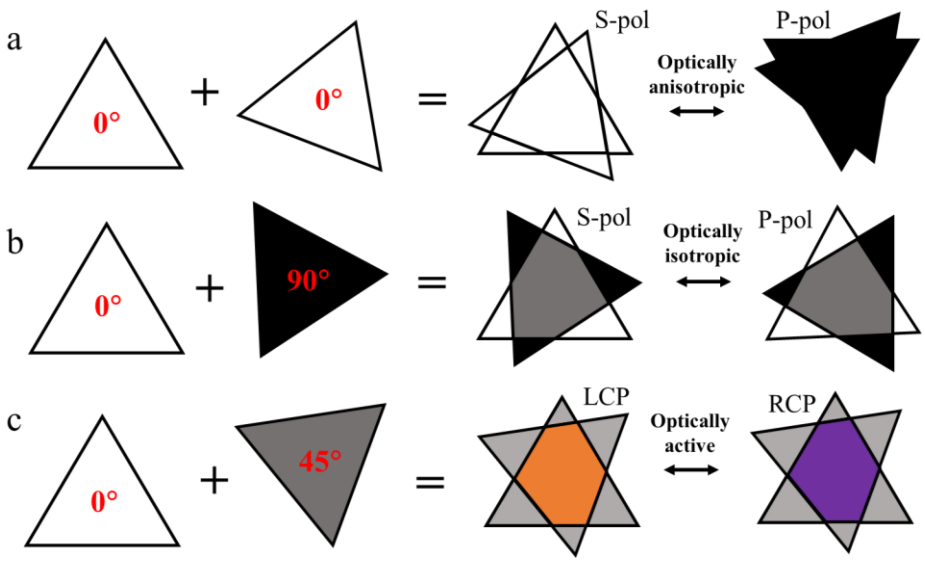

Figure 7.5. Using 2D molecular crystals as atomically-thin building blocks for artificial solids with tunable light-matter interactions. Stacking two anisotropic crystals a) with their optical axes aligned produces another optically anisotropic crystal, b) with their optical axes orthogonal produces an optically isotropic crystal, and c) with their optical axes at any other angle produces an optically active, or chiral, crystal.

We can further use the same anisotropic PTCDA/WS_2 building blocks to produce a crystal that is *optically isotropic*, i.e., responds similarly to light of any polarization, by stacking two crystals in a way that their major axes are exactly perpendicular to each other (**Fig. 7.5b**). If we stack the crystals at any twist angle (**Fig. 7.5c**), the result is an *optically active* (chiral) crystal, which responds differently to light of different *circular* polarizations (right-handed vs. left-handed). If linearly-polarized light is shown on an optically active crystal, it will rotate the

polarization of the light. The thicker the crystal, the stronger this effect. Hence, one can imagine producing a structure where different areas of a chip exhibit different responses to polarized light, all being formed from the same atomically-thin starting material.

Unfortunately, our initial attempts at the experiment described **Fig. 7.5**, which we tried using the stacking process developed by Mannix and Ye *et al.*,[17] were successful. This was because these giant WS_2 triangles are difficult to pick up from the support wafer—a result of both the extreme reaction conditions used to produce large WS_2 single-crystals on SiO_2 wafers, as well as the elevated-temperature PTCDA deposition. Although it would be difficult to improve on the WS_2 growth side, the molecular crystals could probably be deposited at lower temperatures if the vacuum level during the deposition was increased (recall the arguments from Section 5.6). Another alternative could be to use single-crystal TMDs grown via epitaxy on a single-crystal wafer such as sapphire. Optimizing this process is tricky, but this growth can be carried out under milder reaction conditions, and the resulting wafer-scale single-crystals films can indeed be delaminated from the sapphire substrate.[25]

7.4 Electrochromic Device Applications

In the previous section, we discussed the processes necessary to transform a material platform towards application: modification, patterning, and initial steps for integration. In this section, we will take the integration phase further, by implementing the stacking and transfer processes we described above to produce proof-of-concept devices that take advantage of the strong and spectrally-dependent optical anisotropy of these molecular domains.

7.4.1 Dielectric Screening of Absorption

Our idea for implementing these materials in electrochromic devices—devices that reversibly modulate the optical response (in this case, reflectivity) of a material through the

application of voltage—comes from observations that we made while attempting the stacking experiments with PTCDA films. **Figure 7.6a** shows the cross-polarized reflection anisotropy spectra (θ_A = 3º) of films of PTCDA deposited on MoS_2 that was grown on SiO_2/Si wafers (i.e., this data is similar to **Fig. 6.17c**, except the support substrate in **Fig. 6.17** was a transparent fused silica wafer, so the peaks have different magnitudes and polarities than what we see in **Fig. 7.6a**). The top spectrum (black line) shows what the response looks like when the film is "as-deposited", meaning it was removed from the deposition reactor and imaged immediately after cooling (final reactor temperature usually between 50-80ºC). The three colored asterisks indicate the peaks in the reflectance anisotropy, which correspond to 1) the lower Davydov state of the first vibronic band (red) and 2) the upper Davydov state of the first vibronic band (green), and 3) the second vibronic band (blue). Selected images of this film taken at various wavelengths are shown in **Fig. A7.4a**, where the peaks marked by the three asterisks are boxed using the same

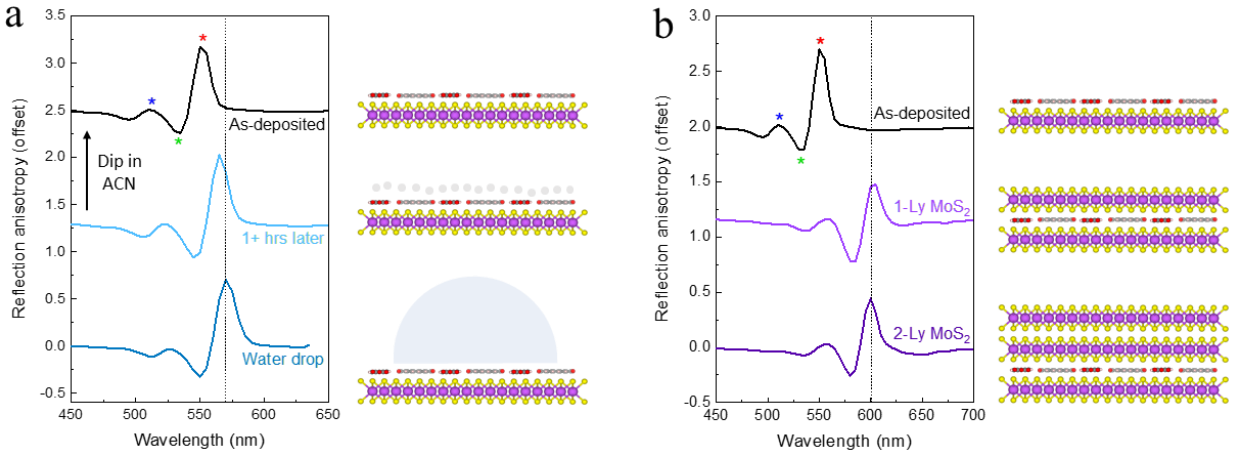

Figure 7.6. Environmental sensitivity of ultrathin molecular layers. a) Reflection anisotropy spectra of an as-deposited PTCDA film (black line), the same film after sitting at room temperature for 1+ hrs (light blue line), and the film with a drop of water on the surface (dark blue line). Schematics of the films are given to the right of each spectrum. Rinsing a film in the middle state with acetonitrile returns it to the as-deposited state. b) Reflection anisotropy spectra of an as-deposited PTCDA film (black line), the film after stacking one layer of MoS_2 on top (light purple line), and the same film after stacking a second layer of MoS_2 on top (dark purple line). Schematics of the films are given to the right of each spectrum. Colored asterisks indicate the three peaks in the anisotropy and dashed vertical lines are to guide the eye.

colors (note the images are shown at irregular intervals due to space constraints). For an as-deposited PTCDA film on MoS_2, the lower Davydov state is at 550 nm.

Interestingly, if we allow the film to sit in air for one or more hours and then remeasure the same area, we find that the entire spectral response shifts to lower energies by 15 nm—resulting in the middle plot in **Fig. 7.6a** (light blue line; dashed vertical line to guide the eye). From the selected images of the spectrum shown in **Fig. A7.4b**, it is clear that the only difference between the two film responses is the peak positions, while the magnitude of the reflectance is conserved for all domains at all wavelengths. This shift even occurs if the film is kept in the reactor (under vacuum) for an extended period of time after reaching room temperature. If we continue waiting, there is no additional shift in the response, even after years of sitting in air. We also experience a shift of similar magnitude for the PDI and MPDI films, indicating a general phenomenon. For the redshifted spectrum for PTCDA, the lower Davydov state is at 565 nm, which is actually the peak position that we report in our experiments in Chapter 6. For all of those measurements, we waited until the film responses settled to their stable (redshifted) value before collecting the data, and we did this for every molecular crystal, in order for the responses to be comparable.

We further find that this change is reversible, and that the original ("as-deposited") state can be recovered by dipping the film in acetonitrile and allowing the solvent to evaporate. From these experiments, we conclude that this shift in the spectral response is not the result of some change in the molecular film itself, but a change in the environment around the film. In particular, we believe that the changes are due to the adsorption of gas molecules to the surface of the film, most likely water, after the film has sat at room temperature for a period of time (see schematics next to each spectrum in **Fig. 7.6a**). This is not too surprising, since we know that

even single-molecule absorption spectra exhibit shift small amounts when performed in different solvents, as a result of the differences in the interactions of the molecules with the various solvents.

The notable observation here though, is how surface-sensitive the response is for these ultrathin molecular crystals. We test this by putting a drop of water on the surface of the film and taking another spectrum. The result is shown as the bottom plot in **Fig. 7.6a** (dark blue line), with the images given in **Fig. A7.4c** (images are blurry because we imaged directly through the water droplet instead of using a coverslip, since the thinner layer of water evaporates too quickly to complete the measurement). The presence of a thick layer of water only appears to shift the spectrum further by ~5 nm, indicating that the molecules indeed only "feel" the first few atomic layers near their surface.

We investigate this phenomenon more controllably by stacking layers of MoS_2 on top the PTCDA film. The top spectrum (black line) in **Fig. 7.6b** again shows the cross-polarized reflection anisotropy ($\theta_A = 3^o$) of a film of PTCDA as-deposited on MoS_2 that was grown on a SiO_2/Si wafer, with the images given in **Fig. A7.5a**. This spectrum was again taken immediately after the reactor cooled, so the lowest energy peak (red asterisk/red box) is at 550 nm. If we stack one additional layer of MoS_2 on top of this film using the established stacking technique (see adjacent schematics in **Fig. 7.6b**),[23] the peaks in the resulting spectrum exhibit a substantial shift of 50 nm. This can be seen more from in **Fig. A7.5b**, where the MoS_2/PTCDA/MoS_2 film exhibits significant response below 580 nm, while the as-deposited film showed effectively no response at those wavelengths. Unlike the case of the water adsorbing to the surface (**Fig. 7.6a**), however, where the intensities of the peaks were the same, the strength of the anisotropy drops upon the addition of MoS_2 layers in **Fig. 7.6b**. This is expected though, since we know from the

discussion in Section 6.3 that the MoS_2 layer adds to the isotropic background, reducing the overall anisotropic response. We further find that stacking second layer of MoS_2 on top of the film (i.e., a film of MoS_2/MoS_2/PTCDA/MoS_2) does not result in any additional spectral shift (**Fig. 7.6b** and **Fig. A7.5c**), consistent with our earlier observations of the surface-sensitivity of this absorption shift.

These spectral shifts that we observe due to the change in environment around the monolayer molecular film can be attributed to dielectric screening effects, which have previously been studied for monolayer PTCDA films deposited on monolayer WSe_2 grown on bulk graphite and bulk Au substrates.[26] We first saw this effect in the absorption spectra in **Fig. 6.13**, where the HOMO-LUMO gap of PTCDA is reduced by 35 nm when going from solution to a crystal sitting on MoS_2 (this value includes both the shift due to the aggregation of PTCDA molecules into a crystal, plus another shift due to the presence of the MoS_2). Interestingly, adding a layer of MoS_2 on the other side of the PTCDA film (i.e., **Fig. 7.6b**) actually reduces the HOMO-LUMO gap by 50 nm—an even greater amount than the first shift—although it is unclear why this is the case.

7.4.2 Active Modulation by Electrical Gating

The experiments in the previous subsection showed that we can "passively" modulate the reflectance signal of these molecular films. This brings the question: is there a way to actively (and reversibly) modulate the optical response? Effectively, the stacking experiments illustrated that a small change in the electron density around atomically-thin molecular crystals induces a large change in their optical properties. Hence, one could wonder what would happen if we were to change the electrical density in another way—such as by electrical gating. Indeed, optoelectronic measurements of inorganic 2D materials such as MoS_2 show that their absorption

can be reversibly increased or decreased by changing the doping level of the material via electrical gating.[27]

Using these ideas, we tried to see if changing the electron density of the MoS_2 by gating could induce a change in the absorption of the PTCDA film by proximity. The design of the electrochromic devices we fabricated for our first attempt at these experiments is shown in **Fig. 7.7a**. Here, we are using the 300 nm SiO_2/Si substrate to apply the backgate to an MoS_2-PTCDA/MoS_2 film, where 50 nm thick Au pads were used to verify that the devise was properly conducting before performing the gating experiments. Ideally, we would use a film of just PTCDA on MoS_2 for this experiment (not the stacked film, which already exhibits a large spectral shift to begin with), but traditional photolithography and electrode deposition processes would destroy the PTCDA film (this was prior to the development of the polymer-free photolithography process developed by Poddar and Zhong, *et al*.).[18] For this reason, we stacked a MoS_2 film on top of the PTCDA film as a protective layer and then asked Baorui Chang to carry

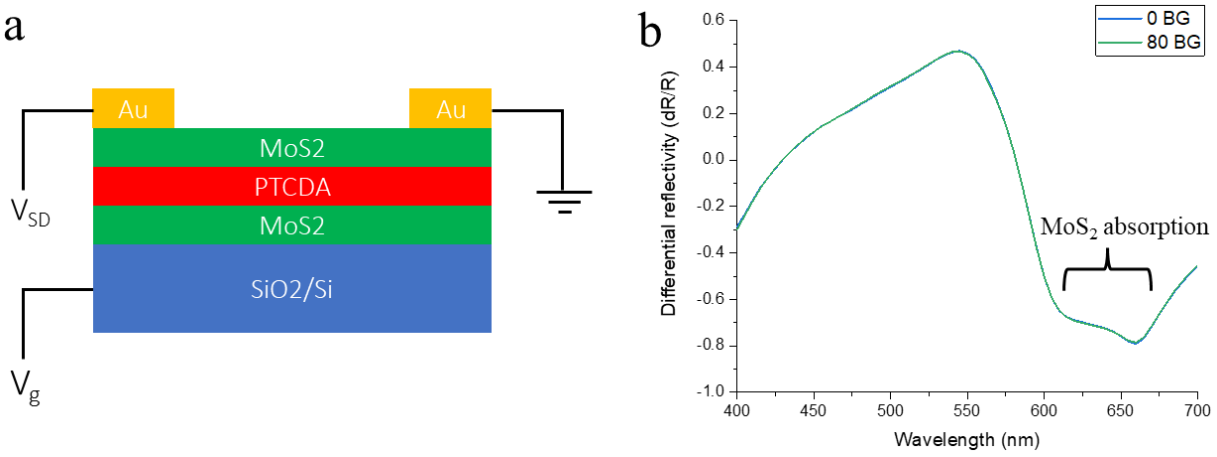

Figure 7.7. Attempt at modulating the optical response of a PTCDA film by backgating the MoS_2 layer. a) Schematic of the device design, and b) differential reflectance spectra of a PTCDA domain in the channel area of the device when applying a backgate of 0V (blue line) and 80V (green line). The two spectra overlap exactly, even in at the energies where the MoS_2 absorption dominates.

out the channel patterning and electrode deposition using standard photolithographic techniques. The Au pads were 500 x 500 μm and the channel dimensions were ~200 x 300 μm.

The setup used to perform the optical measurement simultaneously while applying the backgate is shown in **Fig. A7.6**. We mounted the device to a chip carrier affixed to a printed circuit board (PCB), using a wire bonder to make the connections to the chip carrier. This structure was fixed on the stage of the polarized optical system, which was equipped with a 20x objective with a 1 cm working distance. The PCB was then connected to a breakout box, which was used to route the signals to and from the electrical measurement station. We began by performing source-drain measurements to confirm that charges were being injected into the bottom MoS_2 layer and verify that the backgate (BG) was working (output and transfer curves shown in **Fig. A7.7**). Although the amount of current flowing through the device at the maximum voltage possible for the setup (V_{BG} = 80V) appear to be quite small (few μA), this is typical for transistors made from these MOCVD-grown MoS_2 films using photolithography where the metal contacts were directly deposited (i.e., high contact resistance).

After checking the device conductivity, we stopped the electrical measurement and took a cross-polarized differential reflectance spectrum to determine the ungated (i.e., V_{BG} = 0V) optical response of the film. We then set the gate to 80V (with the drain electrode grounded) and repeated the spectrum using the same acquisition conditions. These two spectra (taken from the same PTCDA domain) are overlaid in **Fig. 7.7b**. The features in the spectra are broad because the substrate is non-transparent and because there is an additional layer of MoS_2 on top of the PTCDA film, but we can clearly see that there is no optical difference between the 0V state and the 80V state. However, even the region of the spectra where the MoS_2 absorbs (i.e., below 600 nm) show no difference. Since we already know it is possible to change the absorption of MoS_2

via electrical gating (coupled with the fact that the device was poorly conducting to being with), this indicates that the reason for seeing no change in the PTCDA response could just be due to insufficient gate being applied.

We then revised our device design to use an electrolyte to apply the gate, which is much more effective at gating. We also changed the device fabrication process to avoid the photolithography and electrode deposition steps, to reduce the contact resistance and improve the conductivity of the MoS_2 layer. The design of the electrolyte-gated device is shown in **Fig. 7.8a**. It looks similar to the backgated device, except the Au contacts are coated with photoresist (PR) to isolate them from the gate, which is applied using a drop of an ionic liquid in contact with a Ag wire. We used an ionic liquid for the gate instead of an aqueous electrolyte solution because the water evaporated too quickly over the course of the measurement and has a small electrochemical stability window. However, the ionic liquid 1-ethyl-3-methylimidazolium

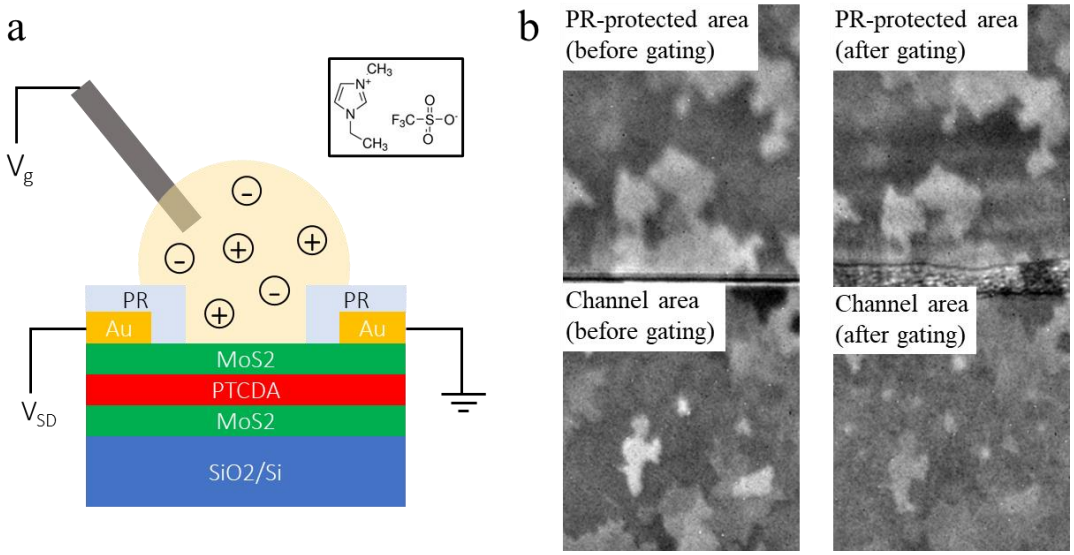

Figure 7.8. Attempt at modulating the optical response of a PTCDA film by electrolyte gating the MoS_2 layer. a) Schematic of the device design, with the structure of the ionic liquid given in the top-right inset. b) Cross-polarized images (taken at 600 nm) of a device before (left panel) and after (right panel) applying a gate of +1V for roughly 20 min (both images taken at $V_g = 0$). The upper halves of the images show the photoresist-coated area outside of the channel (i.e., ungated area) and the lower halves of the images show the channel area.

trifluoromethanesulfonate (structure shown top right corner of **Fig. 7.8a**) has a boiling point of 300C and an electrochemical stability window of at least ±2V. Because PTCDA is soluble in this ionic liquid though, we still had to keep the top layer of MoS_2 to protect the molecular film.

Optical images of devices used for this study are shown in **Fig. A7.8**. This process was developed by Yu Zhong and Preeti Poddar, and the fabrication for our experiments was also carried out by Preeti Poddar. Originally, we designed the device to have three electrodes patterned on the surface of the stacked film: source, drain, and gate. Briefly, sets of three Au electrodes were fabricated on a SiO_2/Si substrate using conventional photolithography, which were designed such that pads for probing were 10 mm away from the channel. This would allow us to directly probe the electrodes using probe tips that were connected to the electrical measurement station, rather than go through the process of setting up a PCB to route the electrical signals. The electrodes were peeled off the substrate (using a KOH etch) and transferred to the stacked MoS_2/PTCDA/MoS_2 film. Next, a laser scriber[18] was used to etch away the area of the stacked film between the to-be channel and the gate electrode, as well as etch a box around the entire gate electrode to isolate it from the source and drain electrodes. Finally, the electrodes were coated with photoresist (PR) and windows were patterned in the PR layer to expose 1) the channel area plus a portion of the gate electrode and 2) the Au pads for probing. The purpose of the PR layer is to isolate the source and drain electrodes from the electrolyte and limit the size of the channel (~50 x 50 μm) without having to pattern the entire stack.

We started by testing the efficacy of the patterned gate electrode. Although the output and transfer curves shown in **Fig. A7.9a** indicate that the device is conducting and that the gate is working, the current running through the channel is only a few μA. If we cut off the patterned gate electrode and use a Ag wire to apply the gate instead, we see a 10-fold increase in the

current (**Fig. A7.9b**). Hence, we concluded that the use of a on-chip gate needed further optimization (related to electrode size and/or material choice) and proceeded to use the design in **Fig. 7.8a**, where the gate is applied though a wire that is inserted into the electrolyte droplet (for convenience, in the actual experiment we directly used the steel probe tip instead of a Ag wire, which we also found to provide effective gating).

After confirming that the gate was functional, we took a reference cross-polarized reflectance spectrum at $V_g = 0V$ (no voltage at the source and drain electrode grounded). An image from this spectrum (taken at $\lambda = 600$ nm) is shown in the left panel of **Fig. 7.8b**, where the top half of the image is a portion of the MoS_2/PTCDA/MoS_2 stack that is coated with PR (i.e., ungated area serving as a "control"), and the bottom half is the area of the stack to be gated. We then applied $V_g = +1V$ and took another spectrum. During this acquisition, we noticed that the contrast of the stack in the gated area started to become weaker. After the acquisition, we stopped applying the gate and repeated the $V_g = 0V$ spectrum. The result is shown in the right panel of **Fig. 7.8b**, where the image is scaled the same as the left panel. The ungated area (i.e., top half of image that was protected by PR) looks similar before and after the gating (wrinkles in the after image are likely from intercalation of the ionic liquid into the PR, causing swelling). However, we can see that the area that was gated now exhibits significantly weaker contrast than before the application of the gate.

It is unclear the origin of this irreversible reduction in anisotropy of the PTCDA layer, which was unexpected since the molecular film was trapped between two layers of MoS_2 (i.e., should not be dissolving). This is also odd because the amount of current flowing through the device during the gating should not be significant, so we would not expect any electrochemical process/reaction to be happening here, although this now seems like a possibility (i.e.,

degradation of the PTCDA layer by oxidation). It is also possible that the gating somehow induced the reordination of the PTCDA molecules into a disordered film, which would also cause a reduction of the anisotropic response.

7.4.3 Electrochemically-Tunable Optical Responses

Although we were not able to see a reversible change in the PTCDA response by gating the MoS_2 layer, the electrolyte gating experiment discussed in the previous subsection showed promise for another method of controlling the spectral response: using the PTCDA (not the MoS_2) as the active layer. Unlike semiconducting MoS_2, however, 2D molecular crystals are insulating in-plane (only pi-stacked molecular crystals are weakly semiconducting due to significant orbital overlap between molecules; crystals bound by weak hydrogen bonds are insulating). So, although it is not possible to "dope" the molecular layer in the same sense as one could for an inorganic crystal, it is possible to inject electrons that remain localized on each molecule, i.e., through chemical or electrochemical reduction.

Figure 7.9a shows the reversible, two-electron reduction of PDI[28] (also applicable to PTCDA and PDI derivatives). Unlike the case of inorganic crystals, where small amounts of doping causes relatively minor changes in intensity or peak position,[27] injecting one or more electrons onto a single molecule dramatically alters the spectral response, as seen from the absorption spectra of PDI, PDI^{1-}, and PDI^{2-} derivatives shown in **Fig. 7.9b**.[28] Hence, one can envision a kind of "on-chip" electrochemical device, such as the one schematically depicted in **Fig. 7.9c**. Sweeping the voltage across such a device would tune the absorption range and magnitude of the optical anisotropy, such that the response could be switched on or off depending on the wavelength of excitation. Furthermore, substituting the liquid electrolyte for a

solid-state electrolyte would enable integration with other electronic components, paving the way for atomically-thin electrochromic technologies.

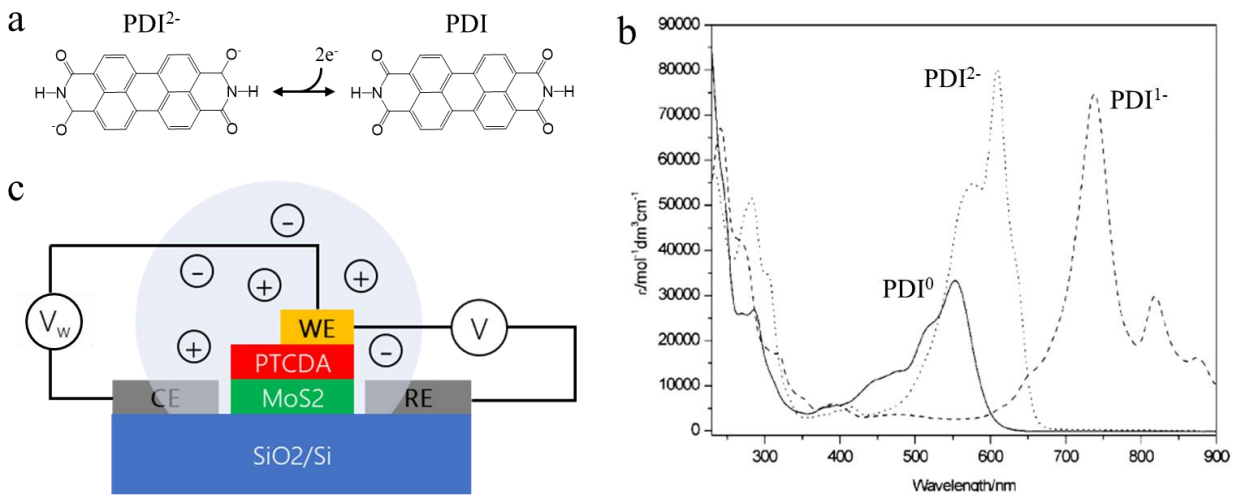

Figure 7.9. Idea for modulating the optical response of a PTCDA film by electrochemical reduction of the PTCDA molecules. a) The reversible two-electron reduction of PDI, b) solution-phase absorption spectra of PDI derivatives in the 0, -1, and -2 oxidation states, prepared via electrochemical reduction, and c) schematic of an "on-chip" electrochemical cell proposed for the experiment. The electrolyte is solid-state, and the working electrode (WE), reference electrode (RE), and counter electrode (CE) are all fully-patterned on the surface of the wafer. Graph in part (b) is reproduced from Ref. 28.

7.5 Summary

In this chapter, we introduced ideas and proof-of-concept experiments for taking our 2D molecular films and working towards implementation in functional technologies: from synthesis to modification to patterning to integration. We discussed opportunities for synthesizing complex molecular solids, such as bimolecular crystals, or using the perylene-based molecular crystals as templates to grow large crystals of organic materials that traditionally have very small domain sizes. We then described the possibilities for performing post-synthetic modification reactions, for example, by taking advantage of organic and organometallic reaction chemistries to attached larger compounds to the surface of inorganic 2D materials using the molecular film as a scaffold, or by applying some kind of stimulation, such as heat or light, to initiate a change in the

molecular layer post-deposition. We also presented numerous methodologies for patterning the molecular films, either by patterning the TMD layer prior to deposition, or by selectively pattering the molecular layer post-deposition and subsequently redepositing another material in the void areas. Lastly, we showed the potential for integration, enabled by the ability of these films to be transferred and stacked. The molecular films can be combined with other materials to produce artificial solids whose compositions are defined at the atomic-scale, allowing us to design materials with desired properties (such as light-matter interactions) from the bottom-up. The stacking and transfer techniques further allowed us to demonstrate opportunities in electrochromic devices, based on the ultra-sensitivity of the optical responses of these atomically-thin films to changes in their dielectric environment or charge state.

7.6 Appendix

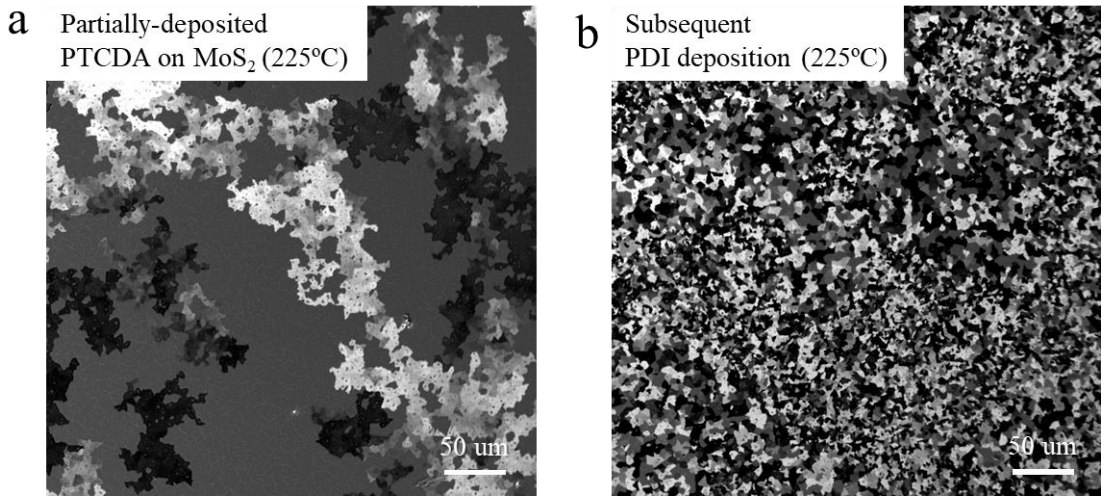

Figure A7.1. a) Partial film of PTCDA on MoS_2 that was deposited at T = 225ºC, and b) subsequent deposition of PDI on the film from (a), using the same temperature. The entire film in (b) is composed of pure PDI domains, but the morphology retains some characteristics of the original PTCDA film.

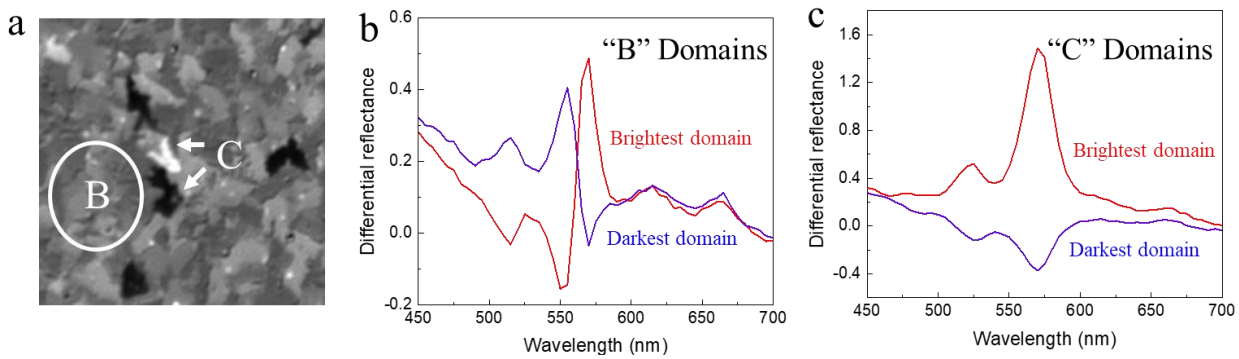

Figure A7.2. a) Same film described in Fig. 7.1a, images at θ_A = -3º and λ = 550 nm, b) full cross-polarized spectrum of the brightest and darkest of the domains labeled "B", and c) full cross-polarized spectrum of the brightest and darkest of the domains labeled "C".

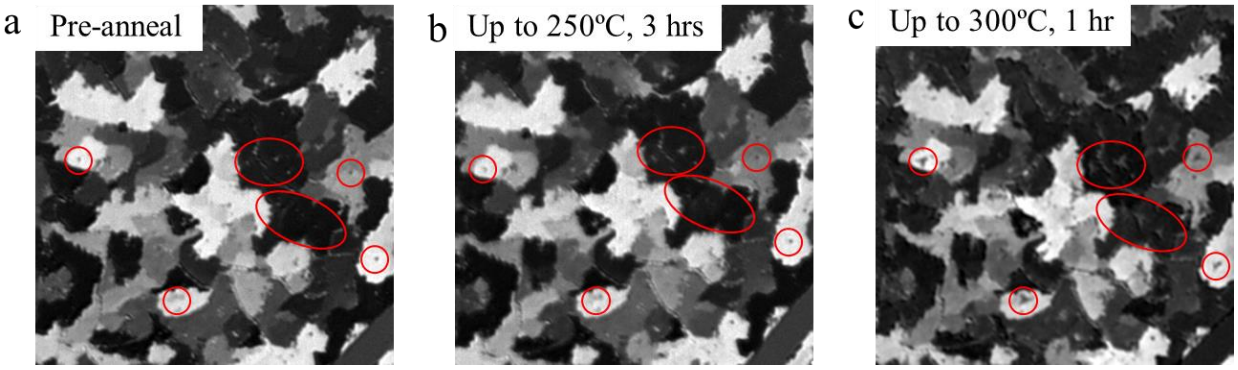

Figure A7.3. Cross-polarized images of a) a nearly-continuous film of PTCDA on MoS_2, b) the same film after annealing at various increasing temperatures up to 250ºC for a total of 3 hours, and c) the same film after annealing up to 300ºC for an additional 1 hour. Red circles indicate holes in the PTCDA film, to guide the eye.

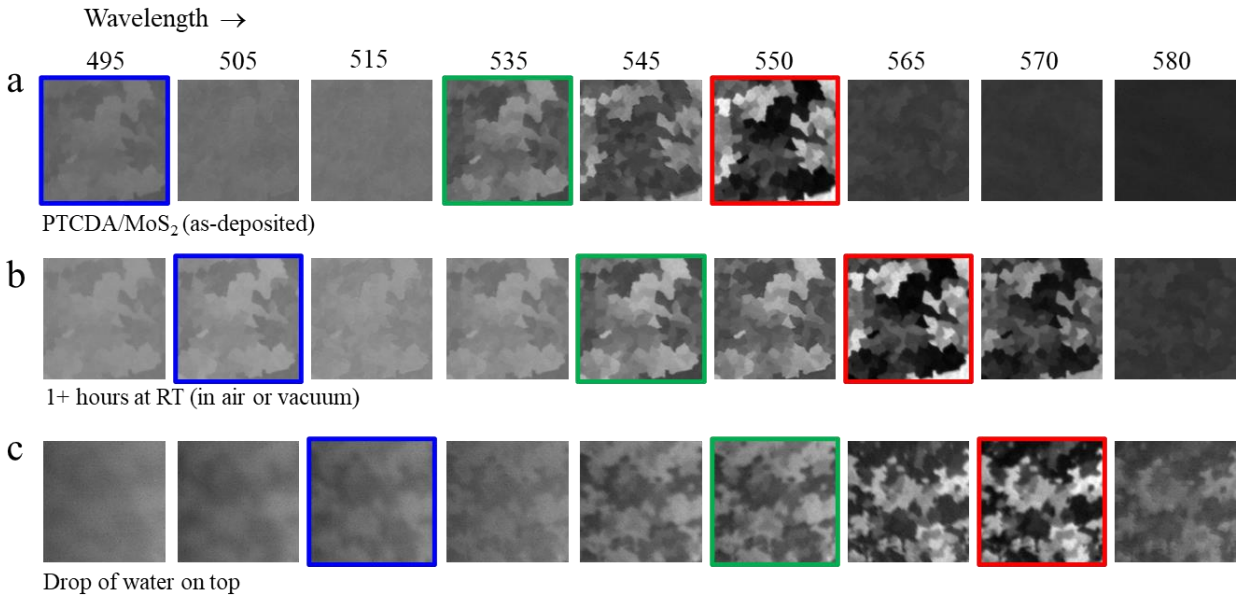

Figure A7.4. Selected images (wavelengths labelled above (a)) from the cross-polarized reflection spectra shown in Fig. 7.6a: a) an as-deposited PTCDA film, b) the film after sitting at room temperature for 1+ hrs, and c) the film with a drop of water on the surface. Colored boxes indicate the same peaks in the anisotropy that are marked with asterisks in Fig. 7.6a. Note the intervals between images are uneven due to space constraints. Each image is 50 x 50 µm.

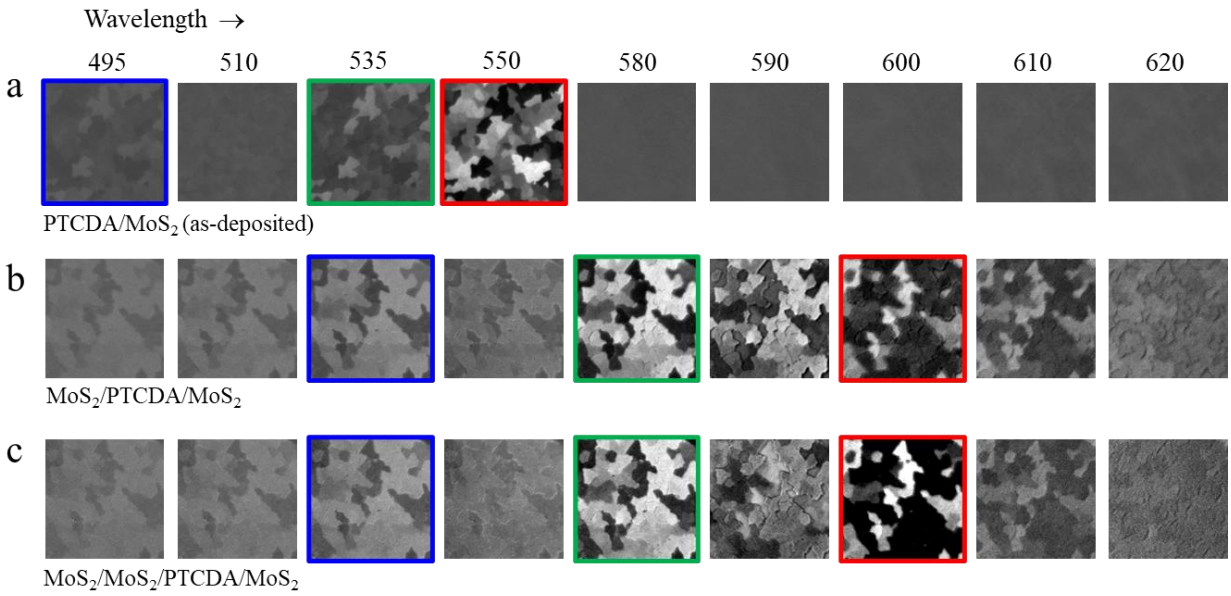

Figure A7.5. Selected images (wavelengths labelled above (a)) from the cross-polarized reflection spectra shown in Fig. 7.6b: a) an as-deposited PTCDA film, b) the film after stacking one layer of MoS_2 on top, and c) the film after stacking a second layer of MoS_2 on top. Colored boxes indicate the same peaks in the anisotropy that are marked with asterisks in Fig. 7.6b. Note the intervals between images are uneven due to space constraints. Each image is 50 x 50 µm.

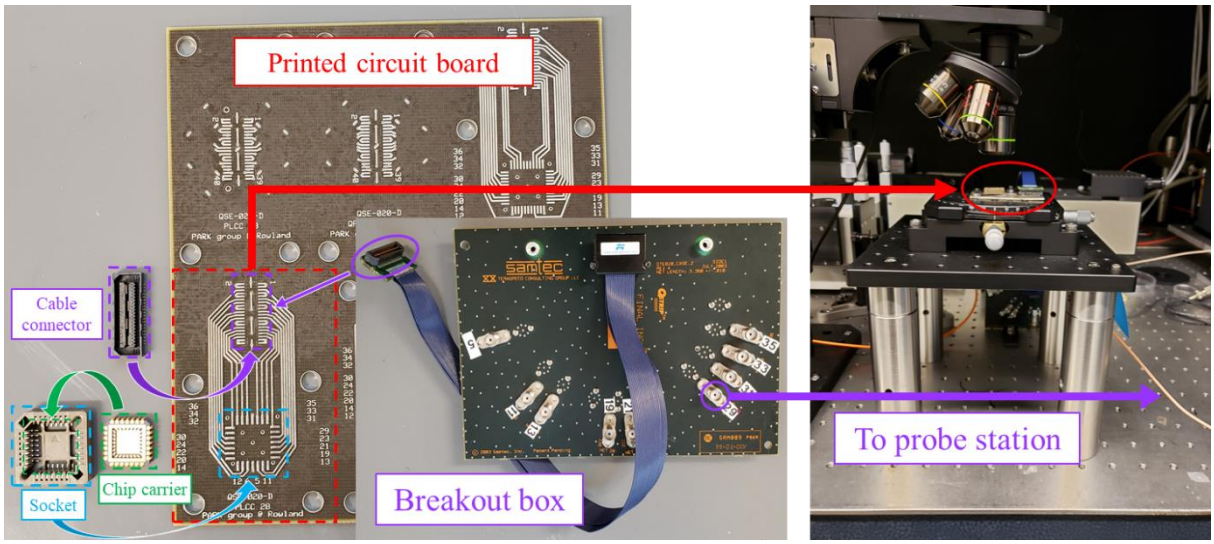

Figure A7.6. Setup used to perform the simultaneous optical and electrical measurements described in Fig. 7.7. The device was mounted to a chip carrier (indicated in green), which was placed inside a socket (indicated in light blue) that was soldered onto a PCB (indicated in red). A cable connector was soldered onto the other end of the PCB, which was connected to a breakout box from which the electrical signals were routed to the probe station (all indicated in purple). The final structure (PCB with the device wire-bonded and cable attached) was mounted to the stage underneath cross-polarized microscope (red circle in rightmost image).

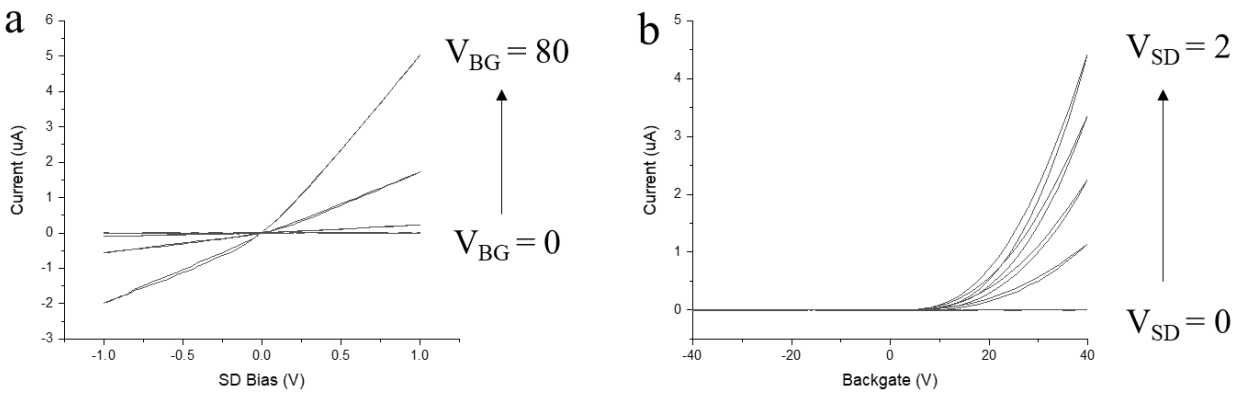

Figure A7.7. Electrical characteristics of a backgated device like the one shown in Fig. 7.7. a) Output curves taken by sweeping the source-drain voltage at various backgate voltages from 0V to 80V, and b) transfer curves taken by sweeping the backgate at various source-drain voltages from 0V to 2V.

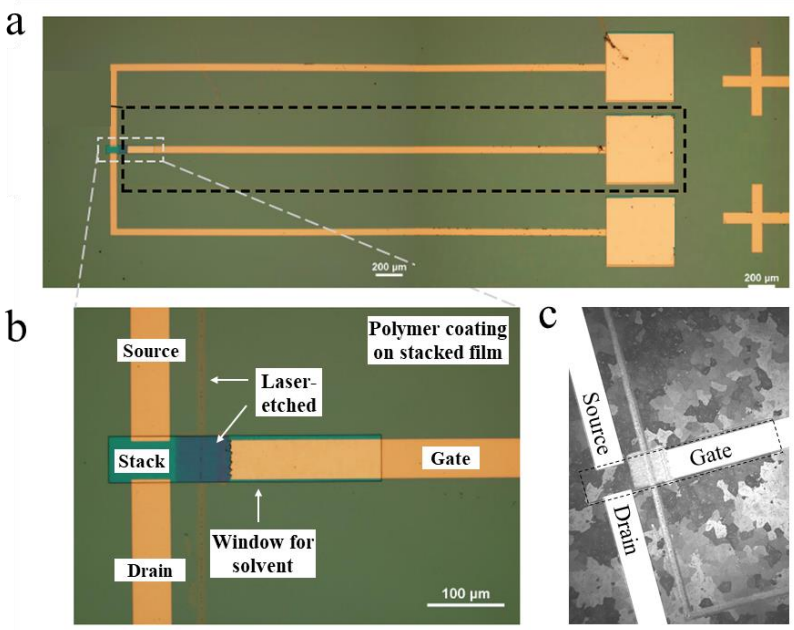

Figure A7.8. Optical images of the original design for the device shown in Fig. 7.8 (i.e., using a patterned gate electrode), where (a) shows the three 10-mm-long electrodes transferred onto the stacked MoS_2/PTCDA/MoS_2 film, and (b) shows a magnified image of the channel area. c) What the device looks like under cross-polarizers, where the polymer window is outlined with the dashed black box. The final device that was actually used looked the same, except the patterned gate was not connected, and the gate was applied to the ionic liquid drop

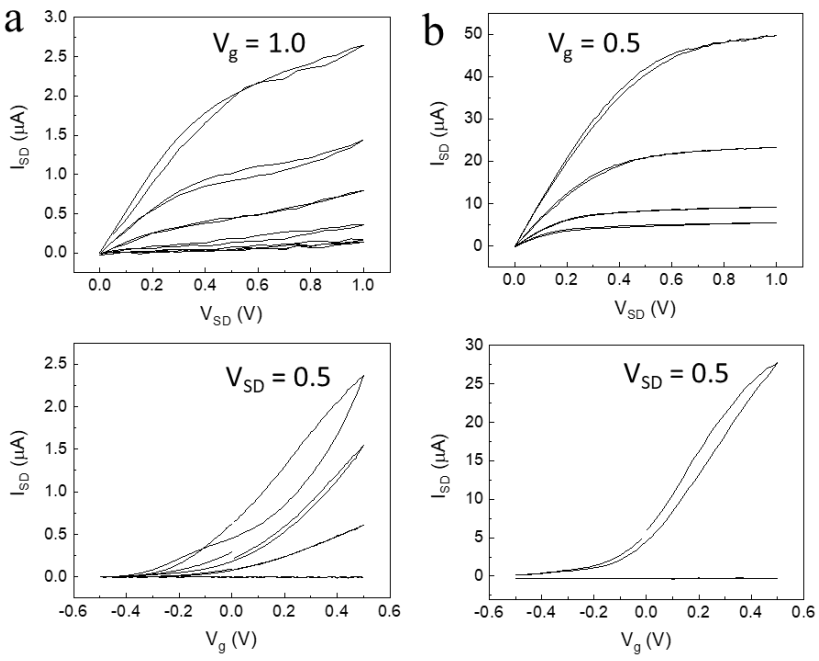

Figure A7.9. Electrical characteristics of an electrolyte-gated device similar to the one shown in Fig. 7.8, where the method for applying the gate was either a) a patterned Au gate electrode and b) a Ag wire. The top panels show the output curves taken by sweeping the source-drain voltage at various backgate voltages from 0V to 1V for (a) and 0V to 0.5V for (b). The bottom panels show the transfer curves taken by sweeping the backgate at various source-drain voltages from 0V to 0.5V.

7.7 References

(1) Wang, C.; Dong, H.; Jiang, L.; Hu, W. Organic Semiconductor Crystals. *Chem. Soc. Rev.* **2018**, *47* (2), 422–500.

(2) Zhang, X.; Dong, H.; Hu, W. Organic Semiconductor Single Crystals for Electronics and Photonics. *Adv. Mater.* **2018**, *30* (44), 1801048.

(3) Ostroverkhova, O. *Handbook of Organic Materials for Electronic and Photonic Devices*; Woodhead Publishing: Duxford, United Kingdom, 2019.

(4) Jones, W. *Organic Molecular Solids Properties and Applications*; CRC Press: Boca Raton, FL, 1997.

(5) Jazbinsek, M.; Günter, P. Molecular Crystals and Thin Films for Photonics. In *Handbook of Organic Materials for Electronic and Photonic Devices*; Elsevier, 2019; pp 177–210.

(6) Datta, S.; Grant, D. J. W. Crystal Structures of Drugs: Advances in Determination, Prediction and Engineering. *Nat Rev Drug Discov* **2004**, *3* (1), 42–57.

(7) Hunger, K. The Effect of Crystal Structure on Colour Application Properties of Organic Pigments*. *Review of Progress in Coloration and Related Topics* **1999**, *29* (1), 71–84.

(8) Lee, S. K.; Zu, Y.; Herrmann, A.; Geerts, Y.; Müllen, K.; Bard, A. J. Electrochemistry, Spectroscopy and Electrogenerated Chemiluminescence of Perylene, Terrylene, and Quaterrylene Diimides in Aprotic Solution. *J. Am. Chem. Soc.* **1999**, *121* (14), 3513–3520.

(9) Hieulle, J.; Silly, F. Two-Dimensional Hydrogen-Bonded Nanoarchitecture Composed of Rectangular 3,4,9,10-Perylenetetracarboxylic Diimide and Boomerang-Shaped Molecules Resulting from the Dissociation of 1,3,5-Tris(4-Aminophenyl)Benzene. *ACS Omega* **2020**, *5* (8), 3964–3968.

(10) Álvarez, L.; Peláez, S.; Caillard, R.; Serena, P. A.; Martín-Gago, J. A.; Méndez, J. Metal-Organic Extended 2D Structures: Fe-PTCDA on Au(111). *Nanotechnology* **2010**, *21* (30), 305703.

(11) Liu, Y.; Guo, J.; Zhu, E.; Liao, L.; Lee, S.-J.; Ding, M.; Shakir, I.; Gambin, V.; Huang, Y.; Duan, X. Approaching the Schottky–Mott Limit in van Der Waals Metal–Semiconductor Junctions. *Nature* **2018**, *557* (7707), 696–700.

(12) Sreeprasad, T. S.; Berry, V. How Do the Electrical Properties of Graphene Change with Its Functionalization? *Small* **2013**, *9* (3), 341–350.

(13) Kamm, J. M.; Iverson, C. P.; Lau, W.-Y.; Hopkins, M. D. Axial Ligand Effects on the Structures of Self-Assembled Gallium–Porphyrin Monolayers on Highly Oriented Pyrolytic Graphite. *Langmuir* **2016**, *32* (2), 487–495.

(14) Wang, Y.; Iglesias, D.; Gali, S. M.; Beljonne, D.; Samorì, P. Light-Programmable Logic-in-Memory in 2D Semiconductors Enabled by Supramolecular Functionalization: Photoresponsive Collective Effect of Aligned Molecular Dipoles. *ACS Nano* **2021**, *15* (8), 13732–13741.

(15) Wang, X.; Tabakman, S. M.; Dai, H. Atomic Layer Deposition of Metal Oxides on Pristine and Functionalized Graphene. *J. Am. Chem. Soc.* **2008**, *130* (26), 8152–8153.

(16) Alaboson, J. M. P.; Wang, Q. H.; Emery, J. D.; Lipson, A. L.; Bedzyk, M. J.; Elam, J. W.; Pellin, M. J.; Hersam, M. C. Seeding Atomic Layer Deposition of High- *k* Dielectrics on Epitaxial Graphene with Organic Self-Assembled Monolayers. *ACS Nano* **2011**, *5* (6), 5223–5232.

(17) Mannix, A. J.; Ye, A.; Sung, S. H.; Ray, A.; Mujid, F.; Park, C.; Lee, M.; Kang, J.-H.; Shreiner, R.; High, A. A.; Muller, D. A.; Hovden, R.; Park, J. Robotic Four-Dimensional Pixel Assembly of van Der Waals Solids. *Nat. Nanotechnol.* **2022**, *17* (4), 361–366.

(18) Poddar, P. K.; Zhong, Y.; Mannix, A. J.; Mujid, F.; Yu, J.; Liang, C.; Kang, J.-H.; Lee, M.; Xie, S.; Park, J. Resist-Free Lithography for Monolayer Transition Metal Dichalcogenides. *Nano Lett.* **2022**, *22* (2), 726–732.

(19) Zhong, Y.; Cheng, B.; Park, C.; Ray, A.; Brown, S.; Mujid, F.; Lee, J.-U.; Zhou, H.; Suh, J.; Lee, K.-H.; Mannix, A. J.; Kang, K.; Sibener, S. J.; Muller, D. A.; Park, J. Wafer-Scale Synthesis of Monolayer Two-Dimensional Porphyrin Polymers for Hybrid Superlattices. *Science* **2019**, *366* (6471), 1379–1384.

(20) Guimarães, M. H. D.; Gao, H.; Han, Y.; Kang, K.; Xie, S.; Kim, C.-J.; Muller, D. A.; Ralph, D. C.; Park, J. Atomically Thin Ohmic Edge Contacts Between Two-Dimensional Materials. *ACS Nano* **2016**, *10* (6), 6392–6399.

(21) Levendorf, M. P.; Kim, C.-J.; Brown, L.; Huang, P. Y.; Havener, R. W.; Muller, D. A.; Park, J. Graphene and Boron Nitride Lateral Heterostructures for Atomically Thin Circuitry. *Nature* **2012**, *488* (7413), 627–632.

(22) Gao, H.; Suh, J.; Cao, M. C.; Joe, A. Y.; Mujid, F.; Lee, K.-H.; Xie, S.; Poddar, P.; Lee, J.-U.; Kang, K.; Kim, P.; Muller, D. A.; Park, J. Tuning Electrical Conductance of MoS_2 Monolayers through Substitutional Doping. *Nano Lett.* **2020**, *20* (6), 4095–4101.

(23) Kang, K.; Lee, K.-H.; Han, Y.; Gao, H.; Xie, S.; Muller, D. A.; Park, J. Layer-by-Layer Assembly of Two-Dimensional Materials into Wafer-Scale Heterostructures. *Nature* **2017**, *550* (7675), 229–233.

(24) Novoselov, K. S.; Mishchenko, A.; Carvalho, A.; Castro Neto, A. H. 2D Materials and van Der Waals Heterostructures. *Science* **2016**, *353* (6298), aac9439.

(25) Yu, H.; Liao, M.; Zhao, W.; Liu, G.; Zhou, X. J.; Wei, Z.; Xu, X.; Liu, K.; Hu, Z.; Deng, K.; Zhou, S.; Shi, J.-A.; Gu, L.; Shen, C.; Zhang, T.; Du, L.; Xie, L.; Zhu, J.; Chen, W.; Yang, R.; Shi, D.; Zhang, G. Wafer-Scale Growth and Transfer of Highly-Oriented Monolayer MoS_2 Continuous Films. *ACS Nano* **2017**, *11* (12), 12001–12007.

(26) Zheng, Y. J.; Huang, Y. L.; Chen, Y.; Zhao, W.; Eda, G.; Spataru, C. D.; Zhang, W.; Chang, Y.-H.; Li, L.-J.; Chi, D.; Quek, S. Y.; Wee, A. T. S. Heterointerface Screening Effects between Organic Monolayers and Monolayer Transition Metal Dichalcogenides. *ACS Nano* **2016**, *10* (2), 2476–2484.

(27) Mak, K. F.; He, K.; Lee, C.; Lee, G. H.; Hone, J.; Heinz, T. F.; Shan, J. Tightly Bound Trions in Monolayer MoS2. *Nature Mater* **2013**, *12* (3), 207–211.

(28) Slater, A. G.; Davies, E. S.; Argent, S. P.; Lewis, W.; Blake, A. J.; McMaster, J.; Champness, N. R. Bis-Thioether-Substituted Perylene Diimides: Structural, Electrochemical, and Spectroelectrochemical Properties. *J. Org. Chem.* **2013**, *78* (7), 2853–2862.